La borsa di dottorato è stata cofinanziata con risorse del
Programma Operativo Nazionale Ricerca e Innovazione 2014-2020 (CCI 2014IT16M2OP005)
Fondo Sociale Europeo, Azione I.1 “Dottorati Innovativi con caratterizzazione Industriale”

UNIVERSITA’ DELLA CALABRIA

Dipartimento di FISICA

Dottorato di Ricerca in Scienze e Tecnologie Fisiche, Chimiche e dei Materiali

CICLO XXXIII

IMPLEMENTATION AND CHARACTERIZATION OF FILMS FOR ELECTROCHROMIC DEVICES, ENERGETICALLY SELF-SUFFICIENT, TO DEVELOP THE ENERGY SAVING OF BUILDINGS

Settore Scientifico Disciplinare FIS/07

Coordinatore: Ch.ma Prof.ssa Gabriella Cipparrone

Firma __ Firma oscurata in base alle linee guida del Garante della privacy

Supervisore: Dr. Marco Castriota

Firma Firma oscurata in base alle linee guida del Garante della privacy

Dottoranda: Dott.ssa Carmen Rizzuto

Firma Firma oscurata in base alle linee guida del Garante della privacy

To my Family

Table of Contents

Abstract

The need to reduce the energy consumption from the excessive use of non-renewable resources such as fossil fuels and the growing emissions of CO_2 into the atmosphere, estimated at about 30-40 % [1] has helped to direct research towards the development of technologies dedicated to the delicate issue of energy saving. Within the construction sector, the largest contribution to energy loss, about 25-35 % comes from the use of inefficient windows [2]. The idea of improving the efficiency of buildings by developing the "Zero Energy Buildings" (ZEB) technology is based precisely on the use of a modern concept of window, now defined as dynamic and better known as "Smart Window" [3]. Industrial research is therefore projected toward the improvement of existing devices and the implementation of new solutions able to control the transmission values of the incident solar radiation, the energy recovery that follows, and the control of the flow of energy as a function of the cyclical variation of the seasons [4].

The introduction of electrochromic technology in the manufacture of smart windows has marked a significant improvement in the construction sector, as it is estimated that it is possible to reduce the energy consumption necessary for the heating or cooling of the rooms of a building, by up to 30% [5].

The theme of the research is the synthesis and characterization of electrochromic materials, to be used in the realization of electrochromic devices energetically self-sufficient for the promotion of energy-saving of buildings.

First, the study of tungsten trioxide (WO_3) and titanium dioxide (TiO_2) thin films has been reported. WO_3 and TiO_2 thin films were synthesized with the Sol-gel method and then, they were annealed at different annealing temperatures. The structural properties regarding to the morphological characterization of the synthesized films (amorphous and crystalline) have been evaluated through Micro-Raman Spectroscopic investigations. The electrochemical properties of films have been characterized by Cyclic Voltammetry. The diffusion coefficients of lithium ions have been evaluated for each film electrode that has been immersed in liquid electrolyte and gel polymer electrolyte systems.

Each film has been used as the electrode for assembling the electrochromic devices in the classic "*sandwich*" configuration, using a PMMA- gel polymer electrolyte polymeric in

a solution of lithium perchlorate in propylene carbonate. The resulting electrochromic devices have been characterized by Cyclic Voltammetry. Subsequently, the main technological properties such as the variation of transmittance, the switching times, and the coloration efficiency, which are depending on the morphology of the individual electrodes and by the temperature of thermal treatment, were investigated by UV-Vis-NIR spectroscopy.

Later, two classes of potential electrolytes valid for the construction of an electrochromic device have been investigated. The first consists of a liquid electrolyte based on a lithium salt, lithium perchlorate in propylene carbonate solution, and in a mixture of propylene carbonate and ethylene carbonate. The second class involves a polymer gel electrolyte based on Poly(methylmethacrylate). A detailed structural, electrochemical, and thermal characterization by ATR-FTIR Spectroscopy, Cyclic Voltammetry, Differential Scanning Calorimetry technique, and Thermal Gravimetric Analysis have been proposed to select the best electrolyte system to be used in electrochromic devices.

Afterward, the realization of an electrochromic device "all-in-one" based on an electrochromic mixture of viologen-ferrocene of dimensions (10 cm ×10 cm) has been discussed. The realization of a homogeneous mask of spacers inside the device has been realized by using the photolithography technique. The electrochromic properties of the device have been investigated through Cyclic Voltammetry. The structural properties of the device in the OFF/ON states have been characterized by Micro-Raman Spectroscopy, while the optical performance of the device in terms of transmission modulation, color contrast ratio, and coloration efficiency were estimated by UV-Vis-Nir Spectroscopy.

Finally, the industrial proposal concerning the design of systems to be used for the construction of *large-area* electrochromic devices is presented. Three specific industrial prototypes have been developed to perform the automated operations of device filling, thin film deposition on substrate, and device closure with a UV system.

Moreover, the Etching process for the production of ITO tracks on glass sheets has been discussed. The treated glass sheets have been subsequently used for the construction of a prototype of an *"all-in-one"* electrochromic device based on the electrochromic mixture of a salt of viologen and ferrocene of dimensions (16 cm × 16 cm). The exclusivity of the

developed prototype, concerns the matrix of pixels that compose it, where every single pixel can be electrically powered.

References

[1] C. G. Granqvist, I. P. Bayrak Pehlivan, G. A. Niklasson, *Surf. Coat. Technol*., (2018) **336** 133-138.

[2] Global Alliance for Buildings and Construction, International Energy Agency, and the United Nations Environment Programme (2019): 2019 global status report for buildings and construction: Towards a zero-emission, efficient and resilient buildings, and construction sector.

[3] M. Casini, *International Journal of Civil and Structural Engineering*, (2015) **2** 230-238.

[4] A. Cannavale, U. Ayr, F. Fiorito, F. Martellotta, *Energies*, (2020) **13** 1449.

[5] C. M. Lampert, *Solar Energy Materials and Solar Cells*, (1998) **52** 207-221.

Abstract

L'esigenza di ridurre il consumo energetico proveniente dall'uso smisurato di risorse non rinnovabili come i combustibili fossili e le crescenti emissioni di CO_2 nell'atmosfera, stimato per circa il 30-40 % [1] ha contribuito ad indirizzare la ricerca verso lo sviluppo di tecnologie dedicate al delicato tema del risparmio energetico. Nell'ambito del settore delle costruzioni il maggior contributo alla perdita di energia, circa il 25-35% deriva dall'utilizzo di finestre poco efficienti [2]. L'idea di migliorare l'efficienza degli edifici sviluppando la tecnologia "*Zero Energy Buildings*" (ZEB) è basata proprio sull'utilizzo di un concetto moderno di finestra, adesso definita dinamica e meglio conosciuta come "Finestra Intelligente o *Smart Window*" [3]. La ricerca industriale è quindi proiettata verso il miglioramento dei dispositivi esistenti e sull'implementazione di nuove soluzioni in grado di controllare i valori di trasmissione della radiazione solare incidente, il recupero energetico che ne consegue ed il controllo del flusso di energia in funzione del variare ciclico delle stagioni [4].

L'introduzione della tecnologia elettrocromica nella produzione delle finestre intelligenti ha segnato un notevole miglioramento nel settore edilizio, in quanto si stima che è possibile abbattere i consumi energetici necessari per il riscaldamento o il raffreddamento degli ambienti di un edificio, fino al 30% [5].

Il tema della ricerca riguarda la sintesi e la caratterizzazione di materiali elettrocromici, da impiegare nella realizzazione di dispositivi elettrocromici energeticamente autosufficienti ai fini della promozione del risparmio energetico degli edifici (*Energy Saving*).

Inizialmente è stato affrontato lo studio di film sottili di tungsteno triossido (WO_3) e biossido di titanio (TiO_2). I film sottili sono stati sintetizzati con il metodo *Sol-gel* e successivamente sono stati sottoposti a trattamenti termici a diverse temperature. Le proprietà strutturali con particolare riferimento alla caratterizzazione morfologica dei film sottili sintetizzati (amorfi e cristallini) sono state valutate mediante indagini spettroscopiche Micro-Raman. Le proprietà elettrochimiche dei film sottili sono state caratterizzate mediante Voltammetria ciclica ed espresse in termini di coefficienti di diffusione di ioni litio, valutati per i film immersi come elettrodi in sistemi elettrolitici liquidi e gel polimerici.

Gli stessi poi, sono stati utilizzati per assemblare dispositivi elettrocromici composti nella classica configurazione "sandwich", a base di un gel polimerico elettrolitico di poli(metilmetacrilato) in una soluzione elettrolitica di perclorato di litio in carbonato di propilene. I risultanti dispositivi elettrocromici sono stati sottoposti a caratterizzazione elettrochimica mediante Voltammetria Ciclica. Successivamente, le principali proprietà tecnologiche quali la variazione di trasmittanza, i tempi di accensione e spegnimento e l'efficienza di colorazione dei sistemi, dipendenti dalla morfologia dei singoli elettrodi e dalle temperature di trattamento termico, sono stati investigate mediante Spettroscopia UV-Vis-NIR.

A seguire, sono state investigate due classi di elettroliti potenzialmente valide per la costruzione di un device elettrocromico. La prima classe consiste di un elettrolita liquido basato su un sale di litio, litio perclorato in soluzione di carbonato di propilene e in una miscela di propilene carbonato ed etilene carbonato. La seconda classe comprende invece un elettrolita gel polimerico a base di poli(metilmetacrilato). Una dettagliata caratterizzazione strutturale, elettrochimica e termica mediante Spettroscopia ATR-FTIR, Voltammetria ciclica e le tecniche di Calorimetria a Scansione Differenziale e di Analisi Termogravimetrica sono state proposte al fine di selezionare il miglior sistema elettrolitico da impiegare in dispositivi elettrocromici.

In seguito è stata discussa la realizzazione di un dispositivo elettrocromico "*all-in-one*" a base di una miscela elettrocromica viologeno-ferrocene di dimensioni (10 cm × 10 cm). La realizzazione di una maschera omogenea di spaziatori all'interno del device è stata ottenuta facendo uso della tecnica della fotolitografia. Le proprietà elettrocromiche del device sono state investigate mediante Voltammetria ciclica. Le proprietà strutturali del dispositivo negli stati di accensione e spegnimento sono state caratterizzate mediante Spettroscopia Micro-Raman, mentre le prestazioni ottiche del device in termini di modulazione della trasmittanza, contrasto cromatico ed efficienza di colorazione sono state stimate tramite la Spettroscopia UV-Vis-Nir.

Infine, viene presentata la proposta industriale riguardante la progettazione di sistemi da impiegare per la costruzione di dispositivi elettrocromici "*large-area*". Sono stati sviluppati tre prototipi industriali specifici per eseguire le operazioni automatizzate di riempimento del device, deposizione di film sottili su substrato e chiusura del device con

sistema UV. È stato affrontato anche lo studio del processo di Etching per la produzione di piste di ITO su superfici di vetro. I vetri trattati sono stati successivamente impiegati per la costruzione di un prototipo di un dispositivo elettrocromico "*all-in-one*" basato sulla miscela elettrocromica a base di un sale di viologeno e ferrocene di dimensioni (16 cm × 16 cm). L'unicità del prototipo sviluppato, riguarda la matrice di pixels che lo compone, dove ogni singolo pixel può essere alimentato elettricamente.

Riferimenti Bibliografici

[1] C. G. Granqvist, I. P. Bayrak Pehlivan, G. A. Niklasson, *Surf. Coat. Technol*., (2018) **336** 133-138.

[2] Global Alliance for Buildings and Construction, International Energy Agency, and the United Nations Environment Programme (2019): 2019 global status report for buildings and construction: Towards a zero-emission, efficient and resilient buildings, and construction sector.

[3] M. Casini, *International Journal of Civil and Structural Engineering*, (2015) **2** 230-238.

[4] A. Cannavale, U. Ayr, F. Fiorito, F. Martellotta, *Energies*, (2020) **13** 1449.

[5] C. M. Lampert, *Solar Energy Materials and Solar Cells*, (1998) **52** 207-221.

Introduction

"*Making our homes and buildings fit for a greener future-2021*" is the new proposal presented by the European Union which achieves to support the development of renewable and less polluting energy systems for our homes and public buildings. The proposal aims to decrease emissions, save energy, tackle energy poverty, improve quality of life and generate jobs and growth [1]. Also, the European Parliament approved the final Energy Performance of Buildings Directive, in which are taking into account-all measures that will accelerate the rate of building renovation and allow to realize new smarter buildings in terms of energy efficiency and saving [2]. It can be estimated that consumption of the energy from fossil sources is responsible for about 30–40% of primary energy consumption worldwide [3] and, according to the Global Status Report 2018, edited by the United Nations, building construction and operations accounted for nearly 40% of energy-related carbon dioxide (CO_2) emissions in 2017 [4]. In the buildings sector, the main loss of energy is through glazing, and according to the Department of Energy of the United States, the main energy losses are due to inefficient windows and it is a value varying from 25 % to 35 %. The increasing demand to improve the efficiency of buildings, and consequently the development of the called "Zero Energy Buildings" (ZEB) base on the new concept of a dynamic window or commonly known as "Smart Window" are the new challenge of the industrial and scientific world. A dynamic window or "Smart Window" is a transparent solution that requires an accurate design to reduce energy consumption for heating or cooling, to change color, or to opacify to ensure privacy [5].

All the industrial solutions are continuously focused on the improvement of existing devices or on the implementation of new solutions able to control the energy light transmission values, focusing on the choice of new performant material, accurate design, and improvement of high-performance glass systems and the control of the incident solar radiation. The introduction of electrochromic technology in the fabrication of smart windows is quite interesting. The first quantitative estimation of energy saving in buildings due to smart windows is done by the consideration of the half amount of quantity of incident radiation above the windows is visible light and so the amount of controllable energy is about 340 kWh/(m^2×year), considering a visible modulation

between 7% and 75%. [6]. A further estimation has been confirmed by a minimum value for yearly energy savings of about 170 kWh/(m^2×year) [6]. Investigated potential energy savings in buildings, due to integration of near-infrared EC devices throughout U.S. climate regions, finding up to 50% energy saving by dynamic simulations have been carried out and found that near-infrared EC devices can modulate thermal radiation while remaining transparent to visible light, without affecting either daylighting or building aesthetics [7, 8]. Recently studies estimated through the combination of many simulations and experimental data, the effect of the innovative solid-state electrochromic devices. The lowest global energy uses were reported for the innovative EC device, capable of reducing energy uses per floor area from 28.7kWh/ (m^2 × year) to 20.7 kWh/(m^2 × year) [9].

The research activity has been focused on the study, synthesis, and characterization of some materials to be used in electrochromic devices. The obtained electrochromic devices can transform the existing windows into "Smart Windows", also capable of promoting savings in terms of energy and costs of buildings.
In this Ph.D. work, quite important has been the development of a "pilot plant" that shows the main used strategies in order to make a real scale-up of the electrochromic technology developed in the laboratory (TRL-4) to a prototype for industrial applications (TRL-7).

In Chapter 1 is given a brief overview of the field of electrochromic materials, the basic elements which compose the devices, and the classic parameters used to characterize the performance of the devices. Starting from the definition of the Electrochromism phenomena, the main classes of electrochromic materials have been presented, from the inorganic electrochromic materials passing through the organic electrochromic materials. Some aspects regarding the type of electrolytes with a particular interest in the field of liquid electrolytes and gel polymer electrolytes are also shown.

In Chapter 2 the explanation of the theoretical principles of the main synthesis technology *i.e.*, the Sol-Gel technique and the deposition technique (spin-coating) used for the preparation of the investigated electrochromic materials taking into account especially, the thin films of tungsten trioxide and the titanium dioxide among the metal oxides, is shown.

Chapter 3 is composed of four sections in which are presented the theoretical aspects of some techniques used in the present work: Raman Spectroscopy, Infrared Spectroscopy, Impedance Spectroscopy, Cyclic Voltammetry, Differential Scanning Calorimetry and Thermogravimetric Analysis.

In Chapter 4, the Results and Discussion of the present work have been presented. First, the work has been focused on the study of thin films of tungsten trioxide and titanium dioxide after specific thermal treatments. The electrochemical and structural properties of these films have been characterized. Then, these films have been assembled in electrochromic devices and the structural, electrochemical, and optical characterization have been shown. Later, the liquid electrolytes and the gel polymer electrolytes have been deeply investigated from the point of view of ion associations, electrochemical, and thermal properties. The study of an electrochromic device based on Ethyl viologen diperchlorate, 1,1'-Diethyl Ferrocene, Bisphenol-A glycerolate diacrylate, and Irgacure 651, has been shown. The photolithography technique concerning the use of the photoresist which is useful for the fabrication of the essential component of the electrochromic device has been given. Interesting aspects concerning the industrial implementation of potential equipment for the fabrication of large-area electrochromic devices have been reported. A detailed presentation regarding the use of the etching process for the fabrication of patterned ITO tracks suitable for large-area electrochromic devices has been discussed.

In the "Conclusions and Future Perspective, " a summary of the conclusions and the future perspectives are discussed.

References

[1] https://ec.europa.eu/commission/presscorner/detail/en/fs_21_3673

[2] https://ec.europa.eu/commission/presscorner/detail/en/IP_18_3374

[3] C. G. Granqvist, I. P. Bayrak Pehlivan, G. A. Niklasson, Surf. Coat. Technol., (2018) 336 133-138.

[4] Global Alliance for Buildings and Construction, International Energy Agency, and the United Nations Environment Programme (2019): 2019 global status report for buildings and construction: Towards a zero-emission, efficient and resilient buildings, and construction sector.

[5] M. Casini, *International Journal of Civil and Structural Engineering*, (2015) **2** 230-238.

[6] A. Azens, A.; C. G. Granqvist, *J. Solid State Electrochem*. (2003) **7** 64-68.

[7] N. DeForest, A. Shehabi, J. O'Donnell, G. Garcia, J. Greenblatt, E. S. Lee, S. Selkowitz, D. J. Milliron, D.J., *Build. Environ*., (2015) **89** 107-117.

[8] N. DeForest, A. Shehabi, G. Garcia, J. Greenblatt, E. Masanet, E. S. Lee, S. Selkowitz, S. Milliron, *Build. Environ.,* (2013) **61** 160-168.

[9] A. Cannavale, F. Martellotta, P. Cossari, G. Gigli, U. Ayr, *Applied Energy*, (2018) **225** 975-985.

CHAPTER 1

Electrochromic Materials and Devices

1.1. The Electrochromism Phenomena

Electrochromism is a well-known phenomenon capable of providing the required variation in the optical properties, and presently some full-scale electrochromic smart windows are undergoing [1, 2]. Electrochromic materials are chemical species (donor or acceptor of electrons) that exhibit in general a visible and reversible color change in response to an external stimulus between two states, the bleached and the colored state or between more colored states [3-5]. The first evidence of electrochromism has been observed in the electrochromic tungsten oxide (WO_3) in the late 1960s [6] where the ability of the electrochromic material to modify its optical properties from transparent to dark/opaque after the reversibility insertion/extraction of charges under a small applied voltage has been studied in both amorphous and crystalline thin films of WO_3. Recent advancement in electrochromism technology is towards nanotechnology [7], which helps electrochromic devices to obtain energy savings and supports electrochromic glazing technology, the fabrication cost, and extended life-time of the device, overcoming the problem of the electrochromic device degradation.

1.2 Electrochromic Devices (ECDs)

An electrochromic device (ECD) is a combination of anodic and cathodic electrochromic materials in addition to some transparent ion conductors and glass or transparent flexible polymer, where the application of an electric field between the cathode and the anode can be realized in the ion movement in the device [8]. A typical ECD is composed of five layers known as *sandwich-configuration* as shown in Figure 1.2.1 [3] where there are: 1) two transparent Conducting Oxide substrates (TCO) based on glass for buildings-related applications or polymers such as polyethylene terephthalate (PET) or polycarbonate (PC), 2) an Ion Storage layer or electrochromic layer (cathodic EC material), 3) a transparent Liquid electrolytes or Polymer electrolytes acting as an ion-conducting layer and 4) another Electrochromic layer as Counter Electrode (anodic EC).

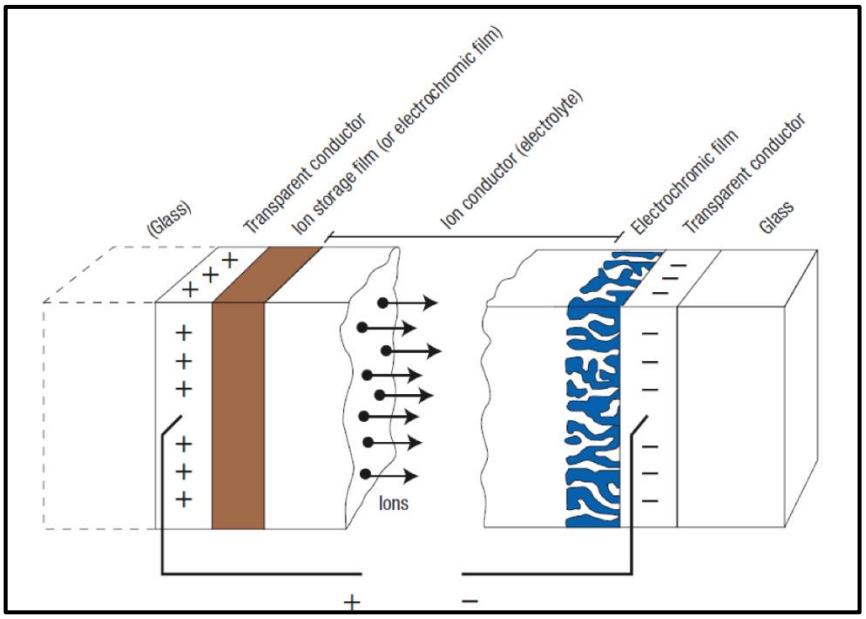

Figure 1.2.1. Schematization of an electrochromic device in a sandwich-configuration. The figure is taken from [9].

The reversible ion intercalation and de-intercalation processes between the ion storage and the counter electrode materials are responsible for the coloration or transparency of the device. The electrochromic devices can be used in both automotive and building industries for the fabrication of displays [10], electronic paper [11], smart windows [12, 13], rearview mirrors [14], helmet visors [15], and climate-adaptive buildings shells [16].

1.3. Electrochromic Materials

Electrochromes are materials that display electrochromic properties and they have been classified into three major types as a function of the physical state that they adopt during their neutral state and in the electrochromic process [17]:

1) *Type I* are electrochromes exist in their solution states. The electrochromic material diffuses through towards the surface of the electrode and undergoes a transfer process at the solid-liquid interface to reveal a color change. It can be present in the form of the reduction at the cathode or in the form of oxidation at the anode.

2) *Type II* are soluble electrochromes in their neutral states, where they show colorless. Then, when they diffuse from the cathode towards the anode, they undergo an electron transfer reaction and reveal a color state.
3) *Type III* are solid electrochromes (as thin films or particles) that they prevent their phase in all times of the electrochromic process.

Electrochromism can be observable in numerous materials such as inorganic and organics and they are further classified into different classes as Inorganic Metal oxides, Metal coordination complexes, Organic molecular dyes, and Organic conductive polymers.

Electrochromic devices based on organic materials possess some advantages such as intense coloration, ease of structural modification, low cost, and good processability. Electrochromic devices made up of inorganic materials are characterized by good electrochemical stability, a wide range of working temperatures. The implementation of electrochromic devices based on the nanocomposites i.e., the combination of the good properties of complementary organic and inorganic materials is the new frontier.

1.3.1. Inorganic Metal Oxides: WO_3 and TiO_2

The inorganic metal oxides are electrochromic materials based on transition metal oxides such as WO_3, V_2O_5, Nb_2O_5, TiO_2, $Ir(OH)_3$, $Ni(OH)_2$, etc., where their colors derive from the charge-transfer optical transitions. They exhibit highly colored states in the color range of blue and gray [4]. In their solid-state, metal transitions adopt a lattice structure that is attributable to octahedral geometry. When they are in their neutral states, the metal atom possesses identical oxidation states. During the electrochromic process, the metal undergoes two processes: the first is a reduction or oxidation reaction that is associated with to change of its valency that is ascribable to a color change of the electrochromic process. The second process is known as the intercalation or de-intercalation of ions in the available sites of the lattice structure to balance the cation or the anion after the redox process. [3].

Tungsten trioxide (WO_3) is a cathodic electrochromic material that has been long-studied for its interesting properties. Tungsten trioxide crystals possess a cubic structure also known as perovskite structure based on corner-sharing WO_6 octahedra, with W atoms situated at the center of the octahedra as shown in Figure 1.3.1.1 [18].

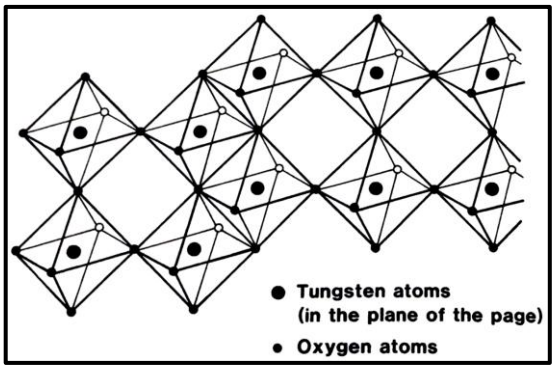

Figure 1.3.1.1. Illustration of a corner-sharing and edge-sharing arrangements of octahedra lattice in a WO_3 crystal. The Figure is taken from [18].

Temperature treatments are responsible for the antiferroelectric displacements of W atoms and the rotations of oxygens that implicate deviations from the ideal cubic lattice. WO_3 thin films can exhibit two processes. The first process is ascribed to the classical electrochromic mechanism. WO_3 thin films are transparent where all the W atoms exhibit a +6-oxidation state (W^{VI}) and they have a blue color associated with the +5-oxidation state (W^{V}) when the W atoms undergo the reduction process. The second process is related to the formation of the Tungsten Bronzes M_xWO_3 where M being an atom from the first column in the Periodic Table.

So, in general, as a function of the injected charge, WO_3 thin films exhibit different color changes moving from dark blue (x = 0.2), purple (x = 0.6) to red (x = 0.7) which are caused by photo affected intervalence charge transfer (CT) between adjacent (W^{V}) and (W^{VI}) sites and finally to bronze (x = 0.8 – 0.1), as schematized in Scheme 1.3.1.1 [19]:

$$WO_3 + x\,(M^+ + e^-) \;\rightleftharpoons\; M_x M^{(VI)}_{(1-x)} M^{(V)}_{(x)} O_3$$

Scheme 1.3.1.1. Tungsten trioxide electrochromic reactions.

As reported in Figure 1.3.1.2 [18] for M_xWO_3 bronzes with $0 \leq x \leq 1$ and M = H^+, Li^+, Na^+, K^+, Rb^+ and Cs^+, the crystal structure of the Tungsten Bronzes depends on the type and density of the species added to the WO_3 host structure. The cubic phase (perovskite) occurs at x large values for ions with large ionic radii. Tetragonal phases are found for low and medium x values for Li_xWO_3 and Na_xWO_3 and at intermediate x values for K_xWO_3. The hexagonal phase is found when the bronzes incorporate small x values of

large cations such as K_xWO_3, Cs_xWO_3, and In_xWO_3. For the H_xWO_3, the correspondent bronzes are shown as $WO_{3-x}(OH)_x$ because of the statistical probability of the bond between hydrogen atoms and the oxygen atoms of the hydroxyl groups, with an orthorhombic phase for x =1, tetragonal phase for x = 0.23 and a cubic phase for x = 0.5.

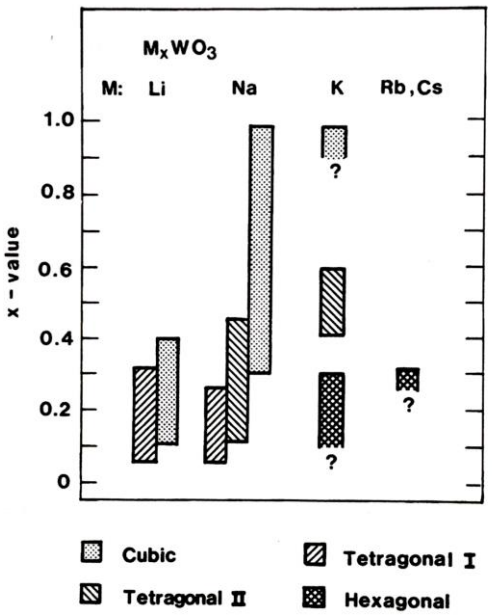

Figure 1.3.1.2. Composition ranges for the cubic, tetragonal I and II, and hexagonal phases of crystalline M_xWO_3 bronzes. The Figure is taken from [18].

Small ions can be accommodated in a small structure such as the cubic. The tetragonal structures can host inside their triangular channels the K^+ ions, while the hexagonal configurations have sufficient large tunnels for large ions like K^+, Rb^+, and Cs^+. A schematic representation of the available site for the intercalation of ions is shown in Figure 1.3.1.3.

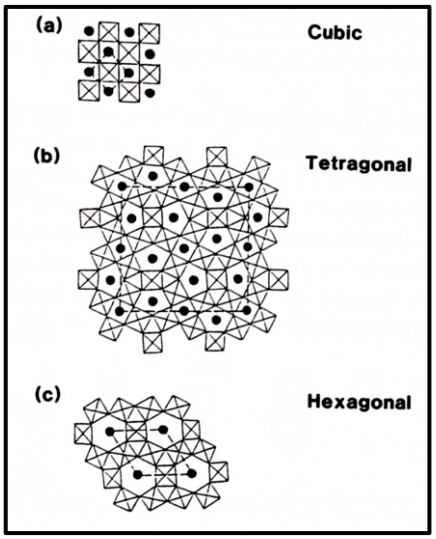

Figure 1.3.1.3 Atomic arrangements for crystalline tungsten bronzes with a) cubic (perovskite) b) tetragonal I, and c) hexagonal structure. The black circles indicate the available sites for ion insertion. The Figure is taken from [19].

Titanium dioxide (TiO_2) belongs to the cathodic electrochromic materials. It shows different crystal structures denoted as Rutile, Anatase, and Brookite at normal pressure and a stable structure TiO_2 (II) in conditions of high pressure (Figure 1.3.1.4) [19]. The lattice structure of TiO_2 crystals is distorted TiO_6 octahedra composed of six O^{2-} atoms that surround the Ti^{4+} atoms [18]. TiO_2 in the Anatase phase shows interesting electrochromic properties. The Anatase phase of tetragonal symmetry has a structure composed of TiO_6 octahedra sharing two adjacent edges with two other octahedra to form a planar double chain. These vacant sites can accommodate small ions such as H^+ and Li^+ [20]. The Anatase can be converted into an amorphous phase and then when it is treated at about 900 °C, it undergoes its more stable phase denoted the Rutile phase. The Rutile phase is described by a hexagonal close-packed oxygen lattice, where the metal is octahedrally central-coordinated to form edge-shared chains. All these crosslinked chains produce the same number of vacant channels that can host ionic species like H^+ and Li^+. The electrochromism reactions of the transparent TiO_2 describe the intercalation/de-intercalation of small ions (H^+ and Li^+) and they are shown in Schema 1.3.1.2:

$$TiO_2 + xH^+ + xe^- \rightleftharpoons TiO_{2-x}(OH)_x$$

$$TiO_2 + xLi^+ + xe^- \rightleftharpoons Li_xTiO_2$$

Scheme 1.3.1.2. Titanium dioxide electrochromic reactions.

Where $TiO_{2-x}(OH)_x$ and Li_xTiO_2 are hydroxylated or lithiated adsorbed material.

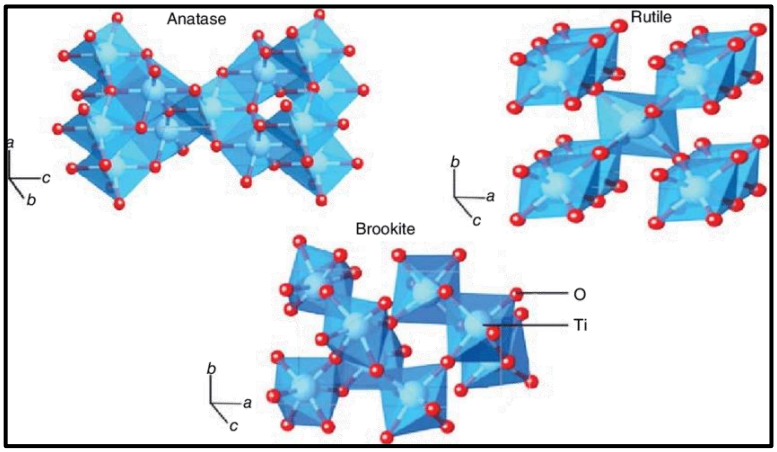

Figure 1.3.1.4. Different crystal structures of titanium dioxide (anatase, rutile, brookite). The Figure is taken from [21].

1.3.2. Metal coordination complexes

Metal Coordination complexes are electrochromic materials characterized by important chromophoric properties arising essentially from metal-to-ligand charge transfer (MCLT), intervalence charge transfer transition (IVCT), intra-ligand excitation and electronic transitions. They show intense color changes and high redox activities [18, 22].

Examples of metal coordination complexes useful for the fabrication of electrochromic devices are the $[M^{II}(bipy)_3]^{2+}$ series, where the metal M^{II} switched to the M^{III} redox state and it lost its intense MLCT absorption band. The complexes of Fe^{II}, Ru^{II} and Os^{II} are characterized by interesting color changes as reported $[Fe(bipy)_3]^{2+}$ (red), $[Ru(bipy)_3]^{2+}$ (orange) and $[Os(bipy)_3]^{2+}$ (green) [4].

Another example of metal coordination complexes are the Metallophthalocyanines compounds (MPcs). Such compounds have a metal either at the center of a single

phythalocyanine ring (Pc) if it is a transition metal or positioned between two Pc rings in a sandwich structure-type complex if the metal belongs to the lanthanide series, where their π systems can interact each other [4, 23]. These compounds can switch in the reduction from green, to blue and then to violet color, while in the oxidation they can pass from yellow to red color because of ring-based redox processes as in the case of [Lu $(Pc)_2$] complex films. [4]. They can offer also, fast response time, good reversibility, and some film degradation after a large number of cycles [24].

Prussian Blue ($[Fe^{III}\ Fe^{II}\ (CN)_6]$ or PB) is the prototype of a number of polynuclear transition-metal hexaoxidation cyanometallates with the formula $M'_k[M''(CN)_6]_l \cdot mH_2O$ (*k, l, m* integral) and M', M'' are transition metals in their different oxidation numbers. This electrochromic material shows an intense blue coloration arising from IVCT transitions between the mixed-valence iron states and can be removed by oxidation and reduction [25].

Prussian blue complex switches rapidly from blue color to green color (Prussian green) in the partial oxidation of its chromophore center as following (Scheme 1.3.2.1.a):

$$[Fe^{III}Fe^{II}(CN)_6] + e^- + \rightleftharpoons \left\{ [Fe^{III}Fe^{II}(CN)_6]_{2/3}\,[Fe^{II}(CN)_6]_{1/3} \right\}^{1/3^-} + 2/3e^-\,(green)$$

Scheme 1.3.2.1.a. Partial oxidation reaction of Prussian blue to Prussian green.

Then, starting from its pure blue state, it can be converted by electrochemical oxidation into the yellow (Prussian brown) state as following (Scheme 1.3.2.1.b):

$$[Fe^{III}Fe^{II}(CN)_6]^-(blue) \rightleftharpoons [Fe^{III}Fe^{III}(CN)_6] + e^-(yellow)$$

Scheme 1.3.2.1.b. Oxidation reaction of Prussian Blue into Prussian brown.

In the end, its reduction can determine the loss of the color (Prussian white) as following (Scheme 1.3.2.1.c):

$$[Fe^{III}Fe^{II}(CN)_6]^- + e^-(blue) \rightleftharpoons [Fe^{II}Fe^{II}(CN)_6]^{2-} + (cololess)$$

Scheme 1.3.2.1.c. Reduction reaction of Prussian blue into Prussian white.

Early PB-based electrochromic devices included only Prussian blue as electrochromic material, then the combination of PB as anodically electrochromic material and the tungsten trioxide acting as cathodic material, have been developed [23]. In this case, the electrochromic device experiences a redox process that involved the reduction and the oxidation of the complementary materials as following (scheme 1.3.2.2) where it switches from a blue to a transparent state and *vice versa*:

$$[Fe^{III}Fe^{II}(CN)_6]^- \ (blue) \rightleftharpoons [Fe^{II}Fe^{II}(CN)_6]^{2-} \ (transparent)$$

$$WO_3 + x(M^+ + e^-)(transprent) \rightleftharpoons M_x W^{VI}_{(1-x)} W^V_x O_3 (blue)$$

Scheme 1.3.2.2. Redox process involved in an electrochromic device based on PB-WO_3 systems.

1.3.3. Organic Molecular Dyes: Viologens

The 1,1'-disubstituted-4,4'-bypiridium salts commonly known as "Viologens" are a prominent class of organic electrochromic materials [26, 27]. These chemicals show electrochemical properties and they have been used as herbicides, electron-transfer mediators and redox indicators [27]. The combination of the availability of 4,4'-bipiridine and the ease of varying the nature of the quaternizing agent has allowed the focus of the research into the study of the viologens [27]. Three common redox states of the viologens are known and they are shown in Scheme 1.3.3.1.

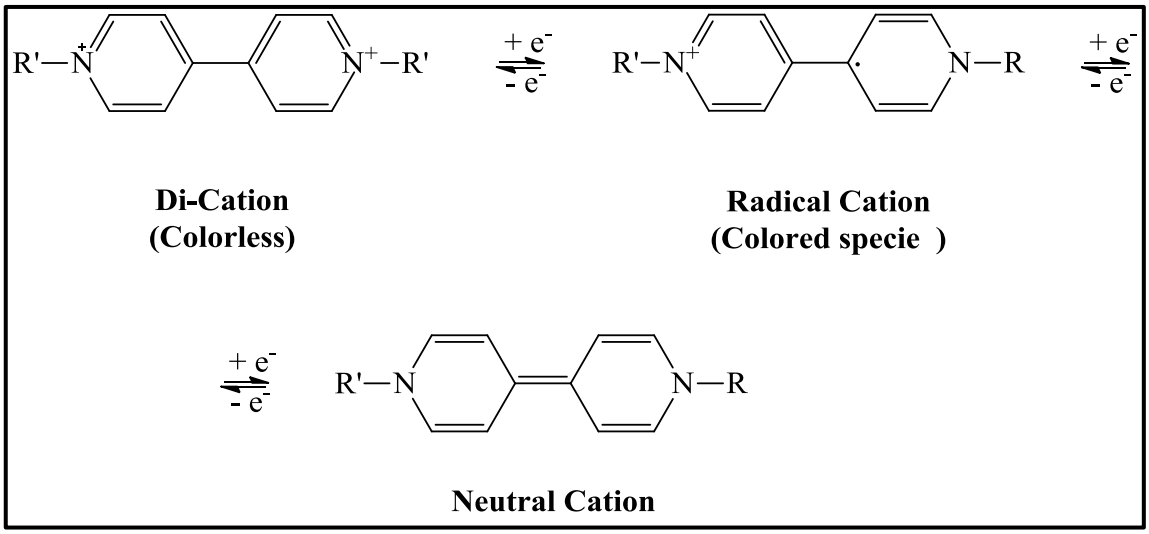

Scheme 1.3.3.1. Redox state of a generic Viologen specie.

The di-cation specie is the most stable and it is colorless. The radical cation is the reduction monomer which shows an intense colored state and the neutral cation can also show low color changes from the radical cation because no optical charge or internal transition in the visible region is accessible. The function of the nitrogen substituents R, R' establish the color choice of the radical cation. Alkyl groups shows blue-purple color changes and the aryl groups such as the N, N'-bis-(4-cyanophenyl) substituent promotes a green color [4]. Recent progress has been seen in the implementation of electrochromic devices based on viologen-TiO_2 (Anatase) systems to take advantage of the contrast ratio and color efficiency of the nanostructured wide bandgap of the TiO_2 for dye-sensitized solar cells [28].

1.3.4. Organic Conductive Polymers

Thin films of conducting polymer-based on aromatic molecules such as pyrrole, thiophene, aniline, furan, carbazole, azulene and indole unit in the thin film form exhibit electrochromic properties. In their conducting oxidized state, they possess positive change carries, counter anions (*p*-doping) and they have a delocalized π-electron band structure. With the electrochemical reduction, the electronic conjugation is removed and the undoped electrically neutral state will be present [4].

The bandgap of undoped conducting polymer between their conduction band (the lowest unoccupied band) and the corresponding valence band (the highest occupied band) gives them optical properties suitable for the electrochromic devices. The magnitude of the band gap establishes the color change between the doped and the undoped state of the thin film polymer. Examples of the main organic conductive polymer used in the electrochromic devices as thin films are poly(pyrrole)s, poly(thiophene)s PEDOT, and poly(aniline)s PAni.

Poly(pyrrole) in its oxidized (doped form) is blue-violet and after the electrochemical reduction the resultant undoped form shows a yellow-green color (Scheme 1.3.4.1). Then after multiple switching color steps, the polymer reaches out to a visible film degradation

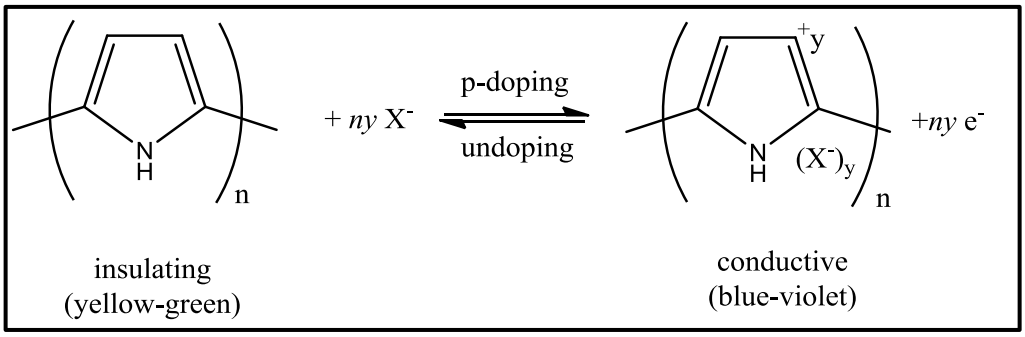

Scheme 1.3.4.1. *p*-doping process of a generic oxidized Poly(pyrrole).

As well as in the case of the poly(pyrrole)s, the p-doping/un-doping process of the poly(thiophene)s follow a similar mechanism as shown in the Scheme 1.3.4.2 [29].

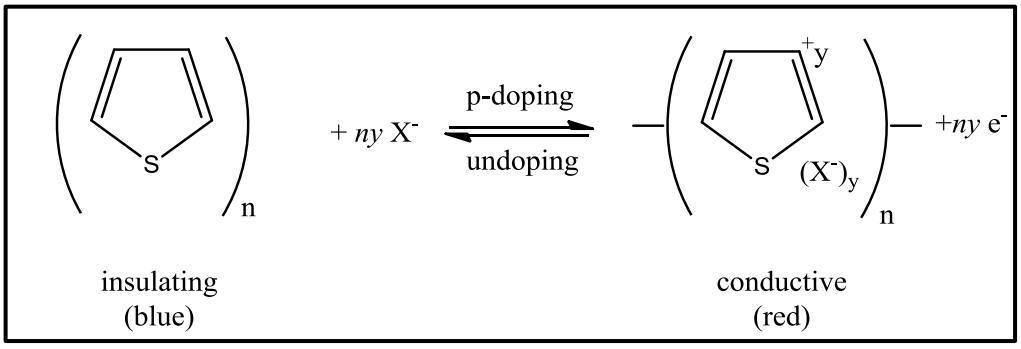

Scheme 1.3.4.2. *p*-doping process of a generic oxidized Poly(pyrrole).

Starting from the thiophene monomer which has a characteristic blue color in the doped state and a red color in the undoped state, the colors of the conductive polymers can be tuned just by choosing suitable substituents. Monomers such as 3-methylthiophene and 3,4-dimethylthiophene monomers switch from a deep blue color (oxidized) to a red color (reduced) and from dark blue (oxidized state) to pale brown (reduced), respectively [29]. The electrochromic properties of polymer films are directly connected also to the position of the substitutes. The conductive polymer prepared from oligomers based on 3-methylthiophene cover a wide range of color changes between the oxidized and the reduced state [29].

Electrochromic properties of poly(aniline)s depend on different conditions such as the oxidation state, the protonation state, and the pH values of the electrolyte [30]. Poly(aniline)s (PANI) are poly-electrochromic materials because they exhibit different

color variations which are associated with a specific species as depicted in Scheme 1.3.4.3 [30] The pernigraniline corresponds to the fully oxidized form, while the leucomeraldine is the fully reduced form [31]. Both pernigraniline and emeraldine may occur as either salts or bases [32, 33]. Complementary electrochromic devices based on Poly(aniline) which are combined with Prussian blue have been proposed. The electrochromic device has been realized by the combination of the colored state of the PANI in the oxidized state with the blue-colored state of the Prussian blue, which shows electrochromism as the reversible color change from deep blue to green [34].

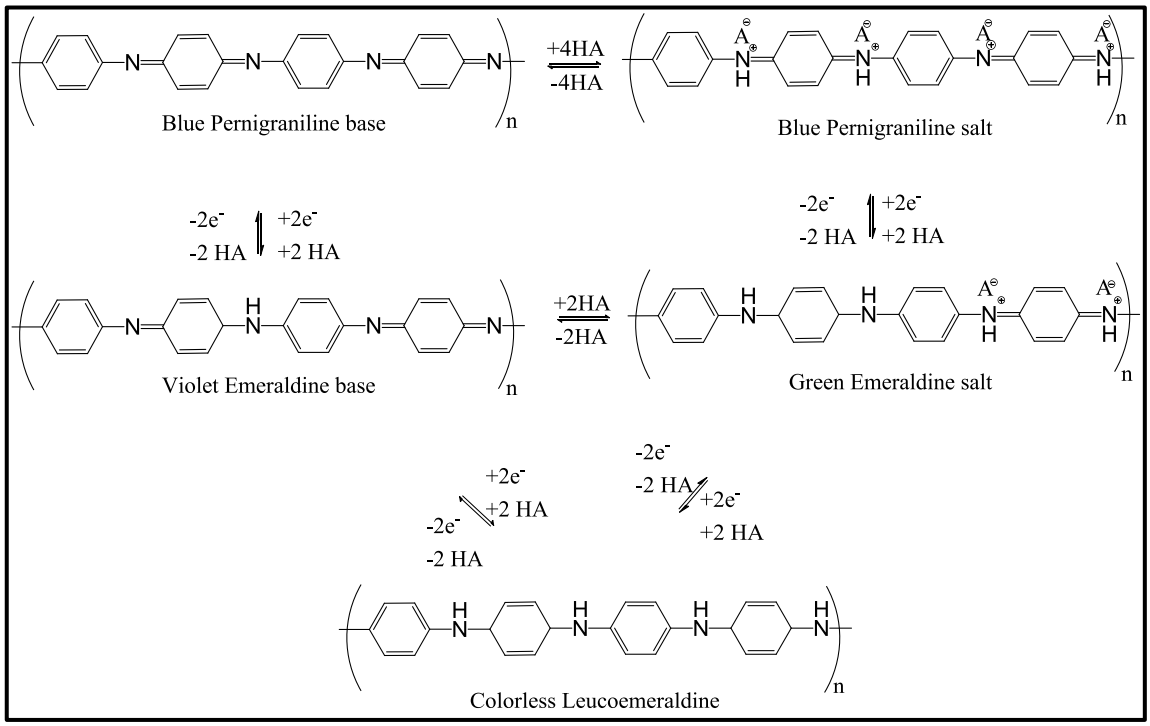

Scheme 1.3.4.3. Redox pathways of the Poly(aniline) species.

1.4. Electrolytes for Electrochromic devices

The electrolyte is a fundamental component of an electrochromic device because it ensures ionic transport between the two electrodes to balance the charges which are produced during the redox process inside the electrochromic device. In general, electrolytes are classified into three main classes: liquid electrolytes, solid electrolytes,

and gel polymer electrolytes [18]. Liquid electrolytes are essentially composed of an inorganic salt dissolved in an organic solvent of high dielectric constant and low viscosity [35, 5]. They are widely used for lithium-ion batteries because they can offer high ionic conductivity, but some disadvantages such as the excessive consumption of flammable organic solvents, the leakage of electrolytes, the presence of bubbles, and low chemical stability define them destine [5, 36]. Solid electrolytes including inorganic solid electrolytes and polymer electrolytes have also attracted increasing interest in the fabrication of ion batteries and fuel cells [36]. Solid electrolytes exhibit also some limitations such as lower ion mobility which results in slow switching and loss of transparency of electrochromic devices [5]. Polymer electrolytes offer a lot of advantages over liquid and inorganic solid electrolytes. They show high ionic conductivity at room temperature, appreciable mechanical strength, high electrochemical window, high cationic or anionic transference number, and stability against the electrodes. In addition, they are not hygroscopic, are easy to prepare, and are low cost [37].

Gel Polymer Electrolytes (GPEs) are electrolytes composed of a liquid plasticizer incorporated in a salt-polymer system known as a gelled polymer matrix. They can be prepared by heating a mixture of polymer and Li salt with a plasticizer. [37]. The transport of the ions is related to the physical structure of the polymer matrix. If the polymer matrix is composed of connected micropores, then the ions can diffuse about them, and the ionic conductivity of the GPE is related to the properties of the liquid which is trapped in the polymer matrix. Otherwise, when the polymer matrix is homogenous, the ion can diffuse through the swollen gel [37]. GPEs offer good mechanical strength, high ionic conductivity, and electrochemical stability. Polymer matrix used for the preparation of GPEs are poly(ethyleneoxide) (PEO) [38], poly(methylmethacrylate) (PMMA) [39-41], poly(vinylidene) fluoride (PVdf) [42], poly(acrylonitrile) (PAN)[43] and also copolymers [44]. GPEs have been studied also in different arrangements for electrochromic device purposes such as gel [45], blend [46], with the addition of ionic liquid [47] and, the confinement of polymer electrolyte in nanopores of alumina membranes has also been investigated to improve the ionic conductivity of the polymer electrolyte [48].

PMMA belongs to the acrylate family with a chemical structure depicted in Scheme 1.4.1. It is a colorless polymer with a glass transition temperature (T_g) ranging from 100 °C to 130 °C and a density of 1.20 g cm^{-3} at room temperature. It shows high resistance to

sunshine exposure and appreciable thermal stability between 100 °C and -70 °C. Its physical properties such as T_g, crystallinity, and solubility depend on the structure of the monomer and on the structure of the linkage. PMMA shows three different typologies of tacticity: isotactic, syndiotactic, and atactic [49] characterized by the following glass transition temperatures 55 °C, 130 °C and 120 °C, respectively [50, 51].

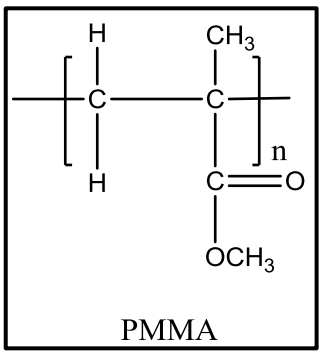

Scheme 1.4.1. The structure of Poly(methylmethacrylate) (PMMA)

Because of its amorphous nature, flexible chains, high transparency, good solubility, and good ionic conductivity wide adopted in the electrochromic device in combination with propylene carbonate, ethylene carbonate, or a mixture of plasticizers [49, 50]. The application of the PMMA as composed polymer electrolyte of PAN and PMMA has been prepared in PC and EC to obtain the maximum ionic conductivity at room temperature. It also shows perfect compatibility with PVDF because it neutralizes the crystallinity character of PVDF [52], in gel polymer electrolytes made by TiO_2 and liquid electrolytes based on $LiClO_4$-EC/PC systems [53] and in gel polymer electrolytes composed of a copolymer of PMMA-clay [54].

Plasticizers *i.e.*, solvents for electrolytes are low-molar -mass organics, organic solvents, or ionic liquid (ILs) used to increase the content of the amorphous phase in a polymer electrolyte and promote segmental motion [55]. In addition, they should be able to dissolve salts to sufficient concentrations, be fluid, do not establish chemical interaction with the system, promote the dissociation of ion pairs, should to remain liquid in a wide range of temperatures, and be economical and safe [55, 56]. The cyclic diesters of carbonic acid with a particular interest in Propylene Carbonate (PC) and Ethylene Carbonate (EC) are the most promising electrolyte solvents or plasticizers used for both lithium battery and electrochromic devices (Scheme 1.4.2). These solvents help to solvate

the Li^+ and facilitate their mobility inside the polymer matrix, improving the ionic conductivity up to 10^{-3} S cm^{-1} because of the C=O polar group and the ether-linkage (-O-). And, their mixture is more effective for increasing the ionic conductivity compared with a single solvent because it is the result of the combination of viscosity and dielectric permittivity [57].

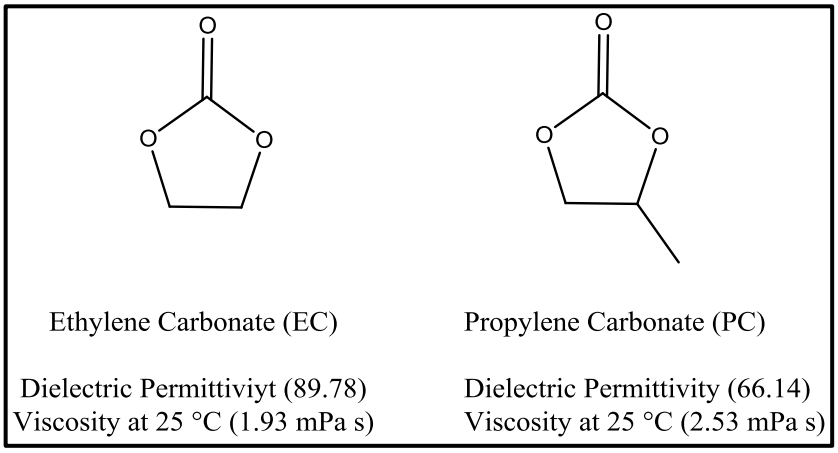

Scheme 1.4.2. Chemical structure and dielectric permittivity and viscosity of PC and EC used in rechargeable lithium-ion batteries [58].

1.5 Electrochromic Performance Parameters

The performance requirements that should be tested for an electrochromic device are the optical contrast, the coloration efficiency, the optical memory, the life cycle, and the switching time.

The *Optical contrast* (ΔT) is an important parameter used to evaluate the color change in electrochromic materials and devices. It refers to the difference in optical transmittance of different colors at the same wavelength [59]. It can also define as a function of the absorbance and evaluated at the maximum wavelengths (λ_{max}) where the absorption changes are the largest between the redox states, which can occur in the visible region and/or near-infrared (NIR) region [8].

The Coloration Efficiency (CE) is an operating parameter that serves to assess the power consumption of the electrochromic material [8]. It is defined as the change in optical density per unit of charge injected/rejected, and given by (Equation 1.5.1):

$$CE = \Delta OD/Q = \Delta[\log(T_b/T_c)]/Q \quad (1.5.1)$$

Where Q is the injected charge per unit area and is proportional to the number of color centers, T_b and T_c are the transmittances in the bleached and in the colored states, respectively [17]. For electrochromic applications, a higher CE value is beneficial as it signifies that a high optical change can be obtained under a small amount of charge and thus, lower power consumption and higher energy efficiency [8].

The *Optical Memory* of an electrochromic device is defined as the time that the electrochromic material retains its colored state after the removal of the applied electrical bias [9] and it depends on the duration for which the electron can be 'trapped' in the specific redox state of the material. It is used to approximate the capacity of the electrochromes to operate without the need for a continuous power supply [8]. Materials with low optical memory reveal a 'self-erasing' behavior and they thereby require a constant supply of electricity to maintain their oxidized/reduced state. Materials with high optical memory can sustain their last redox state for extended durations.

The *Life Cycle* is a measure of the electrochemical stability of the electrochromic device. It is defined as the number of times that the device can be cycled between its bleached/colored states, before its degradation [60].

The *Switching Time* defines the time required by the electrochromic device to switch between the bleached and the colored states and *vice versa* as a response to an applied potential. The switching time is defined as the time taken for the electrochromes to switch to a conventional value of 95% of its full switch. Other approaches to quantify the switching times include measurements of the duration needed for part or all the necessary charges to be injected [8].

1.6 References

[1] C. G. Granqvist in *"Electrochromic Mater. Devices: An Introduction to Materials and Devices"*, Wiley - VCH Verlag GmbH & Co., Germany (2015), 1-40.

[2] A. Azens, C.G. Granqvist, *J. Solid State Electrochem.*, (2003) **7** 64 -66.

[3] J. W. Xu, M. H. Chua, K. W. W. Shah in *"Chapter 1 - Introduction to the Electrochromism"*, Royal Society of Chemistry (2019) 1-21.

[4] R. J. Mortimer, *Annu. Rev. Mater. Res.*, (2011) **41** 241-268.

[5] Y. Alesanco, A. Vinuales, J. Rodriguez, R. Tena-Zaera, *Materials*, (2018) **11** 1-27.

[6] S.K. Deb, *App. Opt. Suppl*., (1969) **3** 192.

[7] D. T. Gillaspie, R. C. Tenent, A. C. Dillon, *J. Mater. Chem*., (2010) **20** 9585-9592.

[8] C. G. Granqvist, P. C. Lansakera, N. R. Mlyukaa, G. A. Niklassona, E. Avendanob, *Solar Energy Materials and Solar Cells*, (2009) **93** 2032-2039.

[9] C. G. Granqvist, *Nat. Mater*., (2006) **5** 89-90.

[10] R. J. Mortimer, A. L. Dyer, J. R. Reynolds, *Displays*, (2006) **27** 2-18.

[11] U. Bach, D. Corr, D. Lupo, F. Pichot, M. Ryan, *Adv. Mater*., (2002) **14** 845-848.

[12] D. T. Gillaspie, R. C. Tenent, A.C. Dillon, *J. Mater. Chem*., (2010) **20** 9585-9592.

[13] A. Llordes, G. Garcia, J. Gazquez, D. J. Milliron, *Nature*, (2013) **500** 323-326.

[14] W. L. Tonar, H. J. Byker, K. E. Siegrist, J. S. Anderson, K. L. Ash, (1999) Patent 5-928-572.

[15] C. M. Lampert, *Mater. Today*, (2004) **7** 28-35.

[16] R. C. G. M. Loonen, M. Trcka, D. Costola, J. L. M. Hensen, *Renew. Sustain. Energy Rev*., (2013) **25** 483-493.

[17] W. T. Neo, M. H. Chua, j. W. Xu, in *"Chapter 2 - Fundamentals of Electrochromic Materials and Devices-"*, Royal Society of Chemistry (2019) 22-50.

[18] C. G. Granqvist in *"Handbook of Inorganic Electrochromic Materials"*, Elsevier Science B. V.: Amsterdam, The Netherlands (2002).

[19] R. J. H. Clark in "The Chemistry of Titanium and Vanadium" Elsevier, Amsterdam, (1968).

[20] T. Ohzuku, M. T. Kodama, T. Hirai, *J. Power Sources*, (1984) **14** 153.

[21] S.N. Karthick, K. V. Hemalatha, S. K. Balasingam, F. M. Clinton, S. Akshaya, H. Kim, H., in *"Chapter 1- Dye-Sensitized Solar Cells: History, Components, Configuration, and Working Principle. In Interfacial Engineering in Functional Materials for Dye-Sensitized Solar Cells"*; Wiley: Hoboken, NJ, USA, (2019) 1-16.

[22] P. M.S. Monk, R. J. Mortimer, D. R. Rosseinsky, in *"Electrochromism and Electrochormic devices",* Cambridge UK: Cambridge Uni. Press, (2007).

[23] R. J. Mortimer, *Chemical Society Reviews*, (1997) **26** 147-156.

[24] G.C. S. Collins, D. J. Schiffrn, *J. Electrochem. Soc*., (1985) **132** 1835.

[25] V. D. Neff, *J. Electrochem. Soc*., (1978) **125** 886-887.

[26] P. M.S. Monk, R. J. Mortimer, D. R. Rosseinsky, in *"Electrochromism: fundamentals and applications"* VCH, Weinheim, (1995).

[27] P. M. S. Monk in *"The Viologens: Psychochemical Properties, Synthesis and applications of the salts of 4,4'-bipyridine"*, J. Wiley and Sons, Chichester, (1998).

[28] B. O'Regan, M. Gratzel, *Nature*, (1991) **353** 737-740.

[29] M. Mastragostino in *"Chapter 7: Electrochromic devices in Applications of Electroactive Polymers"* Springer Netherlands, (1993) 223-249.

[30] P. R. Somani, S. Radhakrishnan, *Materials Chemistry and Physics, (2002)* **77** 117-133.

[31] Z. A. Boeva, V. G. Sergeyev, *Polymer Science Ser. C,* (2014) **56** 144-153.

[32] A. G. MacDiarmid, S. K. Manohar, J. G. Masters, Y. Sun, H. Weiss, A. J. Epstein, *Synthetic Metals*, (1991) **41** 621-626.

[33] A. G. MacDiarmid, A. J. Epstein, *Faraday Discuss. Chem. Soc*., (1989) **88** 317-332.

[34] A. G. Macdiarmid, J. C. Chiang, A. F. Richter, A. J. Epstein, *Synthetic Metals*, (1987) **18** 285-290.

[35] P. Bonhote, E. Gogniat, F. Campus, L. Walder, M. Gratzel, *Displays*, (1999) **20** 137-144.

[36] L. Long, S. Wang, M. Xiao, Y. Meng, *J. Mater. Chem. A*, (2016) **4** 10038-10069.

[37] M. Kotobuki in "Chapter 1-Polymer Electrolytes: State of the Art", Wiley-VCH Verlag GmbH & CO.KGaA (2020).

[38] A. Chakrabarti, R. Filler, B. K. Mandal, *Solid State Ionics*, (2010) **180** 1640-1645.

[39] M. Kucharski, T. Lukaszewicz, P. Mrozek, *Opto-Electron. Rev*., (2004) **12** 175-180.

[40] S. S. Sekhon, S. A. Agnihotry, S.A. *Solid State Ion*., (2000) **136** 1189-1192.

[41] S. A. Agnihotry, S. S.; Pradeep, *Solid State Ion.*, (2000) **136** 573-576.

[42] S. W. Choi, S. M. Jo, W. S. Lee, Y. R. Kim, *Adv. Mater*., (2003) **15** 2027-2032.

[43] S. W. Choi, J. R. Kim, S. M. Jo, W. S. Lee, Y. R. Kim, *J. Electrochem. Soc*., (2005) **152** A989-A995.

[44] P. Yan, Z. Huang, Y. Lin, X. Wu, Y. Yang, D. Wang, F. Chen, C. Zhang, D. He, *Ionics*, (2015) **21** 593-599.

[45] I. Nicotera, C. Oliviero, G. Ranieri, A. Spadafora, M. Castriota, E. Cazzanelli, *J. Chem. Phys*. (2002) **117** 7373-7380.

[46] I. Nicotera, L. Coppola, C. Oliviero, M. Castriota, E. Cazzanelli, *Solid State Ionics* (2006) **177** 581-588.

[47] M. Castriota, T. Caruso, R. G. Agostino, E. Cazzanelli, W.A. Henderson, S. Passerini, J. *Phys. Chem. A* (2005) **109** 92-96.

[48] M. Castriota, D. Teeters, *Ionics* (2005) **11** 220-225.

[49] V. K. Takur, G. Ding, J. Ma, P. S. Lee, X. Lu, *Adv. Mater*., (2012) **24** 4071-4096.

[50] U. Ali, K. Bt. Juhanni, A. Karim, N. A. Buang, *Polymer Reviews*, (2015) **0** 1-28.

[51] L. Chang, E. M. Woo, *Polymer Chemistry*, (2010) **1** 198-202.

[52] X. H. Flora, M. Ulgaganathan, S. Rajendran, *International Journal of Polymeric Materials and Polymeric Biomaterials*, (2013) **62** 737-742.

[53] L. Zhou, N. Wu, Q. Cao, B. Jing, X. Wang, Q. Wang, H. Kuang, *Solid State Ionics*, (2013) **249** 93-97.

[54] J. Sharma, S. Sekhon, *Solid State Ionics*, (2007) **178** 439-445.

[55] S. klongkan, J. Pumchusak, *Electrochim. Acta*, (2015) **161** 171-176.

[56] K. Xu, *Chem. Rev*., (2004) **104** 4303-4417.

[57] L. R. A. K. Bandara, M. A. K. L. Dissanayake, B. E. Mellander, *Electrochim. Acta*, (1998) **43** 1447-1451.

[58] J. Y. Song, Y. Y. Wang, C. C. Wan, *J. Electrochem. Soc*., (2000) **147** 3219-3225.

[59] M. Zhu, J. Zeng, H. Li, X. Zhang, P. G. Liu, *Synthetic Metals*, (2020) **270** 116579.

[60] A. A. Argun, P. H. Aubert, B. C. Thompson, I. Schwendeman, C. L. Gaupp, J. Hwang, N. J. Pinto, D. B. Tanner, A. G. Macdiarmid, J. R. Reynolds, *Chem. Mater*., (2004).

CHAPTER 2

Sol-Gel Process

2.1 Sol-Gel Process: Principles

The Sol-Gel process has therefore attracted extensive attention among researchers because it is a unique technique for the preparation of inorganic polymers or ceramics. Basically, the process involves some steps which are summarized as following [1]:

1) Synthesis of the sol starting from hydrolysis and partial condensation of alkoxides;
2) Formation of the gel *i.e.*, formation of metal–oxo–metal or metal–hydroxy–metal bonds via condensation.
3) Aging of the gel network with consequently resulting in the expulsion of solvent.
4) Drying of the gel either to form a dense xerogel or an aerogel.
5) Removal of surface M–OH groups through calcination treatment at high temperatures.

The process involves some advantages such as the production of high chemical purity, production of powder materials with high surface area, the increased chemical homogeneity in multi-component systems, need low temperature of preparation, but also, some disadvantages such as the excessive cost of the equipment and some times of the chemical precursors and long processing time [2].

The functional materials prepared by sol-gel are classified as photocatalyst, nonlinear optical materials, ferroelectrics, and superconductors, simple and complex no silica oxides such as TiO_2, ZrO_2, Al_2O_3, ZnO, WO_3, Nb_2O_5 and rare earth oxides [3].

2.2 Sol-Gel Mechanism

When a metal cation M^{z+} presents in the salt form, and is dissolved in water, it can exhibit high reactivity, and can be solvated by water molecules as following (Scheme 2.2.1) [4, 5].

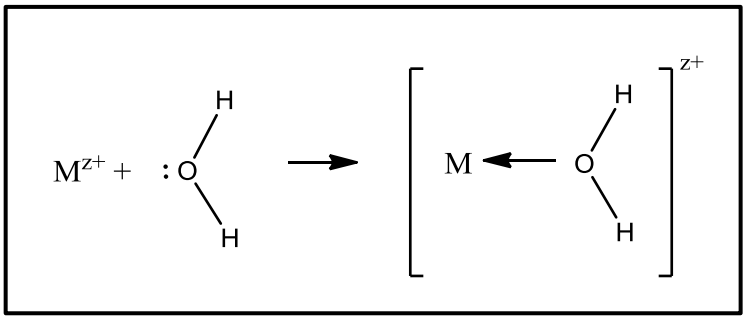

Scheme 2.2.1. Hydrolysis mechanism of metal ions M^{z+}.

If the metal cations belong to transition metals, in this case, the charge transfer involves the filled bonding orbital of the water molecules and the empty *d* orbital of the transition metal, with a consequence increasing the acidic character of the water molecules. Depending on the magnitude of the charge transfer, the hydrolysis can be explained as the following equilibria (Scheme 2.2.2) [4, 5].

$$[M(OH)_2]^{z+} \rightleftharpoons [M(OH)]^{(z-1)+} + H^+ \rightleftharpoons [M=O]^{(z-2)+} + 2H^+$$

Scheme 2.2.2. Hydrolysis mechanism of Transition Metals.

Where the species $[M(OH)_2]$, [M(OH)] and (M=O) can be expressed in a formula that considers the coordination number of water molecules (N) around the metal and the molar ratio of the hydrolysis (h) as reported in Table 2.2.1.

Molar Ratio of hydrolisys (h)		**Complex Species**	
h = 0		Aquo-ion	$[MO_NH_{2N}]^{2+}$
h = 2 N		Oxy-ion	$[MO_N]^{(2N-z)^-}$
0 < h < 2 N	h > N	Oxo-Hydroxo complex	$[MO_X(OH)_{N-X}]^{(N+X-z)^-}$
	h < N	Hydroxo-Aquo complex	$[M(OH)_X(OH_2)_{N-X}]^{(z-X)+}$
	h = 0	Hydroxo complex	$[M(OH)_N]^{(N-z)-}$

Table 2.2.1. Complex species of inorganic precursors in water solution as a function of the molar ratio of hydrolysis (h) and coordination number of water molecules (N).

The series of equilibria of Scheme 2.2.2 is easily moved to the right than in the water itself when the pH is increased (*i.e.*, if a base is added). In addition, the next condensation

reaction needed the presence of M-OH units, which can be obtained by the control of the pH and the valence of the metal. Essentially, three possibilities can be considered for the shifting of the M-OH formation as deducted from the diagram of charge Z versus pH depicted in Figure 2.2.1 [6]. The diagram helps in the identification of the species as a function of the charge and the pH value of the water solution. In particular, the oxo-hydroxo and oxo complex are formed in the whole range of pH for Z is equal to >+5. For values of Z < +4 the aquo-hydroxy and hydroxo complexes are in. For Z equal to +4, the tetravalent cations are borderline and a high number of precursors can be formed.

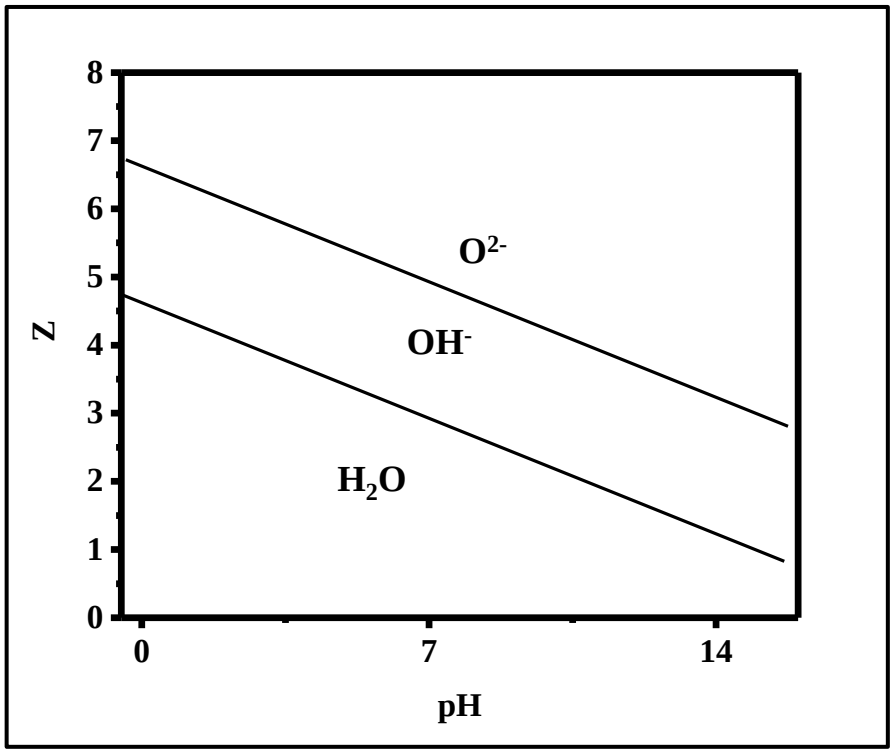

Figure 2.2.1. Charge (Z) vs. pH diagram indicating the domains of aquo (H_2O), hydroxo (OH^{-}), and oxo (O^{2-}) species. The Figure is taken from [6].

The Condensation reaction can be realized following two possible nucleophilic mechanisms: nucleophilic substitution and nucleophilic addiction. The condensation reaction can follow the first or the second mechanism depending on the coordination of the metal. If the preferred coordination is realized, then the condensation can occur by the mechanism of Nucleophilic Substitution (SN). Otherwise, when the preferred coordination is not satisfied, the condensation can occur by the mechanism of

Nucleophilic Addiction (AN). Both mechanisms are reported in Scheme 2.2.3 a-b, respectively [5].

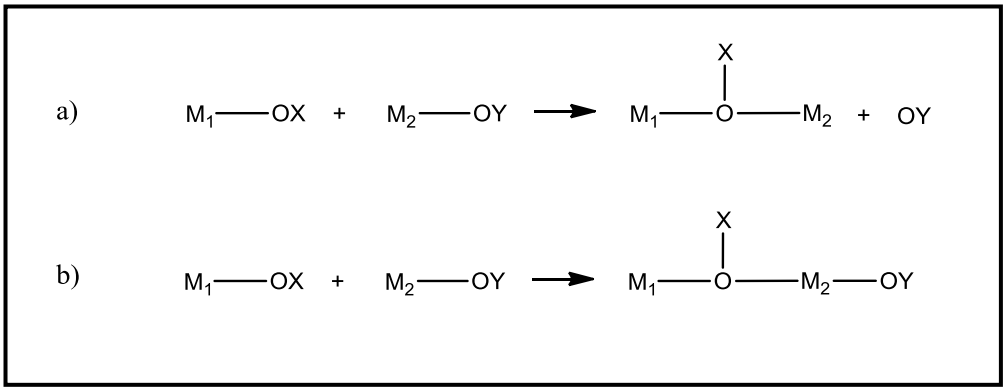

Scheme 2.2.3. Preferred metal-coordination in the condensation reaction *via* SN mechanism (a) and not preferred metal-coordination *via* AN mechanism (b).

Oxo ions are good nucleophilic species but poor leaving groups. The condensation can be realized only if one reactant specie is coordinatively unsaturated. Aquo ions are good leaving groups but they are poor nucleophiles and the condensation cannot be realized. Hydroxo ions contain both good nucleophiles and leaving groups such as H_2O and OH species and in this case the condensation can be occured as soon as one OH specie is present around the coordination sphere of the metal [5]. The condensation reaction can be realized in the hydroxo domain, by adding an acid to oxy-ions or a base to aquo ions. A special case of the condensation process is the Olation, where an *ol* bridge (*i.e.*, hydroxy bridge) is realized between two metal centers in the hydroxo-aquo precursors, $[M(OH)_X(OH_2)_{N-X}]^{(z-X)+}$. They follow a nucleophilic substitution mechanism where the water molecules are the leaving group and the hydroxy group is the nucleophile (Scheme 2.2.4 a-b) and the possible water bridges can be formed [5].

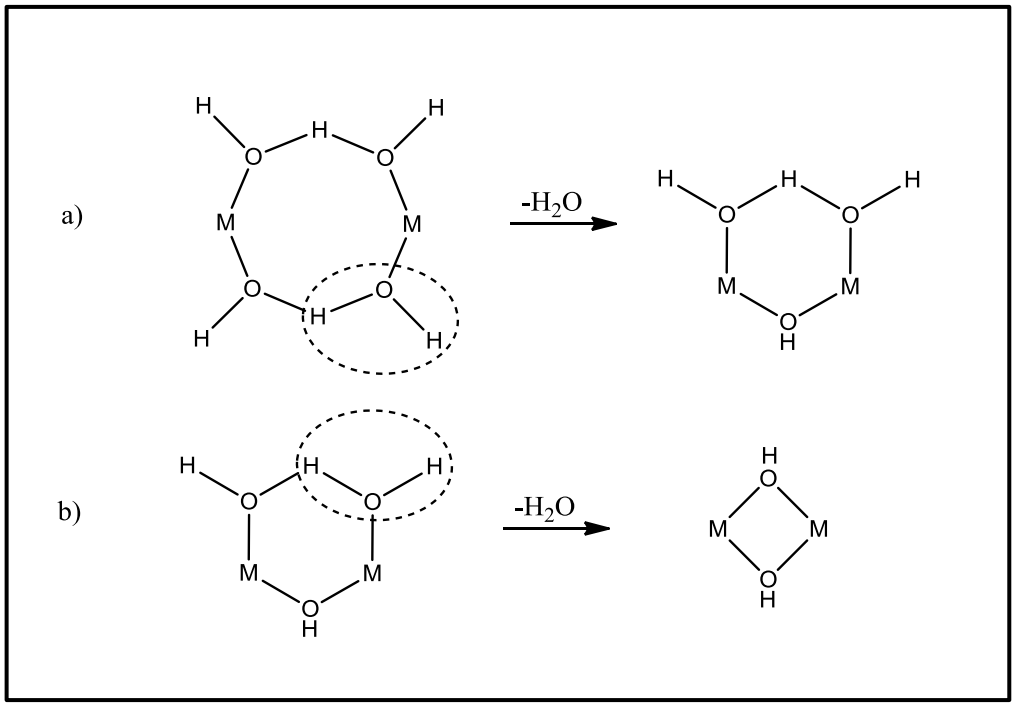

Scheme 2.2.4. Olation process in the Hydroxo-Aquo precursors following a nucleophilic substitution mechanism (SN).

Another kind of condensation process is known Oxolation and it involves the formation of an oxo bridge between two metal centers. It occurs in the oxo-hydroxo precursors, $[MO_X(OH)_{N-X}]^{(N+X-z)^-}$ following in this case the nucleophilic addition mechanism (Scheme 2.2.5).

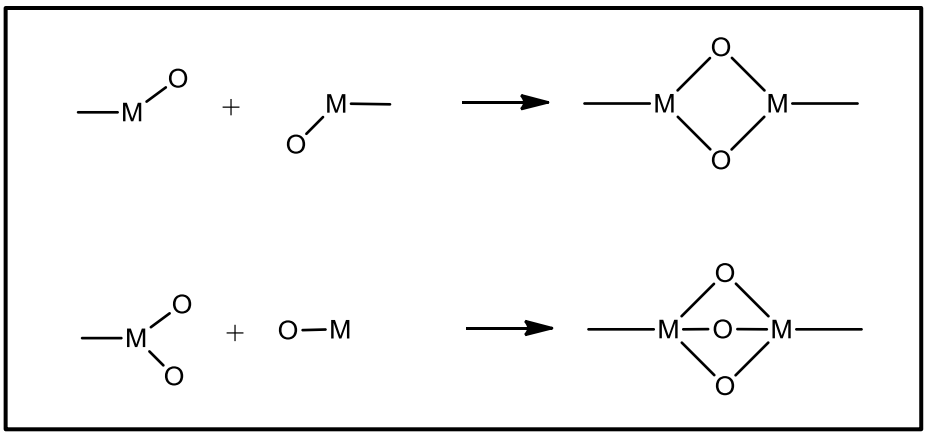

Scheme 2.2.5. Oxolation process in the Oxo-Hydroxo precursors following a nucleophilic addition mechanism (AN).

When the metal is coordinatively saturated the oxolation process proceeds first with a nucleophilic addiction and then with the elimination of water molecule with the resulting formation of the M-O-M bond (Scheme 2.2.6) [5].

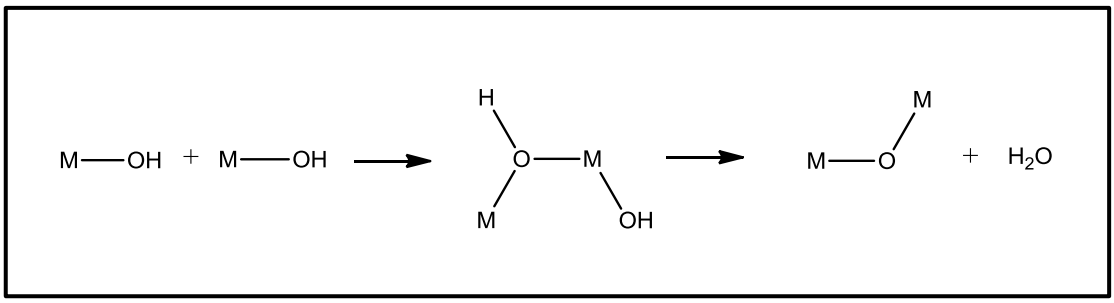

Scheme 2.2.6. Oxolation process for coordinatively saturated metals following a nucleophilic addition mechanism (AN) and elimination of water molecule (E).

Metal alkoxides $[M(OR)_n]$ are common precursors used in sol-gel synthesis. Because of the high electronegativity of the -OR group which stabilizes the metal in the highest oxidation state, their sol-gel synthesis is essentially based on two reactions: 1) hydrolysis and 2) condensation. Hydrolysis and condensation mechanisms for coordinatively saturated metals are shown in Scheme 2.2.7. Their synthesis in absence of catalyst specie, are based on nucleophilic substitution and nucleophilic addition, followed by a proton transfer and an elimination of the protonated specie *via* alkoxylation (with the elimination of alcohol molecule) or oxolation reactions (loss of water molecule).

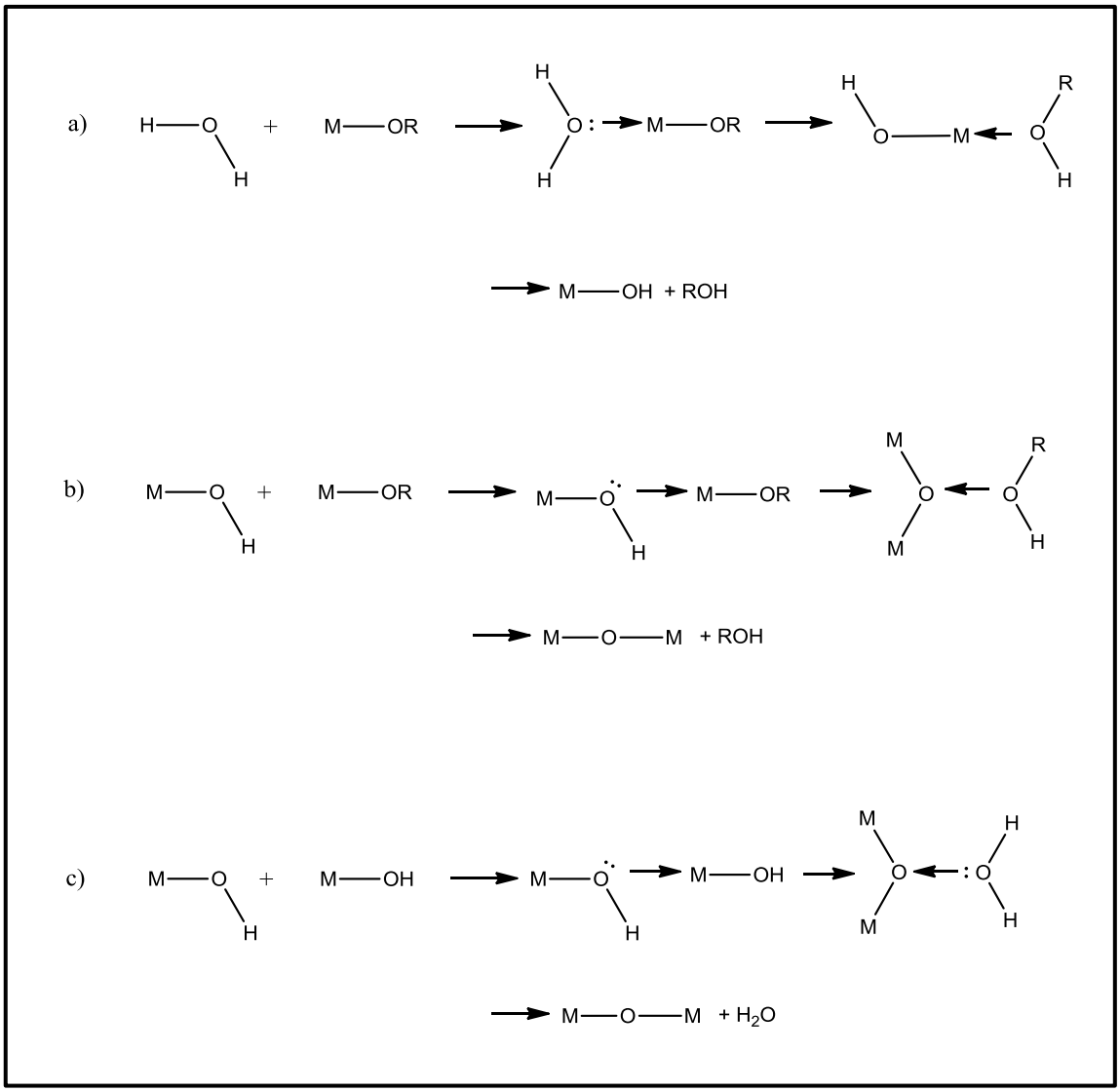

Scheme 2.2.7. Sol-gel synthesis of Metal Alkoxides comprising of: a) hydrolysis reaction through nucleophilic substitution or addition mechanism, b) condensation reaction *via* alkoxylation with the elimination of alcohol and c) condensation reaction *via* oxolation mechanism with loss of water molecule.

The catalyst can influence the rates of both hydrolysis and condensation and the structure of the condensed products. An acid catalyst serves to protonate negatively charged alkoxide groups to produce a good leaving group, while a basic catalyst serves to produce strong nucleophilic species via deprotonation of hydroxo ligands. (Scheme 2.2.8 a-b).

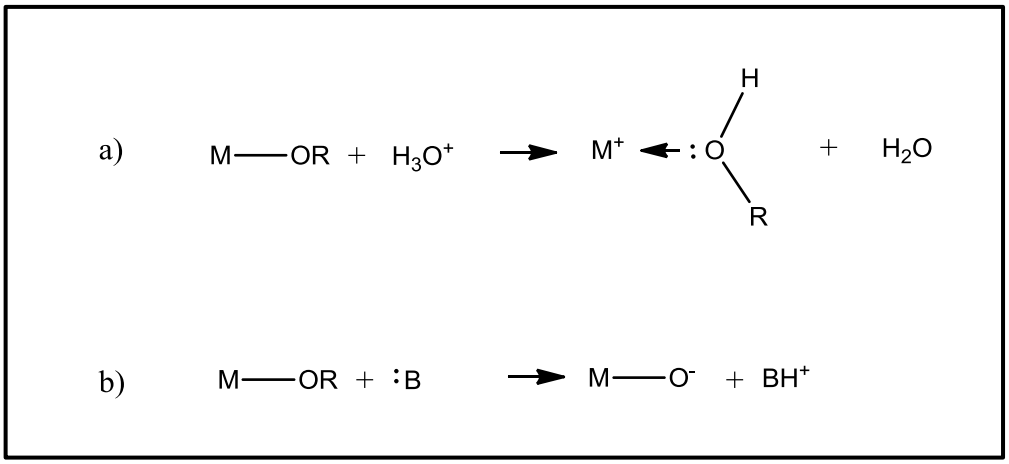

Scheme 2.2.8. The role of a) acid catalyst and b) alkaline catalyst in the sol-gel synthesis of metal alkoxides.

The structure of condensed products depends on the relative rates of the four reactions: hydrolysis, oxolation, alkoxylation, and olation. The contributions of each of these reactions depend in turn on internal parameters such as the nature of the metal atom and alkyl groups and the molecular complexity as well as external parameters such as *r*, the choice of catalyst, concentration, solvent, and temperature.

The sol-gel routes for the deposition of thin WO_3 and TiO_2 thin films have been employed principally in view of further electrochromic applications.

Metal alkoxides can strongly react with water and their preparation should be conducted inside an inert environment such as in a dry box or glove box to prevent the water contamination of the condensed products. Tungsten trioxide thin films were prepared by dissolving $WOCl_4$ in isopropanol anhydrous under a dry atmosphere. A highly exothermic reaction took place under development of HCl gases. The $WOCl_4$ solution turns yellow and after stirring for few hours a colorless solution is obtained. The reaction is the following (Scheme 2.2.9) After stirring for one night the solution is ready for coating [11, 12].

$$WOCl_4 + x\,ROH \rightleftharpoons WOCl_{4_X}(OR)_X + xHCl\uparrow$$

Scheme 2.2.9. Sol-gel synthesis of WO_3.

For the sol-gel of Titanium dioxide, the treatment with isopropanol anhydrous has been conducted [12, 13]. In addition, the use of glacial acetic acid as a catalyst or chelating

agent has been considered useful to overcome the strong reactivity of the alkoxide towards H_2O which often gives uncontrolled precipitation and limits the synthesis process [14].

For the preparation of electrochromic thin films of tungsten trioxide and of titanium dioxide, the following routes have been used, as shown in Scheme 2.2.10.

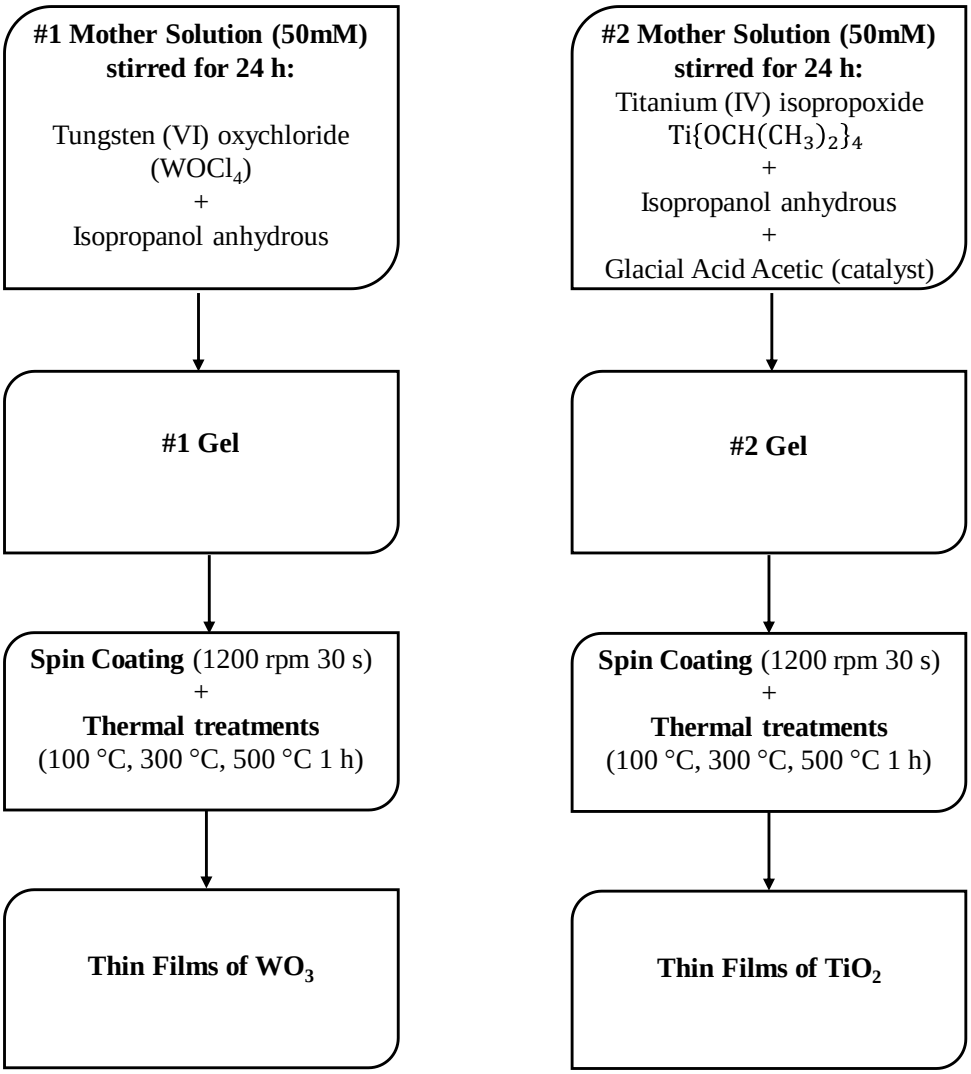

Scheme 2.2.10. Preparation procedure of tungsten trioxide and titanium dioxide thin films by the sol gel process.

2.3 Spin-Coating Technique of Metal Alkoxide "Sol"

The reactive sol-gel mixture of Metal Alkoxides can be deposited by the Spin-Coating technique. The most important advantage of sol-gel processing over conventional coating

methods is the ability to control precisely the microstructure of the deposited film, *i.e.*, the pore volume, pore size, and surface area. [9]. The spin-coating technique is a conventional method used for the deposition of uniform and thin film.

This technique consists of four steps [9]: 1) deposition, 2) spin-up, 3) spin-off and 4) evaporation. Experimentally a small amount of the sol solution is directly deposited onto the center of specific support such as glass [10, 11]. Then in the spin-up stage, the support is rotated at high speed to spread the coating material by the centrifugal force. In general, the higher the rotations speed, the thinner the film [14, 15] and by selecting the appropriate spin rate, it is possible to modulate the film thickness [15]. In fact, the centrifugal force overcomes the force of gravity and the rapid thinning quickly undo all inertial forces other than centrifugal force. In the spin-off stage, the excess liquid moves away to the perimeter of the support as droplets. In addition, as the film is thinner *i.e.*, it reaches the desired thickness the rate of removal of excess liquid by spin-off slows down, and the greater the resistance to flow. In the fourth stage, evaporation takes over as the primary mechanism of thinning. Using the spin coating, it is possible to obtain in general a uniform film because during the spin-off stage the liquid becomes uniform in thickness and it preserves this state at the end of the process. This is true in the consideration of the viscosity do not change over the substrate [16] and because it is due to the contribution of two forces: the centrifugal force and the friction or viscous force. The first drives the flow radially outward, while the second act radially but inward [17]. In the initial of the spin-off stage, the thickness of the uniform film is defined following Equation 2.3.1:

$$h(t) = h_0/(1 + 4\rho\varpi^2 h_0^2 t/3\eta)^{1/2} \tag{2.3.1}$$

Where h_0 is the initial thickness, t is time, and ω is the angular velocity with ρ and ω assumed constant. It is important to consider that the evaporation in the last stage is unchanged and considering that liquid sol as a Newtonian liquid, the final thickness of the film can be expressed by the Equation 2.3.2 [18].

$$h_f = \left(1 - \frac{\rho_{A0}}{\rho_A}\right)\left(\frac{3\eta me}{2\rho_{A0}\varpi^2}\right)^{1/3} \tag{2.3.2}$$

Where ρ_A is the density of the solvent, ρ_{A0} is the initial density and e is the evaporation rate.

2.4 References

[1] A. E. Danks, S. R: Hall, Z. Schnepp, *Mater. Horiz*., (2016) **3** 91.

[2] S. G. Ullattil, P. Periyat, in *"Chapter 9 Sol-Gel Synthesis of Titanium Dioxide"*, Springer International Publishing AG (2017) 271-283.

[3] S. Sakka, in *"Chapter 11 - Sol Gel Process and Applications"*, Elsevier Inc. (2013) 883-910.

[4] J. Livage, M. Henry, C. Sanchez, *Progress in Solid State Chemistry*, (1988) **18** 259-342.

[5] C. J. Brinker, G. W. Scherer, in *"Chapter 2 - Hydrolysis and Condensation I: Nonsilicates"*, Academic Press (1990) 20-95.

[6] U. Schubert in *"Chapter 1-Chemistry and Fundamentals of the Sol–Gel Process"* (2015) 1-27.

[7] B.C. Bunker, J.A. Voigt, D.L. Lamppa, D.H. Doughty, E.L. Venturini, J.F. Kwak,D.S. Ginley, T.J. Headley, M.S. Harrington, M.O. Eatough, R.G. Tissot, W.F. Hammetter, *Mater. Res. Soc*., (1988) **121** 373.

[8] P. Judeistein, R. Morineau, J. Livage, *Solid State Ionics*, (1992) **51** 239-247.

[9] C. J. Brinker, G. W. Scherer, in *"Chapter 13-Film Formation. Sol-Gel Science"*, (1990) 786–837.

[10] M. Ikawa, T. Yamada, H. Matsui, H. Minemawari, J. Tsutsumi, Y. Horii, M. Chikamatsu, R. Azumi, R. Kumar, T. Hasegawa, *Nat. Commun*., (2012) **3** 1176.

[11]] M. Hershcovitz, I.E. Klein, *Microlelectron. Reliab*., (1993) **33** 869-880.

[12] J. Livage, D. G. Ganguli, *Solar Energy Materials & Solar Cell*, (2001) **68** 365-381.

[13] M. H. Shimen, S. A. A. AlSaati, F. Z. Razooqi, *Journal of Physics Conf. Series*, (2018) 132 1-11.

[14] F. Zhang, C. Di, N. Berdunov, Y. Hu, Y. Hu, X. Gao, Q. Meng, H. Sirringhaus, D. Zhu, *Adv. Mater*., (2013) **25** 1401-1407.

[15] M. K. Ahmad, N. A. Rasheid, A. Zain Ahmed, S. Abdullah, M. Rusop, *AIP Conference Proceedings*, (2008) **1017** 109-113.

[16]] A. Uzum, K. Fukatsu, H. Kanda, Y. Kimura, K. Tanimoto, S. Yoshinaga, Y. Jiang, Y. Ishikawa, Y. Uraoka, S. Ito, *Nanoscale Res. Lett*., (2014) **9** 659

[17] L.E. Scriven in "*Better Ceramics Through Chemistry"* C.J. Brinker, D.E. Clark, and D.R. Ulrich (Mat. Res. Soc, Pittsburgh, Pa.) (1988) 717-729.

[18] B. Higgins, *Phys. Fluids*, (1986) **29** 3522-3529.

CHAPTER 3

Section A

Raman Spectroscopy

3.1 Raman Spectroscopy: A Brief Introduction

Raman Spectroscopy is a branch of Vibrational Spectroscopy, which analyses the diffuse light from a sample to allow an easy interpretation and highly structural identification of the structural properties of chemicals based on their vibrational characteristic [1-5]. First evidences of the Raman scattering were observed by Indian scientist C. V. Raman in 1928, which earned him the Nobel Prize in 1931.

If monochromatic radiation of frequency ϖ_0 is allowed to interact with molecules, some part of the radiation is transmitted, some reflected and some scattered. Focusing on the scattered radiations, they may contain not only the original frequency ϖ_0 but also pairs of new frequencies of the type $(\varpi_0 + \nu_M)$ and $(\varpi_0 - \nu_M)$, where ν_M are the frequencies of some transition that occur in the material. The scattered radiations without change of frequency ϖ_0 is known as Rayleigh or also Elastic Scattering.

The scattering depends on the transitions of the material and it is called Raman Scattering or inelastic Scattering. In the Raman scattering, the bands characterized by frequencies lower than the frequency of the incident radiation are called Stokes, while the bands with higher frequencies are called Anti-Stokes. Figure 3.1.1 shows the energetic scheme of both Raman and Rayleigh scattering.

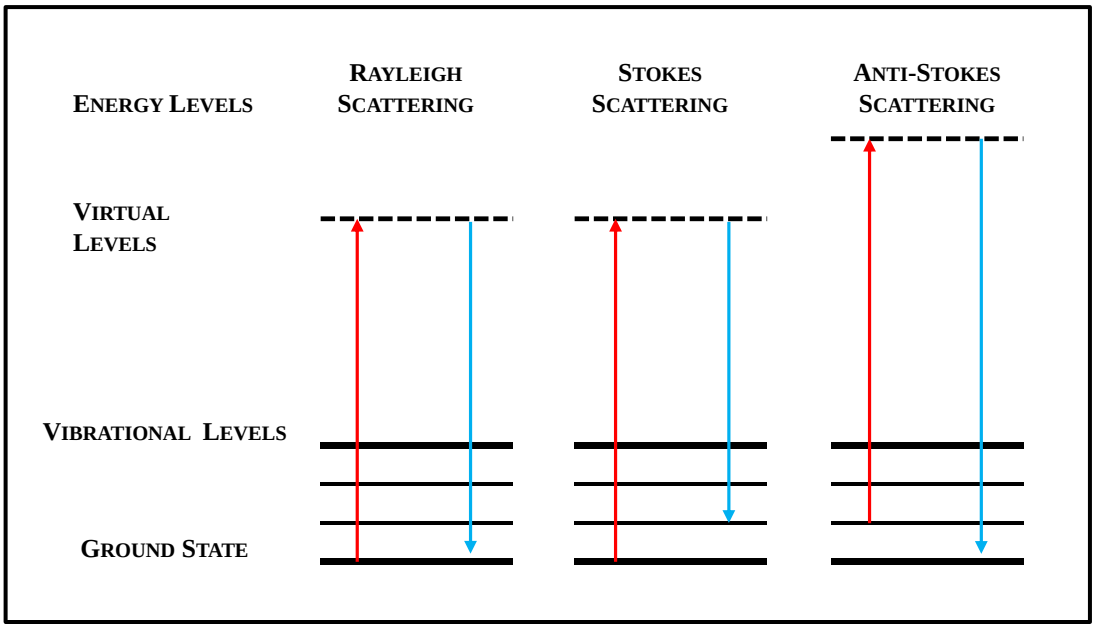

Figure 3.1.1. Schematic representation of Raman and Rayleigh scattering. The Figure is taken from [6].

3.2 Classic Model for Raman Spectroscopy

The Raman effect is an effect of radiation-matter interaction that can only be interpreted by means of quantum mechanics; however, it is possible to provide a qualitative description of the phenomenon from the classical point of view. The light is a transverse wave, the electric and magnetic fields oscillate perpendicularly between them and with respect to their propagation direction $\vec{v}$ as depicted in Figure 3.2.1.

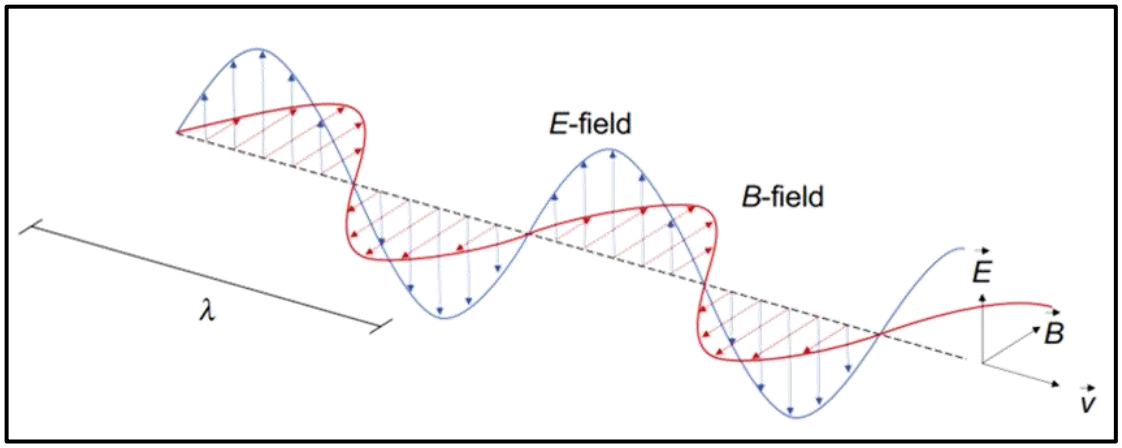

Figure 3.2.1. Schematization of the propagation of the electric field ($\overrightarrow{E}$) and of the magnetic field (H) components of the light. The Figure is taken from [7].

The direction of the electric field is called the Polarization direction of the light. The electric field vector ($\vec{E}$) over time varies according to Equation 3.2.1:

$$\vec{E} = E_0 \, cos(\varpi_1 t) \qquad 3.2.1$$

where $\vec{E}$ is the electric field vector, ω_1 is the oscillation frequency of the electric field, E_0 is the amplitude and t is the time.

The electrons of the molecule under the action of an intense electric field, are distributed around the nuclei and then the molecule polarizes acquiring a moment of electrical dipole induced $\vec{P}$ by the electric field vector $\vec{E}$of the radiation incident given by (Equation 3.2.2):

$$\overrightarrow{P} = \overleftrightarrow{\alpha}\vec{E} \qquad 3.2.2$$

where $\overleftrightarrow{\alpha}$ is the polarizability tensor, which is a second order rank tensor.

The origin of the scattered radiation is attributed to the oscillating electric dipole moments induced by the incident electromagnetic radiation. The intensity *I* of the scattered radiation radiated by an oscillating electric dipole induced by an electric field of the radiation incident (ϖ_1) depends on the high frequency at fourth power and it is given by (Equation 3.2.3):

$$I = \frac{\omega_s^4 p_0^2 sin^2\theta}{32\pi^2\varepsilon_0 c_0^3} = \frac{\pi^2 c_0 \tilde{v}_s^4 p_0^2 sin^2\theta}{2\varepsilon_0} \qquad (3.2.3)$$

Where ϖ_s ($\varpi_s = 2\pi c_0 \tilde{v}_s$) and p_0 are the frequency and the amplitude of the induced electrical dipole, θ is the angle between the electrical field of the radiation and the axis of the dipole.

Considering just one molecule, which is able only to vibrate, the variation of its polarizability can be expressed by each component (α_{xy}) in a Taylor series in according to the normal coordinate of vibrations:(Equation 3.2.4):

$$\alpha_{xy} = (\alpha_{xy})_0 + \sum_k \left(\frac{\delta\alpha_{xy}}{\delta Q_k}\right)_0 Q_k + \frac{1}{2}\sum_{k,l}\left(\frac{\delta^2\alpha_{xy}}{\delta Q_k \delta Q_l}\right)_0 Q_k Q_l + \cdots \qquad 3.2.4$$

Where $(\alpha_{xy})_0$ is the value of α_{xy} in the equilibrium configuration and $Q_k Q_l$ are the normal vibration coordinates associated to the molecular frequencies ω_k and ω_l and the summations are over all the normal coordinates.

Considering the harmonic approximation, the Equation 3.2.4 can be simplified to the first power of Q, by introducing the new term $(\alpha'_{xy})_k$ that is equal to $\left(\frac{\delta\alpha_{xy}}{\delta Q_k}\right)_0$ as following (Equation 3.2.5 and 3.2.6):

$$(\alpha_{xy})_k = (\alpha_{xy})_0 + (\alpha'_{xy})_k Q_k \qquad 3.2.5$$

$$(\alpha'_{xy})_k = \left(\frac{\delta\alpha_{xy}}{\delta Q_k}\right)_0 \qquad 3.2.6$$

The new term $(\alpha'_{xy})_k$ corresponds to the components of the tensor called polarizability tensor $\vec{\vec{\alpha}}_k$. All its components are polarizability derivates respect the normal coordinate.

The Equation 3.2.7 gives the vectoral form, with the introducing of the scalar quantity Q_k expressed in the Equation 3.2.8 as following:

$$\vec{\alpha}_k = \vec{\alpha}_0 + \vec{\alpha}'_k Q_k \quad 3.2.7$$

$$Q_k = Q_{k_0} \cos(\varpi_k t + \delta_k) \quad 3.2.8$$

Where $Q_{k_0}$and δ_k are the amplitude of the normal coordinate and the phase factor, respectively.

The frequency dependence of the electric field of the incident radiation is expressed as (Equation 3.2.9):

$$\vec{E} = \hat{E}_0 \cos(\varpi_1 t) \quad 3.2.9$$

Considering Equations 3.2.7, 3.2.8 and Equation 3.2.9, is possible to write the induced electric dipole moment vector $\vec{P}$ expressed in Equation 3.2.2, in a new form as (Equation 3.2.10):

$$\vec{\boldsymbol{P}} = \vec{\alpha}_0 \hat{E}_0 \cos(\varpi_1 t) + \frac{1}{2}\vec{\alpha}'_k \hat{E}_0 [\cos(\varpi_1 t + \varpi_k t + \delta_k) + cos(\varpi_1 t - \varpi_k t - \delta_k)] \quad 3.2.10$$

In Equation 3.2.10 some terms are relevant: the term $\vec{\alpha}_0 \hat{E}_0 cos\varpi_1 t$ is associated the classical Rayleigh scattering, the term $\frac{1}{2}\vec{\alpha}'_k \hat{E}_0 \cos(\varpi_1 t + \varpi_k t + \delta_k)$ defines the Anti-Stokes bands of the Raman Scattering and the term $\frac{1}{2}\vec{\alpha}'_k \hat{E}_0 cos(\varpi_1 t - \varpi_k t - \delta_k)$ describes the Stokes bands of the Raman Scattering.

The Rayleigh scattering has the same phase of the incident radiation, but this is not true for the Raman scattering. In the Raman scattering the quantity $\delta_k$defines the phase of the normal vibration Q_k respect the electrical field. The Rayleigh scattering is due to the oscillation at ϖ_1 of the electric dipole induced by the electric field of the incident radiation. The Raman scattering is produced by the electric dipole which oscillates at the induced frequencies $\varpi_1 \pm \varpi_k$ when the electrical dipole oscillating at the frequency $\varpi_1$is modulated by the systems oscillation at frequency ϖ_k.

The Raman scattering can be observed when at least one component of the $\vec{\alpha}'_k$ be non-zero respect to the normal coordinate in the consideration of the harmonic approximation. If the time-dependent of the normal coordination Q_k is taken into account, in the case of the anharmonicity, some terms ascribed to the bands called overtones $\cos(2\varpi_k t + \delta_{2k})$; $\cos(3\varpi_k t + \delta_{3k})$ *etc.* and the combination of weaker tones $\cos(\varpi_k t + \delta_{kl})$; $\cos(\varpi_l t + \delta'_{kl})$ should to be considered. The resulting induced electric dipoles will oscillate in according to additional frequency terms $(\varpi_1 \pm 2\varpi_k)$ *etc.*, and $\varpi_1 \pm (\varpi_1 \pm \varpi_1)$ *etc.*

3.3 Infrared Spectroscopy

The phenomenological approach of the Infrared Spectroscopy (IR) is based on the phenomena in which the light is passed through a sample and the intensity of the transmitted light is measured at each frequency that corresponding to the vibrational energies of the sample and by its characteristic structure.

This phenomenon can be explained on a molecular level by introducing the concept of the permanent dipole moment of a molecule [8].

For a system of two charged particles (+e and -e) that are positioned at a fixed distance r, the permanent electric dipole moment, μ is given by the Equation 3.3.1:

$$\mu = e\, r \tag{3.3.1}$$

For a complex system such as the polyatomic molecule, the Equation 3.3.1 can be written in the Equation 3.3.2, introducing the association of the dipole moment with the cartesian coordinates, that in this case is expressed for the x coordinate as following:

$$\mu_x = \sum_i e_i x_i \tag{3.3.2}$$

Where e_i is the charge of the ith atom and x_i is referred to the x cartesian coordinate. The molecular dipole moment varies in time as results of the motion of the molecules.

The selection rules help us indicating which transitions will be observable in the spectrum by the indication on which transitions will have zero intensity and transitions will have nonzero intensity. The first kind of observable transitions are forbidden, while the second type are said to be allowed. The spectrum will be characterized by the presence of transitions that are called infrared active and other kind that will be Raman active, but considering the symmetry the molecule, transitions may appear in one, in another spectrum, both or neither. When a molecule is placed in electrical field, it can experiment an induced dipole moment μ_{ind} which is proportional to the strength of the electrical field. The induced dipole moment is equal to (Equation 3.3.3):

$$\vec{\mu}_{ind} = \vec{\vec{\alpha}}\vec{\varepsilon} \qquad 3.3.3$$

Where α is the polarizability of the molecule and it represents the constant of proportionality.

The selection rules for the fundamental transitions establish that: *A vibrational transition is IR active if the dipole moment of the molecule changes during the vibrations.*

If the polarizability of the molecule changes during the vibration, then the vibrational transition is Raman active.

For a molecule to be IR active there must be a change in dipole moment because of the vibration that occurs when IR radiation is absorbed. According to the Equation 3.3.2 for any molecule, the dipole moment is composed of three cartesian components. So, this means, that if only one of these three components changes during the vibration, then the transition will be considered IR active.

Otherwise, in the case of Raman spectroscopy, the transitions will be active as a consequence of the variation of the property of the polarizability of the molecules. The polarizability contemplates the complexity of the chemical bonds. The property of polarizability as defined in Equation 3.2.2 can be rewritten by making the polarizability tensor for the Cartesian coordinates as following (Equations 3.3.4, 3.3.5 and 3.3.6):

$$\mu_{ind}(x) = \alpha_{xx}E_x + \alpha_{xy}E_y + \alpha_{xz}E_z \qquad 3.3.4$$

$$\mu_{ind}(y) = \alpha_{yx}E_x + \alpha_{yy}E_y + \alpha_{yz}E_z \qquad 3.3.5$$

$$\mu_{ind}(z) = \alpha_{zx}E_x + \alpha_{zy}E_y + \alpha_{zz}E_z \qquad 3.3.6$$

Also expressed in the matrician form as in the Equation 3.3.7:

$$\begin{bmatrix} \mu_{ind}(x) \\ \mu_{ind}(y) \\ \mu_{ind}(z) \end{bmatrix} = \begin{bmatrix} \alpha_{xx} & \alpha_{xy} & \alpha_{xz} \\ \alpha_{yx} & \alpha_{yy} & \alpha_{yz} \\ \alpha_{zx} & \alpha_{zy} & \alpha_{zz} \end{bmatrix} \begin{bmatrix} E_x \\ E_y \\ E_z \end{bmatrix} \quad 3.3.7$$

The polarizability tensor is symmetry with (Equations 3.3.8, 3.3.9 and 3.3.10):

$$\alpha_{xy} = \alpha_{yx} \quad 3.3.8$$

$$\alpha_{xz} = \alpha_{zx} \quad 3.3.9$$

$$\alpha_{yz} = \alpha_{zy} \quad 3.3.10$$

And is possible to conclude that a Raman transition will be active if one of the six components of the polarizability tensor changes during the vibration.

The transition moment integral gives information about the probability of a transition occurring. In the case of an IR transition, the transition moment integral can be written as a dipole moment operator $\hat{O}$ as described in Equation 3.3.11:

$$M_{vv'}^2 = \left[\int_{-\infty}^{+\infty} \Psi^*(v') \hat{O} \, \Psi^*(v) d\tau \right]^2 \quad 3.3.11$$

If the probability of a vibrational transition is proportional to the square of the transition moment integral, then a transition is considered as allowed when the quantity $M_{vv'} \neq 0$. Also, in this case, the dipole moment operator $\hat{O}$ has three components for IR transitions and six different components for Raman too. Known the symmetry behavior of Ψ(ν'), Ψ(ν) and also, the operators $\hat{\mu}$ e $\hat{\alpha}$, the selection rules can be reformulated as following:

If the direct product (Equation 3.3.12):

$$\Gamma[\psi(v')] \times \Gamma[\psi(\hat{\mu})] \times \Gamma[\psi(v)] \quad 3.3.12$$

will contains the total symmetric belonging to the point group, then the transition ν → ν' will be IR active.

If the direct product (Equation 3.3.13):

$$\Gamma[\psi(\upsilon')] \times \Gamma[\psi(\hat{\alpha})] \times \Gamma[\psi(\upsilon)] \qquad 3.3.13$$

will contains the total symmetric belonging to the point group, then the transition ν → ν' will be Raman active.

3.4 Raman Microprobe Equipment

A classic Raman equipment provides that the laser beam passes through a high numerical aperture microscope objective and focuses on the sample. Many types of excitation sources include lasers based on argon (351.1–514.5 nm), krypton (337.4–676.4 nm), and He–Ne (632.8nm) and the most recent diode lasers which operate at 785, 810, or 830 nm, and also pulsed lasers such as Nd:YAG (1064nm). The scattered light from the sample is then passed through the monochromator that is used to disperse the collected radiation onto the multichannel detector. Among the detectors, intensified diode arrays or Charge Coupled Device (CCD) are the most common type that allows simultaneous detection of a large spectral range. Figure 3.4.1 shows a classic Micro-Raman spectrometer and its main components.

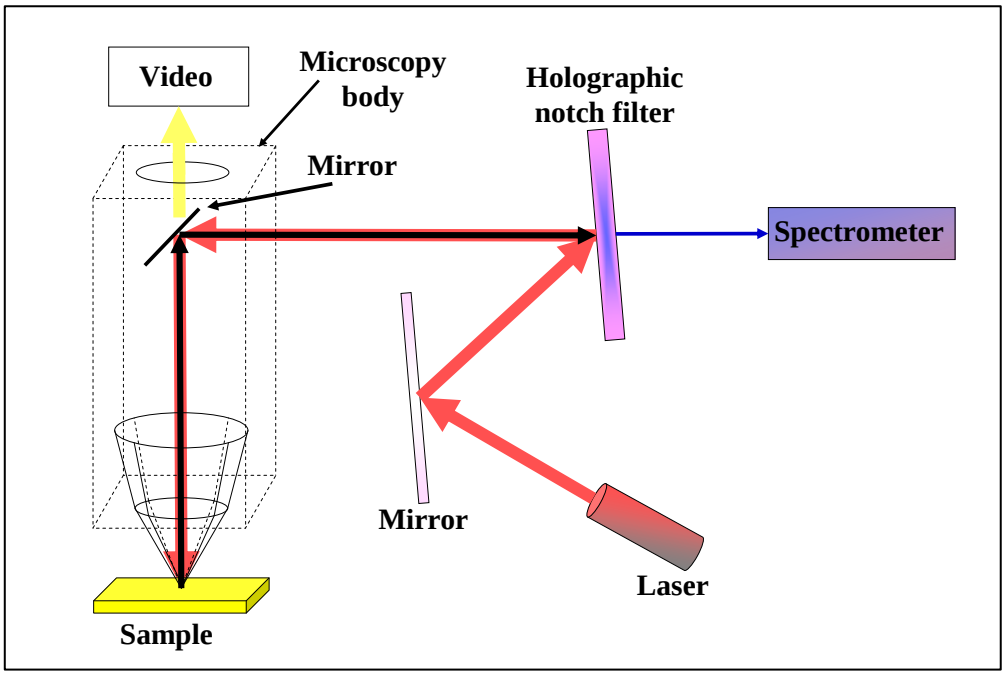

Figure 3.4.1. Micro-Raman spectrometer setup.

The instrument used to perform Raman Spectroscopy is the Micro-Raman-LABRAM by Jobin Yvon *Srl*. The instrument introduces an innovation concerning the Backscattering geometry ($\theta = \pi$) which provides the combination of a classical Raman spectrometer with an optical microscope. In this way is possible to investigate and collect Raman spectra of small regions of the samples in the magnitude order of about 2-15 μm which is can be related at the same time to laser sources emitting in the visible region of the spectrum [1, 9, 10]. Using the microscope, the scattered Raman radiation can pass efficiently through, and be collected on the glass lenses and this means that for the sample or for a part of the sample which can be aperture optically, is possible to record the specific Raman spectrum. The resultant Raman spectrum will own a specific property, it will feature a specific spatial resolution which is a function of the wavelength of the laser sources adopted [10]. Traditional Raman microscopes suffer from limited resolution along the optical axis due to the conventional microscope coupling, but modern instruments have achieved clear improvements in resolution with the integration of a confocal-designed microscope. Classic microscopes have so far focused only on the X–Y plane, but confocal Raman microscopy refers to the ability to spatially filter the analysis volume of the sample, in the XY (lateral) and Z (depth) axes. In confocal microscopy, an adjustable pinhole is applied to obstruct the out-of-focus signals from above and below the focal plane. In this way is possible to obtain some depth profiling of the material and, the final spectrum is free from the background signals and the fluorescence. The z-axis resolution for confocal Raman is about 1 mm [6, 9].

The main components of the adopted instrument are summarized in Table 3.4.1.

Components	Properties
Laser	He-Ne 17 mW laser, polarised 500:1 (λ=632,817 nm)
Holographic Notch Filter	Super Notch Plus used a dichroic mirror. Drop off Stokes edge <120 cm^{-1}, now 200 cm^{-1}
Confocal Hole	Adjustable between 0 and 1500 μm (scaled on the sample by a factor: 1.4X Objective magnification)
Microscope	High Stability BX40. Focus graduation 1 μm. Objectives (10x NA 0.25, 50x NA 0.7, 100x NA 0.9.

Components	Properties
	Other objectives available (Long work distance 20x, 50x) Illumination by transmission and reflection for opaque samples. Macro adapter for mounting of macro 40 mm objective under a microscope. Color camera for the observation of the sample.
External Lasers available and the Laser entrance	(Notch exchange is required) Ar^+, 457.8, 514.532 nm, K^+ 647.1, 752.5 nm, Yag doubled, diode-pumped 532 nm, Laser diode 785 nm. Removable mirrors for external Laser. HeNe beam can be directed externally through the external laser entrance for easier external laser alignment.
Spectrograph	Stigmatic 300 mm focal length spectrograph. Two gratings mounted on the same shaft 1800 g/mm (holographic) and 600 g/mm (ruled or holographic). Sinus arm drive. Laser diode for alignment.
CCD Detector	Peltier cooled 1024×256, 16-bit dynamic range (pixel size 27 µm).
Computer	Labspec software and VITES video card for TV image digitalization.
Separated electronic box	Alimentation of the laser, drive of hole, slit, gratings, shutters, scanners, alimentation of the laser diode for alignment
Options	Motorized XY microscope stage for point by point on laser scanning imaging. Resolution 0.1µm, reproducibility 1 µm. Raman 90 ×60 mm. Y piezo table for imaging with laser scanning (X direction), range 100 µm. "PIFOC" Z-actuator for automatic focusing of microscope objective or z-scanning (range 0-100 µm). Autofocus device for microscope objective (correction of focus between +/- 5 µm).

Components	Properties
	Temperature controlled cells. Set of filters (notch + interferential) for external laser.

Table 3.4.1 Main Components of the Raman equipment.

3.5 References

[1] D. A. Long, in "Raman Spectroscopy" Butterworths & CO, LTD London (1971).

[2] R. L. McCrerry in *"Raman Spectroscopy for Chemical Analysis"*, John Wiley & Sons, New York (2000).

[3] D. A. Long in "The Raman Effect", John Wiley & Sons, Chichester, (2002).

[4] R. S. Krishnan, R. K. Shankar, *J. Raman Spectrosc*., (1981) **10** 1.

[5] D. A. Long in "Raman Spectroscopy" McGraw-Hill, Inc., New York (1977).

[6] C. Marcott, M. Padalkar, N. Pleshko, *Comprehensive Biomaterials II,* (2017) **3** 498-518.

[7] M. Beckers, B. Weise, S. Kalapis, T. Gries, G. Seide, C.-A. Bunge in *"Chapter 2- Basics of light guidance"* Elsevier Ltd. (2017).

[8] D. C. Harris, M. D. Bertolucci, in "Symmetry and Spectroscopy. An Introduction to Vibrational and Electronic Spectroscopy" Dover Pubblications, New York (2015).

[9] G. Turrell, J. Corset, in *"Raman Microscopy: Development and Applications"*, Academic Press, San Diego (1996).

[10] E. Smith, G. Dent, in *"Chapter 2- The Raman experiment – Raman Instrumentation, Sample Presentation, Data Handling and Practical Aspects of Interpretation"*, John Wiley & Sons Ltd, The Atrium, Southern Gate, Chichester, England (2005).

Section B

Impedance Spectroscopy

3.6 Impedance Spectroscopy: A Brief Introduction

Impedance Spectroscopy also known as Electrochemical Impedance Spectroscopy (EIS) is a powerful technique used for the characterization of electrical properties of the materials and their interfaces using electronically conducting electrodes and a briefly introduction to the technique is presented [1-6]. EIS is focused on the study of the properties of the mobile or bound charge in the bulk or in the interfacial regions of the sample. EIS can be applied to a wide range of investigated materials, ranging from liquid, solid or in gel composition [1]. Electrical measurements can be realized using an electrochemical cell composed of two identical electrodes of cylindric or paralleled shape, applied to the face of the sample in the case of solid or immersed in the liquid material, in a neutral atmosphere.

EIS compared to other common electrochemical technique such as Cyclic Voltammetry or Chronoamperometry, offers the possibility to evaluate kinetics and mass transport behavior [7, 8], batteries [9], determining diffusion coefficients [10, 11] and rate constants [12], characterizing corrosion processes [13], elucidating the mechanisms of the reactions occurring on the surface of the electrode [14].

Interesting electrochemical characterization of lithium-ion batteries based on polymer electrolytes like Polyethylene oxide (PEO) has been studied by EIS, by making the lithium electrode/PEO polymer electrolyte stable using a self-assembled molecular system [15-20].

EIS can be used also, for the study of the electrical behavior of electrochromic materials and electrochromic devices [21]. In the case of electrochromic devices, where the identification of the contribution of each layer is difficult, the adoption of a simplified model of the equivalent circuit is fundamental. In this new assumption, the electrochromic device can be considered as it is based on only two electrochromic layers or else only interface properties can be considered. The ion conductor is modeled by a pure resistance or even neglected. For quality control of electrochromic devices, EIS is a very time-consuming process, since a spectrum down to low frequencies should be taken at a number of equilibrium potentials [22].

The aging of electrochromic materials can be also characterized by EIS because this technique is sensitive to the material degradation [23]. The aging of electrochromic device based on tungsten oxide was characterized by EIS, through measurements of the impedance in the colored and bleached states of the electrochromic device. When the electrochromic device is in the colored state, the resultant impedance data in the high frequency region do not show significant variations. In the bleached state of the electrochromic device the impedance change became larger the higher the applied potential after every cycle.

The characterization of the ion conduction of polymer electrolytes such as PEO confined in nanopores of alumina to increase the PEO conductivity was provided by EIS [24]. EIS demonstrated that the ion conduction can be realized in two different regions: the bulk polymer electrolyte in the pores and the interface between the pore walls and the polymer electrolyte [24].

EIS is currently used for the fabrication of gas sensors based on semiconducting metal-oxide nanomaterials (WO_3, ZnO, SnO_2 and TiO_2) to identify and measure different toxic gases which are present in trace levels such as H_2S [25]. The contribution of this technique in this area is the estimation of some interesting properties like grain bulk, grain boundary, interface between sensitive layer and electrode, that aid to demonstrate the mechanism of a toxic gas sensor and its interaction with the target toxic gas.

EIS became a promising experimental approach in biological and medical applications. This electrochemical technique plays an important role in the cell research because it gives essential details regarding the interaction of metal electrodes with biological matter and liquids, biosensing technologies and diagnosis of diseases, including cancer and virus detection [26].

3.7 Basics of Impedance Measurements

A typical EIS experiment consists of the application of an electrical stimulus (voltage or current) to the electrodes and observing the resultant response in terms of resulting voltage or current, in the consideration that the properties of the systems are time-independent. Considering the application of a sinusoidal potential excitation, the response

to this potential is an AC current signal that can be analyzed as a sum of sinusoidal functions with Fourier series. Usually, the EIS is measured with the application of small voltage and this means that the electrochemical cell follows a pseudo linear behavior *i.e.*, at the corresponding sigmoidal potential the response of the current is a sigmoid at the same frequency, but shifted of a certain quantity known as phase shift, ϕ as depicted in Figure 3.7.1.

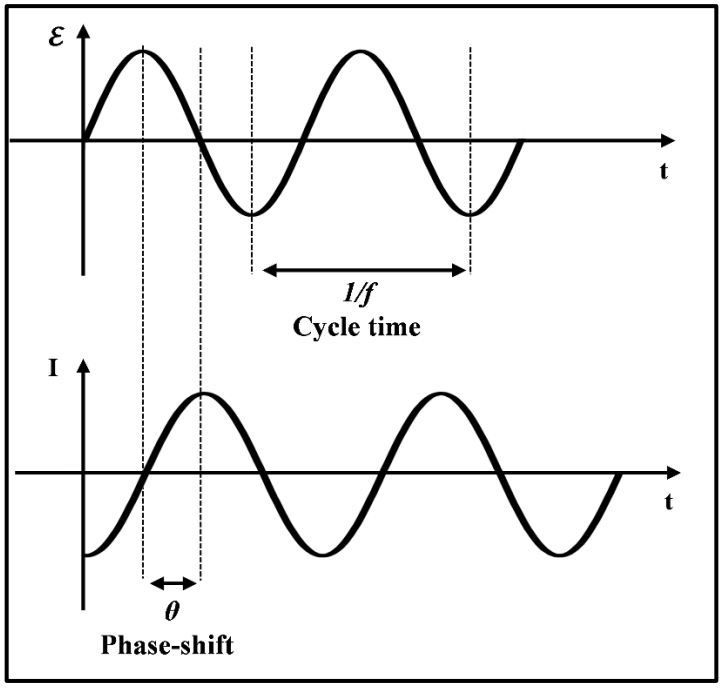

Figure 3.7.1. Sinusoidal Current response for a linear electrochemical cell. The Figure is taken from [2].

The applied voltage can be expressed as following (Equation 3.7.1):

$$\mathcal{E}(t) = \mathcal{E}_0 \sin(\omega t) \qquad 3.7.1$$

Where $\mathcal{E}(t)$ is the potential at the time *t*, $\mathcal{E}_0$ is the amplitude of the signal and ϖ is the frequency. The resulting current is given (Equation 3.7.2):

$$I(t) = I_0 \sin(\omega t + \theta) \qquad 3.7.2$$

Where I_0 is the amplitude and θ is the phase angle.

Considering the contribution of the resistance R in the Ohm's Law, an expression of the Impedance *(Z)* can be written as following (Equation 3.7.3):

$$Z = \frac{\mathcal{E}(t)}{I(t)} = \frac{\mathcal{E}_0 \sin(\omega t)}{I_0 \sin(\omega t + \theta)} = Z_0 \frac{\sin(\omega t)}{\sin(\omega t + \theta)} \quad 3.7.3$$

Impedance is a property that it depends on the magnitude of the Z_0 quantity and by the phase angle θ.

Considering the Euler's relation in Equation 3.7.4 the applied voltage $\mathcal{E}(t)$ and the resulting current $I(t)$ can be reformulated as following (Equations 3.7.5 and 3.7.6) to obtain a clearly definition of the Impedance expressed in the Equation 3.7.7:

$$e^{(j\theta)} = (cos\theta + j \sin\theta) \quad 3.7.4$$

$$j = \sqrt{-1}$$

$$\mathcal{E}(t) = \mathcal{E}_0 e^{(j\omega)} \quad 3.7.5$$

$$I(t) = I_0 e^{(j\omega t - j\theta)} \quad 3.7.6$$

$$Z = \frac{\mathcal{E}(t)}{I(t)} = Z_0 e^{(j\theta)} = Z_0(cos\,\theta + j \sin\theta) \quad 3.7.7$$

The resultant formula of Z, can be interpreted as the impedance of a complex function (Equation 3.7.8) As a complex function, the impedance is composed of two components, a real (Z') and an imaginary (Z'').

$$|Z| = \sqrt{Z'^2 + Z'^2} \quad 3.7.8$$

$$\theta = -tan^{-1}\left(\frac{Z'}{Z''}\right)$$

Figure 3.7.2 shows the Nyquist plot of the Impedance as vector $|Z|$, which is characterized by the real component on the x-axis on the y-axis the corresponding imaginary component. The angle between the vector $|Z|$ and the x-axis is the phase angle $\theta = (\arg Z)$. From the plot is not possible to deduce the relation between the points of the semicircle and the corresponding frequency at which they were recorded. In addition, the plot shows low-frequency data on the right side of the plot and higher frequency data on the left.

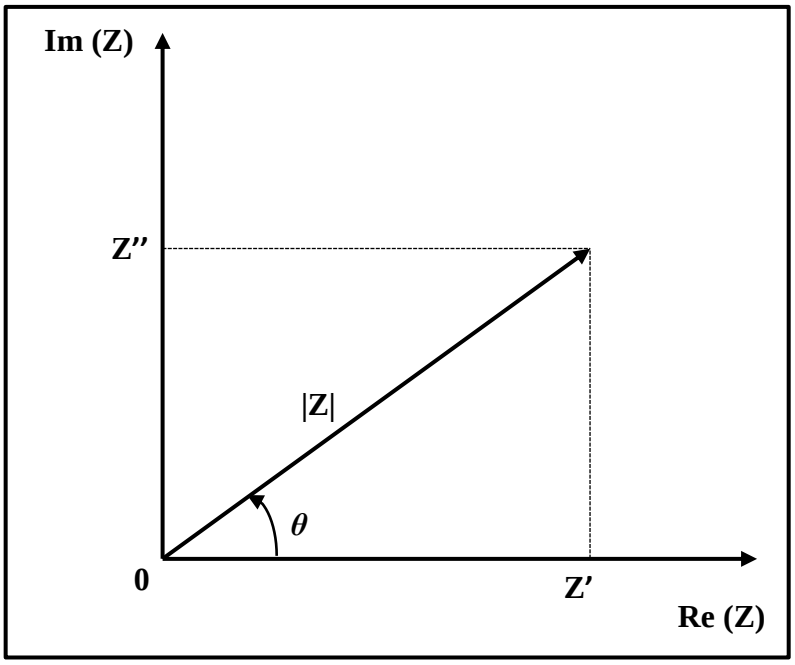

Figure 3.7.2. Nyquist plot for a linear electrochemical cell. The Figure is taken from [1].

3.8 Physical Elements for Equivalent Circuit Elements

Usually, a flow diagram as the example shown in Figure 3.8.1 can be useful for the interpretation of the EIS data. In fact, the experimentally impedance data for a given system should be analyzed by using a mathematical model based on a physical theory, which predicts the theoretical impedance $Z_t(\varpi)$ or empirical equivalent circuit $Z_{ec}(\varpi)$. The use of the mathematical model or the construction of the equivalent circuit provides useful data of impedance that they can be compared with the experimental impedance data $Z_e(\varpi)$ of the system by an accurate fitting procedure (for example the Complex Nonlinear Least Square fitting procedure, CNLS) and to obtain the best electrochemical characterization of the system.

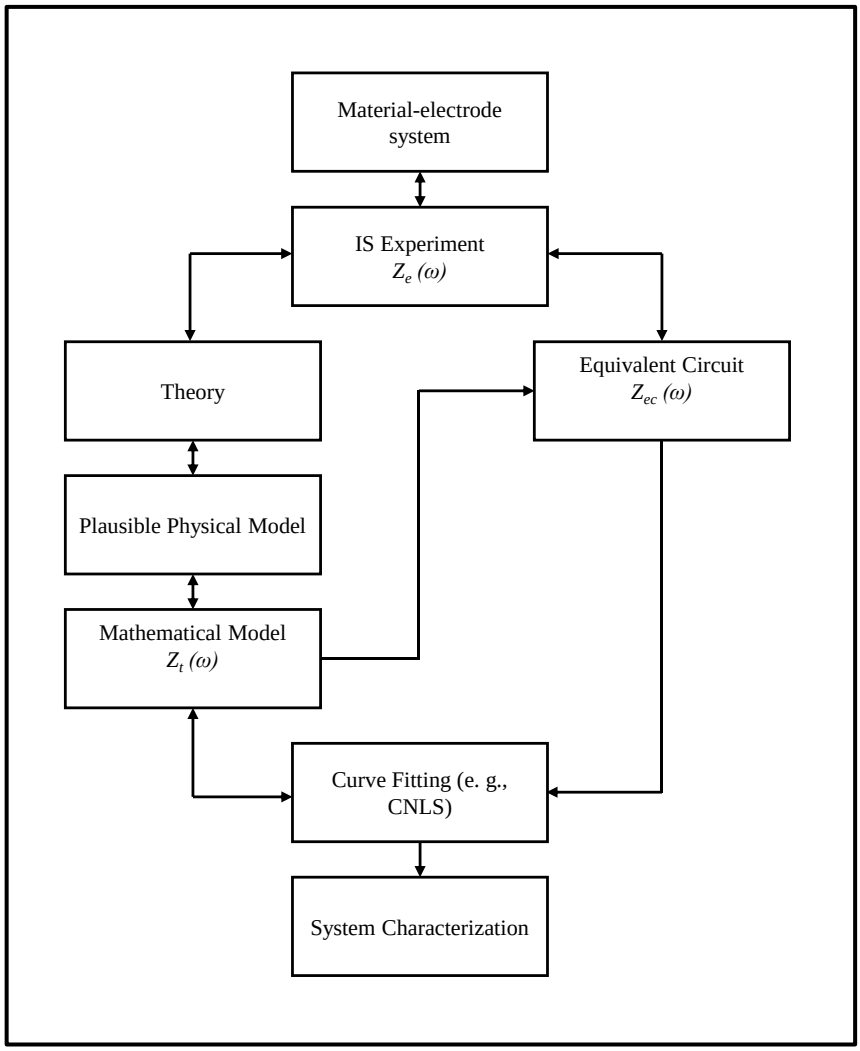

Figure.3.8.1. Flow diagram for the EIS data interpretation. The Figure is taken from [1].

For the construction of the empirical equivalent circuit, it important to consider the common electrical elements such as resistors, capacitors, and inductors and they possible combination (in serial and in parallel).

Considering an electrochemical cell and its resistance which is known as the electrolyte resistance R_s and that is referred to the solution resistance between the counter and the reference electrodes. The resistance of an ionic solution depends on many factors such as the ionic concentration, type of ions, temperature and by the geometry of the area in which the current is flown. In the approximation of a uniform current flux, the resistance of an electrochemical cell of area *A*, thickness *l*, is given by (Equation 3.8.1):

$$R = \rho \frac{l}{A} \qquad 3.8.1$$

Where ρ is known as the resistivity of the solution. The reciprocal quantity indicated as σ (S cm^{-1}) is the conductivity S cm^{-1} of the solution defined by the following (Equation 3.8.2):

$$\sigma = \frac{l}{R\,A} \qquad 3.8.2$$

Another interesting kind of resistance is known as charge transfer resistance, R_{CT}. For a metal substrate *M* which is put in contact with an electrolyte solution, the equilibrium into the solution is (Equation 3.8.3):

$$M \rightleftharpoons M^{n+} + ne \qquad 3.8.3$$

The rate of the heterogenous charge transfer reaction referred to the metal diffuse into the electrolyte solution depends on some factors such as the kind of reaction, the concentration of the electrolyte solution, the temperature and potential. According to the Faraday's law, the relation between the current and the potential can be written as following (Equation 3.8.4):

$$i = i_o \left[\left(\frac{C_o}{C_o^*} e^{\frac{\alpha\, nF\eta}{RT}} \right) - \left(\frac{C_R}{C_R^*} e^{\frac{-(1-\alpha)nF\eta}{RT}} \right) \right] \qquad 3.8.4$$

Where i_o is the exchange current density, C_o and C_o^* are the concentration of the oxidant at the electrode surface and in the bulk, C_R and C_R^* are the concentration of the reductant at the electrode surface and in the bulk. α is the order of the reaction, n is number of electrons involved, T is the temperature, R is the gas constant and η is the over potential.

For a specific case, in which the concentration at electrode surface is the same of the concentration in the bulk, is possible to written the Equation 3.8.4 as following (Equation 3.8.5):

$$i = i_o \left[\left(e^{\frac{\alpha\, nF\eta}{RT}} \right) - \left(e^{\frac{-(1-\alpha)nF\eta}{RT}} \right) \right] \qquad 3.8.5$$

This relation is known as the Butler-Volmer and it is valid only in the case in which the polarization depends only by the kinetics of the charge transfer. When the over potential is small, the Butler-Volmer equation can be simplified as following (Equation 3.8.6) which is useful for the determination of the exchange current density:

$$R_{CT} = \frac{RT}{nFi_o} \quad 3.8.6$$

The impedance generated by the diffusion process is known as Warburg impedance and it depends on the frequency of the potential perturbation. The contribution of Warburg impedance is important at low frequencies, where the reactants can move faster. Considering the diffusion process in a layer of infinite thickness, the Warburg impedance is defined as following (Equation 3.8.7):

$$Z_w = \sigma(\varpi)^{-1/2}(1-j) \quad 3.8.7$$

Where ϖ is the radial frequency and the term σ is called Warburg coefficient and it equal to (Equation 3.8.8):

$$\sigma = \frac{RT}{n^2F^2A\sqrt{2}}\left(\frac{1}{C_o^*\sqrt{D_o}} + \frac{1}{C_R^*\sqrt{D}_R}\right) \quad 3.8.8$$

Where D_o and D_R are the diffusion coefficient of the oxidant and the reductant, A is the area of the electrode and n is the number of electrons involved.

For a diffusion process in layer of finite thickness, the Warburg impedance is known as Warburg *finite* and it can be defined as the following (Equation 3.8.9):

$$Z_o = \sigma\varpi^{-1/2}(1-j)\tanh\left(\delta\left(\frac{j\omega}{D}\right)^{\frac{1}{2}}\right) \quad 3.8.9$$

Where δ is the Nernst diffusion layer thickness and D corresponds to the average value of the diffusion coefficients of the diffusing species.

The Warburg impedance on the Nyquist plot is shown as a line with a slope of 45°.

The capacitors can act as a constant phase element and the relative impedance is equal to (Equation 3.8.10):

$$Z_{CPE} = \frac{1}{(j\varpi)^{\alpha}Y_o} \quad 3.8.10$$

Where α varying between 0.9-1.0 and Y_o is the capacitance. For a capacitor which acts like a constant phase element, the term α is less than one.

For a pure inductor, the impedance is given by (Equation 3.8.11):

$$Z_L = j\varpi L \qquad 3.8.11$$

Where L is known as the inductance. Experimentally, the presence of the inductance element is associated with the electrical equipment and the cabling.

3.9 References

[1] J. R. Macdonald, W. B. Johnson, in *"Chapter 1-Fundamentals of Impedance Spectroscopy"* John Wiley & Sons, Inc. (2018).

[2] M. Aljarrah, F. Salman, *J. Inst. Eng. India Ser. D*, (2021) **102** 237-242.

[3] I. D. Raistrick, J. R. Macdonals, D. R. Franceschetti, in *"Chapter 2-Theory"* John Wiley & Sons, Inc. (2018).

[4] P. W. Atkins, in "*Physical Chemistry"*, Oxford University Press (1990).

[5] M. E. Orazem, B. Tribollet, in *"Chapter 4 - Electrical Circuits"* John Wiley& Sons, Inc, (2008).

[6] Nadia O. Laschuk, E. Bradley Easton, Olena V. Zenkina, *RSC Adv*., (2021) **11** 27925-27936.

[7] T. Dhandayuthapani, R. Sivakumar, R. Ilangovan,C. Gopalakrishnan, C. Sanjeeviraja, A. Sivanantharaja, R. Hari Krishna, *J. Solid State Electrochem.*, (2018) **22** 1825-1838.

[8] N. O. Laschuk, A. Obua, I. I. Ebralidze, H. Fruehwald, J. Poisson, J. G. Egan, F. Gaspari, E. B. Easton, O. V. Zenkina, *ACS Appl. Electron. Mater*. (2019) **1** 1705-1717.

[9] D.D. Stupin, E. A. Kuzina, A. A. Abelit, A. K. Emelyanov, D. M. Nikolaev, M. N. Ryazantsev, S.V. Koniakhin, M. V. Dubina, *ACS Biomater. Sci. Eng*., (2021) **6** 1962-1986.

[10] N. O. Laschuk, A. Obua, I. I. Ebralidze, H. Fruehwald, J. Poisson, J. G. Egan, F. Gaspari, E. B. Easton, O. V. Zenkina, *ACS Appl. Electron. Mater*., (2019), **1**, 1705-1717.

[11] J. Huang, *Electrochim. Acta*, (2018) **281** 170-188.

[12] V. Ganesh, S. K. Pal, S. Kumar and V. Lakshminarayanan, *J. Colloid Interface Sci*., (2006) **296** 195-203.

[13] F. Fasmin and R. Srinivasan, *J. Electrochem. Soc*., (2017) **164** 443-455.

[14] L. Manjakkal, E. Djurdjic, K. Cvejin, J. Kulawik, K. Zaraska, D. Szwagierczak, *Electrochim. Acta*, (2015) **168** 246-255.

[15] R. N. Mason, M. Smith, T. Andrews, D. Teeters, *Solid State Ionics*, (1999)**118** 129.

[16] M. Le Granvelet-Mancini, L. Honeycutt, D. Teeters, *Electrochimica Acta*, (2000) **45**, 1491.

[17] M. Le Granvalet-Mancini, T. Hanrath, D. Teeters, *Solid State Ionics*, (2000) **283** 1-4.

[18] M. Le Granvalet-Mancini, D. Teeters, *Power Sources*, (2001) **624** 97-98.

[19] Decker, D.S., Teeters, D., *International Journal of Hydrogen Energy*, (2014) **39** 3025.

[20] N. R. Brown, T Makkapati, D. Teeters, *Solid State Ionics* (2016) **288** 207.

[21] G.A. Niklasson, S. Malmgren, M. Stromme, in *"Chapter 4-Impedance response of electrochromic materials and devices"* Wiley: Hoboken (2018).

[22] N. Bonanos, B. C. H. Steele, E. P. Butler in "Chapter 4-Application of Impedance Spectroscopy" John Wiley & Sons (2018).

[23] E. Pehlivan, G. A. Niklasson, C.G. Granqvist, P. Georen, *Phys. Status Solidi A*, (2010) **207** 1772-1776.

[24] M. Castriota, D. Teeters, *Ionics*, (2005) **11** 220-225.

[25] V. Balasubramani, S. Chandraleka, T. Subba Rao, R. Sasikumar, M. R. Kuppusamy, T. M. Sridhar, *Journal of The Electrochemical Society*, (2020) **167** 037572.

[26] N. Meddingsa, M. Heinrichb, F. Overney, J. S. Lee, V. Ruiz, E. Napolitano, S. Seitz, G. Hinds, R. Raccichini, M. Gabercsek, J.Parkl, *Journal of Power Sources*, (2020) **480** 228742.

Section C

Cyclic Voltammetry

3.10 Cyclic Voltammetry

Cyclic Voltammetry (CV) is a versatile electrochemical technique useful for the understanding the mechanisms of redox reactions. It provides rapid information also on the thermodynamic redox processes, the reversibility of a reaction, and the kinetics of an electron transfer processes [1]. This analytical technique studies the cyclability of a time-varying potential, that varies linearly when it is applied to an electrode immersed in an unstirred solution (electrochemical cell). The resulting current (i) is measured as a function of the applied potential [1].

In a typical CV experiment, the potential of the working electrode (WE) is controlled versus a reference electrode (RE). Typical reference electrodes suitable are the saturated calomel electrode (SCE) or the couple AgI/AgCl. The control of the potential between the WE and the RE electrode can be assumed as an excitation signal and in the case of the CV, the linear potential is linear scanned using a triangular waveform [2]. The triangular waveform of the potential in CV is shown in Figure 3.10.1 [3].

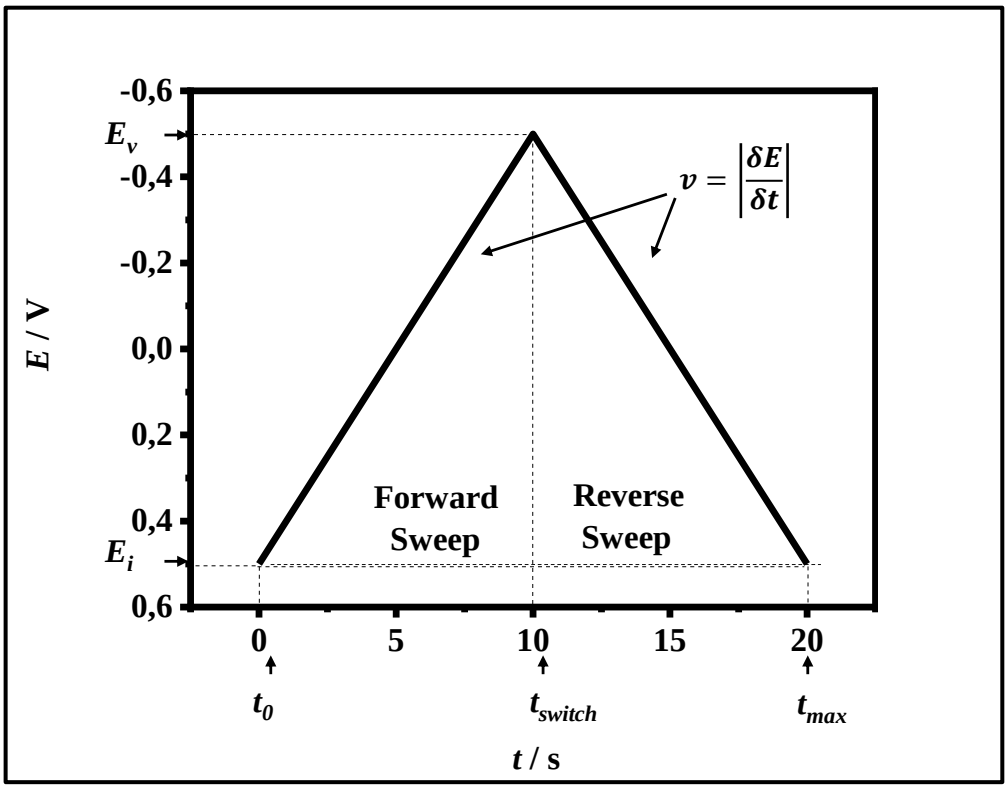

Figure 3.10.1. Schematization of the applied triangular waveform potential during cyclic voltammetry. The Figure is taken from [3].

As a consequence of this kind of excitation signal, the potential of the WE can sweep between two values, which are called switching potentials [2]. The starting potential of the electrode is labeled E_i. In the forward sweep, the application of the excitation signal at the initial t_o causes the electron transfer process *i.e.*, it is responsible for the scan of the potential from the starting potential to the vertex potential E_v versus the SCE (negative potential). At the switch-time indicated as t_{switch}, the scan direction is inverted. In the reverse sweep the potential is scanned towards positive potentials from E_v to the E_i at the maximum of the time t_{max}. Then, repeating cycles can be performed. The speed of the forward and the reverse sweep corresponds to the scan rate (υ) expressed in terms of mV/s and it represents the slope of the line. The scan rate indicated that during the experiment is possible to observe that the voltage varied linearly from the initial potential to the vertex potential and back again. The scan rate can be defined as following (Equation 3.10.1):

$$v = \frac{\delta E}{\delta t} \qquad 3.10.1$$

The role of the scan rate in the electrochemical experiment is fundamental because this term controls how fast the applied potential is scanned. Fast scan rates mean that high currents can be observed [3, 4].

The plotting of the current I (amperes) measured at the working electrode during the potential scan gives a characteristic cyclic voltammogram as depicted in Figure 3.10.2 [3].

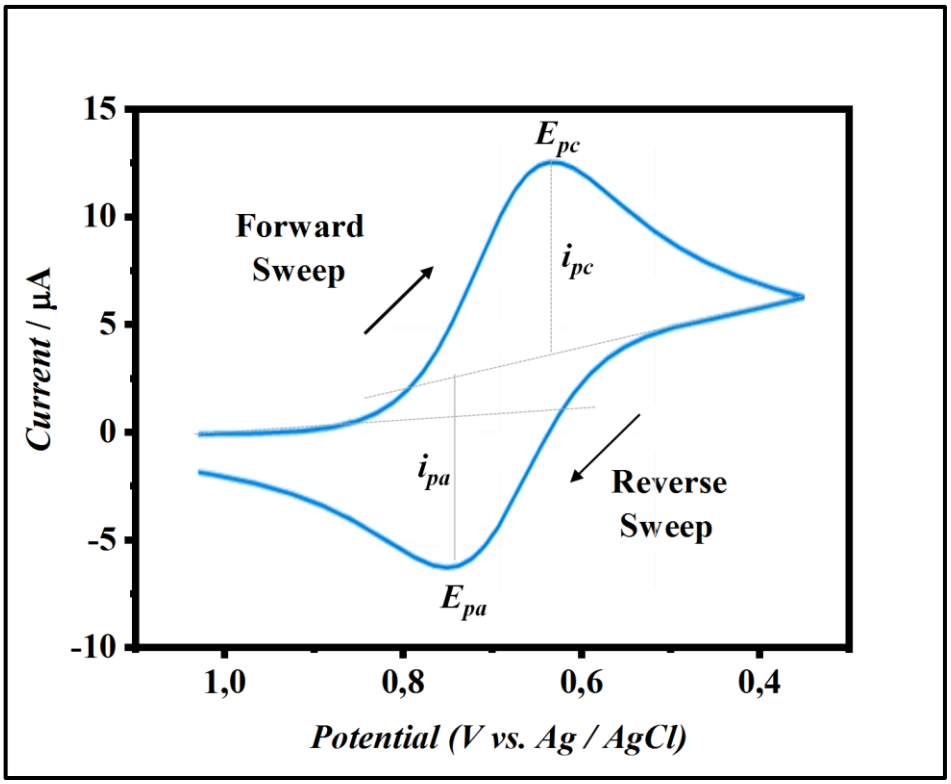

Figure 3.10.2. Cyclic Voltammogram corresponding to the triangular time waveform. The Figure is taken from [3].

The black arrows indicate the direction of the forward and reverse sweep during the CV experiment. The current is considered as the response signal which is due to the excitation signal. The voltammogram is characterized by the presence of some features (peaks) on which the reduction and the oxidation processes are based. The analysis of these features provides important information regarding the electrochemical behavior of the involved species and of the redox process considered. From the voltammogram, some variables can be considered such as the cathodic peak potential (E_{pc}), the anodic peak potential (E_{pa}), the cathodic peak current (i_{pc}) and the anodic peak current (i_{pa}). Considering the kinetic regimes, an electrochemical reaction can be classified as: reversible, *quasi*-reversible and irreversible [5].

For electrochemically reversible reaction, which is characterized by a fast electron transfer between the electrode and the analyte, the cathodic and the anodic current peaks are coincident and the difference between them is equal to the peak-to-peak separation parameter (ΔE_p) that is estimated as reported in Equation 3.10.2 [4]:

$$\Delta E_p = \left|E_{pa} - E_{pc}\right| = \frac{2.303\ RT}{nF} \qquad 3.10.2.$$

Where R is the universal gas constant, T is the temperature, n is the number of the electrons involved in the half-reaction of the redox process and F is the constant of Faraday. Chemical reversibility means also whether the analyte is stable upon reduction then it can subsequently be re-oxidized.

At 25 °C the Equation 3.10.3 can be rearranged as following (Equation 3.10.3) [4]:

$$\Delta E_p = \left|E_{pa} - E_{pc}\right| = \frac{0.0592}{n} \qquad 3.10.3.$$

The formal reduction potential (E_0) for a reversible redox process is given by the Equation 3.10.4 [4]:

$$E_0 = \frac{E_{pa} + E_{pc}}{2} \qquad 3.10.4$$

From a quantitative point of view, the concentration can be related to peak current considering the validity of the Randles–Sevcik Equation for a reversible electron transfer process at 25 °C (Equation 3.10.5) [6]:

$$i_p = 2.69 \times 10^5 \times n^{3/2} \times A \times D^{1/2} \times C_o \times v^{1/2} \qquad 3.10.5$$

where i_p is the peak current (Amperes), A is the electrode area (cm^2), D is the diffusion coefficient (cm^2/s), c is the concentration in (mol/cm^3), and v is the scan rate in (V/s).

The Randles-Sevcik equation can be expressed as a function of current density at fixed temperature 25 ℃, schematically, as (Equation 3.10.6) [7]

$$j_p = 2.69 \times 10^5 \times n^{3/2} \times D^{1/2} \times C_o \times v^{1/2} \qquad 3.10.6$$

Where j_p is the peak current i.e., the cathodic j_{pc} and anodic peaks density current j_{pa} regarding the working area of the electrodes.

The use of the Randles-Sevcik Equation is useful for the estimation of the diffusion coefficients, when the concentration, the electrode area and the scan rate are known parameters.

For slow electron transfer kinetics, the reaction can be assumed an irreversible character. In this case, the position of the potential peaks is shifted as a function of the scan rate and the value of the difference potential peak is greater than the ratio (0.0592/n) [4].

In the case of *quasi*-reversible kinetics, at low scan rates the electron transfer is comparable to a reversible process, while at high scan rates it shows an irreversibility behavior that is confirmed by the increase of the value of the (ΔE_p) parameter. It is convenient for this kind of kinetics to perform various electrochemical experiments at different scan rates. In this way is possible to study the slow kinetic, and determine constate rates by the evaluation of the ΔE_p corresponding to the different scan rates [4].

3.11 References

[1] N. Elgrishi, K. J. Rountree, B. D. McCarthy, E. S. Rountree, T. T. Eisenhart, J. L. Dempsey, *J. Chem. Educ.* (2018) **95** 197−206.

[2] P. T. Kissinger, W. R. Heineman, *Journal of Chemical Education*, (1983) **60** 702-706.

[3] R. G. Compton, E. Laborda, K. R. Ward in "Understanding Voltammetry: Simulation of Electrode Processes" Imperial College Press, London (2014).

[4] D. A. Skoog, D. M. West, F. J. holler, S. R. Crouch in "Fundamentals of Analytical Chemistry, Ninth Edition", Books-Cole, Cengace Learning, USA (2014).

[5] N. Aristov, A. Habekost, *World J. Chem. Educ*., (2015) **3** 115-119.

[6] M. A. Habib, D. Glueck, D., *Sol. Energy Mater*., (1989) **18** 127-141.

[7] P. W. Chen, C. T. Chang, T. F. Ko, S. C. Hsu, K, D. Li, J. Y. Wu, *Nanoporous Sci. Rep.*, (2020) **10** 1-12.

Section D

Differential Scanning Calorimetry

3.12Differential Scanning Calorimetry (DSC): A Brief Introduction

Differential Scanning Calorimetry (DSC) is a thermo-analytical technique that measures the change of the difference in heat flow to the sample and an inert reference sample while they are subjected to a controlled temperature [1, 2]. It is a very powerful technique to evaluate material properties such as glass transition temperature, melting, crystallization, specific heat capacity, cure process, purity, oxidation behavior, and thermal stability.

In condition of constant pressure, the heat flow quantity is equivalent to enthalpy changes as following (Equation 3.11.1):

$$\frac{dq_p}{dt} = \left(\frac{dH}{dt}\right)_p \qquad 3.11.1$$

The Heat flow difference between the sample and the reference is given by (Equation 3.11.2):

$$\Delta\frac{dH}{dt} = \left(\frac{dH}{dt}\right)_{sample} - \left(\frac{dH}{dt}\right)_{reference} \qquad 3.11.2$$

This quantity can be either positive or negative. For an endothermic process, as in the case of the phase transitions, the heat is absorbed and consequently, the heat flow of the sample is higher than the reference, which means that the term $\Delta\frac{dH}{dt}$ is positive. For an exothermic process, the quantity $\Delta dH/dt$is negative because the heat flow of the reference is higher than to the sample. A typical heat flux DSC cell is shown in Figure 3.11.1.

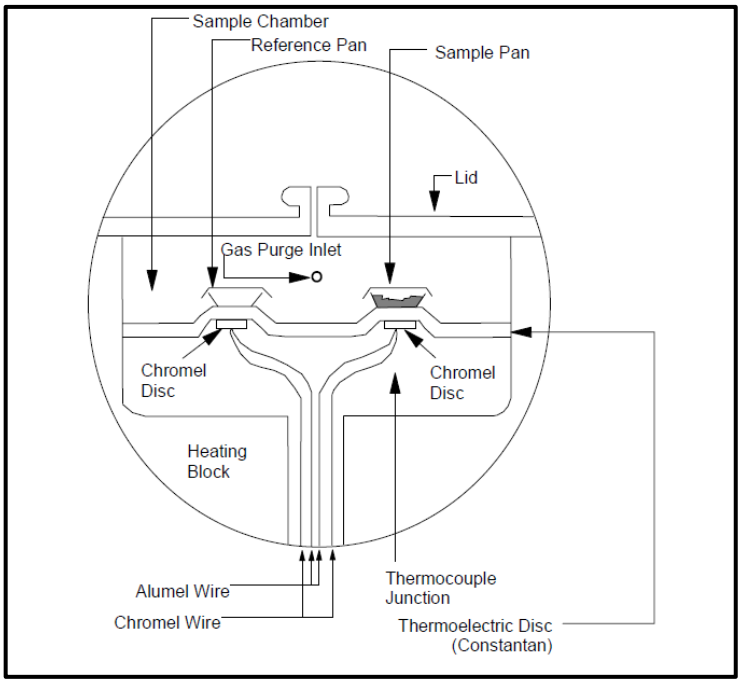

Figure 3.11.1. Design of a typical heat flux DSC cell. The Figure is taken from [3].

A metallic disk is the primary means of heat transfer to and from the sample and reference. The sample, contained in an aluminum pan, and the reference (an empty pan) sit on raised platforms formed in the constantan disk. As heat is transferred through the disk, the differential heat flow to the sample and reference is measured by area thermocouples formed by the junction of the constantan disk and chromel wafers which cover the underside of the platforms. The temperatures of both the sample and reference are increased at a constant rate. The difference in the power to the two platforms, necessary to maintain them at the same temperature, is used to calculate $\Delta dH/dt$. In addition, a flow of nitrogen atmosphere is maintained over the sample to ensure a reproducible and dry atmosphere. At high temperatures, the inert nitrogen atmosphere can eliminate air oxidation of the samples. During the heating of a sample, from room temperature to its decomposition temperature, peaks with positive and negative $\Delta dH/dt$ may be recorded. Each peak corresponds to a heating effect associated with a specific process, such as crystallization or melting.

3.13Glass Transition Temperature

Glass transition temperature (T_g) in polymers is an important type of phase transition. At lower temperatures, the polymer is in a glassy state in which the molecules can move slowly. In the glassy state the polymer is as rigid as the glass. At higher temperatures, when the polymer is heated, its chains become softer and more flexible, like rubber. This state is known as the rubbery state. The temperature at which the polymer from the glassy state makes a transition to a rubbery state is known as the Glass Transition Temperature, T_g [4]. T_g is the result of molecular interactions and it can therefore be used to detect small changes in the structure of samples.

The value of T_g is not a thermodynamic fixed point, so for this reason it depends on several factors such as the cooling and heating rates, the thermal and mechanical history, the method used to determine it and the mobility/flexibility of the polymeric chains. In addition, the presence of groups such as amide, sulfone, carbonyl, *etc*., also known as stiffening groups can modify the T_g. The chain stiffness can reduce the flexibility of the chains and cause an increase of the glass transition temperature. The cross-links between chains restrict rotational motion and raise the glass transition temperature. In this case, higher cross-linked molecule can show higher T_g than that with the lower cross-linked molecule.

The presence of pendant groups can modify the glass transition temperature. Flexible pendant groups such as aliphatic chains can limit the packing of the chains which translates to the decrease of T_g, while bulk pendant groups such as a benzene ring can lead to an increase of the Tg because its steric effect limits the polymeric chain flexibilities.

An interesting effect on the T_g is shown by the role of the plasticizers. Plasticizers are low molecular weight and are added to the polymers to improve the flexibility of the chains. Plasticizers reduce the intermolecular interaction between the chains and lower T_g can achieved. Also, the molecular weight of the polymer contributes to modifying the T_g. The relation between the molecular weight and T_g is known as the Fox-Flory Equation (Equation 3.12.1) [5]:

$$T_g = T_{g,\infty} - \frac{K}{M_n} \qquad 3.12.1$$

Where $T_{g,\infty}$ is the glass transition temperature of a polymer of infinity molecular weight and *K* is the Fox-Flory parameter. It is an empirical parameter that describes the free volume inside the polymer. Considering the Fox-Flory Equation, T_g increases up for polymers with molecular weights of about 20000, then T_g is not affected ash shown in Figure 3.12.1.

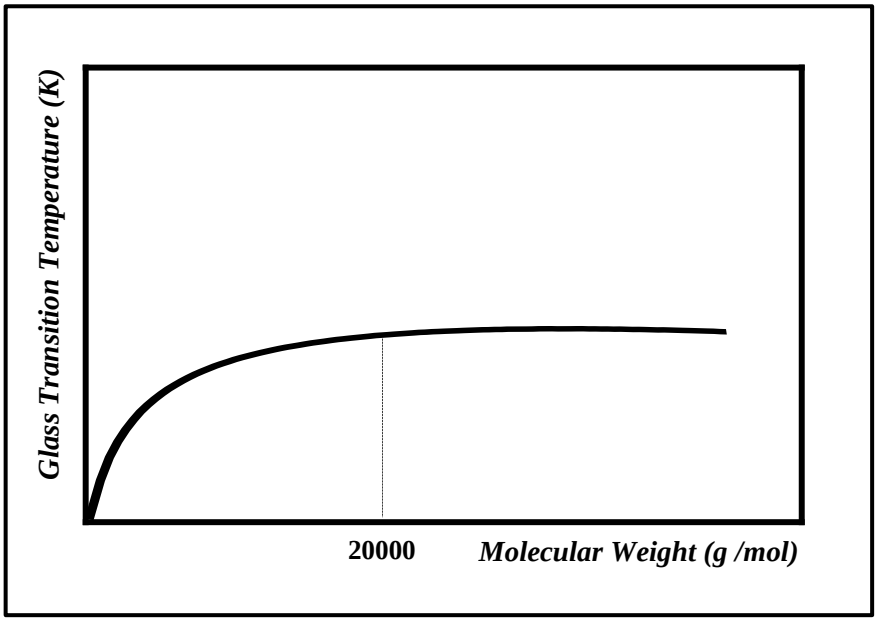

Figure 3.12.1. Glass transition temperature vs. the molecular weight of polymers. The Figure is taken from [4].

In the DSC experiment, Tg is manifested by a change in the baseline, indicating a change in the heat capacity of the polymer. First-order phase transitions have an enthalpy and a heat capacity change for the phase transition. Second-order transitions are manifested by a change in heat capacity, but with no accompanying change in enthalpy. The baselines before and after the transition are extrapolated to the temperature where the change in heat capacity is 50% complete. The integral under the DSC peak, above the baseline, gives the total enthalpy change for the process (Equation 3.12.2):

$$\int \left(\frac{dH}{dt}\right)_{sample} dt = \Delta H_{sample} \qquad 3.12.2$$

Assuming that the heat capacity of the reference is constant over the temperature range covered by the peak, the term referred to as the $\Delta H_{reference}$ can be neglected. Heat capacities

and changes in heat capacity can be determined from the shift in the baseline in the thermogram. The heat capacity, C_p at constant pressure is a temperature derivative of the enthalpy function (Equation 3.12.3). The difference in the heat capacity at a constant pressure between the sample and the reference (Equation 3.12.4) is defined as following:

$$C_p = \frac{dq_p}{dt} = \left(\frac{dH}{dT}\right)_p \qquad 3.12.3$$

$$\Delta C_p = \Delta\left(\frac{dH}{dT}\right)_p = \Delta\frac{dH}{dt}\,\frac{dt}{dT} \qquad 3.12.4$$

Where the quantity dt/dT is the temperature scan rate.

3.14References

[1] G. Hohne, W.F. Hemminger, H. J. Flammersheim, in "Differential Scanning Calorimetry", Springer (2003).

[2] P. Atkins, J. de Paula, in "Atkin's Physical Chemistry" W. H. Freeman and Company, New York (2006).

[3] U. S. Syamala, *J. Bioequiv Availab*., (2018) 5 141-149.

[4] K. Balani, V. Verma, A. Agarwal, R. Narayan, in *"Chapter 1-Physical, Thermal and Mechanical Properties of Polymers"*, The American Ceramic Society, by John Wiley & Sons, Inc. (2015).

[5] D. W. Van Krevelen, K. T. Nijenhuis, in "Chapter 6- Transition Temperatures", Elsevier B. V. (2009).

CHAPTER 4

RESULTS AND DISCUSSION

In Chapter 4, all the main experimental results collected in this Ph.D. work are presented and examined in detail.

Here is a summary of the investigated arguments:

4.1. Study of electrochromic devices made by Tungsten trioxide and Titanium dioxide thin films, synthesized by Sol-Gel method, and annealed at different temperatures.

4.2. Study of Electrolytes suitable for electrochromic devices: An investigation of Plasticizers and Salt concentrations effects on Liquid and Polymer Gel Electrolytes based on poly (methyl methacrylate).

4.3. Fabrication of *all-in-one* liquid-based electrochromic device made by Ethyl viologen diperchlorate, 1,1'-Diethyl Ferrocene, Bisphenol-A glycerolate diacrylate and Irgacure 651 for Energy Efficient Windows.

4.4. *Industrial-level* production of electrochromic devices: Design and Implementation of an automated assembly system of electrochromic devices.

4.1 Study of electrochromic devices made by Tungsten trioxide and Titanium dioxide thin films, synthesized by Sol-Gel method, and annealed at different temperatures

Abstract

In this work, WO_3 and TiO_2 thin films have been obtained by sol-gel spin coating method. The as-deposited samples were annealed at different annealing temperatures in the range between 100 °C and 500°C. After the annealing treatments, such samples were characterized by micro-Raman Spectroscopy. Single electrodes were also used for the estimation of Li^+ ions diffusion in two electrolyte media (liquid electrolyte and gel polymer electrolyte) and then, they have been used as electrodes for assembling various electrochromic devices. The electrochromic devices have been studied by Cyclic Voltammetry and UV-Vis-NIR Spectroscopy. The main technological properties, such as transmittance, coloration efficiency, and switching time (switch ON/OFF) of the electrochromic devices have been related to the annealing temperature to which the used electrode was subjected. The annealing process that led to the electrochromic device with the best technological performances has been identified and a qualitative model has been proposed. The results here shown could be very useful in "Smart Windows" technology for energy-saving applications.

4.1.1. Introduction

Metal-oxide thin films, such as tungsten trioxide (WO_3) and titanium dioxide (TiO_2) are currently among the main candidates to be used as transparent semiconductor materials to make electrochromic and photochromic devices, chemical sensors, and superconductors. The metal-oxide layers can be used for the production, on an industrial scale, of innovative "Smart Windows" because they show excellent chemical stability, mechanical hardness, and optical transmittance. The sol-gel process is one of the most appropriate methods to prepare thin oxide coating. The attention to the sol-gel method is

due to several advantages like the possibility to obtain a transparent thin film of metal oxide, good homogeneity, and good optical properties on different substrates including glass [1]. Electrochromic devices based on WO_3 material have high coloration efficiency, high reversibility, good memory effect, and exhibit low power consumption [2]. WO_3 synthesis could be realized using different methods such as sol-gel technique, sputtering, and spray pyrolysis and it is important to underline how the preparation method could influence the properties of the material [3]. WO_3 thin films can have two structures orders: amorphous and polycrystalline. Amorphous-WO_3 is a cathodic electrochemical material and it has specific optical properties that switch from transparent to blue under double injection of ions and electrons under an applied voltage [4]. Amorphous-WO_3 films are extensively used in electrochromic applications due to their excellent electrochromic properties compared to crystalline films [5]. From a chemical point of view, the electrochromic coloring of tungsten trioxide is a synchronous uptake of electrons and ions into the solid. Characterization of thin WO_3 films for pure electrochromic applications has been proposed [6].

Another kind of material that is commonly used as a coating in various optical applications is Titanium dioxide, TiO_2. Because of its high transparent, high refractive index, and chemical durability it is suitable in both the visible region and near-infrared region of the spectrum for optical. Various methods can be used for its synthesis including sol-gel, sputtering, chemical vapor deposition, and e-beam evaporation processes application [1]. As well-known, TiO_2 can crystallize in three polymorphs like anatase (tetragonal), rutile (tetragonal), and brookite (orthorhombic) [7, 8]. Anatase is the general favored for solution-phase preparation. In an electrochromic device, the use of titanium dioxide as ion storage also increased the contrast of the dark-blue reduced electrochromic layer.

In this work, the sol-gel spin coating method was used to produce metal oxide thin films based on WO_3 and TiO_2. Metal Oxide thin films were annealed at three different temperatures (100 °C, 300 °C and 500 °C) for 1 hour and they were used as electrodes for the assembling of different electrochromic devices. At the start, single electrodes annealed WO_3 and TiO_2 were electrochemically characterized for the estimation of ion transportation (Li^+ ions) in different electrolytes media (liquid electrolyte and gel polymer electrolyte). Then, the annealed electrodes of WO_3 and TiO_2 have been used for the

assembling of electrochromic devices. An exhaustive correlation of the annealing temperature and consequently of the structure state (amorphous or crystalline) with electrochromic, electrochemical, and optical parameters was proposed.

4.1.2. Experimental Section

4.1.2.1. Materials

Tungsten (VI) oxychloride ($WOCl_4$, 98% purity Aldrich), Isopropanol Anhydrous (99.5% purity), Titanium (IV) isopropoxide (99,999% purity) and glacial Acid Acetic (99,99% purity) were purchased from Sigma-Aldrich Company. All the compounds were preserved inside the Glovebox to prevent them from absorbing moisture before preparation and further characterizations. Also, Polymethylmethacrylate, PMMA (Mw = 120000) Lithium perchlorate ($LiClO_4$) and propylene carbonate (PC) were obtained from Sigma-Aldrich Company. Bisphenol-A glycerolate diacrylate and 2, 2-dimethoxy-2-phenyl acetophenone (Irgacure 651) were obtained from Sigma Aldrich and were kept refrigerated. Silica spacers (diameter of 200 μm) were used as spacers.

4.1.2.2. Thin Films preparation

The tungsten trioxide thin films were obtained by the sol-gel technique. The mother solution was prepared in an argon atmosphere in a Glovebox (MBRAUN-Unilab) by dissolving Tungsten (VI) oxychloride ($WOCl_4$, 98% purity) in isopropanol anhydrous (99,5% purity). The mother solution was left to stir for 24 hours. After, it was deposited on Indium Tin Oxide (ITO) coated glass with spin coater (SC10 CaLCTec S.r.l.) at 1200 rpm for 30s.

In addition, titanium dioxide thin films were obtained by the sol-gel technique. A second mother solution was prepared in Argon atmosphere in a Glove box (MBRAUN-Unilab) by dissolving Titanium (IV) isopropoxide ($Ti\{OCH(CH_3)_2\}_4$ 99,999% purity) in isopropanol anhydrous (99,5% purity Aldrich) and glacial acid acetic (99,99% purity, Aldrich). The mother solution was stirred for 24 hours. After, it was deposited on Indium

Tin Oxide (ITO) coated glass with spin coater (SC10 CaLCTec S.r.l.) at 1200 rpm for 30s. The thin films were treated in a furnace at 100°C, 300°C and 500°C for 1 hour in air, respectively. The effect of the calcination process is the decomposition of precursors ($WOCl_4$) and ($Ti\{OCH(CH_3)_2\}_4$) to decompose them and obtain a crystalline sample.

The calcination procedure of thin films has been performed setting by a single cycle of a ramped temperature set up composed of: 1) Equilibrate to room temperature (20°C), 2) Heating to the specific annealing temperature at a heating rate of 30°C min^{-1}, 3) Equilibrate to the specific annealing temperature for 1 hour, 4) Cooling to room temperature at a cooling rate of 30°C min^{-1}, 5) End of a cycle.

4.1.2.3. Fabrication of Electrochromic devices

We prepared several electrochromic devices following the configuration:

ITO-coated glass/WO_3 thin film/Gel Polymer Electrolyte/ TiO_2 thin film/ITO-coated glass

Where the ITO (indium tin oxide)–coated glasses are the two transparent electrodes where the electric field is applied.WO_3 and TiO_2 thin films are both the electrochromic cathodic layers. A mixture of polymethylmethacrylate, PMMA (Mw = 120000, Sigma Aldrich) and 1 M $LiClO_4$ in Propylene carbonate (PC) composed the gel polymer electrolyte, that was injected by capillarity between the two electrodes. A typical sandwich configuration of an electrochromic device is shown in Figure 4.1.2.3.1.

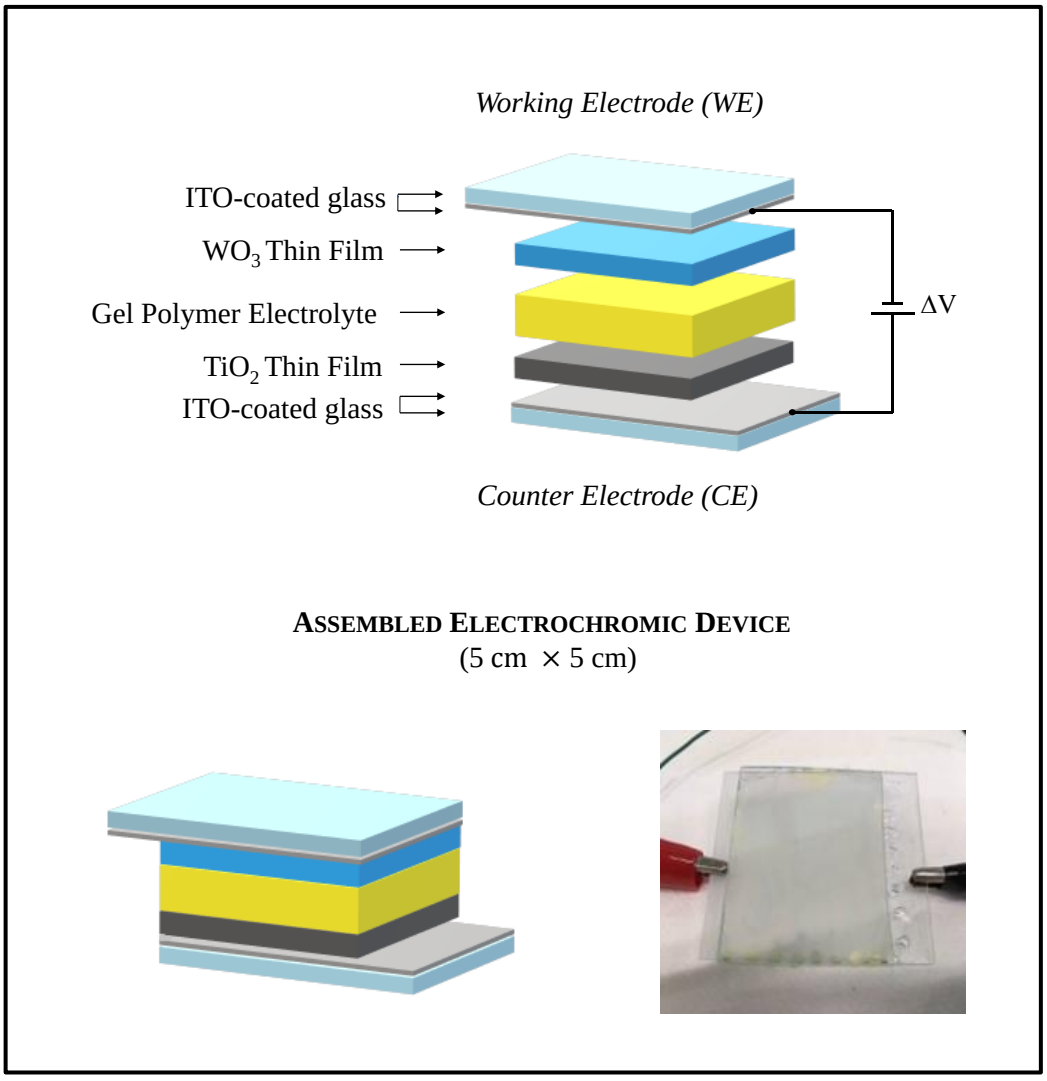

Figure 4.1.2.3.1. Schematic diagram illustrates the 'side-by-side' design of an electrochromic device and a real device.

To prevent the short circuit of the systems, we have introduced Silica spacers of 200 μm. All the systems were sealed using an epoxydic resin composed of Bisphenol-A glycerolate diacrylate and 2, 2-dimethoxy-2-phenyl acetophenone (Irgacure 651) as photo-initiator. The area of the devices is (5 cm × 5 cm). All electrochromic devices were fabricated by the combination of electrodes of WO_3 and TiO_2 at 100 °C, 300 °C, and 500 °C and they are indicated as W_iTi_j, where *W* and *Ti* indicate the WO_3 and TiO_2 electrodes, respectively and the subscripts *x* and *y* indicate their annealing temperature expressed in hundreds, respectively.

4.1.2.4. Characterization of electrochromic devices

Raman spectra of Tungsten trioxide and Titanium dioxide thin films were acquired on Jobin Yvon micro-Raman LABRAM equipped with a CCD detector ((Charge-Coupled Device), an external Nd:YAG laser (λ = 532 nm emission, 50 mW power) as the excitation source and a confocal microscope OLYMPUS BX 40. Neutral filters of different optical densities (OD) were employed to change the laser power. A 50x MPlan Olympus with a numerical aperture of 0.75 was used and the apparent diameter of the focused laser spot was about 2-3μm. The spectral resolution was 2 cm^{-1}. All spectra were imported into OriginPro8 software for fitting manipulation. The baseline-correction procedure was required to adequately fit the band shapes.

Cyclic Voltammetry measurements were carried out on the electrochromic devices with a Potentiostat/Galvanostat, model 2059 low instrument interfaced with Amel instruments-model 7800 interface (Amel Instruments). Junior Assist 2059 software was used for the acquisition of cyclic voltammetry measurement.

UV-Vis-NIR measurements were performed by UV-Vis-NIR Spectrophotometer AvaSpec-2048-Avantes. The equipment included also, a Deuterium-Halogen light source (DH-2000 UV-Vis-Nir Light source Avantes) and Agilent E3632A DC Power Supply (0-15V, 7A). Analyses were conducted at room temperature. Each UV-Vis-NIR measurement was conducted in the wavelength range (400 – 1200 nm). Avaspec75 software was used for the acquisition of UV-Vis-NIR spectra. Origin Pro8 software was used for elaboration data. Smoothing of curves was performed by the Savitzky-Golay method by using 200 points of window, no bound condition and a second polynomial for removing noise from signals.

4.1.3. Results and Discussion

4.1.3.1. Micro-Raman characterization of WO_3 and TiO_2 thin films

Raman spectroscopy has been used in order to study the effect of the annealing temperatures on the structural phases of the WO_3 and TiO_2 thin films.

In Figure 4.1.3.1.2 are shown the representative Raman spectrum of the ITO-glass substrate used as starting reference and the representative Raman spectra collected on the

tungsten trioxide thin films subjected, for one hour, to three different annealing temperatures which are: 100°C, 300°C and 500°C in the range from 300 cm^{-1} to 1300 cm^{-1} at room temperature.

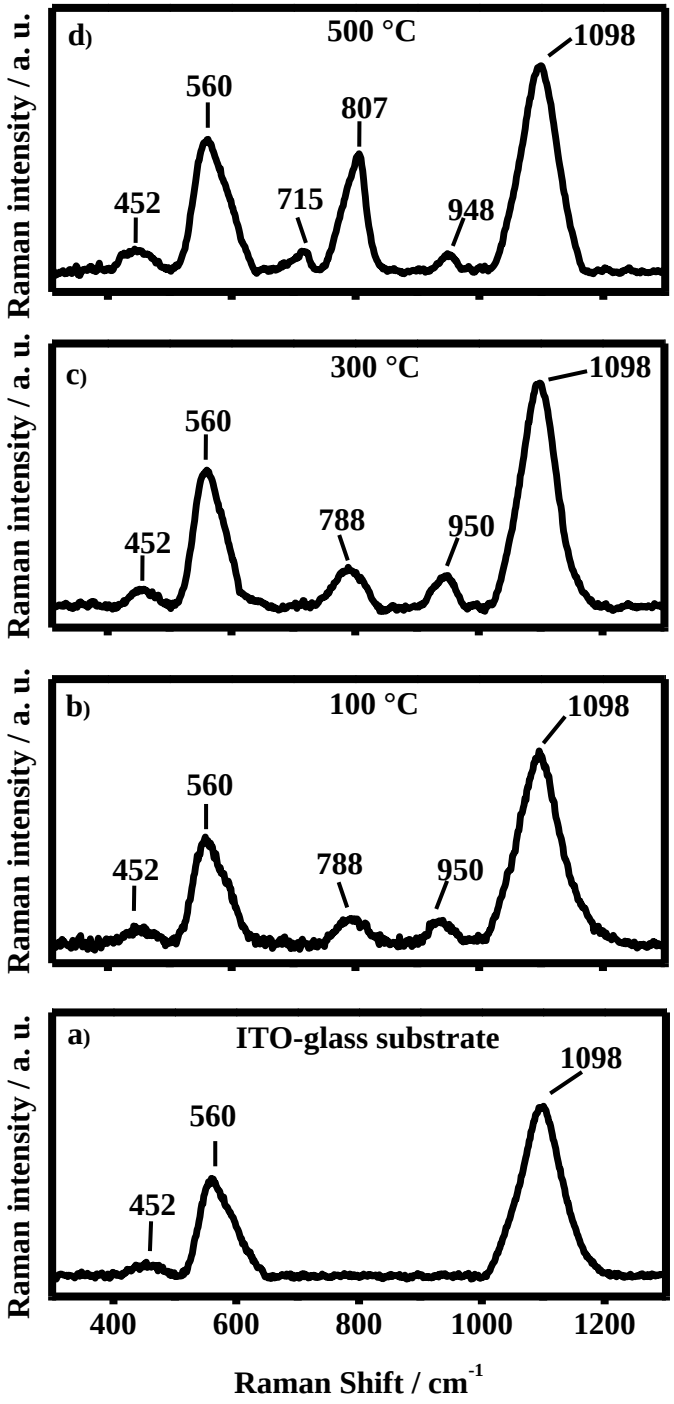

Figure 4.1.3.1.2. Raman spectrum collected at room temperature on: a) ITO-glass substrate (reference) and on WO_3 thin films annealed at: b) 100°C, c) 300 °C, and d) 500 °C.

The Raman modes that fall at about 452 cm^{-1}, 560 cm^{-1} and 1098 cm^{-1}, detected on all the samples, have been ascribed to the ITO-glass substrates, where the tungsten trioxide thin films have been deposited (Figure 4.1.3.1.2.a). The Raman spectrum collected on the tungsten trioxide thin film annealed for 1 hour at 100 °C (Figure. 4.1.3.1.2.b) shows broad bands at about 793 cm^{-1} and 941 cm^{-1} ascribed to the stretching modes W-O and terminal W=O bonds. The presence of such modes indicates that such film is in an amorphous state (*a-WO_3*) [9]. As it is possible to see in Figure 4.1.3.1.2.c, the annealing treatment at 300°C does not change the structural phase of the tungsten trioxide thin film. In fact, the bands at 789 cm^{-1} and 948 cm^{-1} (4.1.3.1.2.c), still due to the stretching modes W-O and terminal W=O bonds confirm that such films are in an amorphous state (*a-WO_3*) [9]. A great effect on the structural phase of the tungsten trioxide thin films has been obtained when the as-deposited thin films were subjected to the highest annealing temperature: 500°C (4.1.3.1.2.d). The two bands at 715 cm^{-1} and 806 cm^{-1} shown in the representative Raman spectrum of 4.1.3.1.3.d, are due to the presence of crystalline tungsten trioxide and in particular of γ-monoclinic phase (γ-*WO_3*) [10, 11]. In this case, the band at 788 cm^{-1}, above assigned to the stretching mode of W-O bonds results to be split into two components at 715 cm^{-1} and 806 cm^{-1} ascribed to the O-W-O stretching modes of the bridging oxygen in WO_3

The representative Raman spectra collected on TiO_2 thin films annealed, for one hour, at 100°C, 300°C and 500°C are shown in Figure 4.1.3.1.3.

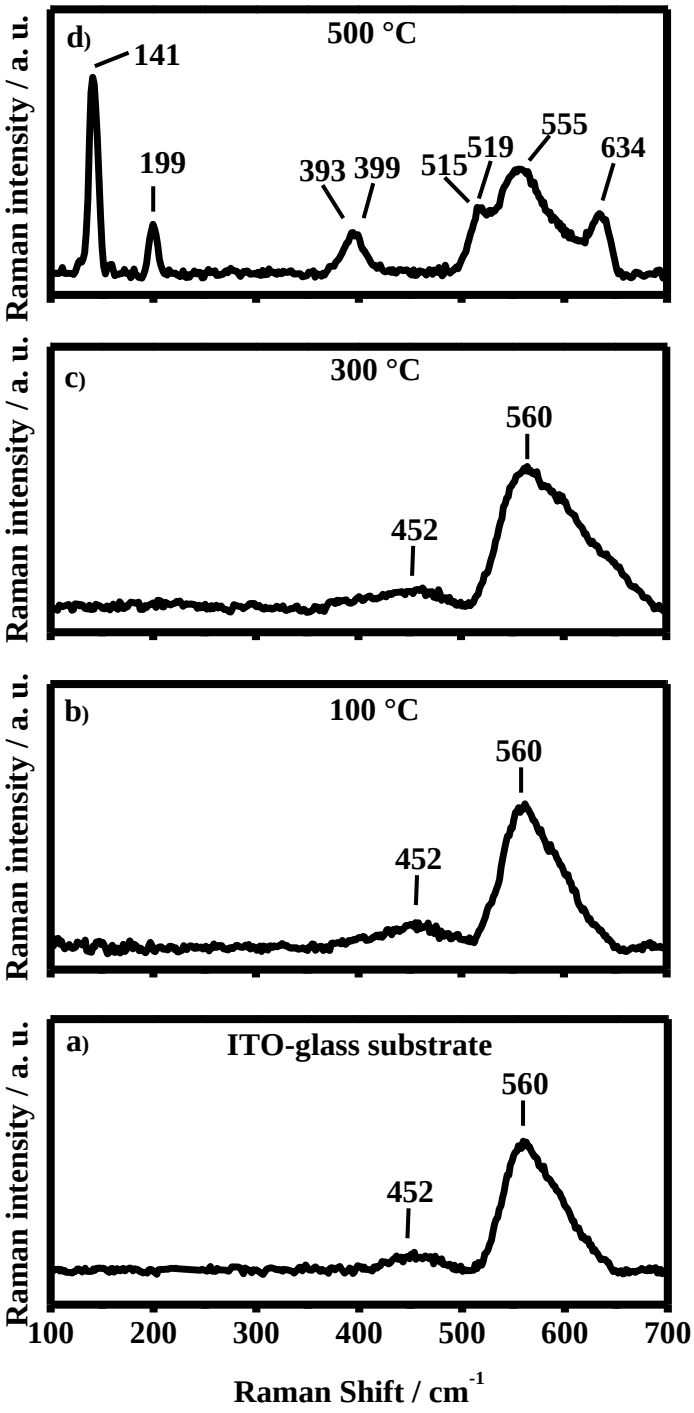

Figure 4.1.3.1.3. Raman spectrum collected at room temperature on TiO_2 thin films annealed at: a) 100°C, b) 300 °C and c) 500 °C.

The Raman modes that fall at about 452 cm^{-1}, 560 cm^{-1} and 1098 cm^{-1}, detected on all the samples, have been ascribed to the ITO-glass substrates, where the titanium dioxide thin films have been deposited (Figure 4.1.3.1.3.a).

As it can be seen in Figures 4.1.3.1.3.b-c, the Raman spectra collected on the titanium dioxide thin films annealed at 100°C and 300°C do not show any detectable Raman features ascribable to the titanium dioxide thin films. The no detectability of Raman features of the TiO_2 is due to the very low Raman cross-section of the amorphous phases with respect to the crystalline ones. In fact, the as-deposited samples annealed at 500°C, as it can be seen in Figure 4.1.3.1.3.d, shows Raman peaks, some of them quite sharp, which is representative of the crystalline phases. The Raman peaks, at 141 cm^{-1}, 199 cm^{-1}, 393 cm^{-1} 399 cm^{-1}, 515 cm^{-1}, 519 cm^{-1} and 634 cm^{-1} are assigned to the TiO_2 in Anatase phase in its tetragonal coordination with space group D_{19} (*An-TiO_2*). In particular, the peaks at 141 cm^{-1} and 199 cm^{-1} are due to the E_g modes, the peaks at 393 cm^{-1} and 399 cm^{-1} are representative of the B_{1g} mode. The Raman bands at 515 cm^{-1} and 519 cm^{-1} are attributed to the A_{1g} and B_{1g} vibrational modes and the peak at 634 cm^{-1} is assigned to the E_g vibrational mode. TiO_2 exists in three different crystal phases (Anatase, Rutile and Brookite) and the structural phase is directly connected to the annealing treatment of the substrate [1, 9]. It is well-known that TiO_2 in the Anatase phase has six active vibrational modes ($A_{1g} + 2B_{1g} + 3E_g$). Brookite has thirty-six active bands of ($9A_{1g} + 9B_{1g} + 9B_{2g} + 9B_{3g}$) and Rutile has four Raman active bands of ($A_{1g}+B_{1g} +B_{2g} +E_g$) [9]. TiO_2 can exist in the amorphous phase up to 300°C. The transformation from an amorphous phase to the Anatase phase takes place at annealing temperatures between 400°C and 600°C, while the conversion of the Anatase into the Rutile phase occurs at a very high temperatures (800 °C) [8].

Table 4.1.3.1.1 summarizes the Raman modes and the relative band positions obtained from each Raman spectrum of WO_3 and TiO_2 thin films as a function of annealing temperatures in accordance with the literature [10-26].

Annealing Temperature /°C	**Structural phase of WO_3 film**	**Raman Shift (cm^{-1})**	**Vibrational mode**
100	Amorphous (*a-WO_3-T_1*)	788, 950	W-O; W=O
300	Amorphous (*a-WO_3-T_3*)	788, 948	W-O; W=O
500	Crystalline (γ-*WO_3-T_5*)	715, 807, 948	O-W-O; W=O

Annealing Temperature /°C	Structural phase of TiO_2 film	Raman Shift (cm^{-1})	Vibrational mode
100	Amorphous (*a-TiO_2-T_1*)	422	/
300	Amorphous (*a-TiO_2-T_3*)	422	/
500	Anatase/Crystalline (An-*TiO_2-T_5*)	141, 199, 393, 399, 515, 519, 637	E_g, E_g, B_{1g}, A_{1g}, B_{1g}, E_g,

Table 4.1.3.1.1. Raman Characterization of the as-deposited WO_3 films and TiO_2 films suitable for the fabrication of electrochromic devices.

4.1.4. Cyclic Voltammetry

4.1.4.1. Lithium-Ions Diffusion in WO_3 and TiO_2 thin films

Lithium-ions diffusion was evaluated in two electrolyte media (liquid or gel polymer electrolyte) for thin films of Tungsten trioxide and Titanium dioxide. An electrochemical cell was constructed to quantify the electrochemical behavior of thin films as depicted in Figure 4.1.4.1.1 The electrochemical cell is composed of a working electrode (WE) which is represented by the annealed electrochromic thin films of oxide (WO_3 or TiO_2) and of a counter electrode (CE) composed of a stainless-steel plate. The sizes of the working electrode and the counter electrode are (5 cm × 1.5 cm × 0.1 cm). Figure 4.1.4.1.2 shows the real configuration of the electrochemical cell used for the C-V investigations.

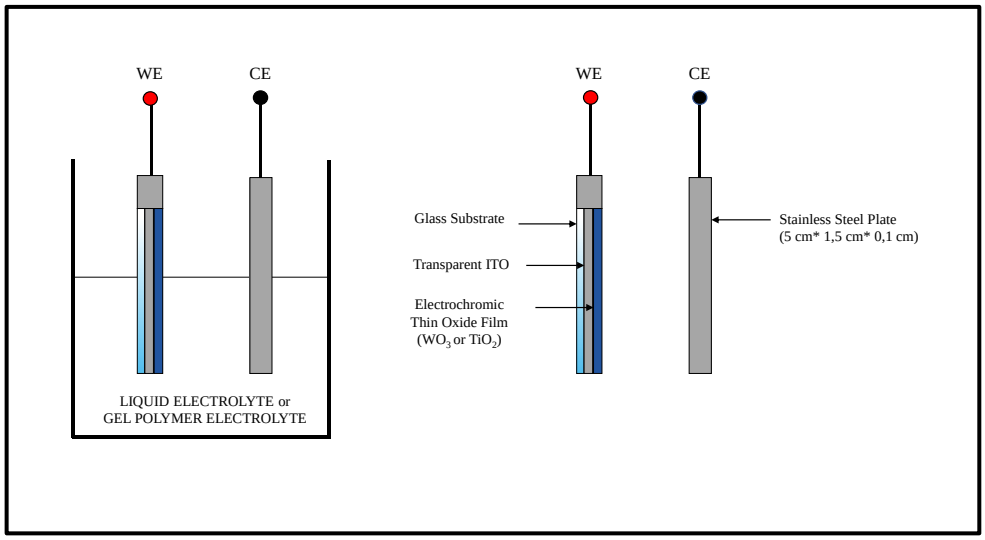

Figure 4.1.4.1.1. Schematic illustration of Electrochemical Cell for Cyclic Voltammetry set-up.

Figure 4.1.4.1.2. Electrochemical cell of Cyclic Voltammetry set-up used for the determination of Li^+ ions diffusion in a liquid electrolyte and in a gel polymer electrolyte.

Both electrodes used as working electrodes were immersed into the liquid electrolyte and made by 1 M solution of Lithium perchlorate in propylene carbonate. Cyclic Voltammetry analyses were performed in the potential range between -3.5 V and 3.5 V. A single-coating was cycled at different scan rates like 50mV s^{-1}, 100 mV s^{-1}, 200 mV s^{-1} and 300 mV s^{-1}. Figure 4.1.4.1.3 shows the cyclic voltammograms acquired on WO_3 films (*a-WO_3 T_1*, *a-WO_3-T_3* and *γ-WO_3-T_5*) cycled at the scan rates of 50 mVs^{-1}, 100 mVs^{-1}, 200 mVs^{-1} and 300 mVs^{-1} in 1 M $LiClO_4$:propylene carbonate electrolyte solution.

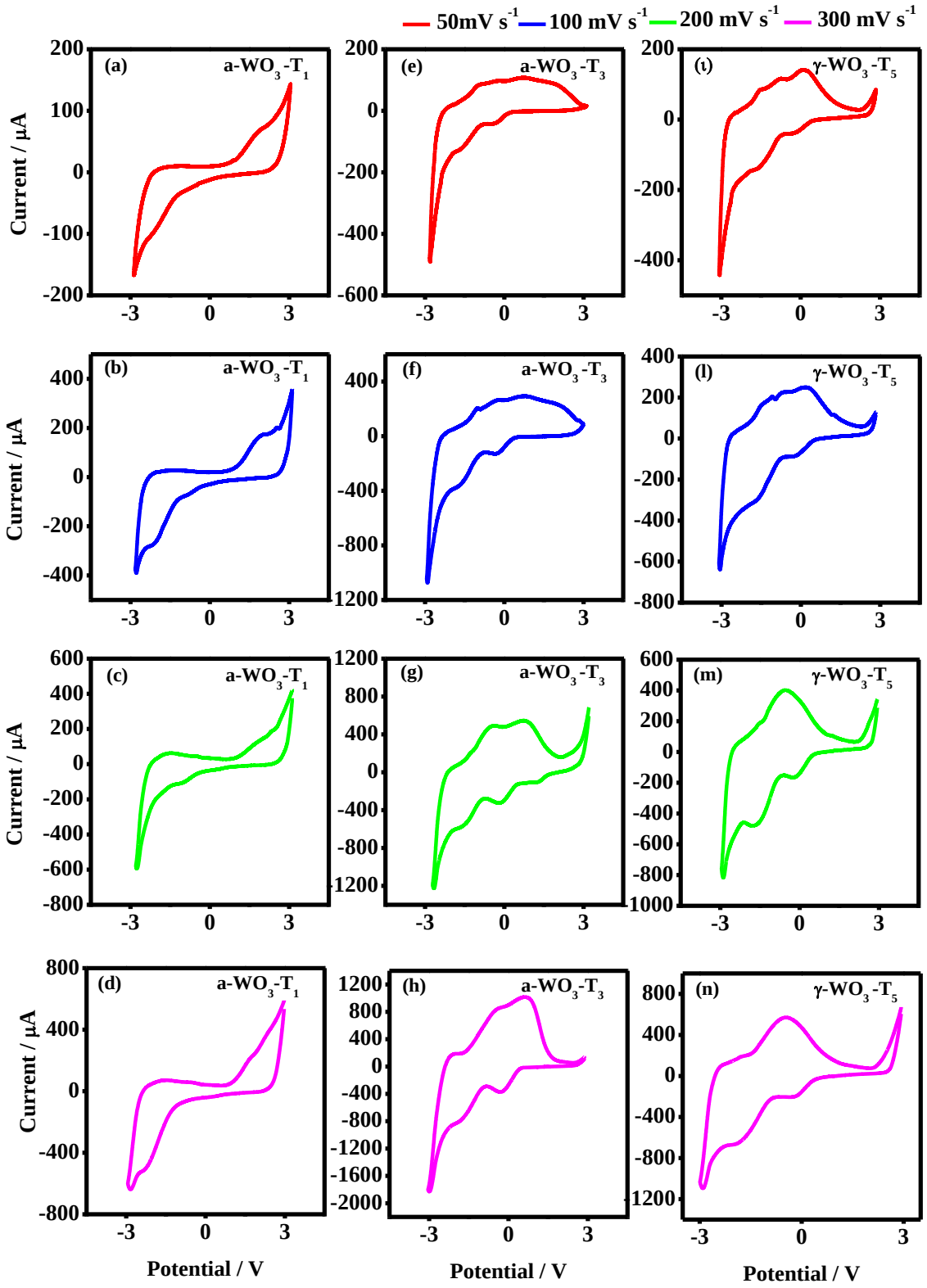

Figure 4.1.4.1.3. Cyclic voltammograms of WO_3 thin films (*a-WO₃ T₁*, *a-WO₃-T₃* and *γ-WO₃-T₅*) cycled at the scan rates of 50 mVs^{-1}(red curves), 100 mVs^{-1} (blue curves), 200 mVs^{-1} (green curves) and 300 mVs^{-1} (magenta curves) in 1 M $LiClO_4$:propylene carbonate electrolyte solution.

In the I-V curves of WO_3 thin films, following the profile of the cathode scan and then, in the direction of the scan of the negative potential is shown the cathode current i_{pc}, while in the profile of the anodic scan or the positive potential, is registered the respective i_{pa} anode current. Both can provide a useful indication of the rates of diffusion of lithium ions. As can be seen from the I-V curves of the tested species (*a*-WO_3-T_1, *a*-WO_3-T_3 and γ-WO_3-T_5) shape of the peak current can be related to the effect of different scan rates. Higher scan rates can increase the intensity of the peak current, while lower scan rates can resolve much better broad peaks [24].

Voltammograms of single-coating of *a-WO₃-T₁* film cycled at 50 mVs^{-1}, 100 mVs^{-1}, 200 mV s^{-1} and 300 mV s^{-1} do not show reduction and oxidation peaks because of the amorphous character of tungsten trioxide during the intercalation/deintercalation of Li^+ ions (Figure 4.1.4.1.3.a-b-c-d). So, the cathodic and anodic spike peak currents give us an indication of the speed of Li^+ ions.

For single coating of *a-WO₃-T₃* film, the I-V curves registered at low scan rates do not show cathodic and anodic current peaks (Figure 4.1.4.1.3.e-f-g-h). At high scan rates such as 200 mV s^{-1}(curve g) and 300 m V s^{-1} (curve h), the I-V curves are more accurate with the appearance of a more definite oxidation peak.

For single-coating of γ-*WO₃-T₅* film, the presence of an anodic peak current is clear evidence of a crystalline character of the film, at which the diffusion of Li^+ ions could occur in the available sites of the oxide network (Figure 4.1.4.1.5.i-l-m-n).

In addition, the I-V curves of *a-WO₃-T₃* and γ-*WO₃-T₅*, show an obvious reduction and oxidant current peaks occurred during the cathodic and anodic potential scanning due to the ITO of the glass support.

Figure 4.1.4.1.4 show the cyclic voltammograms acquired on TiO_2 films (*a-TiO₂-T₁*, *a-TiO₂-T₃* and An-*TiO₂-T₅*) cycled at the scan rates of 50 mVs^{-1}, 100 mVs^{-1}, 200 mVs^{-1} and 300 mVs^{-1} in 1 M $LiClO_4$:propylene carbonate electrolyte solution.

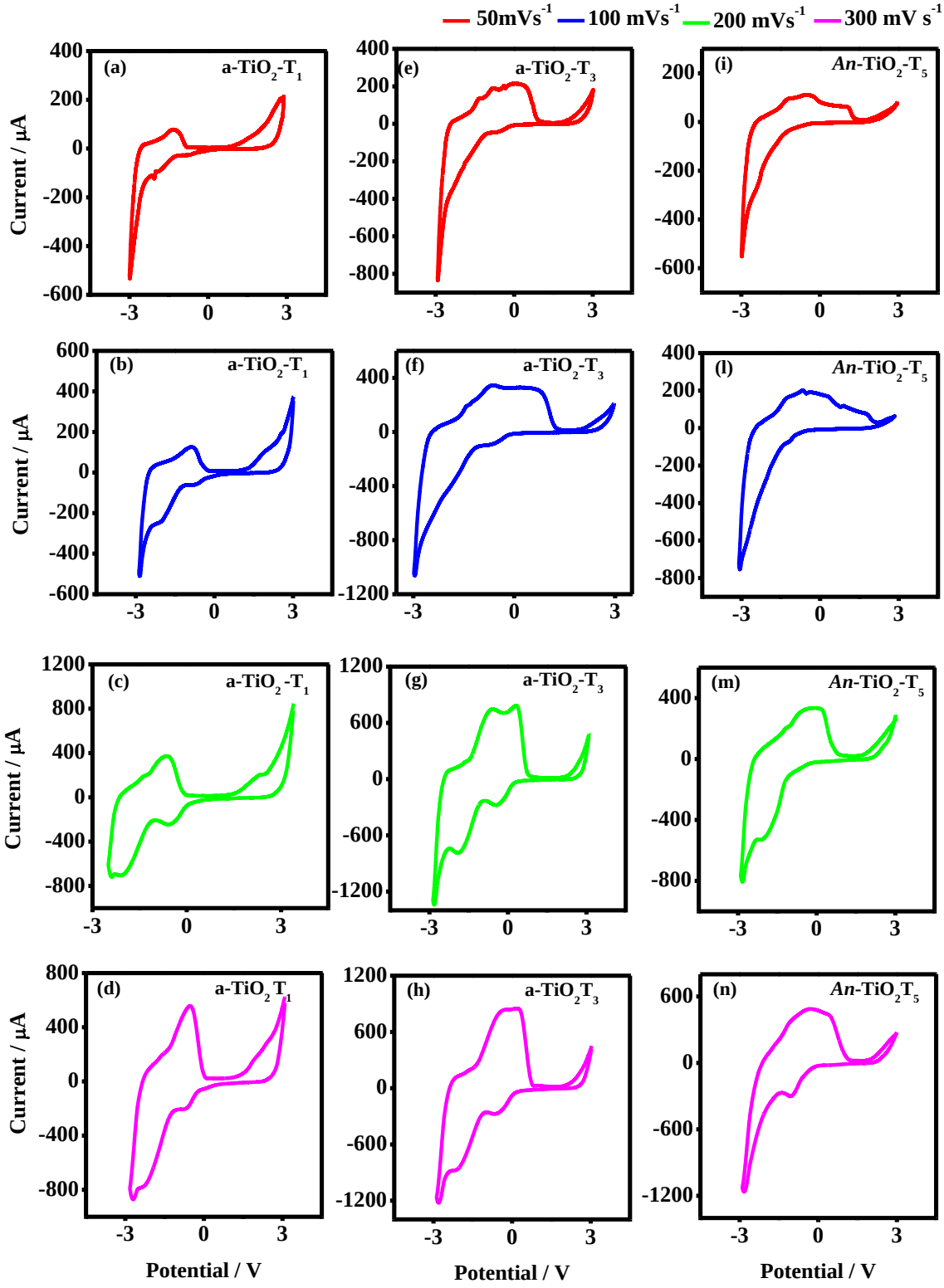

Figure 4.1.4.1.4. Cyclic voltammograms of TiO_2 thin films (*a-TiO₂-T₁*, *a-TiO₂-T₃* and *An-TiO₂-T₅*) cycled at the scan rates of 50 mVs^{-1}(red curves), 100 mVs^{-1}(blue curves), 200 mVs^{-1} (green curves) and 300 mVs^{-1} (magenta curves) in 1 M $LiClO_4$:propylene carbonate electrolyte solution.

In this case, the voltammograms show the redox behavior of TiO_2-working electrodes in a liquid electrolyte solution. Also, in this case, the different shapes of cyclic voltammetry curves are due to the amorphous-crystalline character of the material. The I-V curves of *a-TiO_2-T_1* (Figure 4.1.4.1.4.a-b-c-d) and *a-TiO_2-T_3* films (Figures 4.1.4.1.4.e-f-g-h) are characterized by cathodic spike peak current and an oxidation peak current at which the diffusion of lithium ions occurred that became more definite at high scan rates. In the curves, the redox behavior of ITO is also shown. For the *An-TiO_2-T_5* film, at low scan rates, the reduction of the electrochromic materials is evaluated at the cathodic spike current while the reduction and the oxidation appears more evident at higher scan rates (Figure 4.1.4.1.4.i-l-m-n). The I-V curves show also, the redox behavior of the ITO-covered glass.

The performance of electrochromic thin films was evaluated also, in a gel polymer electrolyte composed of (20:80) % w/w PMMA in 1 M $LiClO_4$ in propylene carbonate solution. The shape of the following cyclic voltammograms is related to the amorphous state or crystalline lattice of oxides and they are comparing to the same registered in a liquid electrolyte solution.

Figure 4.1.4.1.5 show the cyclic voltammograms acquired on WO_3 films (*a-WO_3-T_1*, *a-WO_3-T_3* and γ- *WO_3-T_5*) cycled at the scan rates of 50 mVs^{-1}, 100 mVs^{-1}, 200 mVs^{-1} and 300 mVs^{-1} in gel electrolyte of PMMA in 1 M $LiClO_4$:propylene carbonate electrolyte solution.

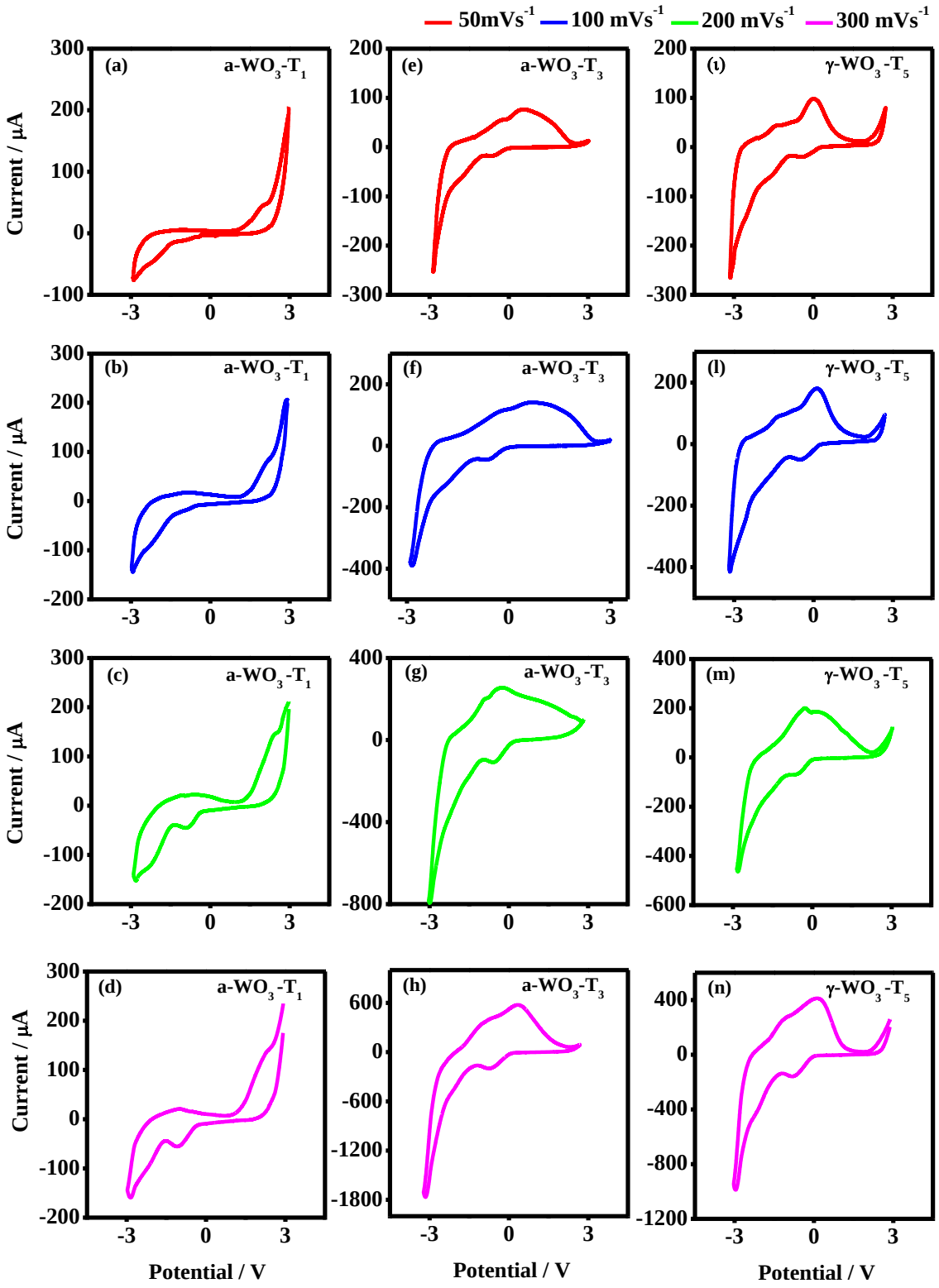

Figure 4.1.4.1.5. Cyclic voltammograms of WO_3 thin films (*a-WO₃ T₁*, *a-WO₃-T₃* and *γ-WO₃-T₅*) cycled at the scan rates of 50 mVs^{-1} (red curves), 100 mVs^{-1}(blue curves), 200 mVs^{-1} (green curves) and 300 mVs^{-1} (magenta curves) in a gel polymer electrolyte based

on PMMA and 1 M liquid electrolyte of lithium perchlorate in propylene carbonate solution.

The I-V curves ascribed to the electrodes based on *a-WO_3-T_1* and *a-WO_3-T_3* films are continuous because of the amorphous character of electrochromic material and they also show the redox behavior of the ITO-covered glass (Figure 4.1.4.1.5.a-b-c-d-e-f-g-h). The I-V curves of *γ–WO_3-T_5* (Figure 4.1.4.1.5 i-l-m-n curves) are more definite in the gel polymer electrolyte medium and the cathodic spike current and the correspondent oxidation peak of γ–WO_3 are easy to find.

Figure 4.1.4.1.6 shows the cyclic voltammograms of TiO_2 film deposited at different annealing temperatures like T_1= 100°C, T_3= 300°C and T_5=500°C cycled in gel electrolyte of PMMA in 1 M $LiClO_4$:propylene carbonate electrolyte solution at 50 mVs^{-1}, 100 mVs^{-1}, 200 mVs^{-1} and 300 mVs^{-1}.

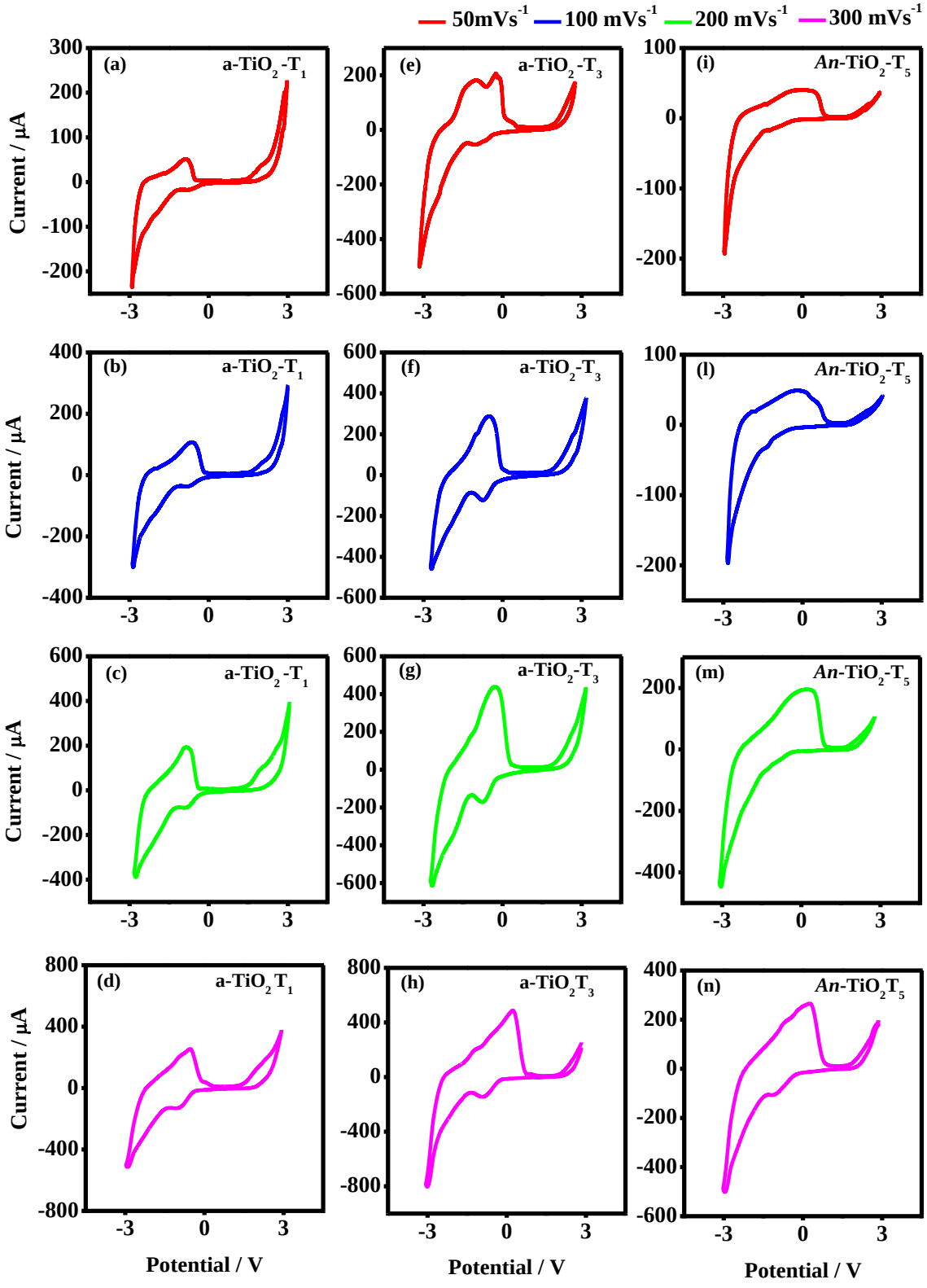

Figure 4.1.4.1.6. Cyclic voltammograms of *a-TiO₂-T₁* thin films cycled at scan rates 50 mV s^{-1} (red curves), 100 mV s^{-1} (blue curves), 200 mV s^{-1} (green curves) and 300 mV s^{-1}

(magenta curves) in a gel polymer electrolyte based on PMMA and 1 M liquid electrolyte of lithium perchlorate in propylene carbonate solution.

As depicted in Figure 4.1.4.1.6, the electrochemical curves of all types of TiO_2 films show a reduction spike current and an oxidation peak. In the case of TiO_2 films treated at 300 °C, this oxidation peak is much better resolved at the slower scanning rate (Figure 4.1.4.1.6.e).

The performances of electrochromic thin films have been evaluated from the diffusion coefficient (D) of the inserted Li^+ ions in liquid and gel polymer electrolyte media. The Diffusion coefficient of Li^+ ions during the intercalation and deintercalation processes into/out of the WO_3 or TiO_2 thin films at a fixed temperature of 298.15 K (25 °C) was evaluated by using the Randles Sevcik equation (Equation 4.1.4.1.1) [27]:

$$i_p = 2.69 \times 10^5 \times n^{3/2} \times A \times D^{1/2} \times C_o \times v^{1/2} \qquad (4.1.4.1.1)$$

Where i_p indicates the anodic i_{pa} and cathodic peak currents i_{pc} (A), n is the number of electrons involved in the reaction, A is the surface area electrode (cm^2), D is the diffusion coefficient ($cm^2\ s^{-1}$), C_o is the concentration of active ions in the electrolyte medium ($mol\ cm^{-3}$) and v is the scan rate ($V\ s^{-1}$). The Randles-Sevcik equation can be expressed as a function of current density at fixed temperature 298.15 K (25 °C), schematically, as (Equation 4.1.4.1.2) [28]:

$$j_p = 2.69 \times 10^5 \times n^{3/2} \times D^{1/2} \times C_o \times v^{1/2} \qquad (4.1.4.1.2)$$

Where j_p is the peak current i.e., the cathodic j_{pc} and anodic peaks density current j_{pa} regarding the working area of the electrodes. To further evaluate Li^+ ions diffusion coefficients in oxide thin films, cyclic voltammograms were carried out with different potential scan rates (50 $mV\ s^{-1}$, 100 $mV\ s^{-1}$, 200 $mV\ s^{-1}$ and 300 $mV\ s^{-1}$).

In Figure 4.1.4.1.7 are shown the trends of the diffusion coefficients calculated for both cathodic and anodic peak density currents for the WO_3 thin films annealed at T_1, T_3 and T_5 in both liquid and gel polymer electrolytes.

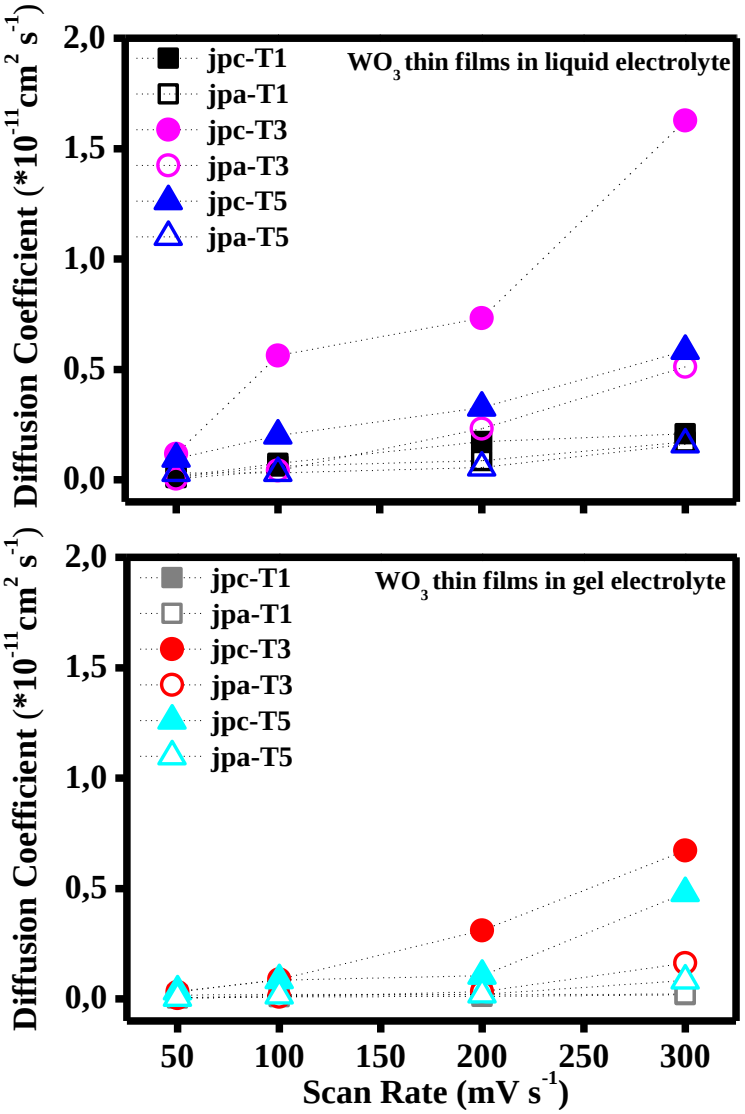

Figure 4.1.4.1.7. Trends of the Diffusion coefficients evaluated at the cathodic and anodic peak density currents for the WO_3 thin films annealed at T_1 = 100 °C, T_3 = 300 °C and T_5 = 500°C in both liquid (1 M $LiClO_4$:PC) and gel polymer electrolyte (20:80 % w/w PMMA:$LiClO_4$:PC).

From the trends of the diffusion coefficients, is possible to deduce that the diffusion values, relative to the intercalated (D_{jpc}) and de-intercalated process of Li^+ ions (D_{jpa}) increase with the increase of the scan rate. In addition, the different annealing temperatures of the substrate of WO_3 films deriving from the sol-gel technique could influence the diffusion of the Li^+ ions as a function of the metal oxide structure. In fact, the highest values of the diffusion coefficient in liquid electrolyte were found for the

amorphous film of WO_3 annealed at 300 °C (*a-WO_3-T_3*) with a value of D_{jpc} = 1.628 × 10^{-11} cm^2 s^{-1} recorded at the scan rate of 300 mV s^{-1}. The crystalline film of WO_3 treated at 500 °C (*γ–WO_3-T_5*) shows lower diffusion coefficients than the amorphous film at 300 °C. The highest value of diffusion coefficient for the crystalline film of WO_3 (*γ–WO_3-T_5*) is found at 300 mV s^{-1} and it is equal to D_{jpc} = 0.584 × 10^{-11} cm^2 s^{-1}. This behavior can be attributed to the different internal organization of the structure of metal oxide film. The fast diffusion of small ions through the channels of an amorphous film is easier than the diffusion in the channels of an ordered crystalline. In addition, there is a difference in the diffusion data between both amorphous thin films of WO_3. The amorphous film of WO_3 annealed at 100 °C (*a-WO_3-T_1*) shows lower diffusion data may be due to the temperature of the thermal treatment, which lends a no complete amorphous character to the film compared to the film treated at 300 °C (*a-WO_3-T_3*).

The lowest data were found in a gel polymer electrolyte medium with respect to the best results registered in a liquid electrolyte. The amorphous film of WO_3 calcinated at 300 °C (*a-WO_3-T_3*) shows the highest diffusion coefficient relative to the cathodic density peak current at 300 mV s^{-1} with a value of D_{jpc} = 0.673 × 10^{-11} cm^2 s^{-1}. Also, at 300 mV s^{-1} for the crystalline *γ–WO_3-T_5* the highest value of diffusion coefficient is D_{jpc} = 0.48 × 10^{-11} cm^2 s^{-1}. The trends of the diffusion coefficients evaluated in the gel polymer electrolyte are lower than the values estimated in the liquid electrolyte and it this behavior is ascribable to the difficulties in the diffusion of the lithium ions when they are in a gel system.

In Figure 4.1.4.1.8 are shown the trends of the diffusion coefficients calculated for both cathodic and anodic peak density currents for the TiO_2 thin films annealed at T_1, T_3 and T_5 in both liquid and gel polymer electrolytes.

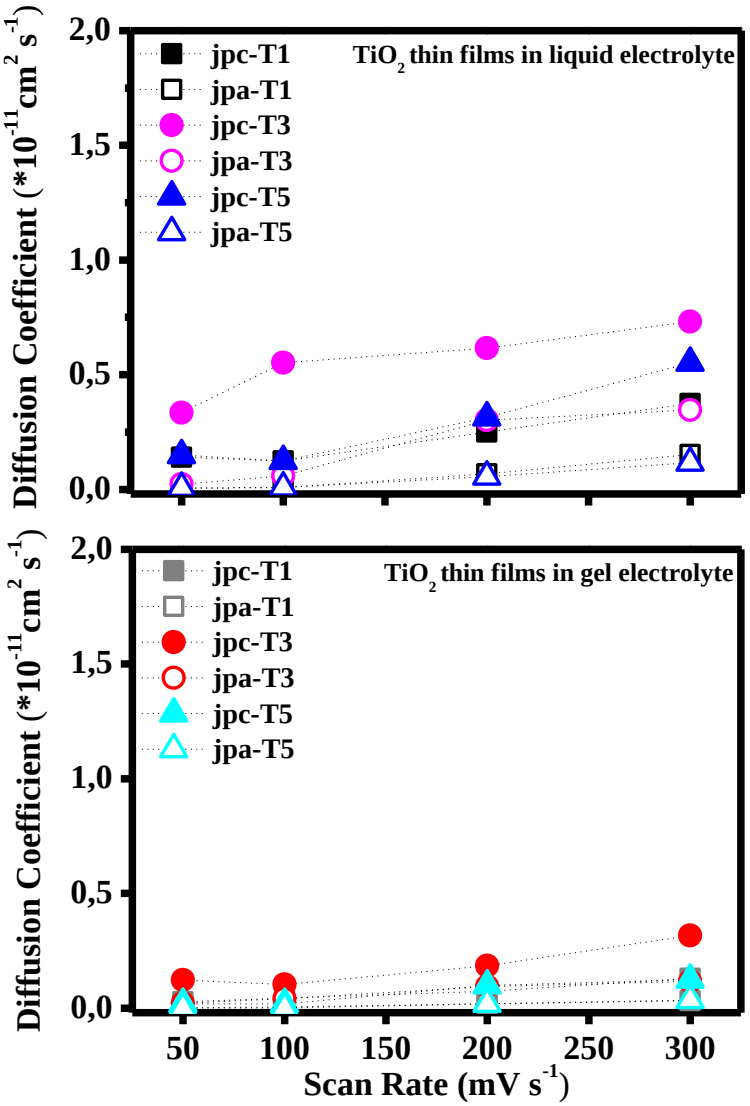

Figure 4.1.4.1.8. Trends of the Diffusion coefficients evaluated at the cathodic and anodic peak density currents for the TiO_2 thin films annealed at T_1 = 100 °C, T_3 = 300 °C and T_5 = 500°C in both liquid (1 M $LiClO_4$:PC) and gel polymer electrolyte (20:80 % w/w PMMA:$LiClO_4$:PC).

From Figure 4.1.4.1.8, the trends of Li^+ ions diffusion estimated in the gel medium show lower results than those registered in the liquid medium. The amorphous film of TiO_2 annealed at 300 °C (*a-TiO₂-T₃*) shows the highest value of diffusion coefficient equal to $D_{jpc} = 0.731 \times 10^{-11}$ cm^2 s^{-1} in the liquid electrolyte medium at the highest scan rate. In the same liquid medium, the crystalline film of TiO_2 is characterized by a diffusion coefficient $D_{jpc} = 0.661 \times 10^{-11}$ cm^2 s^{-1}. In the gel medium, for the amorphous TiO_2 film calcinated at 300 °C *(a-TiO₂-T₃)*, the diffusion coefficient estimated at the highest scan

rate is equal to $D_{jpc} = 0.317 \times 10^{-11}$ cm^2 s^{-1}. The crystalline film of TiO_2 (*An-TiO_2-T_5*) in the gel medium is characterized by a value of diffusion coefficient of $D_{jpc} = 0.123 \times 10^{-11}$ cm^2 s^{-1}.

All the electrochemical parameters such as ip_c, ip_a, jp_c, jp_a and the relative diffusion coefficients D_{jpc}, D_{jpa} of both WO_3 and TiO_2 thin films registered in 1 M $LiClO_4$ in propylene carbonate solution and in a gel polymer electrolyte (20:80) % w/w PMMA in 1 M $LiClO_4$ in propylene carbonate solution, are tabulated in Tables 4.1.4.1.1 and 4.1.4.1.2, respectively.

Sample	Scan Rate	Cathodic Peak Current i_{pc}	Anodic Peak Current i_{pa}	Cathodic Peak Density Current j_{pc}	Anodic Peak Density Current j_{pa}	Diffusion coefficient $D_{j_{pc}}$	Diffusion coefficient $D_{j_{pa}}$
		(mV s^{-1})		(μA)		($\times 10^{-11}$ cm^2 s^{-1})	
a-WO_3-T_1	50	-166	142	-22.1	18.9	0.014	0.010
	100	-389	354	-51.9	47.2	0.074	0.062
	200	-594	421	-79.2	56.15	0.173	0.087
	300	650	590	-86.7	78.7	0.208	0.171
a-WO_3-T_3	50	-487	106	-64.9	14.1	0.117	0.006
	100	-1070	292	-14.3	38.9	0.563	0.042
	200	-1220	685	-163	91.3	0.731	0.231
	300	-1820	1020	-243	136	1.628	0.511
γ-*WO_3-T_5*	50	-442	248	-58.9	33.1	0.096	0.030
	100	-638	249	-85.1	33.2	0.200	0.030
	200	-816	338	-109	45.1	0.327	0.056
	300	-1090	570	-145	76	0.584	0.160
a-TiO_2-T_1	50	-533	779	-71.1	10.4	0.140	0.003
	100	-502	125	-66.9	16.7	0.124	0.008
	200	-712	372	-94.9	49.6	0.249	0.068
	300	-872	557	-116	74.3	0.374	0.152
a-TiO_2-T_3	50	-825	213	-110	28.4	0.334	0.022
	100	-1060	344	-141	45.9	0.552	0.058
	200	-1120	784	-149	105	0.616	0.302
	300	-1220	840	-122	840	0.731	0.347
An-TiO_2-T_5	50	-551	110	-73.5	14.7	0.149	0.006
	100	-503	125	-67.1	16.7	0.124	0.008
	200	-799	335	-107	44.7	0.314	0.055
	300	-1160	486	-155	64.8	0.661	0.116

Table 4.1.4.1.1. Electrochemical parameters ip_c, ip_a, jp_c, jp_a, D_{jpc}, D_{jpa} of both WO_3 and TiO_2 thin films annealed at T_1 = 100 °C, T_3 = 300 °C and T_5 = 500 °C for intercalated Li^+ ions at 50 mV s^{-1}, 100 mV s^{-1} 200 mV s^{-1} and 300 mV s^{-1} scan rates in 1 M $LiClO_4$ in propylene carbonate solution.

Sample	Scan Rate	Cathodic Peak Current i_{pc}	Anodic Peak Current i_{pa}	Cathodic Peak Density Current j_{pc}	Anodic Peak Density Current j_{pa}	Diffusion coefficient $D_{j_{pc}}$	Diffusion coefficient $D_{j_{pa}}$
		(mV s^{-1})		(μA)		($\times 10^{-11}$ cm^2 s^{-1})	
a-WO_3-T_1	50	-75.9	201	-10.1	26.8	0.003	0.018
	100	-143	204	-19.1	27.2	0.010	0.020
	200	-152	198	-20.3	26.4	0.011	0.019
	300	-194	211	-25.9	28.1	0.018	0.022
a-WO_3-T_3	50	-251	76	-33.5	10.1	0.031	0.003
	100	-422	139	-56.3	18.5	0.088	0.009
	200	-794	255	-106	34	0.310	0.032
	300	-1170	575	-25.9	28.1	0.673	0.162
γ-WO_3-T_5	50	-265	98.2	-35.3	13.1	0.035	0.005
	100	-415	180	-55.3	24	0.085	0.016
	200	-463	200	-61.7	26.7	0.105	0.020
	300	-988	412	-132	549	0.480	0.083
a-TiO_2-T_1	50	-234	51.1	-31.2	6.81	0.027	0.001
	100	-298	106	-39.7	14.1	0.044	0.006
	200	-388	193	-51.7	25.7	0.074	0.018
	300	-513	253	-68.4	33.7	0.129	0.031
a-TiO_2-T_3	50	-498	206	-66.4	27.5	0.122	0.021
	100	-458	286	-61.1	38.1	0.103	0.040
	200	-613	438	-81.7	58.4	0.185	0.094
	300	-803	487	-1070	64.9	0.317	0.117
An-TiO_2-T_5	50	-194	40	-25.9	5.33	0.018	0.001
	100	-197	48.9	-26.3	6.52	0.019	0.001
	200	-447	195	-59.6	26	0.098	0.019
	300	-501	265	-66.8	35.3	0.123	0.035

Table 4.1.4.1.2. Electrochemical parameters ip_c, ip_a, jp_c, jp_a, D_{jpc}, D_{jpa} of both WO_3 and TiO_2 thin films annealed at 100 °C, 300 °C and 500 °C for intercalated Li^+ ions at 50 mV s^{-1}, 100 mV s^{-1} 200 mV s^{-1} and 300 mV s^{-1} scan rates in gel polymer electrolyte of PMMA and 1 M $LiClO_4$ in propylene carbonate solution (20:80) % w/w.

The areas of the voltammograms were calculated with numerical integration and they are summarized in Table 4.1.4.1.3. With increasing scan rate, the voltammogram areas increase and this fact could be deeply related to the charge storage capacity of the film.

Sample	Scan Rate (mV s^{-1})	*Liquid Electrolyte* Integrated Area	*Gel Polymer Electrolyte* Integrated Area
a-WO_3-T_1	50	0.00029	0.00014
	100	0.00079	0.00029
	200	0.00083	0.00033
	300	0.00131	0.00034
a-WO_3-T_3	50	0.00068	0.00032
	100	0.00187	0.00065
	200	0.00306	0.00133
	300	0.00419	0.00234
γ-*WO_3-T_5*	50	0.00077	0.00040
	100	0.00148	0.00076
	200	0.00204	0.00082
	300	0.00268	0.00163
a-TiO_2-T_1	50	0.00045	0.00024
	100	0.00074	0.00040
	200	0.00175	0.00068
	300	0.00207	0.00086
a-TiO_2-T_3	50	0.00094	0.00003
	100	0.00170	0.00004
	200	0.00297	0.00123
	300	0.00300	0.00129
An-TiO_2-T_5	50	0.00058	0.00018
	100	0.00111	0.00023
	200	0.00152	0.00070
	300	0.00194	0.00092

Table 4.1.4.1.3. Integrated area of cyclic voltammograms curves as function of scan rates (50 mV s^{-1}, 100 mV s^{-1}, 200 mVs^{-1}, 300 mV s^{-1}) for thin films of metal oxides (WO_3 and TiO_2) annealed at 100 °C, 300 °C and 500 °C.

The intercalated and de-intercalated charges into tungsten and titanium lattice are calculated from the cyclic voltammetry curves by integrating the current and the time following Equation 4.1.4.1.3 [29] and the data are reported in Table 4.1.4.1.4.

$$Q = \int_{t_1}^{t_2} i(t)\, dt \qquad (4.1.4.1.3)$$

Sample	Scan Rate (mV s^{-1})	*Liquid Electrolyte* Intercalated Charge (mC)	*Liquid Electrolyte* Deintercalated Charge (mC)	*Gel Polymer Electrolyte* Intercalated Charge (mC)	*Gel Polymer Electrolyte* Deintercalated Charge (mC)
a-WO_3-T_1	50	-4.08	3.68	-1.63	3.29
	100	-4.68	3.08	-1.54	1.49
	200	-2.72	1.80	-0.97	1.06
	300	-2.69	2.04	-0.70	0.69
a-WO_3-T_3	50	-8.17	4.46	-4.90	3.19
	100	-10.2	9.01	-3.79	3.16
	200	-7.56	4.60	-4.89	3.46
	300	-8.25	6.45	-6.69	3.5
γ-*WO_3-T_5*	50	-11.3	4.34	-4.99	2.82
	100	-8.68	3.73	-4.39	2.71
	200	-6.49	2.87	-2.55	2.43
	300	-5.37	2.85	-3.62	2.61
a-TiO_2-T_1	50	-7.54	1.23	-10.7	7.19
	100	-6.26	0.92	-2.81	0.96
	200	-4.20	2.16	-2.17	0.92
	300	-4.16	2.19	-2.17	1.24
a-TiO_2-T_3	50	-1.15	9.06	-1.07	7.18
	100	-9.85	7.72	-4.43	2.87
	200	-8.06	6.88	-3.08	2.35
	300	-6.09	4.79	-3.58	2.65
An-TiO_2-T_5	50	-9.95	4.40	-3.16	1.78
	100	-7.01	3.93	-1.42	0.92
	200	-4.74	3.04	-2.44	1.80
	300	-4.59	3.00	-1.91	1.55

Table 4.1.4.1.4. Intercalated and de-intercalated charges of WO_3 and TiO_2 thin films annealed at 100 °C, 300 °C and 500 °C, as function of scan rates (50 mV s^{-1}, 100 mV s^{-1}, 200 mVs^{-1}, 300 mV s^{-1}).

4.1.4.2. Cyclic Voltammetry of Electrochromic Devices

Cyclic voltammetry has been performed to follow the reversibility of the electrochromic behavior, the cathodic and anodic current peaks and how those could be related to the annealing temperature of the WO_3 and TiO_2 electrodes used to build the electrochromic devices. The assembled electrochromic devices are based on the combination of WO_3 (T_1, T_3, T_5) and TiO_2 (T_1, T_3, T_5) thin films. The electrochromic layer of WO_3 was selected as the working electrode, while TiO_2 was the counter electrode or ion storage layer and they operated in the open circuit potential mode (OC). Also, the electrolyte layer has an

important role because it can facilitate the electron and the ion movement during the operation of an EC device. All the measurements were conducted by monitoring the current of the system in the selected potential range after five cycles. All devices showed similar electrochemical behavior during cyclic voltammetry investigation. WO_3 and TiO_2 are cathodic electrochromic materials and they cause cathodic coloration (coloring under ion insertion or reduction state). At the start each system was colorless and the dark blue coloration occurred during the negative potential cycle while bleaching occurred during the positive potential cycle. The coloration process of the electrochromic films is described as a function of simultaneous injection of cations and electrons inside the oxide network. Tungsten oxide film underwent to the typical intercalation/de-intercalation process according to (Equation 4.1.4.2.1) [30]:

$$W^{(VI)}O_3(colorless) + xLi^+ + xe^- \rightleftharpoons Li_xW^{(VI)}_{1-x}W^{(V)}_xO_3\ (Blue) \qquad (4.1.4.2.1)$$

where $M^+ = H^+, Li^+, Na^+$, ect and e^- denoting electrons.

The reduction process of the W^{6+} into W^{5+} ions after the injection of lithium ions increases the number of the colour blue centers W^{5+} state. Titanium oxide films works as ion storage and as reported in Equation 4.1.4.2.2 the system underwent the reduction of Ti^{4+} to Ti^{3+} [30]. The redox process is not characterized by an evident color variation.

$$Ti^{(IV)}O_2(colorless) + xLi^+ + xe^- \rightleftharpoons Li_xTi^{(IV)}_{1-x}Ti^{(III)}_xO_2\ (Grey) \qquad (4.1.4.2.2)$$

where $M^+ = H^+, Li^+, Na^+$, ect. and e^- denoting electrons.

At the begin, each system was colorless and the devices become blue during the negative potential cycle and bleaching during the positive potential cycle. Cathodic potentials lead to the reduction of W (VI) ions that are responsible of the blue color of the films, while anodic potentials are responsible for oxidation of W (IV) and bleaching.

Typical colored and bleached states of an electrochromic device based on WO_3 and TiO_2 thin films because of the application of voltage are shown in Figure 4.1.4.2.1.

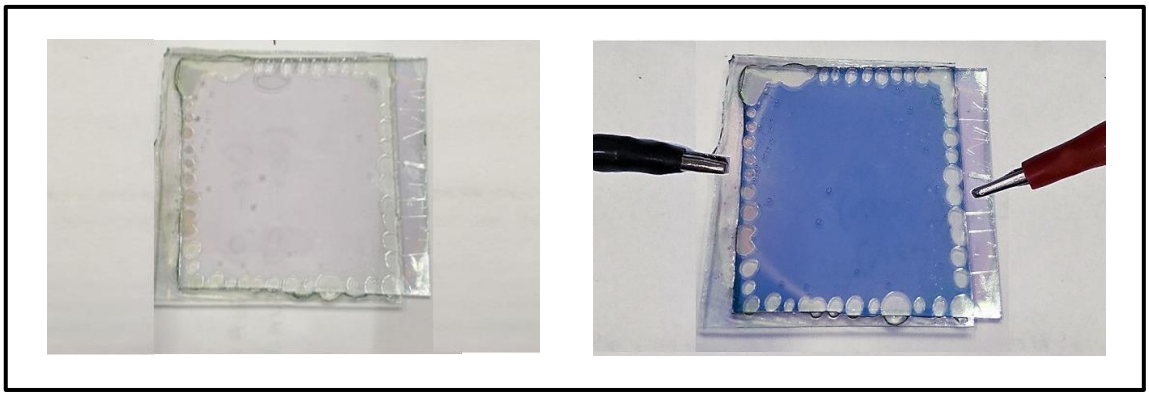

Figure 4.1.4.2.1. State ON and State OFF in an electrochromic device based on WO_3 and TiO_2 annealed-thin film under an applied voltage.

When the electrochromic devices are blue, it means that the Equation 4.1.4.2.1 it is shifted on the right while the Equation 4.1.4.2.2 it is shifted on the left: state ON. When the devices are transparent then the Equation 4.1.4.2.1 it is shifted on the left while the Equation 4.1.4.2.2 it is shifted on the right: state OFF.

Cyclic voltammetry curves of electrochromic systems in gel electrolyte (20:80 % w/w of PMMA in 1 M $LiClO_4$ in propylene carbonate) at a scan rate of 50 mV s^{-1} (blue curves) and of 100 mV s^{-1}(red curves) are shown in Figures 4.1.4.2.2 and 4.1.4.2.3.

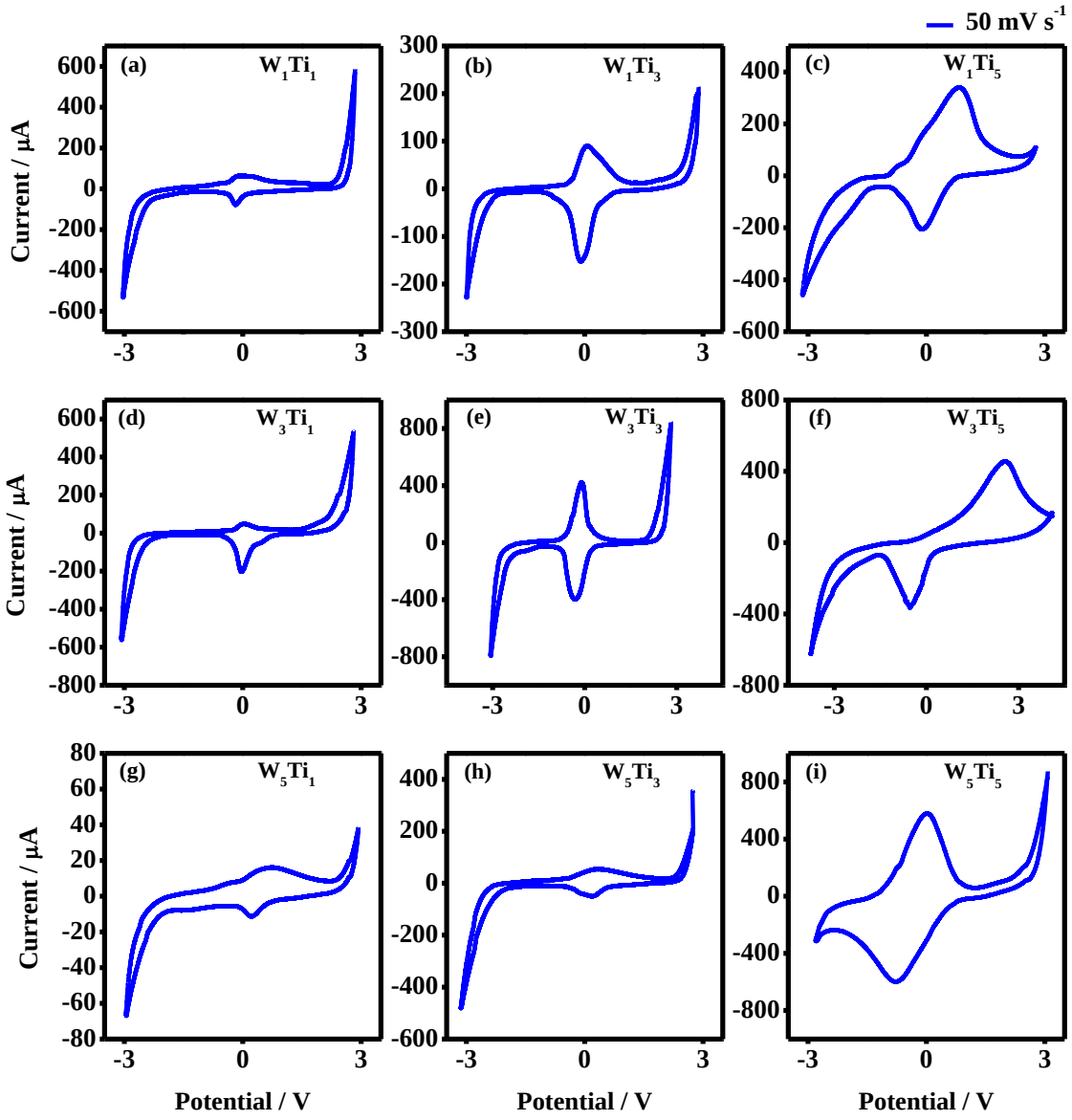

Figure 4.1.4.2.2. Cyclic voltammetry curves of electrochromic systems in gel electrolyte of PMMA in 1 M $LiClO_4$ in propylene carbonate at a scan rate of 50 mV s^{-1}.

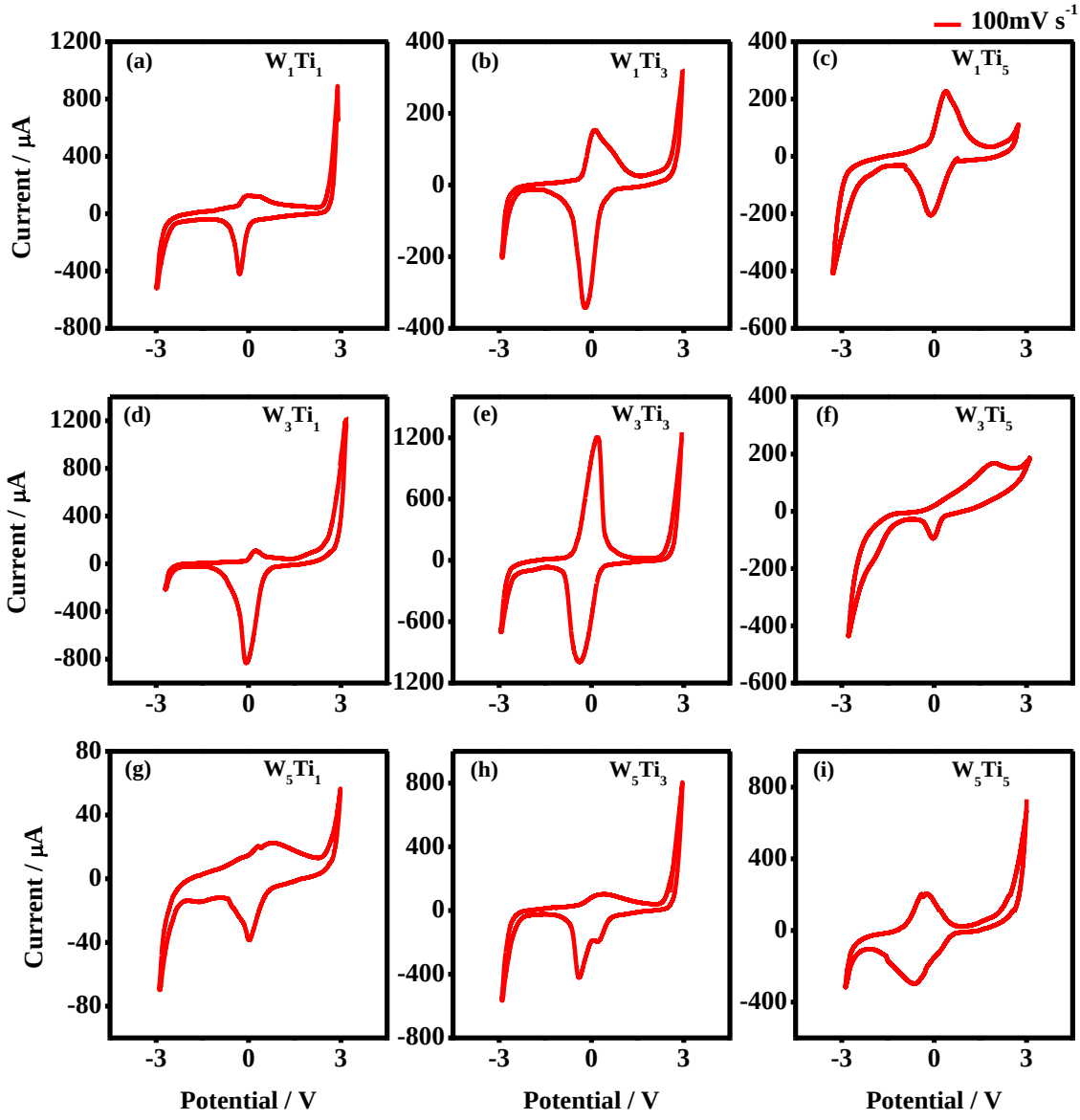

Figure 4.1.4.2.3. Cyclic voltammetry curves of electrochromic systems in gel electrolyte of PMMA in 1 M $LiClO_4$ in propylene carbonate at a scan rate of 100 mV s^{-1}.

All the curves registered for each system show the electrochemical insertion of lithium ions into an oxide network that remains reversible for the tested number cycles. As it can be seen in Figures 4.1.4.2.2.a-i and 4.1.4.2.3.a-i, not all voltammogram show the same profile and some of them results to be deformed and shifted with respect to the center. The deformation and the shifting of the cyclic voltammetry curves is probably due to different ion migrations and electron trapping / de-trapping at the interface of films in the redox process [31], the possible degradation of gel electrolyte under an applied voltage and the probable presence of some impurities as for example water.

The color variation of each device starts at specific cathodic potential because of the electrochromic behavior of metal oxide. As shown in Figure 4.1.4.2.2, at 50 mV s^{-1}, the color change and so the phenomenon of electrochromism is registered for W_1Ti_1 at –0.198 V, for W_1Ti_3 at -0.09 V and for W_1Ti_5 -0.147 V. At 100 mV s^{-1} for the same systems, the corresponding values are -0.287 V for W_1Ti_1, -0.199 V for W_1Ti_3 and -0.118 V in the case of W_1Ti_5 (Figure 4.1.4.2.3). For the systems like W_3Ti_1, W_3Ti_3, W_3Ti_5 the cathodic potentials (or reduction potentials) of working electrodes at 50 mV s^{-1} are recorded at -0.04 V, -0.323 V and -0.523 V. At 100 mVs^{-1} the relative cathodic potentials are equal to -0.102 V for W_3Ti_1, to -0.425 V for W_3Ti_3 and to -0.036 V for W_3Ti_5, respectively. For W_5Ti_1, W_5Ti_3, W_5Ti_5 the correspondent reduction potentials are equal to -0.216 V, -0.187 V, -0.841 V at 50 mV s^{-1}. The reduction potentials registered at 100 mV s^{-1} C are equal to -0.02 V for W_5Ti_1, -0.395 V for W_5Ti_3 and -0.652 V for W_5Ti_5, respectively. Nevertheless, the specific cathodic potentials which turn ON the electrochromic devices have been collected at the scan rates of 50 mV s-1 and 100 mV s-1 and are summarized in the Table 4.1.4.1.5.

Electrochromic device	**Potential at 50 mV s^{-1} (V)**	**Potential at 50 mV s^{-1} (V)**
W_1Ti_1	0.198	-0.287
W_1Ti_3	-0.09	-0.199
W_1Ti_5	-0.147	-0.118
W_3Ti_1	-0.04	-0.102
W_3Ti_3	-0.323	-0.425
W_3Ti_5	-0.523	-0.036
W_5Ti_1	-0.216	-0.02
W_5Ti_3	-0.187	-0.395
W_5Ti_5	-0.841	-0.625

Table 4.1.4.1.5. Cathodic potentials which turn ON the following electrochromic devices: (a) W_1Ti_1, (b) W_1Ti_3, (c) W_1Ti_5, (d) W_3Ti_1, (e) W_3Ti_3, (f) W_3Ti_5, (g) W_5Ti_1, (h) W_5Ti_3 and (i) W_5Ti_5.

4.1.5. UV-Vis Spectroscopy

4.1.5.1. Transmittance modulation and Contrast change

UV-Vis Spectroscopy is a powerful instrument to estimate optical parameters such as transmittance modulation, color efficiency (CE) and switching times of electrochromic devices suitable for recovery energy. The two main parameters to assess the electrochromic behavior of electrochromic devices are the level of coloration or transmittance changes and the switching speeds between the colored and bleached states. The transmittance modulation (%) of each electrochromic device was monitored at fixed potential values equal to 0 V, -1.6 V, -1.8 V, -2 V and 2.8 V in the wavelength region of 400-1200 nm when the systems are in the bleached state (OFF state) and in the colored state (ON state).The transmittance curves of all electrochromic devices are shown in Figure 4.1.5.1.1.

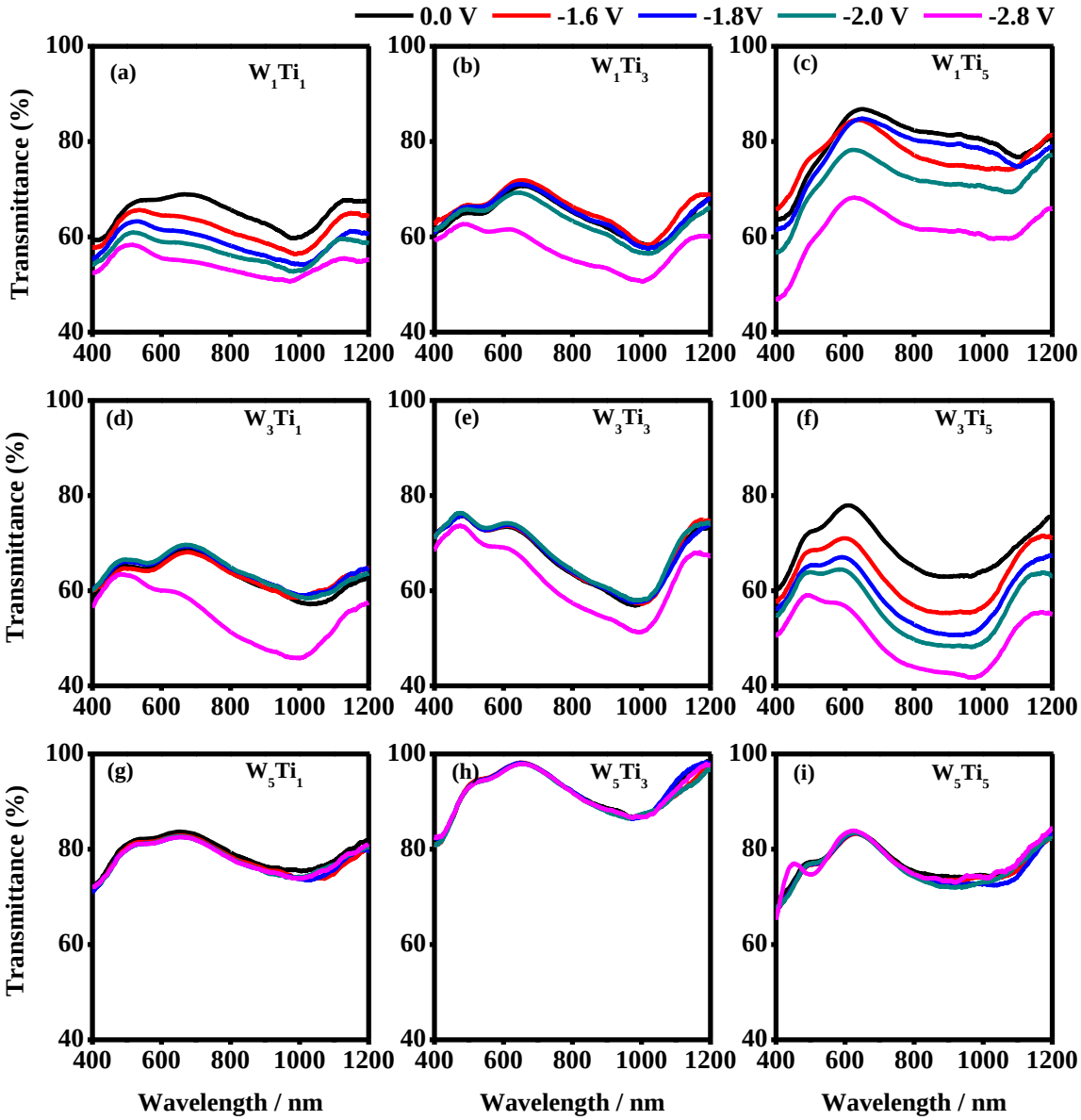

Figure 4.1.5.1.1. Optical transmittance curves acquired for the investigated electrochromic systems in the OFF state (0V, black curves) and in the ON state at: -1.6 V (red curves), -1.8V (blue curves), -2.0V (dark cyan curves), -2.8V (magenta curves) in the wavelength range between 400-1200 nm.

Each curve represents the optical behavior of the electrochromic device when it is put in two operating-conditions: in the OFF state which corresponds to the bleaching system at 0 V and then, in the ON state which matches the colored system after the application of fixed external potential of values -1.6 V, -1.8 V, -2.0 V, -2.8 V.

In each curve of the optical transmittance, is possible to observe a decreasing of the transmittance at specific wavelengths in the investigated UV-Vis-NIR region. As shown in Figure 4.1.5.1.1, systems like W_1Ti_1, W_1Ti_3, W_1Ti_5 and systems such as W_3Ti_1, W_3Ti_3 *and* W_3 Ti_5 (Figure 4.1.5.1.2) are characterized by a reduction of transmittance in the visible region close to 550 nm and in the near infrared region at 1020 nm as consequence of the applied potential exhibiting a light blue coloration. The transmittance modulations of the electrochromic device such as W_5Ti_1, W_5Ti_3, W_5Ti_5 do not show appreciable color variations between the OFF/ON states as shown in Figure 4.1.5.1.3

The transmittance modulation parameter (%) has been evaluated when the system was under 0V (OFF state) and then when it was under -2.8V (ON state). A graphic model depicted in Figure 4.1.5.1.4 have been adopted for a better understanding.

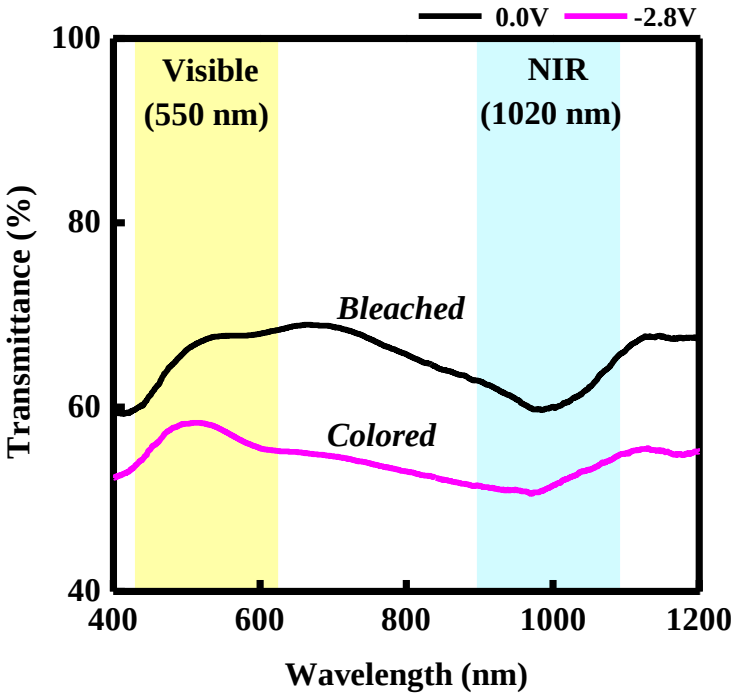

Figure 4.1.5.1.4. Model for the evaluation of the transmittance modulation at 0V ($\%T_{bleached}$) and at -2.8V ($\%T_{colored}$) of electrochromic devices.

At 0V the system is bleached or it is in its OFF state and its percentage transmittance is defined as $\%T_{bleached}$. At -2.8 V, the system is in its ON state *i.e.* it underwent the redox

process and it became colored with a corrispondent percentage transmittance that is defined as $\%T_{colored}$.

Figure 4.1.5.1.5 shows the % transmittance modulation of all electrochromic devices recorded at 550 nm in the Visible region.

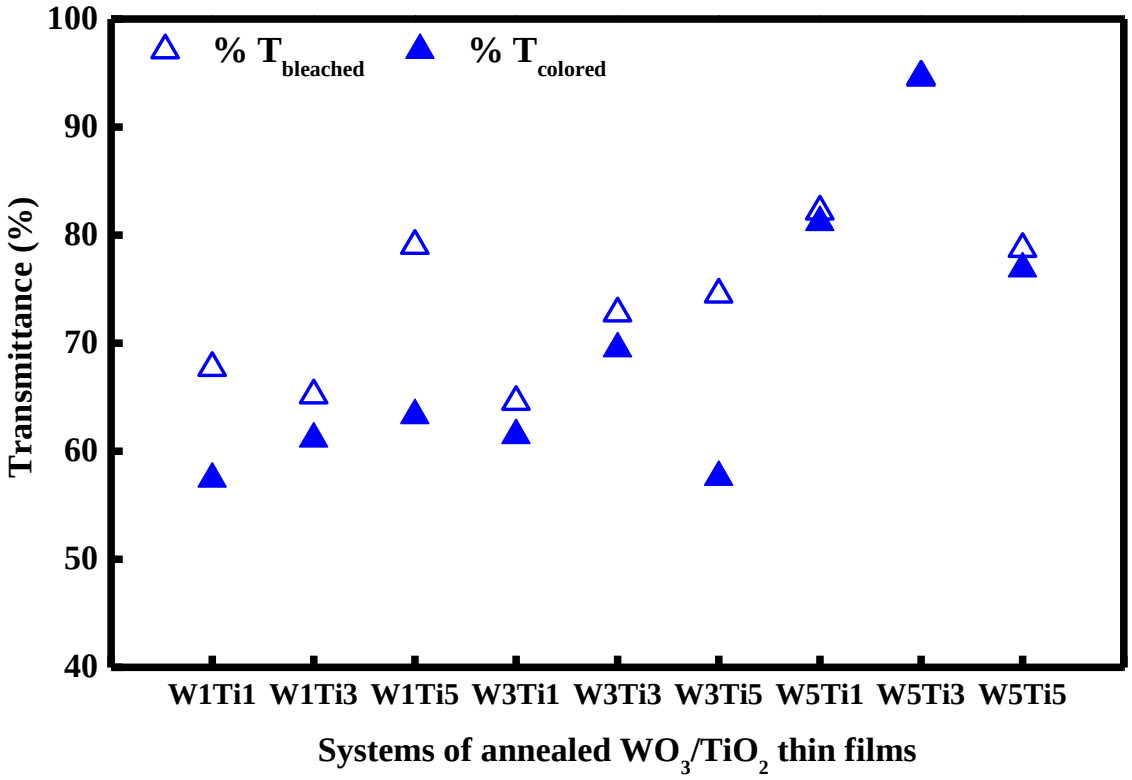

Figure 4.1.5.1.5. Transmittance modulation (%) of electrochromic devices of WO_3 and TiO_2 thin film treated at 100°C, 300°C, 500°C with gel polymer electrolyte of PMMA in 1M $LiClO_4$ in propylene carbonate, quantified in the Visible wavelength region (550 nm).

Systems made by the combination of both amorphous WO_3 and TiO_2 thin films such as W_1Ti_1 shows higher transmittance modulation at 550nm, where the $\%T_{bleached}$ is 67.72 % and the $\%T_{colored}$ is 57.43 %. Systems such as W_1Ti_5 and W_3Ti_5 show the highest transmittance modulations. For the system W_1Ti_5 the $\%T_{bleached}$ is equal to 79.02 % and the $\%T_{colored}$ is 63.31 %, while in the case of the system W_3Ti_5 the $\%T_{bleached}$ is 74.51 and the $\%T_{colored}$ is 57.58 %. In these systems assembled by the combination of amorphous-WO_3 and crystalline-TiO_2 thin films, the transmittance modulation is driven by the amorphous character of WO_3 thin film where the intercalation of Li^+ is fast.

The trend of transmittance modulation at 1020 nm is depicted in Figure 4.1.5.1.6.

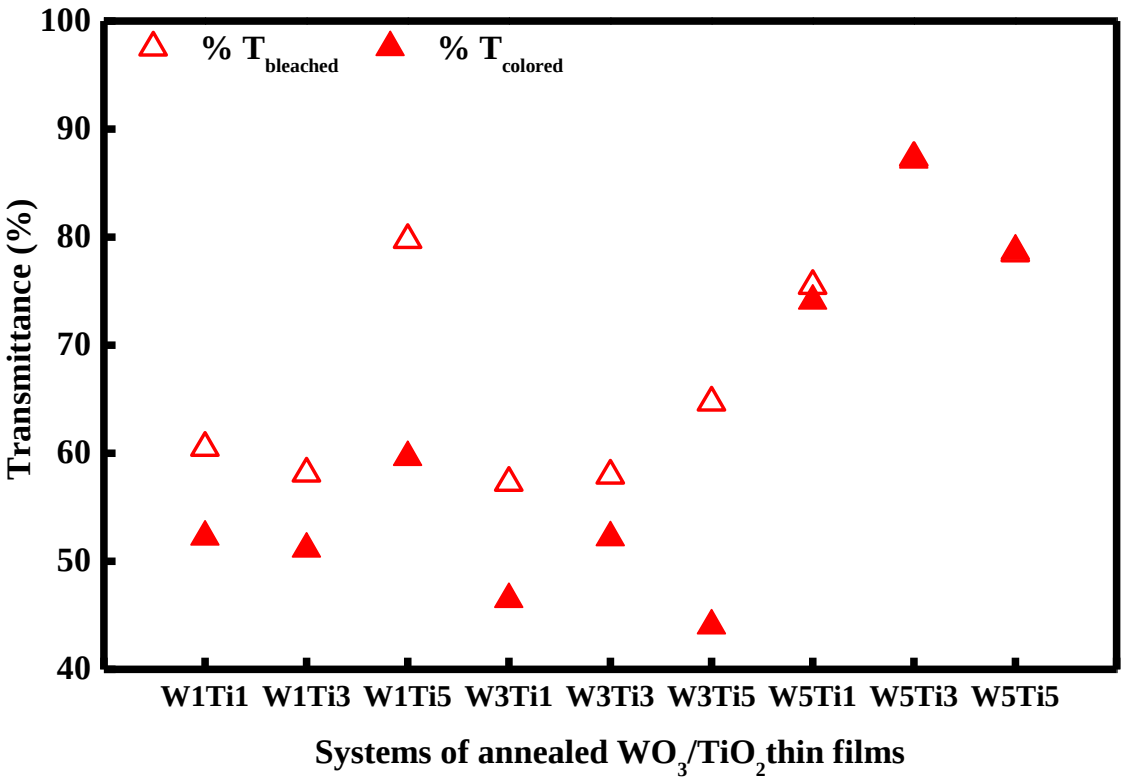

Figure 4.1.5.1.6. Transmittance modulation (%) of electrochromic devices of WO_3 and TiO_2 thin film treated at 100°C, 300°C, 500°C with gel polymer electrolyte of PMMA in 1M $LiClO_4$ in propylene carbonate, quantified in the Near Infrared region, NIR (1020 nm) wavelength region.

A similar tendency of transmittance modulation was found in the Near Infrared region, NIR, focusing at 1020 nm. In this case the systems such as W_1Ti_5 and W_3Ti_5 show a performant transmittant modulations estimated between $\%T_{bleached}$ and $\%T_{colored}$. In particular, the device W_1Ti_5 shows a % $T_{bleached}$ of 79.74 and a % $T_{colored}$ equal to 59.63, while the system W_3Ti_5 the system is characterized by a % $T_{bleached}$ of 64.71 % and a % $T_{colored}$ of 44.03 %. Also, the devices such as W_1Ti_1 W_1Ti_3 and W_3Ti_1 have significant transmittance modulations in accordance with the previously Lithium diffusion coefficients measured for single WO_3 and TiO_2 as-deposited annealed films.

It is important to underline that no consistent color changes can be made by systems W_5Ti_1, W_5Ti_3 and W_5Ti_5 in both the visible and NIR region. For these devices were not

possible to record their electrochromic behaviour because they were fully bleached in the investigated potential range from 0V to -2.8V, probably because of the water content or or to degradation of the gel polymer electrolyte which caused the film damage.

As it is possible to deduce from the investigated electrochromic behavior of all systems in the UV-Vis-NIR measurements, the electrochromic properties of devices are seriously affected by their degree of structure. Annealing treatment of thin films induces modification in their structure and a resultant crystallinity network or amorphous state are direct consequences tat can afflict or exalt the electrochromic performances of the devices.

An ordered structure like the crystalline obtained from the calcination processes can afflict the Li^+ intercalation and deintercalation through its more dense layers and also in this case the transmittance modulation. So, the transmittance modulation results are a combination of different factors like the amorphous and crystalline states of both WO_3 and TiO_2 thin films as function of the annealing temperature.

Table 4.1.5.1.1 summarizes the transmittance modulations (%) registered for the electrochromic devices in the potential range from 0 to -2.8 V in the Visible Region (550nm) and in the Near Infrared Region, NIR (1020 nm) wavelength region.

Electrochromic Device	**Transmittance at bleached state, $\%T_{bleached}$ (0V)**	**Transmittance at colored state, $\%T_{colored}$ (-2.8V)**	**Transmittance at bleached state, $\%T_{bleached}$ (0V)**	**Transmittance at colored state, $\%T_{colored}$ (-2.8V)**
	Visible Region (550nm)		*Near Infrared Region (1020nm)*	
W_1Ti_1	67.72	57.43	60.51	52.24
W_1Ti_3	65.19	61.13	58.14	51.13
W_1Ti_5	79.02	63.31	79.74	59.63
W_3Ti_1	64.57	61.45	57.28	46.48
W_3Ti_3	72.75	69.50	57.93	52.20
W_3Ti_5	74.51	57.58	64.71	44.03
W_5Ti_1	82.18	81.18	75.50	74.10
W_5Ti_3	94.67	94.53	87.32	87.13
W_5Ti_5	78.74	76.88	78.73	78.52

Table 4.1.5.1.1. Transmittance values registered at the bleached state ($\%T_{bleached}$) and at colored state ($\%T_{colored}$) for electrochromic systems of WO_3 and TiO_2 registered in the Visible region (550 nm) and Near Infrared region (1020nm) wavelength region.

4.1.5.2. Coloration Efficiency

The coloration efficiency (CE) is another important parameter usefully for the characterization of the electrochromic devices. The coloration efficiency, CE is defined as the change in optical density ΔOD at a particular wavelength (λ) per unit area of charge (Q) intercalated or extracted from the electrochromic film. It can be calculated according to the following (Equation 4.1.5.2.1) [32-34]:

$$CE(\lambda) = \frac{\Delta OD(\lambda)}{Q} = \frac{log\left(\frac{T_b}{T_c}\right)}{Q} \qquad (4.1.5.2.1)$$

Where T_b and T_c represent the transmittance in bleached and colored states.

Coloration efficiency values of electrochromic devices were estimated in the both visible and near infrared region at approximately 550 nm and 1020 nm. All data are summarized in Table 4.1.5.2.1. The best coloration efficiency values were found for electrochromic devices made by the combination of amorphous WO_3 thin film treated at 100°C and 300°C with crystalline TiO_2 thin film calcined at 500°C. The W_1Ti_5 and W_3Ti_5 systems offer the best coloration efficiency in both wavelengths. These results are a consequence of the structure order of WO_3 and TiO_2 thin films. In the visible region at 550 nm, the higher CE values, 179.10 $cm^2\ C^{-1}$ and 139.93 $cm^2\ C^{-1}$ are obtained for the W_1Ti_5 and W_3Ti_5 devices. In the near infrared region (1020nm) the higher CE values, 234.81 $cm^2\ C^{-1}$ and 209.03 $cm^2\ C^{-1}$ are obtained for the W_1Ti_5 and W_3Ti_5 devices.

Systems of WO_3 and TiO_2thin films annealed at 100°C, 300°C, 500°C	**Coloration Efficiency, CE ($cm^2\ C^{-1}$)**	
	Visible Region (λ = 550 nm)	**Near Infrared Region (λ =1020 nm)**
W_1Ti_1	76.35	68.08
W_1Ti_3	66.20	132.26
W_1Ti_5	179.10	234.81
W_3Ti_1	12.29	51.85
W_3Ti_3	45.17	102.95
W_3Ti_5	139.93	209.03
W_5Ti_1	1.75	2.68
W_5Ti_3	1.45	2.13

W_5Ti_5	7.91	-0.89

Table 4.1.5.2.1. Coloration efficiency at 550 nm and 1020 nm estimated for all electrochromic devices WO_3 and TiO_2 based thin film treated at 100°C, 300°C, 500°C for 1 hour.

4.1.5.3. Switching time

In addition, another important electrochromic parameter such as the switching time, has also been evaluated for the electrochromic systems. The switching time is defined as the time required for the system to reach the 90% in the full transmittance modulation at fixed wavelength or the spanning period between the steady bleached and colored states [34, 35]. To establish the switching time of the electrochromic device, we evaluated the time required by the system to switch between the OFF/ON states measured at the switching potential -2.8V at 1s, 10s, 50s, 100s, 200s, 300s, 400s, 500s, 600 s in the wavelength range (400-1200 nm), respectively. The switching time was determined by measuring the time needed to achieve a fully colored state of the device. The transmittance modulations of the electrochromic devices recorded at 1s, 10s, 50s, 100s, 200s, 300s, 400s, 500s, 600 s under the application of -2.8 V are shown in in Figure 4.1.5.3.1.

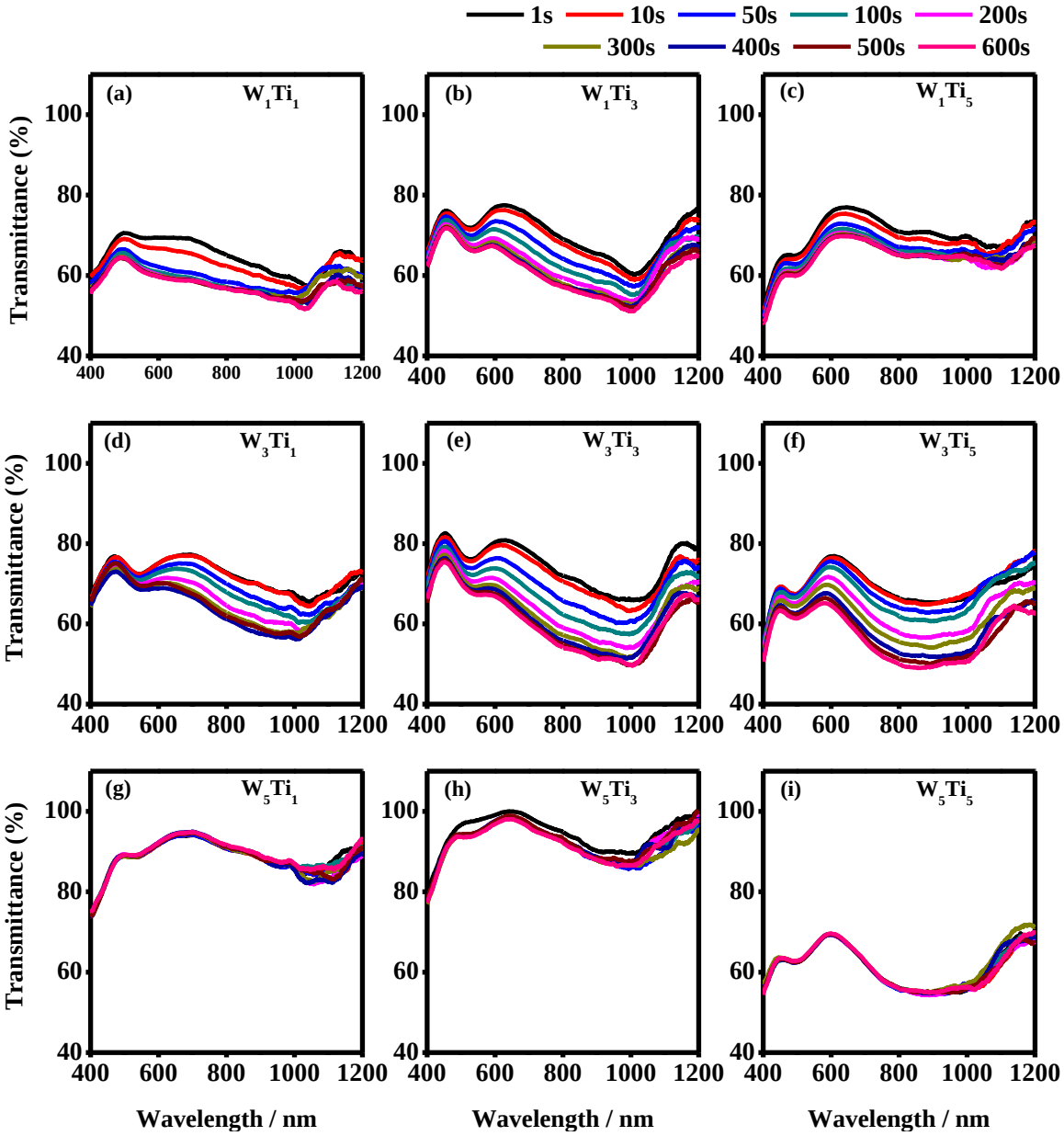

Figure 4.1.5.3.1. Transmittance modulation (%) of electrochromic devices of WO_3 and TiO_2 thin film treated at 100°C, 300°C, 500°C with gel polymer electrolyte of PMMA in 1 M $LiClO_4$ in propylene carbonate, registered at the switching pontetial of -2.8V and at 1s (black curves), 10s (red curves), 50s (blue curves), 100s (dark cyan curves), 200s (magenta curves), 300s (dark yellow curves), 400s (royal blue curves), 500s (wine red curves) and 600s (pink curves).

W_1Ti_5 and *W_3Ti_5* systems show switching times equal to 10 s and 100 s. The *W_1Ti_5* is a system suitable for the promotion of coloration efficiency in the visible region. While,

the W_3Ti_5 is a performant system for the promotion of energy saving of buildings in the near infrared region. For systems such as W_5Ti_1, and W_5Ti_5 was not possible to observe a sufficient color change under the applied voltage to quantify switching times. The W_5Ti_3 shows the worst switching time equal to 500 s but was not possible to quantify a visible color change.

Table 4.1.5.3.1 summarizes the switching times of all electrochromic devices measured at -2.8V in the range from 1 s to 600 s.

Systems of WO_3 and TiO_2 thin films annealed at 100°C, 300°C, 500°C	**Switching Time (s)**
W_1Ti_1	10
W_1Ti_3	50
W_1Ti_5	10
W_3Ti_1	50
W_3Ti_3	50
W_3Ti_5	100
W_5Ti_1	n. a.
W_5Ti_3	500
W_5Ti_5	n. a.

Table 4.1.5.3.1. Switching times of electrochromic systems of combined WO_3 thin films annealed at 100°C, 300°C, 500°C with TiO_2 thin films annealed at 100°C, 300°C, 500°C, immersed in a gel polymer electrolyte made by PMMA in 1 M solution of $LiClO_4$ in propylene carbonate. Switching times were measured at -2.8V from 1 s to 600s in the wavelength range (400-1200 nm). For W_5Ti_1 and W_5Ti_5 the time of 600 s was not sufficient to quantify switching time at -2.8V as a function of the transmittance modulation (n. a. = not available).

4.1.6 Conclusions

The effect of annealing temperature plays an important role for the efficiency of electrochromic devices based on the as-deposited sample of WO_3 and TiO_2 films prepared by sol gel – spin coating method and calcined in the range of temperatures from 100°C to 500°C. Annealing treatment is directly correlated to the transition phase from amorphous to crystalline state thin films.

Micro-Raman Spectroscopy confirms the amorphous-WO_3 thin films annealed at 100 °C and 300 °C by the presence of the bands at about 788 cm^{-1} and 950 cm^{-1}, while the crystalline-WO_3 thin film is confirmed at 500°C with the bands at 715 cm^{-1}, 807 cm^{-1} and 948 cm^{-1}. The amorphous-TiO_2 thin films annealed at 100 °C and 300 °C have been confirmed by the weak and broad band located at about 422 cm^{-1}, while the Anatase-TiO_2 at 500°C has been evidenced by the bands located at 141 cm^{-1}, 199 cm^{-1}, 399 cm^{-1}, 515 cm^{-1}, 519 cm^{-1} and 637 cm^{-1}.

The effect of cyclic voltammetry scan rate on the estimation of diffusion coefficient using Randles-Sevcik method has been assessed experimentally for both WO_3 and TiO_2 thin films in liquid electrolyte and in a gel polymer electrolyte. The Diffusion coefficient values are dependent on a lot of factors such as preparation technique of thin films, amorphous or crystalline state of film and, the values are affected by the nature of electrolyte in which they were evaluated (liquid or gel polymer electrolyte).

From Cyclic Voltammetry measurements we found that the crystallized structures of both WO_3 and TiO_2 film are less favorable for ions diffusion with respect the amorphous structures. High annealing temperature leads to denser layers and as a result the diffusion of Li^+ ions become weak and slowly respects the amorphous structure.

Diffusion coefficient have been established in both liquid and gel polymer electrolyte media. The highest values of diffusion coefficient in the liquid electrolyte have been found for the amorphous film of WO_3 treated at 300 °C (D_{jpc}= 1.628 $\times 10^{-11}$ cm^2 s^{-1}) and for the amorphous film of TiO_2 calcinated at 300 °C (D_{jpc}= 0.731 $\times 10^{-11}$ cm^2 s^{-1}) at the same scan rate (300 mV s^{-1}). In the gel polymer electrolyte, the diffusion coefficients have been lower than the established in liquid medium. The highest values of diffusion coefficient in the gel polymer medium have been established for the amorphous film of WO_3 calcinated at 300 °C (D_{jpc}= 0.673 $\times 10^{-11}$ cm^2 s^{-1}) and for the amorphous film of TiO_2 treated at 300 °C (D_{jpc}= 0.317 $\times 10^{-11}$ cm^2 s^{-1}) at the highest scan rate (300 mV s^{-1}).

Cyclic Voltammetry was also important for the evaluation of reversibility and electrochromism of the electrochromic devices based on annealed WO_3 and TiO_2 electrodes.

UV-Vis-NIR spectroscopic analysis has shown that, among the different electrochromic device built by using WO_3 and TiO_2 annealed at 100 °C, 300 °C and 500 °C, the best

devices have been that made by the TiO_2 annealed at 500°C and WO_3 annealed at 100 °C and 30 0°C (*W_1Ti_5* and *W_3Ti_5*). At 550 nm the *W_1Ti_5* and *W_3Ti_5* devices show higher values of coloration efficiency equals to 179.10 cm^2/C and 139.93 cm^2/C. Whereas, in the NIR region, the same devices show higher values of coloration efficiency equals to 234.81 cm^2/C and 209.03 cm^2/C. The switching times of *W_1Ti_5* and *W_3Ti_5* devices are equal to 10s and 100 s. These electrochromic devices could be used in order to control the light flux but also the heat flux and so, those devices could be used for energy saving applications.

4.1.7 References

[1] D. J. Kim, S. H. Hahn, S. H., S. H. Oh, E. J. Kim, *Mater. Lett.*, (2002) **57** 355–360.

[2] B. Wen-Cheun Au, A. Tamang, D. Knipp, K. Y. Chan, *Opt. Mater. (Amst).*, (2020) **108** 110426.

[3] B. Wen-Cheun Au, K. Y. Chan, D. Knipp, *Opt. Mater. (Amst).*, (2019) **94** 387-392.

[4] G. Leftheriotis, S. Papaefthimiou, P. Yianoulis, *Solid State Ionics*, (2007) **178** 259-263.

[5] K. J. Patel, G. G: Bhatt, S. S. Patel, R. R. Deasi J. R. Ray, C. J. Panchal, P. Suryavanshi, V. A. Kheraj, A. S. Opanasyuk, *Nano-Electron. Phys.*, (2017) **9** 1-4.

[6] M. Castriota, S. Marino, C. Versace, G. Strangi, N. Scaramuzza, E. Cazzanelli, *Mol. Cryst. Liq. Cryst*., (2005) **429** 237-253.

[7] P. Chrysicopoulou, D. Davazoglou, C. Trapalis, G. Kordas, *Thin Solid Films*, (1998) **323** 188-193.

[8] A. Bakri, M. Z. Sahdan, F. Adriyanto, N. A. Raship, N. D. M. Said, S. A. Abdullah, M.S. Rahim, *AIP Conf. Proc.* , (2007) **1788** 1-8.

[9] T. Caruso, M. Castriota, A. Policicchio, A. Fasanella, M. P. De Santo, F. Ciuchi, G. Desiderio, S. La Rosa, P. Rudolf, R. G. Agostino, E. Cazzanelli, *Appl. Surf. Sci*., (2014) **297** 195-204.

[10] E. Cazzanelli, C. Vinegoni, G. Mariotto, A. Kuzmin, J. Purans, *Journal of Solid-State Chemistry*, (1999) **143** 24-32.

[11] A. Kuzmin, J. Purans, E. Cazzanelli, C. Vinegoni, G. Mariotto, *J. Appl. Phys*., (1998) **84** 5515.

[12] Y. Djaoued, S. Balaji, R. Brüning, *J. Nanomater*., (2012) **2012** 1-9.

[13] M. F. Daniel, B. Desbat, J. C. Lassegues, B. Gerand, M. Figlarz,. *J. Solid State Chem.*, (1987) **67** 235-247.

[14] M. Gotić, M. Ivanda, S. Popović, S. Musić, *Mater. Sci. Eng. B Solid-State Mater.*

Adv. Technol., (2000) **77** 193-201.

[15] E. Cazzanelli, C. Vinegoni, G. Mariotto, A. Kuzmin, J. Purans, *Solid State Ionics*, (1999) **123** 67-74.

[16] T. Ohsaka, F. Izumi, Y. Fujiki, *Raman Spectrosc*., (1978) **7** 321-324.

[17] S. Balaji, A. S. Albert, Y. Djaoueda,R. Bruningb, *J. Raman Spectrosc*., (2009) **40** 92-100.

[18] U. Balachandran, N. G. Eror, *J. Solid State Chem*., (1982) **42** 276-282.

[19] M. Rezaee, S. M. Mousavi Khoie, K. H. Liu, *CrystEngComm*., (2001) **13** 5055-5061.

[20] A. S. Yazid, Z. M. Rosli, J. M. Juoi, N. D. Johari, *MATEC Web. Conf*., (2018) **150** 1-5.

[21] M. J. Alam, D. C. Cameron, *Journal of Sol-Gel Science and Technology*, (2002) **25** 137-145.

[22] N. N. Dinh, N. T. T. Oanh, P. D. Long, M. C. Bernard, A. H. Goff, *Thin Solid Films*, (2003) **423** 70-76.

[23] K. Sahbeni, I. Sta, M. Jlassi, M. Kandyla, M. Hajji, M. Kompitsas, W. J. Dimassi, *Phys. Chem. Biophys*., (2017) **7** 1-7.

[24] P. Judeinstein, R. Morineau, J. Livage, *J. Solid State Ionics*, (1992) **51** 239-247.

[25] P. J. Huang, H. Chang, C. T. Yeh, C. W. Tsai, *Thermochimica Acta* (1997) **297** 85-92.

[26] B. Karunagaran, Kyunghae Kim, D. Mangalaraj, Junsin Yi, S. Velumani, *Solar Energy Materials & Solar Cells*, (2005) **88** 199-208.

[27] M. A. Habib, D. Glueck, D., *Sol. Energy Mater*., (1989) **18** 127-141.

[28] P. W. Chen, C. T. Chang, T. F. Ko, S. C. Hsu, K, D. Li, J. Y. Wu, *Nanoporous Sci. Rep.*, (2020) **10** 1-12.

[29] N. Naseri, R. Azimirad, O. Akhavan, A. Z. Moshfegh, *Thin Solid Films*, (2010)

518 2250-2257.

[30] C. G. Granqvist, in *Handbook Of Inorganic Electrochromic Materials, Elsevier Scienc B.V.*, Chapter 6 "Tungsten Oxide Films: Ion Intercalation/Deintercalation Studied by Electrochemical Techniques" (1995) 79-110.

[31] K. H. Heckner, A. Kraft, *Solid State Ionics,* (2002) **152** 899-905.

[32] P. M. S. Monk, R. J. Mortimer, D. R. Rosseinsky, in Electrochromism: Fundamentals and Applications, VCH, Weinheim, Germany (1995).

[33] K. J. Patel, C. J. Panchal, V. A. Kheraj, M. S. Desai, *Mater. Chem. Phys*., (2004) **114** 475-478.

[34] Y. Ren, Y. Gao, G. Zhao, *Ceram. Int.*,(2015) **41** 403-408.

[35] V. K. Thakur, G. Ding, J. Ma, P. S. Lee, X. Lu, *Adv. Mater*., (2012) **24** 4071-4096.

4.2 Study of Electrolytes suitable for electrochromic devices: An investigation of Plasticizers and Salt concentrations effects on Liquid and Polymer Gel Electrolytes based on poly (methyl methacrylate)

Abstract

This work describes the study and the characterization of the electrochemical properties of two classes of electrolytes: the liquid electrolytes and the gel polymer electrolytes. The liquid electrolytes systems are based on lithium salt solution of a single plasticizer such as propylene carbonate and then in a mix of propylene carbonate and ethylene carbonate at the different salt concentrations (0.1, 0.5M, 1 M, 2M). The gel polymer electrolytes are based on Poly(methylmethacrilate) (PMMA) as a polymer matrix and they are prepared in a concentration of (20:80) % w/w between PMMA and lithium perchlorate $LiClO_4$ and single plasticizer propylene carbonate (PMMA-Li-PC) and also, in aconcentration of (20:80) % w/w between PMMA and lithium perchlorate $LiClO_4$ and mix of propylene carbonate and ethylene carbonate (PMMA-Li-PC-EC) at the different salt concentrations (0.1 M, 0.5 M, 1 M, 2 M). The effects of different plasticizers (single and mixed) on the properties of liquid and gel polymer electrolytes have been considered. The variation of conductivity with salt concentration has been studied to evaluate which was the better system for both liquid electrolytes and gel polymer electrolytes. All the spectroscopic data have been evaluated for a better clarification on the variation of ionic conductivities, ion associations and ion-pairing phenomena, electrochemical stability, and thermal stability to establish which is the best system suitable for the electrochromic devices.

4.2.1. Introduction

Electrolytes have an important role in the correct operation of electrochromic devices. Their role is to warrant the ionic transport between two electrodes to balance all the charges that arise from the redox process, which is taking place in an electrochromic device. A good electrolyte system must exhibit high ionic conductivity, high electrochemical stability window, thermal stability, and high transmittance properties.

They are composed of polar organic solvents of high dielectric constant and low viscosity to ease the ion migration through the electroactive material [1].

In the past liquid electrolytes (LEs) were used for ion conduction inside the electrochromic device [2]. In principle, they are a solution of lithium salt dissolved in organic solvents for example propylene carbonate, ethylene carbonate, ethyl methyl carbonate, dimethyl carbonate, and diethyl carbonate or their mixtures [3] They show low viscosity and low surface tension to ensure a good electrolyte wetting that determines a good contact between the electrolyte and active materials. At the same time, they facilitate the use of electrolytes with high ionic conductivity, because of facilitating ion diffusion and the formation of a homogeneous solution. They show high ionic conductivities (10^{-3}∼10^{-2} S cm^{-1}) [4, 5]. Liquid electrolytes exhibit some weaknesses like low chemical stability, the possible formation of bubbles and the widespread use of a lot quantities of organic solvents that are necessary for their preparation [6].

Recently a new class of electrolytes have been introduced instead of liquid electrolytes. Gel polymer electrolytes (GPEs) are a typology of electrolytes made by host polymer matrix (PMMA, PEO, PVC, PVDF, PVDF-HFP, PAN) that can host lithium salt ($LiClO_4$, $LiCF_3SO_3$, $LiBF_4$) immersed into a solution of polar aprotic solvent (PC, EC, DEC, DMC) or their mixtures [1,7-9]. The lithium salt is responsible for conduction in the polymer matrix, and the polymer holds the electrolyte to provide mechanical strength. The diffusion of Li^+ cations through the polymer matrix is done by using a high dielectric solvent that promotes the dissociation of Li^+ and the counterions in the polymer matrix, which ensures the high conductivity of gel electrolyte systems by increasing the ion mobility [10].

Gel polymer electrolytes represent an innovation in the field of electrolytes because they offer many advantages instead of liquid electrolytes such as good thermal stability, wide electrochemical window, high conductivity, and a good combination of properties of liquid and polymer electrolytes reduction in the risk of the electrolyte solution leakage [9]. For a better understanding of the potentiality of gel polymer electrolytes in electrochromic devices, many electrochemical, mechanical, and spectroscopic investigations have been carried out to optimize their performances [10, 11]. Gel polymer electrolytes in different configurations have been proposed in electrochromic devices: gel [11], blend [12], and ionic liquid [13] and to improve the specific conductivity of the

polymer electrolytes the confinement of polymer electrolyte in nanopores of alumina membranes has been achieved [14].

Gel polymer electrolytes made by PMMA polymer are common and they are widely studied [15-21]. Poly (methyl methacrylate) (PMMA) is widely used for the fabrication of electrolytes because of its amorphous structure, which gives it so many important properties like good solubility in the most organic solvents, flexible backbones, good ionic conductivity [19], and high transparency that is a crucial criterion for its application in the electrochromic devices and lithium batteries [22].

In this work, PMMA was dissolved in Li-PC and Li-PC-EC electrolyte solutions at room temperature to obtain transparent and homogeneous gels. Gels were compared to simple Li-PC and Li-PC-EC liquid electrolytes. Structural, electrochemical, and thermal studies were conducted to produce high-performance gel polymer electrolytes suitable for electrochromic devices.

4.2.2. Experimental Section

4.2.2.1. Materials

Poly (methyl methacrylate), PMMA (Mw = 120000) was purchased from Sigma-Aldrich Company. Lithium perchlorate ($LiClO_4$), propylene carbonate (PC), and ethylene carbonate (EC) were obtained from Sigma-Aldrich Company. All the compounds were preserved inside the glove box to prevent them from absorbing moisture prior to preparation and to further characterizations.

4.2.2.2. Preparation of liquid electrolytes and gel polymer electrolytes

All electrolyte systems (liquid and gel polymer electrolytes) have been prepared in a glove box (MBRAUN-Unilab). Two kinds of Lithium perchlorate solutions have been prepared at the following salt concentrations of 0.1 M, 0.5 M, 1 M, and 2M: one is made by dissolving lithium perchlorate in propylene carbonate (Li-PC), and the second one is made by dissolving the salt in a mix of propylene carbonate and ethylene carbonate (Li-PC-EC) with the molar ratio of the two solvents 1:1.

Starting from Li-PC and Li-PC-EC electrolytes solutions, two kinds of PMMA-based polymer electrolytes have been prepared by mixing 20 % w/w of PMMA and 80 % w/w of each electrolyte solution: PMMA-Li-PC and PMMA-Li-PC-EC. Each mixture has been stirred and heated at 100 °C for one hour. In the end, each sample has been left to rest for one night.

4.2.2.3. Characterization of liquid electrolytes and gel polymer electrolytes

AC impedance data of each sample were collected inside the glovebox by using a commercial dip cell, mercury-free Conductivity Probes (Fisherbrand Accumet) with Nominal Cell Constant: 1.0 cm^{-1}. AC Impedance data were made using Solartron SI 1260 Impedance / Gain Phase Analyzer with a 1296 interface. SMaRT Impedance Measurement Software (Solartron Analytical) was used to scan from 10MHz to 1HZ,

while AC Voltage was set at 0,1V. Zview software was used to analyze the AC-Impedance data. The impedance of each sample was measured three times to ensure data reproducibility. Empirical equivalent circuits were used to model ionic conduction of all systems and determine ionic conductivity resistance values.

ATR-FTIR spectra were obtained using Thermo Scientific Nicolet iS50 Fourier Transform Infrared spectrometer using an attenuated total reflection attachment in the absorbance mode in the range between 400 cm^{-1} and 4000 cm^{-1}. The ATR cell had a ZnSe crystal cut at 45°. The average depth of penetration of the infrared radiation, d_p, was calculated by using (Equation 4.2.2.3.1)

$$d_p = \frac{\lambda}{2\pi n_1 (sin^2\vartheta - n_{21}^2)^2} \qquad 4.2.2.3.1$$

where λ is the wavelength of the radiation in air, θ is the angle of incidence (45°), n_1 is the refractive index of the ATR crystal (2.4) and n_{21} is the ratio of the refractive index of the sample to that of the ATR crystal (0.605). Using these values an average depth of infrared radiation into the sample was determined to be approximately 1.0 mm in the region of interest in the absorbance mode in the range 4000-400 cm^{-1}. The number of scans to collect is 32 and the spectral resolution of the data is 1 cm^{-1}. All the measurements were made at room temperature (25 °C).

DSC of the gel electrolyte samples was carried out on DSC2500 (TA instruments, German) in the range -90 °C to 180 °C at a heating cooling rate of 10 °C/min under a constant flow (50mL min^{-1}) of nitrogen to avoid any contact of atmospheric moisture. Each sample was put inside an aluminum pan. The following DSC setup was used: (1) equilibrate to 35 °C, (2) cool to -90 °C at a cooling rate of 10 °C min^{-1}, (3) heat to 180 °C at a heating rate of 10 °C/min, (4) and equilibrate at 35 °C with a cooling rate of 10 °C min^{-1}. Tg was estimated by the discontinuity in the second derivative of the heat flow from DSC thermograms. TGA data were collected on a TA instruments TGA 5500 under nitrogen at 2.5 °C/min.

Electrochemical windows of each sample were determined from the Linear Sweep Voltammetry method (LSV). Linear Sweep Voltammetry measurements were carried out on gel polymer electrolytes in the current range between 0 mA to 200 mA at a scan rate

of 10mV s^{-1} with a Potentiostat PARSTAT 4000+ using an electrochemical cell composed of two steel plates (7.6 cm × 1.27 cm × 0.05 cm).

4.2.3. Results and Discussion

4.2.3.1. AC Impedance and Ionic Conductivities of liquid electrolytes and PMMA-based gel polymer electrolytes

AC Impedance spectroscopy is a powerful method used to estimate the electrical properties of all electrolyte systems (liquid and gel polymer electrolytes). The response of an electrochemical system to an applied current or AC potential can be illustrated in the Nyquist plot, which is a plot of the imaginary impedance versus the real impedance. The Resistivity $\rho, (\Omega\, S)$, and the Ionic Conductivity, $\sigma, (S\, cm^{-1})$of liquid electrolytes and PMMA-based gel polymer electrolytes are calculated from Equations 4.2.3.1.1 and 4.2.3.1.2.

$$\rho = \frac{R_b}{Nominal\ Cell\ Constant} \qquad (4.2.3.1.1)$$

$$\sigma = \frac{1}{R_b} \qquad (4.2.3.1.2)$$

Where R_b is the bulk resistance of the electrolyte, estimated by the fitting model of the Nyquist plot of complex impedance for liquid and gel polymer electrolytes and the *nominal cell constant* is an intrinsic constant of the electrochemical cell that in our case was equal to 1 cm^{-1}. The electrochemical cell and the apparatus used for the AC Impedance measurements are shown in Figure 4.2.3.1.1.

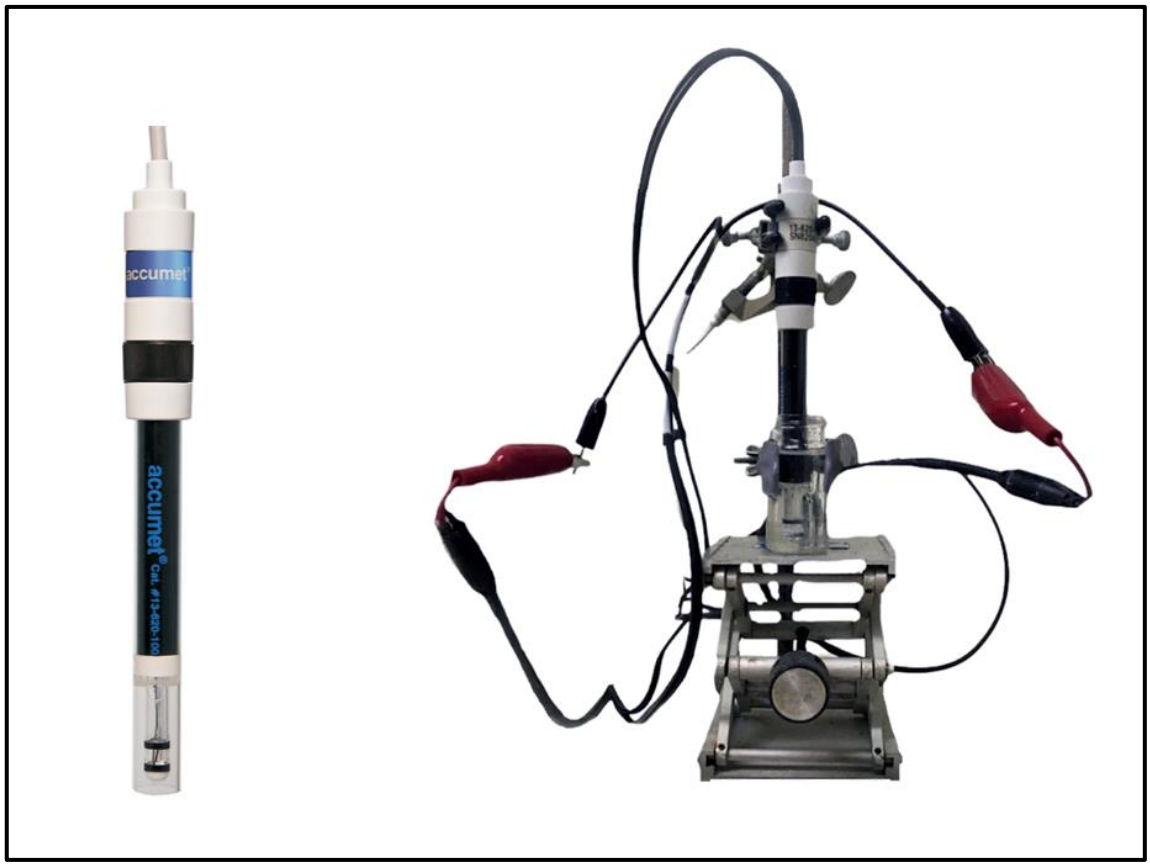

Figure 4.2.3.1.1. Electrochemical dip cell and experimental setup used for the determination of resistivity and ionic conductivity of liquid electrolytes and PMMA based gel polymer electrolytes inside the glove box.

Nyquist plots of liquid electrolytes Li-PC and Li-PC-EC at the salt concentrations (0.1 M, 0.5 M, 1 M, 2 M) were registered in the frequency range between 1 Hz to 1 MHz and they are shown in Figure 4.2.3.1.2.

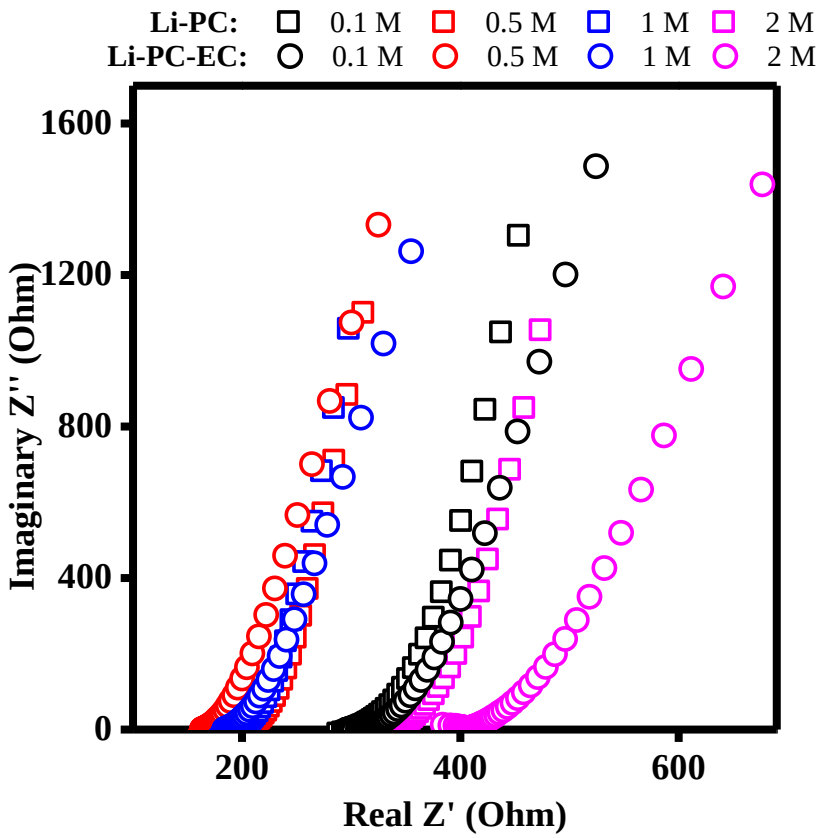

Figure 4.2.3.1.2. Nyquist Plots in the range of 1 Hz to 1 MHz of Li-PC and Li-PC-EC liquid electrolytes at different salt concentrations (0.1 M, 0.5 M, 1 M, 2 M).

For both Li-PC and Li-PC-EC liquid electrolyte systems, in the region of the low frequency, the results show a linear behavior in the complex plane with an angle of 45° to the real axis. The ion diffusion generates a high Warburg impedance which influences the ion conduction of the liquid electrolytes.

Nyquist plots of both PMMA-Li-PC and PMMA-Li-PC-EC gel polymer electrolytes at the salt concentrations (0.1 M, 0.5 M, 1 M, 2 M) were recorded in the frequency range between 1 Hz to 1 MHz and they are shown in Figure 4.2.3.1.3.

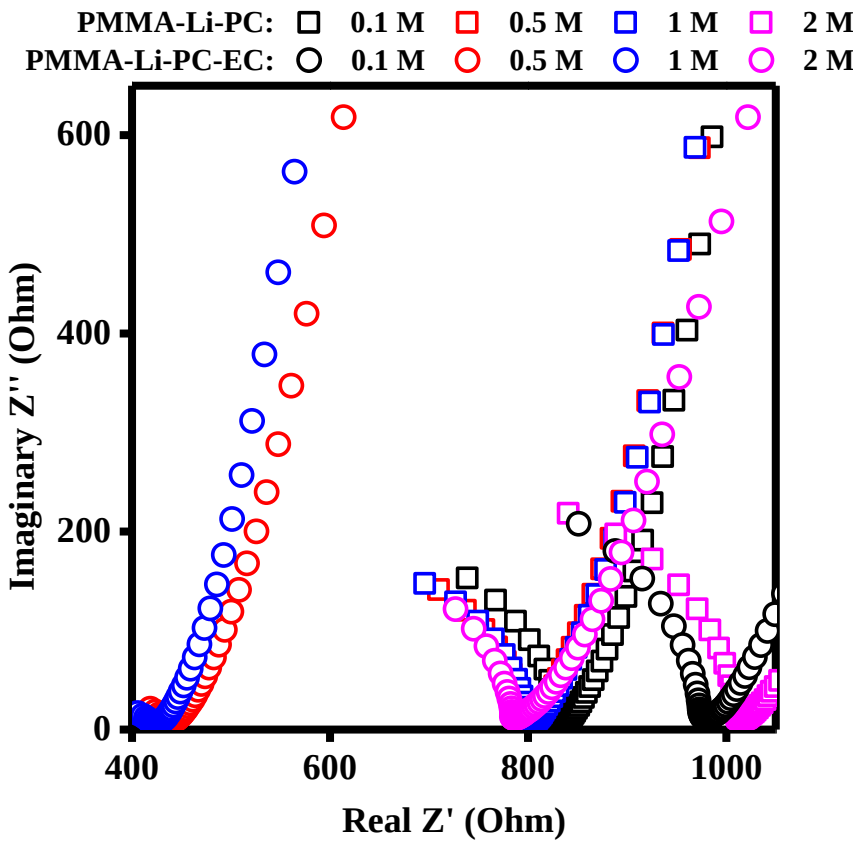

Figure 4.2.3.1.3. Nyquist Plots in the range of 1 Hz to 1 MHz of (20:80) % w/w PMMA-Li-PC and (20:80) % w/w PMMA-Li-PC-EC gel polymer electrolytes at different salt concentrations (0.1 M, 0.5 M, 1 M, 2 M).

The plot is characterized by the presence of ideal semicircles in the region of the high frequencies that we can relate to the ion conduction in the bulk of the sample. The low-frequency region has an inclined line which originates from the effect of electrode polarization. For the gel polymer electrolytes (PMMA-Li-PC and PMMA-Li-PC-EC) a semicircle could be a result of two effects: the presence of the polymer matrix with higher resistance with respect to the liquid solutions and the contribution of the electrode resistance [23].

Charge carriers *i.e.,* ions are the main responsible for the current in the system and therefore, they can contribute to the total ion conductivity of the system [9]. In addition, the contribution of the electrode resistance in the solution of the gel polymer electrolytes could contribute to the initial portion of the ion conduction and it could explain the reason why the semicircle does not appear in the origin of the Nyquist plot. The lower frequency

region is under the diffusion control which is the effect of the diffuse layer resistance of the dip cell as confirmed by the Warburg impedance.

The experimental impedance data for liquid and gel polymer electrolytes have been analyzed by relatively empirical equivalent circuits. The representation of equivalent circuits corresponding to the Nyquist plot is an easy way to provide a clarification of the electrochemical properties of the systems.

The equivalent circuit which describes both types of liquid electrolyte systems (Li-PC and Li-PC-EC) is depicted in Figure 4.2.3.1.4.

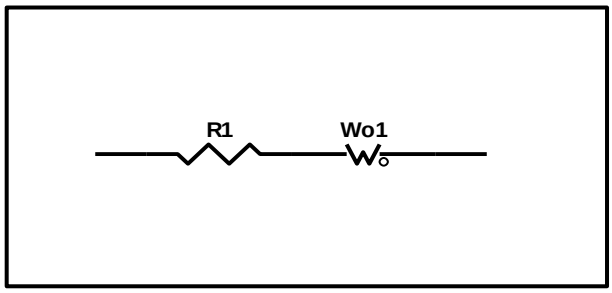

Figure 4.2.3.1.4. Equivalent circuit model for Li-PC and Li-PC-EC liquid electrolytes.

The equivalent circuit is composed of only two electrical elements which are R1 and Wo1 in series, respectively. R1 is the resistor of the system and Wo1 is the Warburg element. The electrochemical process for liquid electrolytes is under diffusion control, so this means that the resistance of the system is only the diffusion-controlled resistance.
The equivalent circuit of the gelled systems based on PMMA-Li-PC and-PMMA-Li-PC-EC is shown in Figure 4.2.3.1.5.

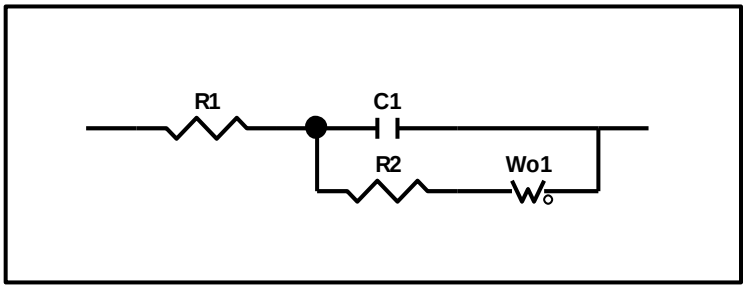

Figure 4.2.3.1.5. Equivalent circuit model for PMMA-Li-PC and PMMA-Li-PC-EC gel polymer electrolytes.

The equivalent circuit is composed of different electric elements: a resistor R1 which describes the electrode resistance in solution, a capacitor C1 and a second resistor R2 in parallel which are attributed to the electrolyte resistance and a Warburg resistance Wo1 in series to R2 which is related to the diffuse layer resistance.

The ionic conductivities were estimated for both liquid (Li- PC and Li-PC-EC) and gel polymer electrolyte systems (PMMA:Li-PC and PMMA-Li-PC-EC) at different salt concentrations (0.1 M, 0.5 M, 1 M, 2 M). The trends of ionic conductivities are shown in Figure 4.2.3.1.6.

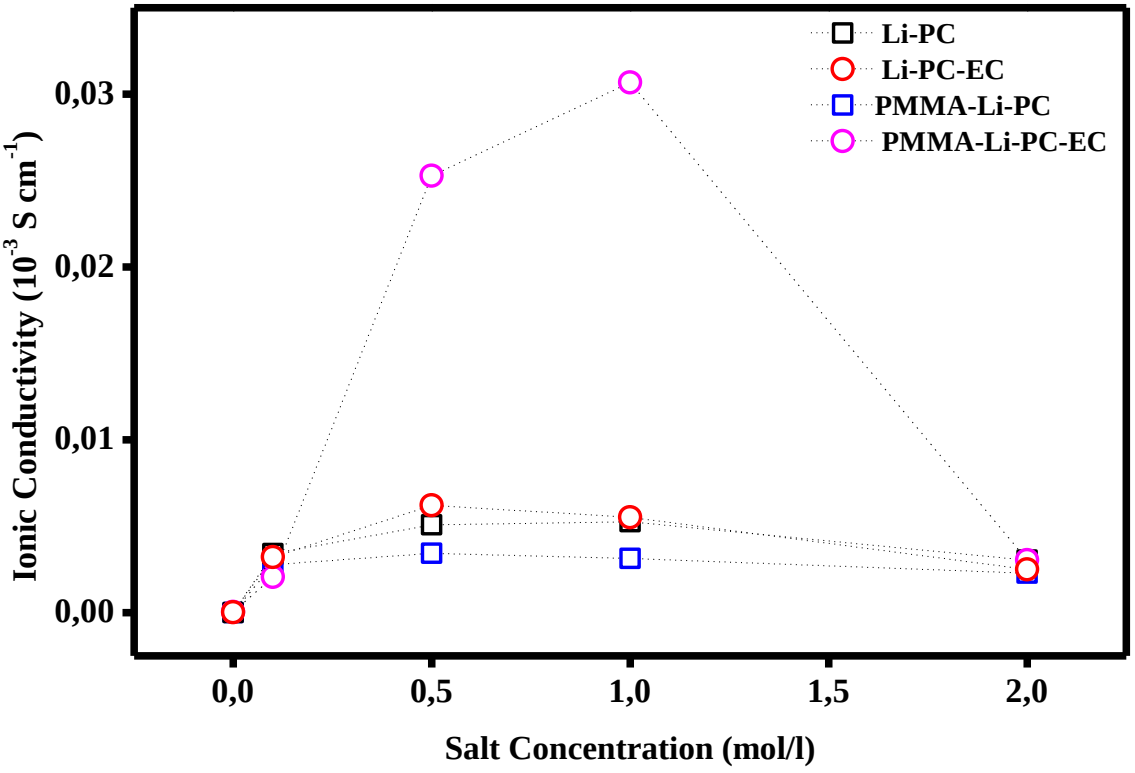

Figure 4.2.3.1.6. Ionic Conductivities as a function of different salt concentrations (0.1 M, 0.5 M, 1 M, 2 M) of liquid electrolytes: Li-PC (black rectangular), Li-PC-EC (red circle) and of gel polymer electrolytes: PMMA-Li-PC (blue rectangular) and PMMA-Li-PC-EC (magenta circle).

Considering the trends of the ionic conductivities of all electrolytes, the maximum value of ionic conductivity for the PMMA-Li-PC occurs at 0.5 M and it is equal to 0.00343 S cm^{-1}. The maximum conductivity value is obtained from the systems PMMA-Li-PC-EC, when the salt concentration is equal to 1 M, having a value of 0.031 S cm^{-1}. The PMMA-

Li-PC value is comparable to values found for similar systems in the literature [16-18]. However, the value for the PMMA-Li-PC-EC is approximately an order of magnitude greater than other PMMA-Li-PC-EC systems studied]15, 20-21]. It is quite interesting results because according to the literature [21], in this case, the presence of the polymeric matrix and the use of the two solvents seem to promote the ionic conductivity in the gel. As reported in the literature [21] a two-fold increase in conductivity for a 1 M salt solution, this work has almost a factor of 10 increase in conduction at the 1 M salt concentration. Conductivity data as a function of lithium-ion concentration indicates that investigating interactions between electrolyte materials, host polymer and solvent plasticizers is very important to understanding the behavior of these systems.

The lithium ions are surrounded by solvent molecules and the number that interacts with the lithium ions depends on the salt concentrations. A higher concentration corresponds to a higher solvation number and this means that the lithium ions can be more interact with the solvent molecules. At lower concentrations, the lithium ions can interact with the polymeric chains because they are surrounded by few solvent molecules and this means that the ions can be moved slowly resulting in a decrease in the ionic conductivity. The addition of the plasticizer is fundamental because it could improve the ionic conductibility of the material. In general, cyclic carbonates have a high dielectric constant required for the efficient transport of lithium ions. Propylene carbonate has a high dielectric constant (64.4 at 25ºC) [24] which means it could increase the number of mobile ions; it could weaken the Colombian forces between anions and cations of the salt because it solubilizes strong electrolytes. It could form the complex [Li^+---*plasticizer*] and reduce the fraction of the [Li^+---*host polymer*] complex with the increasing of the chain's polymer flexibility.

The addition of ethylene carbonate (ε =89.80 at 40°C) [24] to a salt solution of $LiClO_4$ in propylene carbonate could improve the solubility of salt in propylene carbonate [5] because plasticizers have a similar chemical structure, so this means that the associative intermolecular forces developed in the material are similar and have more effect than the singular one.

4.2.4. ATR-FTIR Spectroscopy

4.2.4.1 ATR-FTIR Investigations on pure PMMA, PC, EC and $LiClO_4$

ATR-FTIR spectroscopy is a powerful instrument to confirm the structure of a polymer and to investigate all possible interactions between the electrolyte materials, the host polymer and the plasticizer. All changes in vibrational modes are quantified in terms of shifting the band position and intensity. All there could provide an insight into the interactions of ion-ion and ion-solvent at the molecular level.

In order to investigate the interaction of molecules, the host polymer (PMMA) the pure plasticizers (PC and EC), the pure lithium salt ($LiClO_4$) and also the blends of PMMA:PC and PMMA:PC:EC in the composition of (20:80) % w/w are priory investigated from FTIR. They were used as references to a deeper understanding of all the specific interactions that occurred in the investigated electrolytes.

The FTIR spectrum of pure PMMA powder collected in the spectral range from 500 to 3500 cm^{-1} is shown in Figure 4.2.4.1.1.

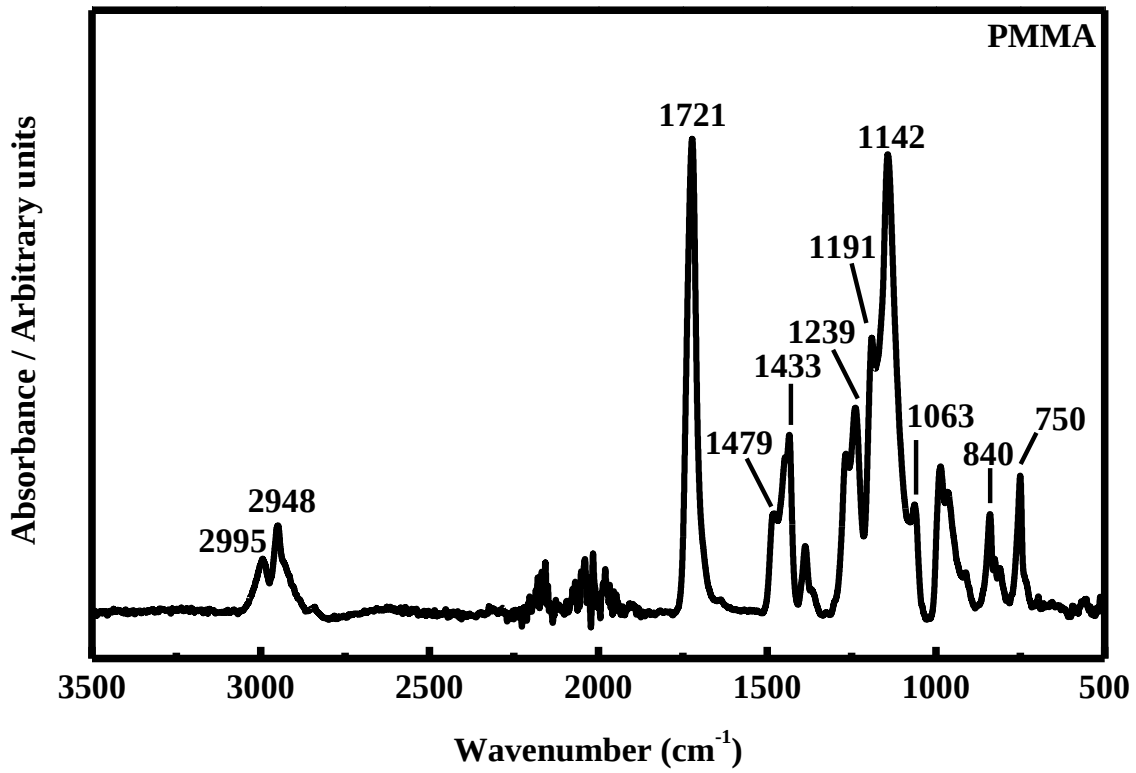

Figure 4.2.4.1.1. Infrared spectra of pure polymethylmethacrylate (PMMA) powder in the range 500-3500 cm^{-1}.

Bands located at 750 cm^{-1} and at 840 cm^{-1} describe the asymmetric and the symmetric rocking of the CH_2 group in PMMA, respectively. The rocking of the α-CH_3 and O-CH_3 bonds are found at 968 cm^{-1} and 987 cm^{-1}, respectively. The stretching of the C-C bond is assigned to the vibrational band located at 1063 cm^{-1}. The two doublets located at 1142 cm^{-1} and 1191 cm^{-1} and at 1239 cm^{-1} and 1266 cm^{-1} correspond to the C-O stretching vibrations of ester groups (υ_4). The symmetric bending of the C-H bond in the α-CH_3 is attributed to the band located at 1387 cm^{-1}. Pure PMMA powder has three bands at 1433 cm^{-1}, 1447 cm^{-1} and 1479 cm^{-1} due to a mixed vibration comprising asymmetric bending of the C-H bond in the C-CH_3/O-CH_3 group and the scissoring of the CH_2 group. The symmetric stretching of the C=O group is located at 1721 cm^{-1}. The two bands at 2948 cm^{-1} and 2995 cm^{-1} can be assigned to the stretching vibration of the C–H bond of the CH_3 group and of CH_2 groups, respectively.

The assignments of main vibrational modes in PMMA are reported in Table 4.2.4.1.1 in accordance with the literature [25-27].

IR Modes of pure PMMA powder	
Wavenumber (cm^{-1})	**Assignments**
750	Asymmetric rocking of CH_2 (skeletal mode)
840	Symmetric rocking of CH_2
968	Rocking of (α-CH_3)
987	Rocking of (O-CH_3)
1063	Stretching of C-C (skeletal mode)
(1142 – 1191)	Stretching of C-O-C
(1239 – 1266)	Stretching of C-O or the C-C-O (ν_4)
1387	Symmetric bending of C-H in (α-CH_3)
1433	Symmetric bending of (C-H) of O-CH_3
1447	Asymmetric bending of (C-H) in (α-CH_3)
1479	Scissoring of CH_2
1721	Symmetric stretching of C=O

IR Modes of pure PMMA powder	
Wavenumber (cm^{-1})	**Assignments**
2948	Symmetric stretching of (C-H) in O-CH_3 + Symmetric Stretching of (C-H) in α-CH_3 + Asymmetric Stretching of CH_2
2995	Asymmetric stretching of (C-H) in O-CH_3 + Asymmetric stretching of (C-H) in α-CH_3

Table 4.2.4.1.1. Observed frequencies in wavenumbers and relative assignments of pure Poly(methylmethacrylate) powder (PMMA).

The spectrum of pure Propylene Carbonate (PC) collected in the spectral range from 500 to 3500 cm^{-1} is illustrated in Figure 4.2.4.1.2.

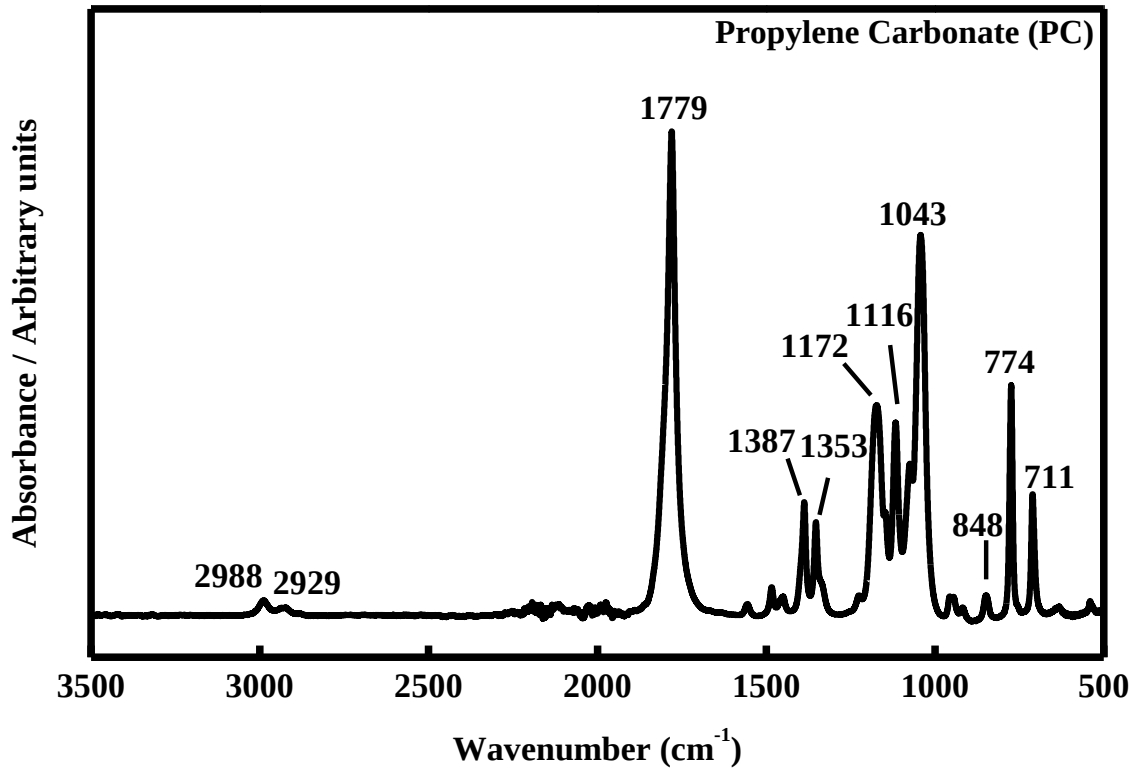

Figure 4.2.4.1.2. Infrared spectra of pure Propylene Carbonate (PC) in the range 500-3500 cm^{-1}.

The local symmetric ring deformation and ring breathing are assigned to the vibrational mode labelled υ_{10} at 711 cm^{-1} while at 774 cm^{-1} the ring deformation is given (υ_{18}). The band located at 848 cm^{-1} is associated with the stretching of the CH_3 group and to the ring breathing mode and they are labelled as υ_9. At 917 cm^{-1} occurs the vibrational band which is assigned to the rocking vibration of the CH_3 group (υ_{32}).

Infrared bands of PC molecules appear as a doublet with peaks located at 948 cm^{-1} (υ_{31}) and 957 cm^{-1} (υ_8) of comparable intensities. The first band describes the rocking vibration of the CH_3 group, while the second band is referred to the ring stretching and to the bending vibration of CH_3 group. The vibrational band at 1043 cm^{-1} is assigned to the C-O ring stretching and is indicated as υ_6 vibrational mode. At 1075 cm^{-1} the asymmetric stretching of the ring labelled as υ_7 is found. The C-H wagging and the C-H bending that are attributed to the vibrational mode υ_{20} are found at 1116 cm^{-1}. The stretching of the C-O bond (υ_5) and the wagging of the C-H bond (υ_5) occured at 1172 cm^{-1}. A strong doublet which describes the symmetric bending of C-H bond (υ_{30}) and the wagging vibrational mode of the C-H bond (υ_{30}) appear at 1353 cm^{-1} and 1387 cm^{-1}, respectively.

The band at 1450 cm^{-1} and 1484 cm^{-1} describe the bending vibration of the C-C-H bond (υ_{30}) and the umbrella vibration of the CH_2 group, respectively. The vibrational stretching located at 1779 cm^{-1} is assigned to the C=O bond of propylene carbonate (υ_1). The C=O stretching band of propylene carbonate appears to be asymmetric as a consequence of the Fermi resonance. In fact, a shoulder located at 1807 cm^{-1} is due to a combination of the bands at 849 cm^{-1} and 957 cm^{-1}, respectively. The symmetric stretching of CH_3 is found at 2988 cm^{-1} (ν_{27}) and 2929 cm^{-1}(ν_{25}), respectively.

The assignments of all vibration modes in PC are reported in Table 4.2.4.1.2 in accordance with the literature [5, 26-30].

IR Modes of pure Propylene Carbonate (PC)		
Wavenumber (cm^{-1})	**Assignments**	**Vibrational Modes**
711	Symmetric ring deformation	ν_{10}
774	Ring deformation	ν_{18}

IR Modes of pure Propylene Carbonate (PC)		
Wavenumber (cm^{-1})	**Assignments**	**Vibrational Modes**
848	Stretching of CH_3 + Ring Stretching (Ring breathing)	ν_9
917	Rocking of CH_3	ν_{32}
948	Rocking of CH_3	ν_{31}
957	Ring Stretching + Bending of CH_3	ν_8
1043	Asymmetric Ring Stretching + Bending of C-H + Twisting of C-C	ν_6
1075	Asymmetric Ring Stretching	ν_7
1116	Wagging of C-H + Bending of C-H	ν_{20}
1172	Stretching of O-C-O + Wagging of C-H	ν_5
1353	Symmetric bending of C-H	ν_{16}
1387	Wagging of C-H + Bending of C-H	ν_{30}
1450	Bending of C-C-H in CH_3	ν_{29}
1484	Umbrella of C-H in CH_3	ν_{15}
1779	Stretching of C=O	ν_1
2929	Symmetric Stretching of C-H	ν_{27}
2988	Asymmetric Stretching of C-H	ν_{25}

Table 4.2.4.1.2. Observed frequencies in wavenumbers and relative assignments of pure Propylene Carbonate (PC).

The spectrum of pure Ethylene Carbonate (EC) collected in the spectral range from 500 to 3500 cm^{-1} is illustrated in Figure 4.2.4.1.3.

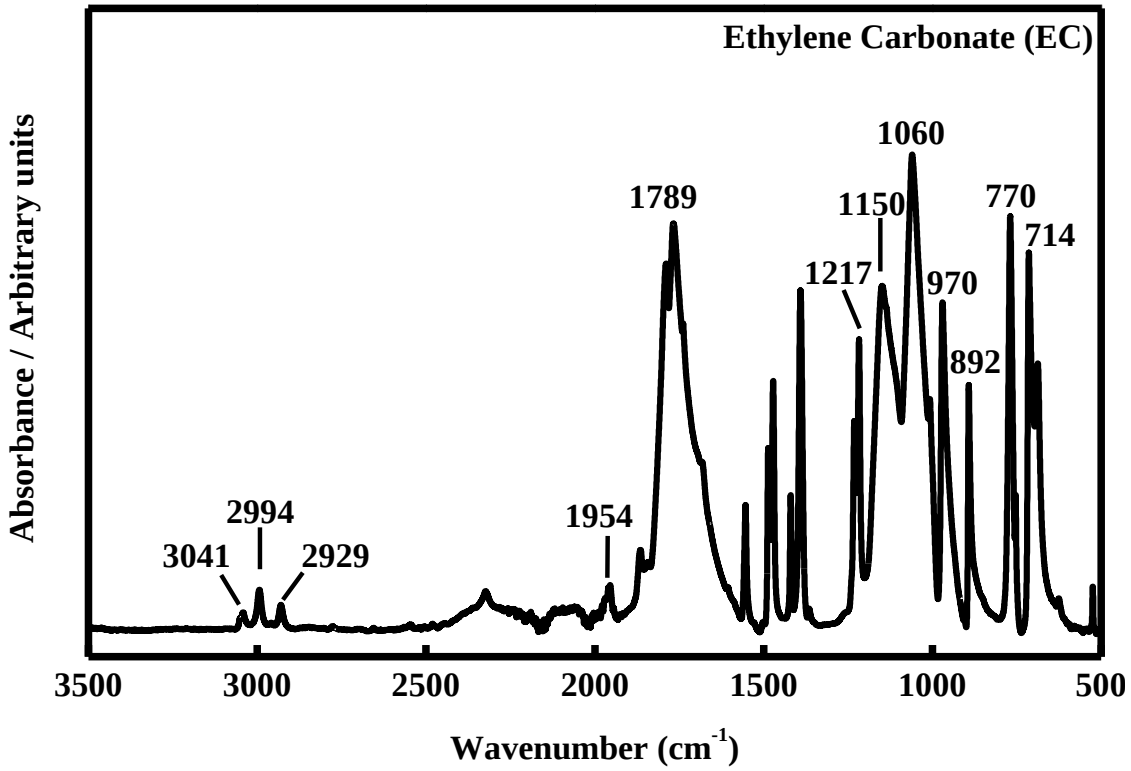

Figure 4.2.4.1.3. Infrared spectra of pure Ethylene Carbonate (EC) in the range 500-3500 cm^{-1}.

The spectrum shows the vibrational stretching also known as the skeletal stretching vibrations at 714 cm^{-1}(υ_8), 892 cm^{-1}(υ_7), 970 cm^{-1} (υ_4) and 1060 cm^{-1}(υ_5) respectively. The vibrations of two adjacent CH_2 groups occur in the different regions of the spectrum: rocking 750-1000 cm^{-1}, twisting 1050-1250 cm^{-1} and wagging 1150-1380 cm^{-1}. At 770 cm^{-1} and 1007 cm^{-1} there are the rocking in-phase and out-of-phase of CH_2 which are also indicated as the vibrational mode labelled υ_{22} and υ_{11}. The bands at 1217 cm^{-1} and 1231 $cm^{-1}$are assigned to the twisting out-of-phase (υ_{21}) and in-phase ($\upsilon_{19} + \upsilon_8$) vibration of CH_2. The out-of-phase wagging vibration of the CH_2 group occurs at 1391 cm^{-1} (υ_4) while the wagging in-phase of the same group is located at 1420 cm^{-1} and it is associated with the vibrational mode υ_{15}. The vibrational mode of the C=O bond is located at 1789 cm^{-1} and it is also indicated as the vibrational mode $2\times\upsilon_7$. The bands at 1553 cm^{-1}, 1682 cm^{-1} and 1954 cm^{-1} are overtones obtained from the combination of the following bands: 770

cm^{-1} ($2\times\upsilon_{22}$), 970 cm^{-1} and 714 cm^{-1} ($\upsilon_4 + \upsilon_8$) and 1060 cm^{-1} and 892 cm^{-1} ($\upsilon_5 + \upsilon_7$). The EC spectrum also shows a characteristic triplet of peaks at 2929 cm^{-1}, 2994 cm^{-1} and 3041 cm^{-1} from the stretching of C-H bonds, associated with the vibrational modes ($\upsilon_{1,}\upsilon_{13}$), υ_{20} and $\upsilon_{21} + \upsilon_3$.

The assignments of all vibration modes of EC and wavenumbers are reported in Table 4.2.4.1.3 according to the literature [28, 31].

IR Modes of pure Ethylene Carbonate (EC)		
Wavenumber (cm^{-1})	**Assignments**	**Vibrational Modes**
714	Ring Bending	ν_8
770	Rocking in-phase of CH_2	ν_{22}
892	Skeletal Ring Breathing	ν_7
970	Symmetric skeletal stretching	ν_4
1007	Rocking out of phase of CH_2	ν_{11}
1060	Symmetric skeletal stretching (ring breathing)	ν_5
1150	Stretching of (C-O) + Wagging of C-H	ν_{10}
1217	Twisting out-of-phase of CH_2	ν_{21}
1231	Twisting in-phase of CH_2	$\nu_{19} + \nu_8$
1391	Wagging out-of-phase of CH_2	ν_4
1420	Wagging in-phase of CH_2	ν_{15}
1486	Bending of CH_2	$\nu_{2,}\nu_{14}$
1553	Overtone of 770 cm^{-1} band	$2\times\nu_{22}$
1682	Overtone of 970 cm^{-1} and 714 cm^{-1} bands	$\nu_4 + \nu_8$

IR Modes of pure Ethylene Carbonate (EC)		
Wavenumber (cm^{-1})	**Assignments**	**Vibrational Modes**
1789	Stretching of C=O	$\nu_2=2\ \nu_7$
1954	Overtone of 1060 $cm^{-1}$and 890 cm^{-1} bands	$\nu_5 + \nu_7$
2929	Symmetric Stretching of C-H	ν_1, ν_{13}
2994	Symmetric Stretching of C-H	ν_{20}
3041	Asymmetric Stretching of C-H	$\nu_{21} + \nu_3$

Table 4.2.4.1.3. Observed frequencies in wavenumbers and relative assignments of pure Ethylene Carbonate (EC).

Figure 4.2.4.1.4 shows the infrared spectrum of pure Lithium perchlorate ($LiClO_4$) powder collected in the spectral range from 500 to 1800 cm^{-1}

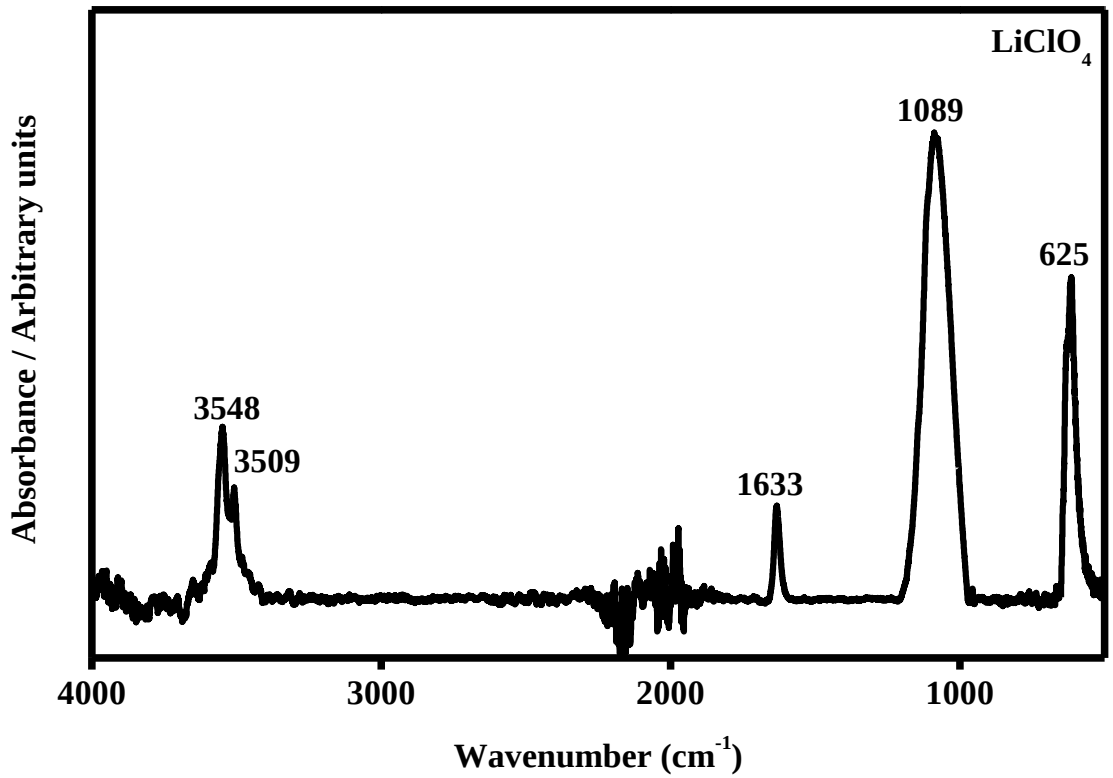

Figure 4.2.4.1.4. Infrared spectra of pure Lithium Perchlorate ($LiClO_4$) in the range 500-1800 cm^{-1}.

The spectrum of pure $LiClO_4$ is characterized by the presence of a band located at 625 cm^{-1} which is assigned to "free" ClO_4^- and a very weak band at 944 cm^{-1} attributed to the ClO_4^- specie. The broadband at 1089 cm^{-1} is associated with the pure $LiClO_4$. The peak at 1633 cm^{-1} is ascribed to the bending of the O-H bond of the water. Also, the bands at 3509 cm^{-1} and 3548 cm^{-1} are assigned to the stretching of O-H bond in the water.

In Table 4.2.4.1.4 are grouped the main vibration assignments and the frequencies $LiClO_4$ in accordance with the literature [28, 32-35].

IR Modes of pure Lithium Perchlorate ($LiClO_4$)		
Wavenumber (cm^{-1})	**Assignments**	**Vibrational Modes**
625	Free ClO_4^-	ν_4
944	ClO_4^-	ν_1

IR Modes of pure Lithium Perchlorate ($LiClO_4$)		
1089	Pure $LiClO_4$	ν_3

Table 4.2.4.1.4. Observed frequencies in wavenumbers and relative assignments of pure Lithium perchlorate ($LiClO_4$).

The infrared spectra of the liquid electrolytes: Li-PC and Li-PC-EC at the different concentrations of $LiClO_4$ (0.1M, 0.5M, 1M, 2M) in the frequency range between 500 cm^{-1} to 2000cm^{-1} are shown in the Figures 4.2.4.1.5 and 4.2.4.1.6, respectively. The spectra put in evidence the main IR modes which have been discussed for the pure PC, EC and $LiClO_4$.

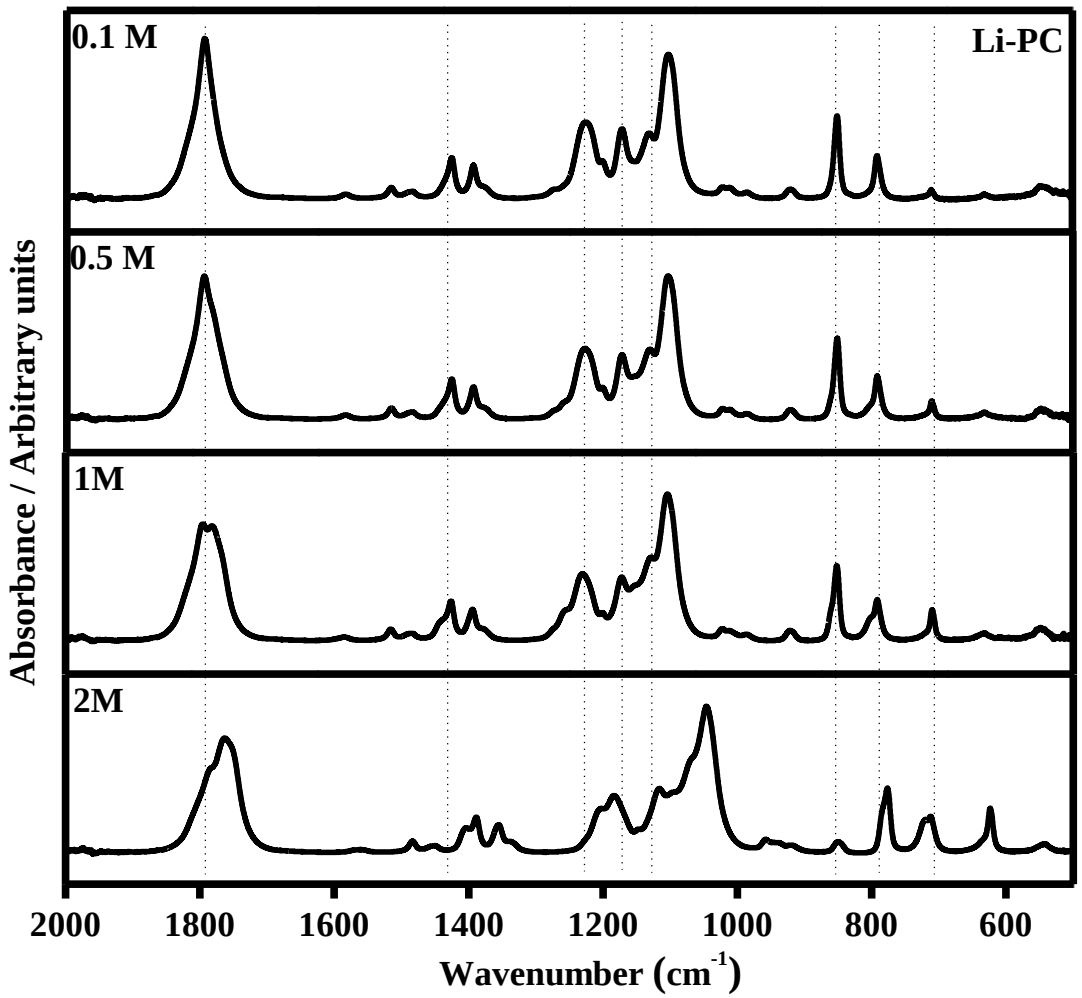

Figure 4.2.4.1.5. FTIR spectra of the liquid electrolyte Li-PC at the different salt concentrations, in the range 500 cm^{-1} 2000 cm^{-1}.

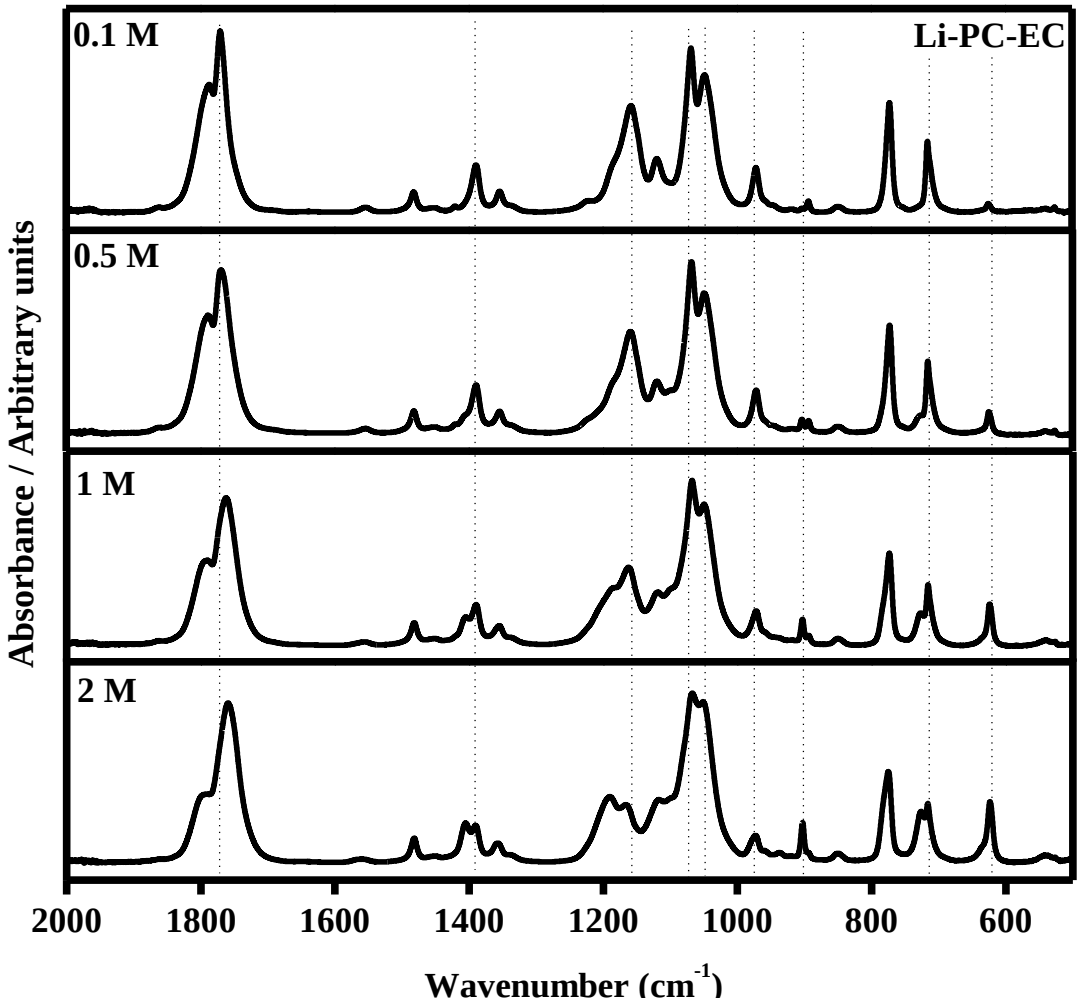

Figure 4.2.4.1.6. FTIR spectra of the liquid electrolyte Li-PC-EC at the different salt concentrations, in the range between 500 cm^{-1} to 2000 cm^{-1}.

The infrared spectra of the gel polymer electrolytes: PMMA-Li-PC and PMMA-Li-PC-EC at the different concentrations of $LiClO_4$ (0.1M, 0.5M, 1M, 2M) in the frequency range between 500 cm^{-1} to 2000 cm^{-1} are shown in the Figures 4.2.4.1.7 and 4.2.4.1.8, respectively.

The spectra put in evidence the main IR modes which have been discussed for the pure PMMA, PC, EC and $LiClO_4$.

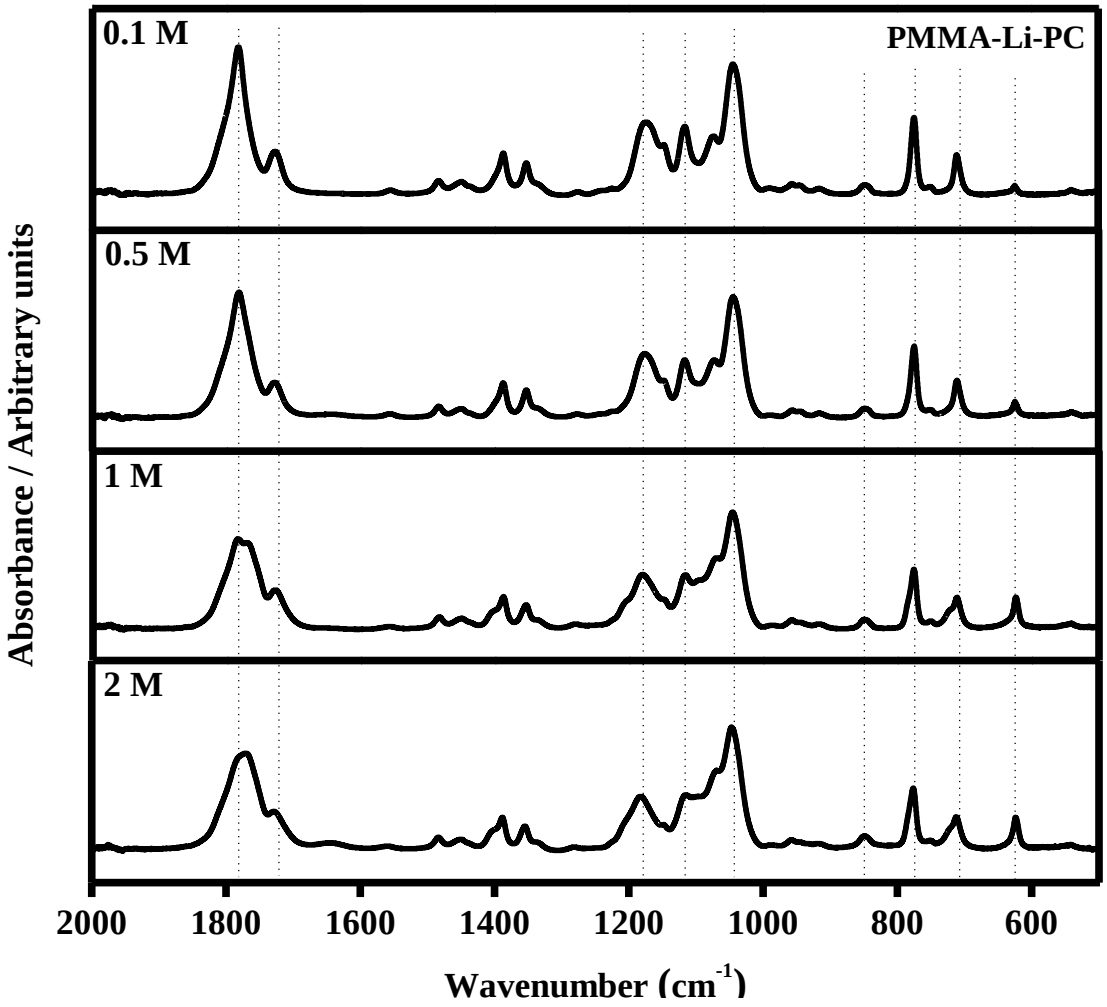

Figure 4.2.4.1.7. FTIR spectra of the gel polymer electrolyte PMMA-Li-PC at the different salt concentrations, in the range between 500 cm^{-1} to 2000 cm^{-1}.

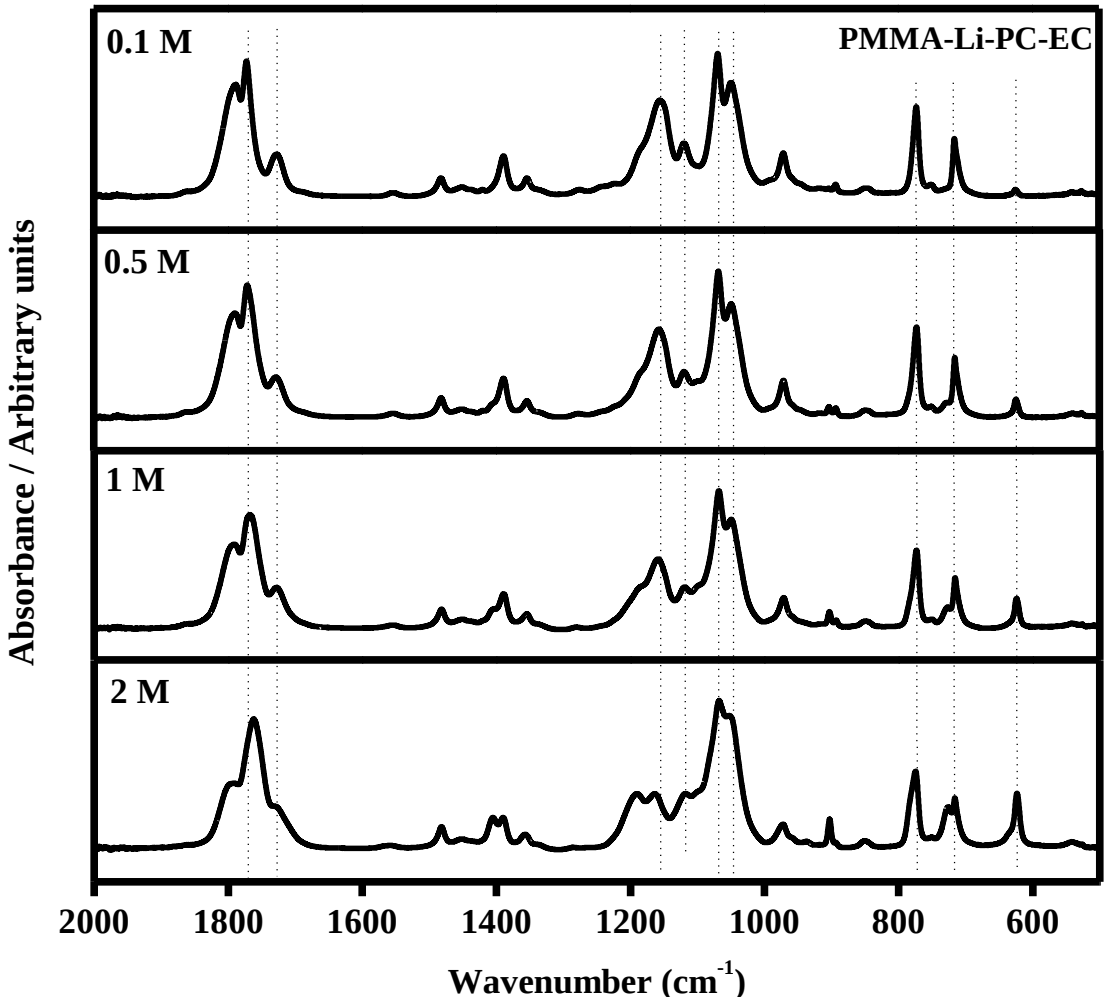

Figure 4.2.4.1.8. FTIR spectra of the gel polymer electrolyte PMMA-Li-PC-EC at the different salt concentrations, in the range between 500 cm^{-1} to 2000 cm^{-1}.

4.2.4.2 ATR-FTIR investigations of interactions and ion associations in liquid electrolytes: Li-PC and Li-PC-EC

ATR-FTIR spectral analyses were made to study the interaction of Li^+ ions with one single plasticizer as propylene carbonate and in a mix of plasticizers based on propylene carbonate and ethylene carbonate (molar ratio 1:1) as a function of the different salt concentrations. It is well-known that the ion-solvent interactions occurred and the IR spectrum clearly exhibits frequency-dependent shifts due to cation association with the plasticizer.

The interactions between the lithium ions and the PC and EC molecules can be seen in the IR spectra because some of the relevant modes appear as bands upshifted in frequency and they are often called satellite bands [11, 12]. To understand the relationship between the satellite bands and the salt concentration, the intensity ratio of the satellite band has been normalized to the total intensity, where the total intensity is defined as the sum of the intensity of the IR band and satellite intensity band. Also, the intensity ratio of the IR band has been normalized to the total intensity.

Propylene carbonate is a polar aprotic solvent with three different sites for electrostatic interaction with lithium cations: two ester-ether oxygen atoms and one carbonyl oxygen atom as available sites. The IR spectra of the liquid electrolyte Li-PC at different salt concentrations (0.1 M, 0.5 M, 1 M, 2 M) is shown in Figure 4.2.4.2.1 The vibrational mode which describes the symmetric ring deformation (ring breathing) of PC molecules is labelled ν_{10} [29] and it is located at 711 cm^{-1} for 0.1 M, 0.5 M and 1M while at 2M it is found at 713 cm^{-1}. Because of the strong interaction between the lithium ions and the PC molecules, a new shoulder appears in the spectra. The new shoulder which is associated with the satellite band (ν_{10}^{*}) is located at 724 cm^{-1} for 0.1M and 0.5M, at 719 cm^{-1} for 1M and at 720 cm^{-1} for 2M, respectively.

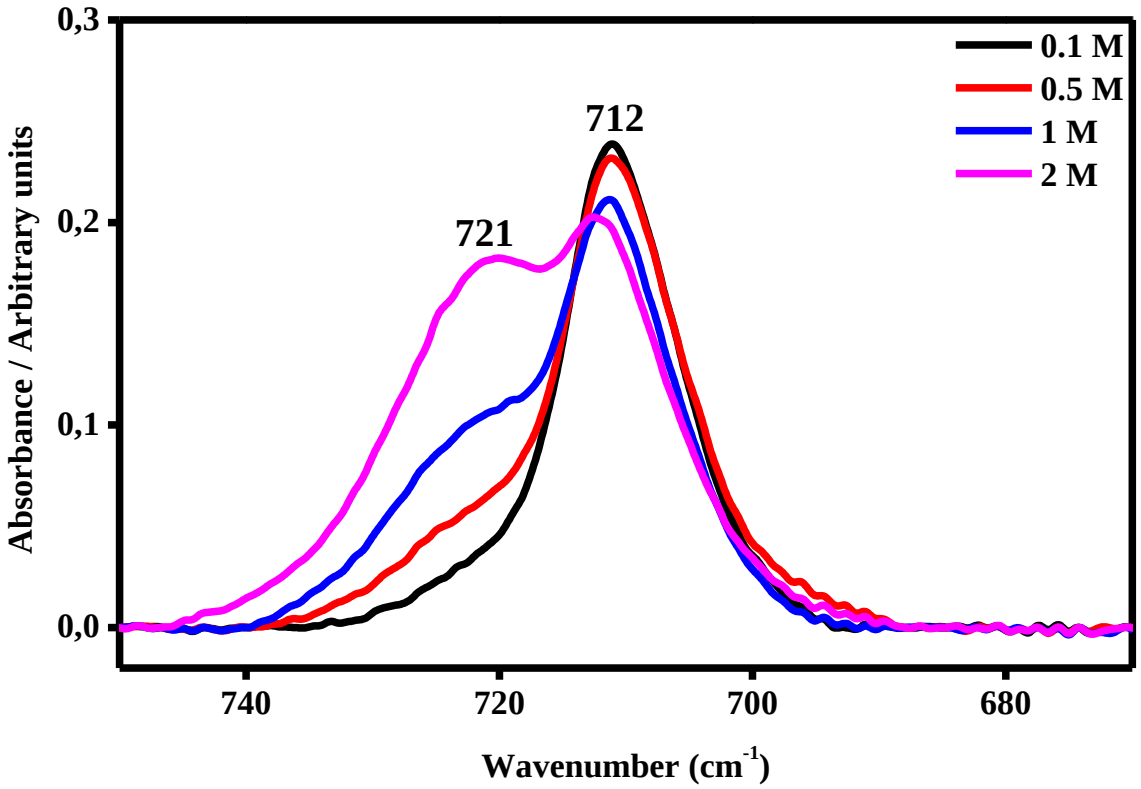

Figure 4.2.4.2.1. The IR mode denominated ν_{10} assigned to the symmetric ring deformation of propylene carbonate (712 cm^{-1}) and its satellite band (ν_{10}^{*}) due to the symmetric ring deformation interaction with lithium ions (722 cm^{-1}) in Li-PC liquid electrolyte at different salt concentrations: 0.1 M, 0.5 M, 1 M and 2 M.

In Figure 4.2.4.2.2 are shown the trends of the relative intensities of the bands ν_{10} and the satellite band ν_{10}^{*} calculated *versus* the salt concentration as the following Equations (4.2.4.2.1-4.2.4.2.2).

$$\frac{Iv_{10}}{Iv_{10} + Iv_{10}^{*}} \qquad (4.2.4.2.1)$$

$$\frac{Iv_{10}^{*}}{Iv_{10} + Iv_{10}^{*}} \qquad (4.2.4.2.2)$$

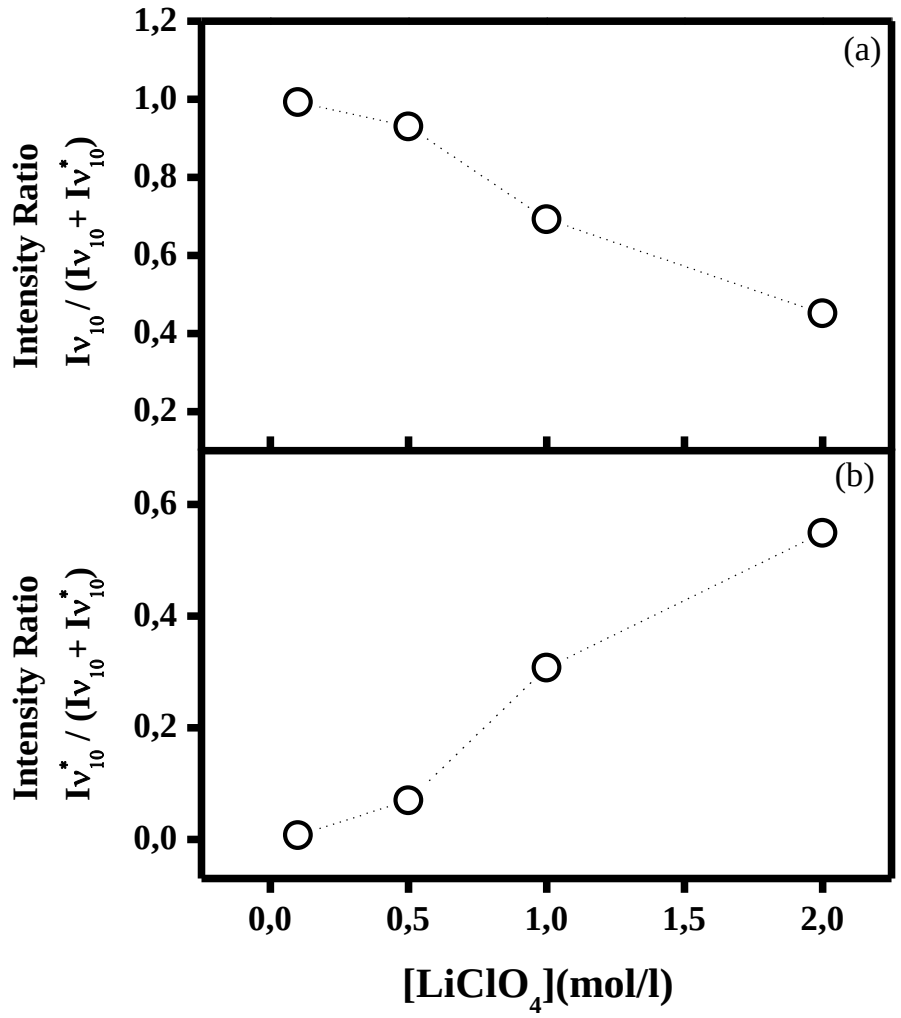

Figure 4.2.4.2.2. Trends of the ratio: (a) $Iv_{10}/\,(Iv_{10} + Iv_{10}^{*})$; (b) $Iv_{10}^{*}/\,(Iv_{10} + Iv_{10}^{*})$; *versus* the salt concentration in Li-PC liquid electrolyte.

The intensity of the ν_{10} band is not $LiClO_4$ concentration-dependent. The intensity of the band ν_{10}^{*} increases as a function of the salt content in the liquid electrolyte because it describes the influence of the lithium ions on the PC molecules as depicted in Figure 4.2.4.2.2.

The effect of the plasticizer's mix in a molar ratio (1:1) on the ion associations in Li-PC-EC liquid electrolyte has also been investigated too. The IR spectra of the liquid electrolyte Li-PC-EC is shown in Figure 4.2.4.2.3. In this case, the combination of the two plasticizers to the lithium cations causes the appearance of a new shoulder (satellite band) at a high frequency that describes the Li^{+}-plasticizers association. The satellite band is related to the sum of the vibrational modes ($\nu^{*}_{8} + \nu^{*}_{10}$) and it is located at 729 cm^{-1} for

0.5 M, at 728 cm^{-1} for 1M, and at 726 cm^{-1} for 2M. The satellite band is directly dependent on the increase of salt content in the liquid electrolyte.

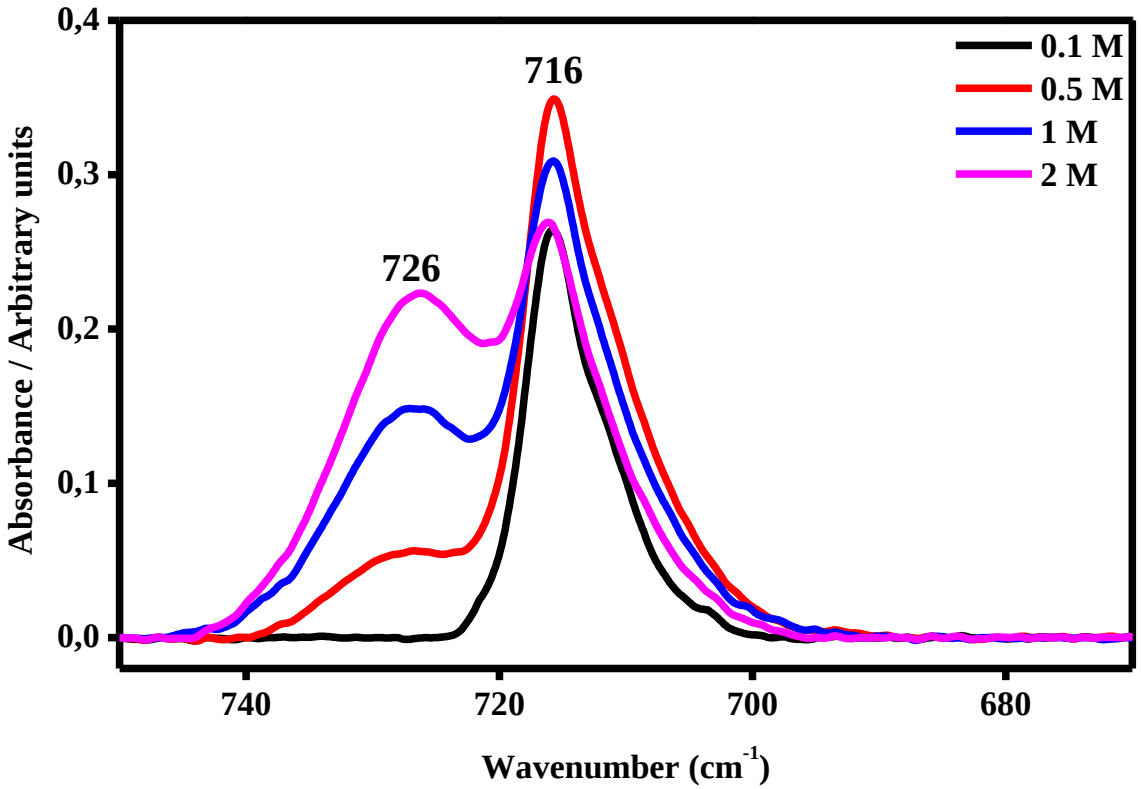

Figure 4.2.4.2.3. The IR band due to the sum of the PC mode denominated ν_{10} and the EC mode denominated ν_8 (716 cm^{-1}) and its satellite band (ν_8^* + ν_{10}^*) due to the interactions between the plasticizers and the lithium ions (727 cm^{-1}) in Li-PC-EC liquid electrolyte at different salt concentrations: 0.1 M, 0.5 M, 1 M and 2 M.

Figure 4.2.4.2.4 shows the trends of the infrared intensity ratio versus the salt concentrations, estimated following the Equations 4.2.4.2.3-4.2.4.2.4.

$$\frac{I\upsilon_8 + I\upsilon_{10}}{(I\upsilon_8 + I\upsilon_{10} + I\upsilon_8^* + I\upsilon_{10}^*)} \qquad (4.2.4.2.3)$$

$$\frac{I\upsilon_8^* + I\upsilon_{10}^*}{(I\upsilon_8 + I\upsilon_{10} + I\upsilon_8^* + I\upsilon_{10}^*)} \qquad (4.2.4.2.4)$$

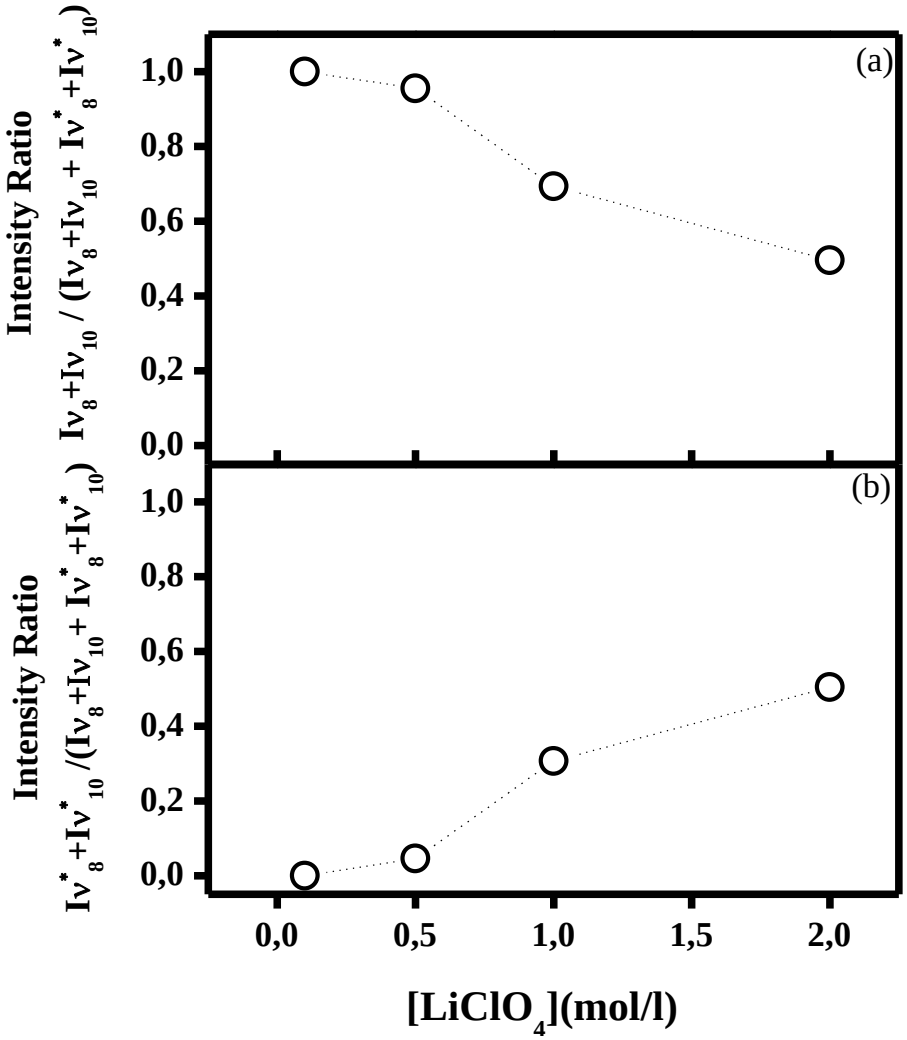

Figure 4.2.4.2.4. Trends of the ratio: (a) $I\upsilon_8 + I\upsilon_{10}/\ (I\upsilon_8 + I\upsilon_{10} + I\upsilon_8^* + I\upsilon_{10}^*)$; (b) $I\upsilon_8^* + I\upsilon_{10}^*/\ (I\upsilon_8 + I\upsilon_{10} + I\upsilon_8^* + I\upsilon_{10}^*)$ *versus* the salt concentration in Li-PC-EC liquid electrolyte.

In Figure 4.2.4.2.4, the first plot (a) confirms a decrease in intensity of the ($\nu_8 + \nu_{10}$) mode in accordance with an increase in the salt concentration. The second plot (b) confirms an increasing intensity for the upshifted band or satellite band ($\nu_8^* + \nu_{10}*$) corresponding to the ion association between the Li^+ cations and the solvent molecules in the liquid electrolyte.

In Figure 4.2.4.2.5 are shown the IR spectra collected on Li-PC liquid electrolytes in the range between 930 cm^{-1} and 1300 cm^{-1}.

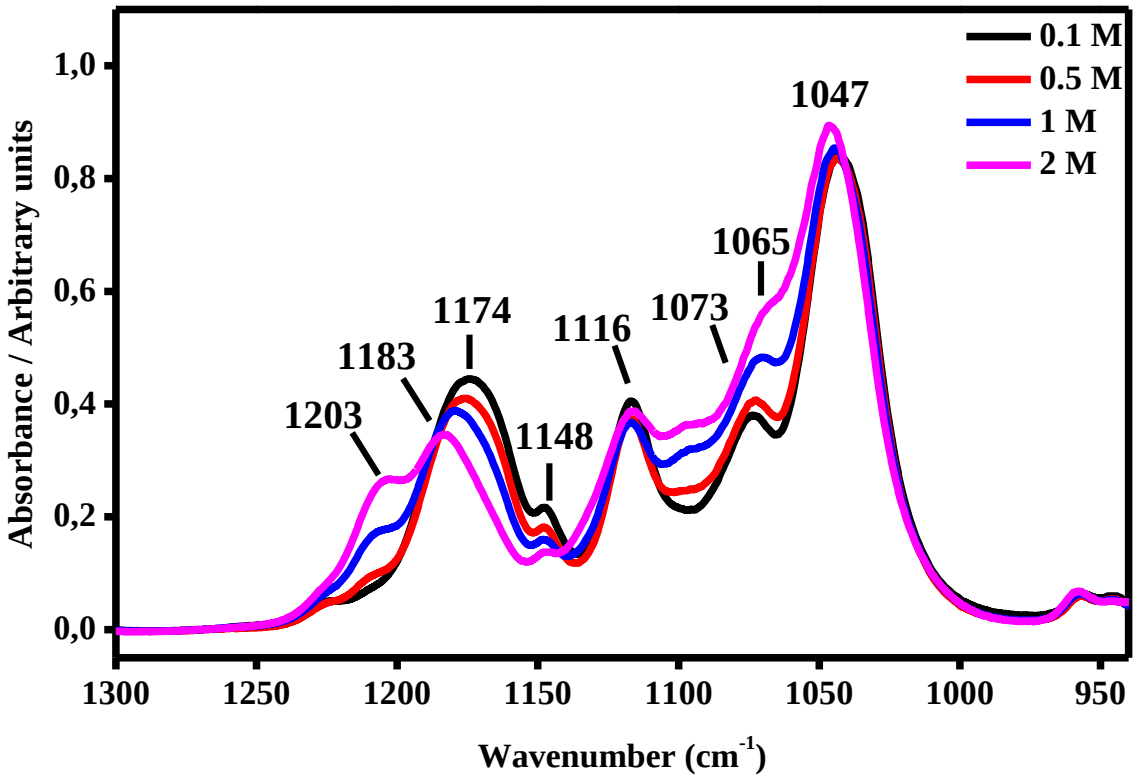

Figure 4.2.4.2.5. The IR spectra in the range between 930 cm^{-1} and 1300 cm^{-1} collected on Li-PC at different salt concentrations: 0.1 M, 0.5 M, 1 M and 2 M.

The region of the O-C-O bond is attributed to the vibrational mode ν_5 and is also influenced by the presence of lithium salt in the Li-PC liquid electrolyte. The stretching of O-C-O bond is found at 1174 cm^{-1} for 0.1M, at 1176 cm^{-1} for 0.5M, at 1179 cm^{-1} for 1M and at 1183 cm^{-1} for 2M [31, 32, 35]. The ring oxygen stretching is located at 1074 $cm^{-1}$for 0.1M, and at 1073 cm^{-1} for 0.5M. It is important to underline that this band is affected by the addition of $LiClO_4$ and a shifting to the lower frequencies has been observed at the highest concentrations. In fact, it is located at 1069 cm^{-1} and at 1065 cm^{-1} in the case of 1 M and 2 M. In addition, a new shoulder at 1206 cm^{-1} for 1M and 1203 cm^{-1} for 2M has been observed.

In Figure 4.2.4.2.6 are shown the IR spectra collected on Li-PC-EC liquid electrolytes in the range between 930 cm^{-1} and 1300 cm^{-1}.

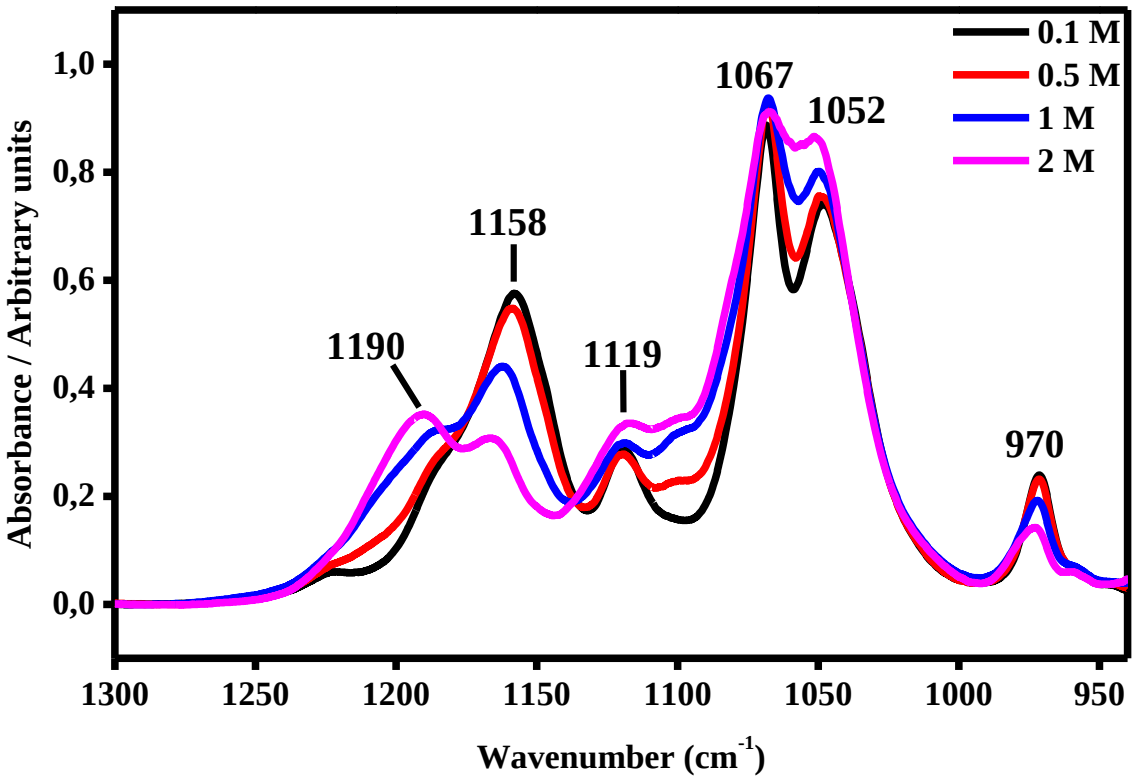

Figure 4.2.4.2.6. The IR spectra in the range between 930 cm^{-1} and 1300 cm^{-1} collected on Li-PC-EC at different salt concentrations: 0.1 M, 0.5 M, 1 M and 2 M.

In the case of the Li-PC-EC, the band located at 970 $cm^{-1}$for all the salt concentrations investigated, is assigned to the vibrational mode υ_4 of the EC molecules. The stretching of the C-O bond and the wagging of the C-H bond are labelled as the vibrational mode ν_{10}. They are also influenced by Li^+ ions concentrations [28, 36]. The ν_{10} band is located at about 1158 cm^{-1} for 0.1M and at 1159 cm^{-1} for 0.5 M, while in the case of the higher concentrations such as 1M and 2M the band is upshifted at the values of 1162 cm^{-1} and 1167 cm^{-1}, respectively. In addition, a new shoulder is found at 1183 cm^{-1} for 0.5M, at 1185 cm^{-1} for 1M and at 1190 cm^{-1} for 2M.

The band at about 1052 cm^{-1} is assigned to the asymmetric O-C-O-O skeletal ring stretching of the plasticizers molecules does not change its intensity.

Other observed bands have been changed in both the relative intensity and the vibrational frequency by the salt concentration in the liquid electrolytes. Figure 4.2.4.2.7 shows the IR spectra of the Li-PC related to the CH_2 wagging spectral region.

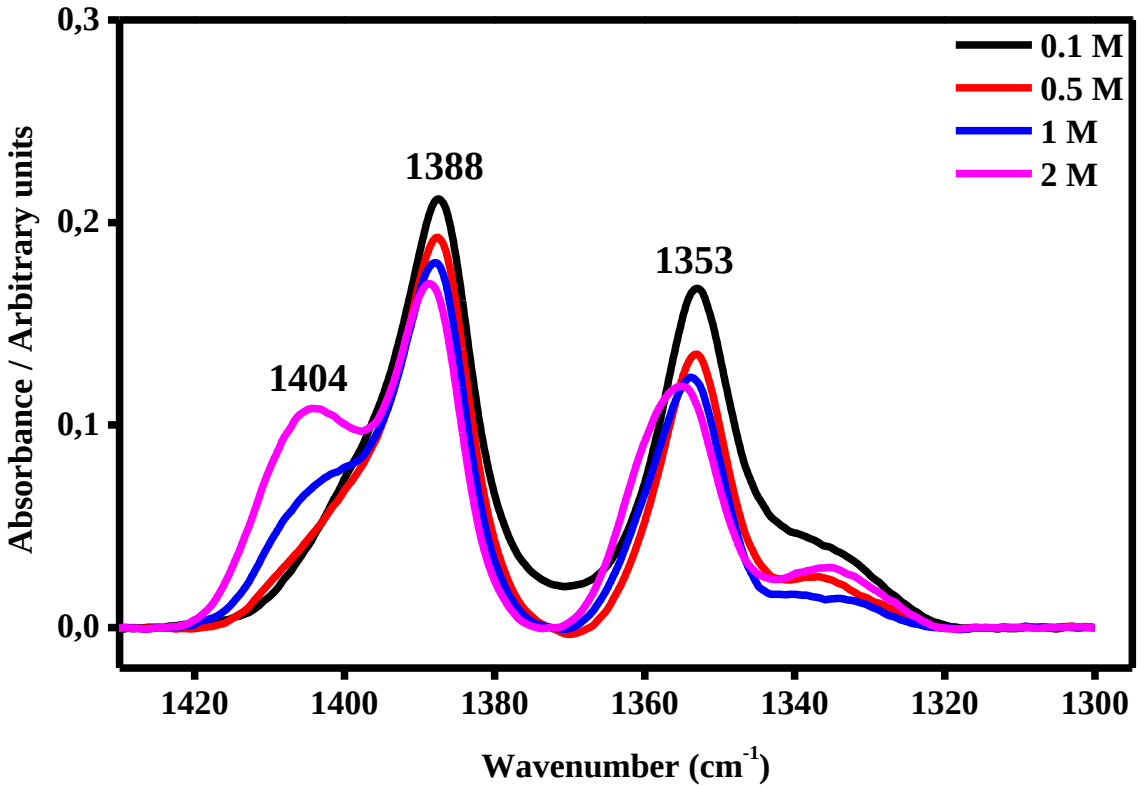

Figure 4.2.4.2.7. The IR band assigned to the CH_2 wagging mode denominated $\nu_{C\text{-}H}$ (1388 cm^{-1}) and its satellite band at $\nu^*_{C\text{-}H}$ (1404 cm^{-1}) in Li-PC liquid electrolyte at different salt concentrations: 0.1 M, 0.5 M, 1 M and 2 M.

The CH_2 wagging deformation mode of the PC molecule is labelled as the vibrational mode $\nu_{C\text{-}H}$ [32]. This vibrational mode is found at 1388 cm^{-1} for 0.1M, at 1387 cm^{-1} for 0.5M, at 1388 cm^{-1} for 1M and at 1389 cm^{-1} for 2M in the Li-PC liquid electrolyte. With the increase in salt concentration, a new shoulder defined by the satellite band assigned to the $\nu^*_{C\text{-}H}$ mode became more evident and it defines the influence of Li^+ cations on PC molecules. The satellite band occurs at 1404 cm^{-1} for both 1M and 2 M.

Figure 4.2.4.2.8 shows the trends of the infrared intensity ratio *versus* the salt concentrations, estimated in accordance with the following Equations 4.2.4.2.5-4.2.4.2.6.

$$\frac{Iv_{C-H}}{Iv_{C-H} + Iv^*_{C-H}} \qquad (4.2.4.2.5)$$

$$\frac{Iv^*_{C-H}}{Iv_{C-H} + Iv^*_{C-H}} \qquad (4.2.4.2.6)$$

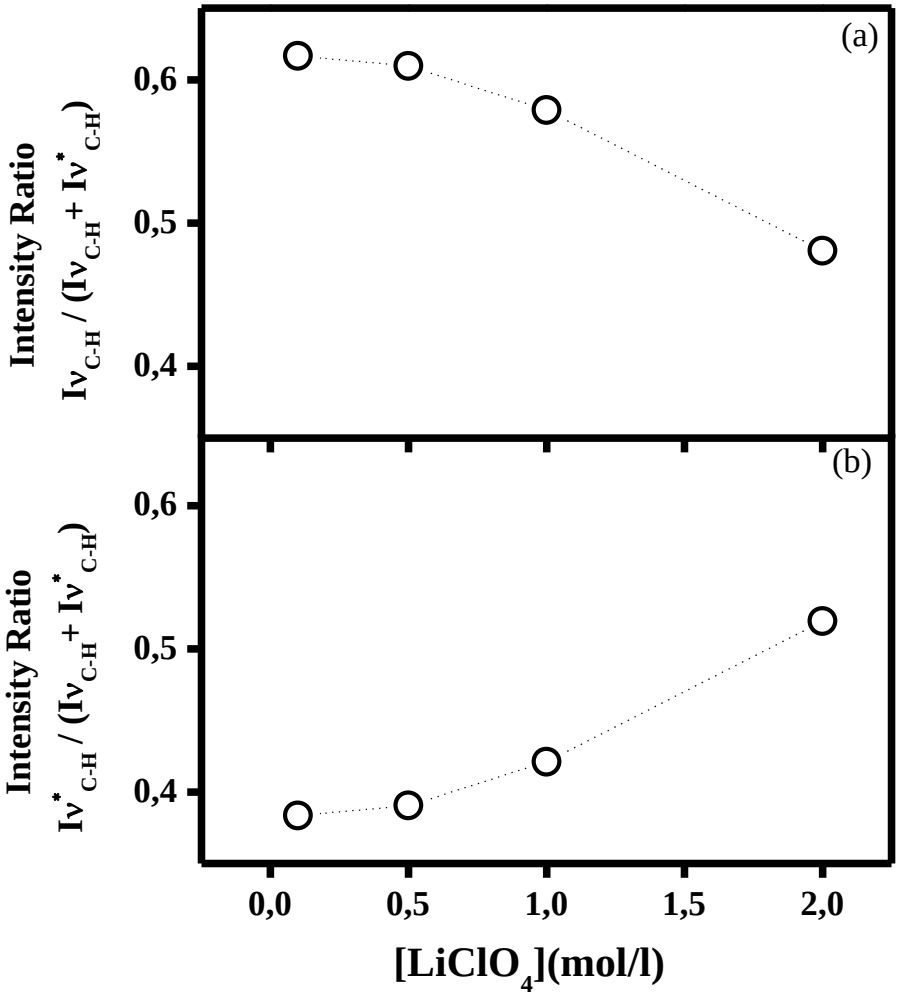

Figure 4.2.4.2.8. Trends of the ratio: (a) $Iv_{C-H}/\ (Iv_{C-H} + Iv^*_{C-H})$; (b) $Iv^*_{C-H}/\ (Iv_{C-H} + Iv^*_{C-H})$ *versus* the salt concentration in Li-PC liquid electrolyte.

The relative integrated intensity of the vibrational mode $\nu_{C\text{-}H}$ decrease with the increase of the concentration of lithium cations in solution. The association that is established between the lithium cations and the ring of the propylene carbonate referred to as the vibrational mode $\nu^*_{C\text{-}H}$ is clearly $LiClO_4$ concentration-dependent and it increases when the salt content increases.

The infrared spectra associated with the wagging of the CH_2 in the mix of plasticizers are shown in Figure 4.2.4.2.9.

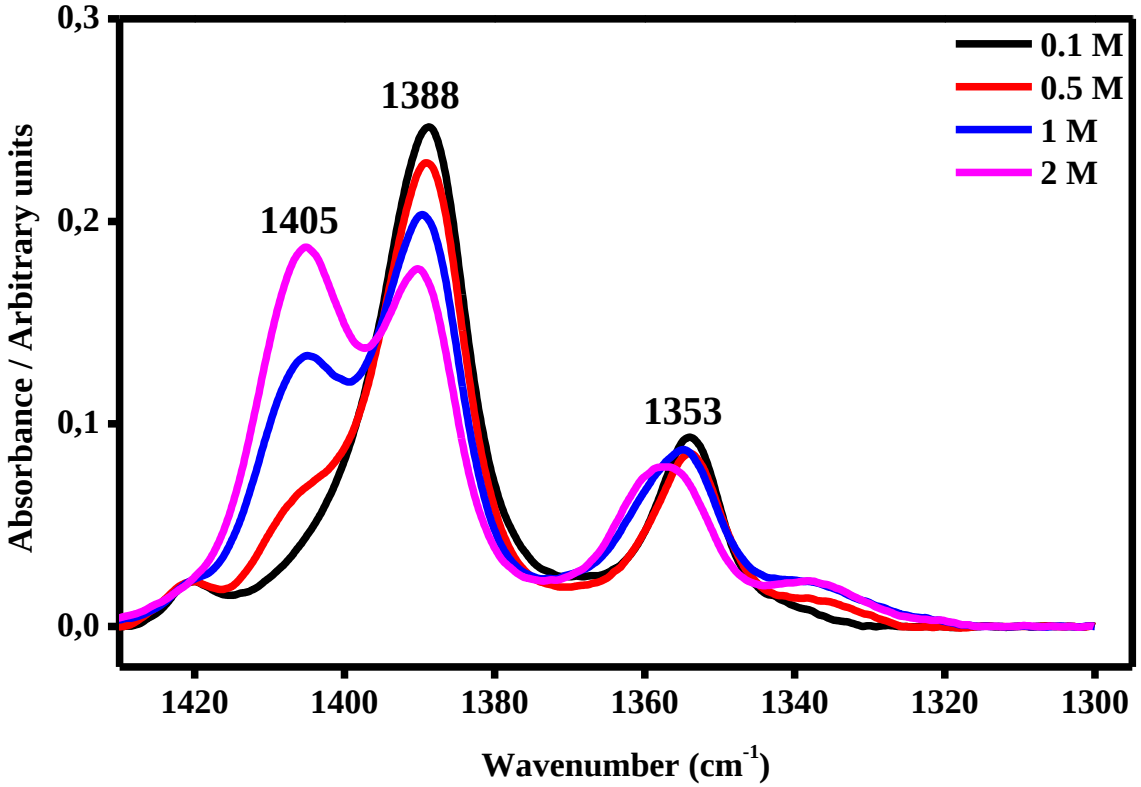

Figure 4.2.4.2.9. The IR band assigned to the CH_2 wagging mode denominated $\nu_{C\text{-}H}$ (1388 cm^{-1}) and its satellite band at $\nu_{C\text{-}H}^{*}$ (~1405 cm^{-1}) in Li-PC-EC liquid electrolyte at different salt concentrations: 0.1 M, 0.5 M, 1 M and 2 M.

In the case of the Li-PC-EC liquid electrolyte, the two CH_2 wagging modes are affected by the lithium salt concentration. The mode $\nu_{C\text{-}H}$ describes the vibrational wagging of the CH_2, while the mode $\nu^{*}_{C\text{-}H}$ represents the satellite band which takes into account the influence of the lithium cations on the PC:EC mix. The mode $\nu_{C\text{-}H}$ is located at 1388 cm^{-1} for all the investigated concentrations. Furthermore, we can observe that with the increasing $LiClO_4$ content in the mix of propylene and ethylene carbonate, the wagging frequency is supported by the existence of a new shoulder which appears at 1404 cm^{-1} for 0.5M and at 1405 cm^{-1} for 1M and 2M, respectively.

The relative integrated intensities of the modes $\nu_{C\text{-}H}$ and $\nu^{*}_{C\text{-}H}$ are estimated in accordance with the Equations 4.2.4.2.7-4.2.4.2.8.as following:

$$\frac{Iv_{C-H}}{Iv_{C-H} + Iv^{*}_{C-H}} \qquad (4.2.4.2.7)$$

$$\frac{Iv^{*}_{C-H}}{Iv_{C-H} + Iv^{*}_{C-H}} \qquad (4.2.4.2.8)$$

The trends of the relationship between the relative integrated intensities and the salt concentration are shown in Figure 4.2.4.2.10.

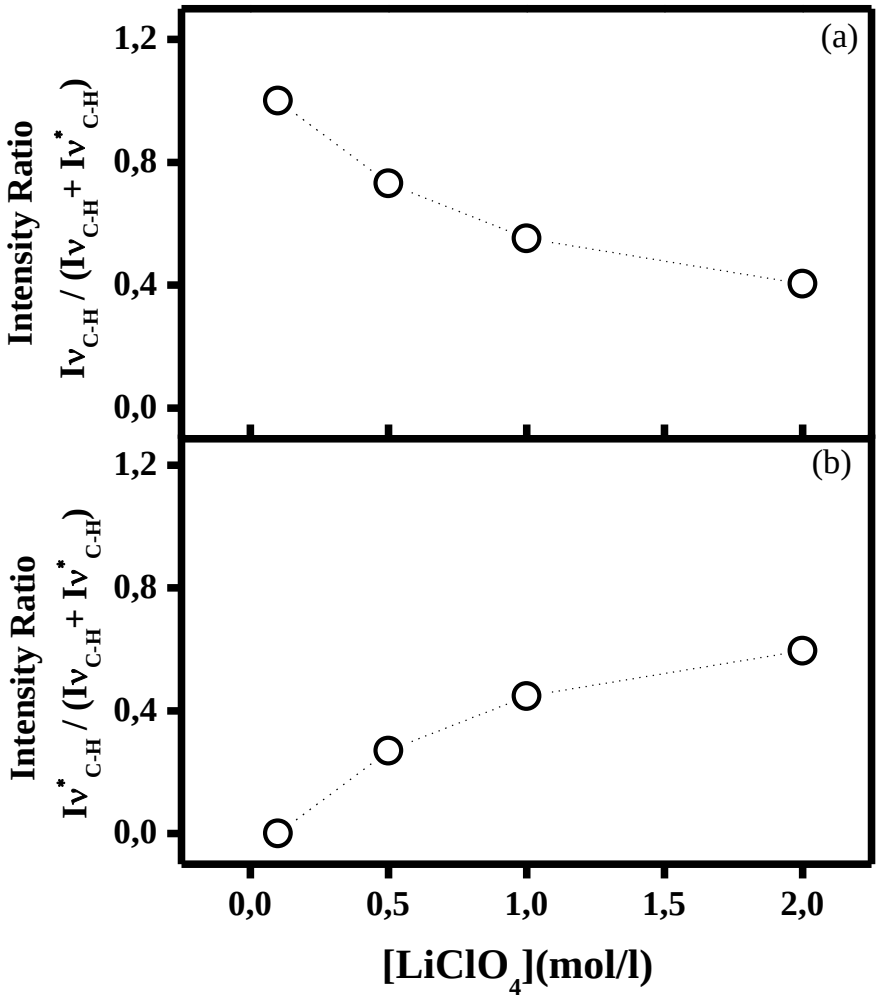

Figure 4.2.4.2.10. Trends of the ratio: (a) $Iv_{C-H}/\,(Iv_{C-H} + Iv^{*}_{C-H})$; (b) $Iv^{*}_{C-H}/\,(Iv_{C-H} + Iv^{*}_{C-H})$ *versus* the salt concentration in Li-PC-EC liquid electrolyte.

We can deduce that the $\nu_{C\text{-}H}$ mode is not dependent on the $LiClO_4$ content in the liquid electrolyte and its integrated intensity decrease when the salt content increases. On the contrary, the $\nu^{*}_{C\text{-}H}$ mode (satellite band) which describes the influence of the Li^{+} cations on EC molecules, is influenced by the increasing of the salt concentration.

The C=O symmetric stretching band has been investigated in Li-PC liquid electrolyte and the infrared spectra is shown in Figure 4.2.4.2.11.

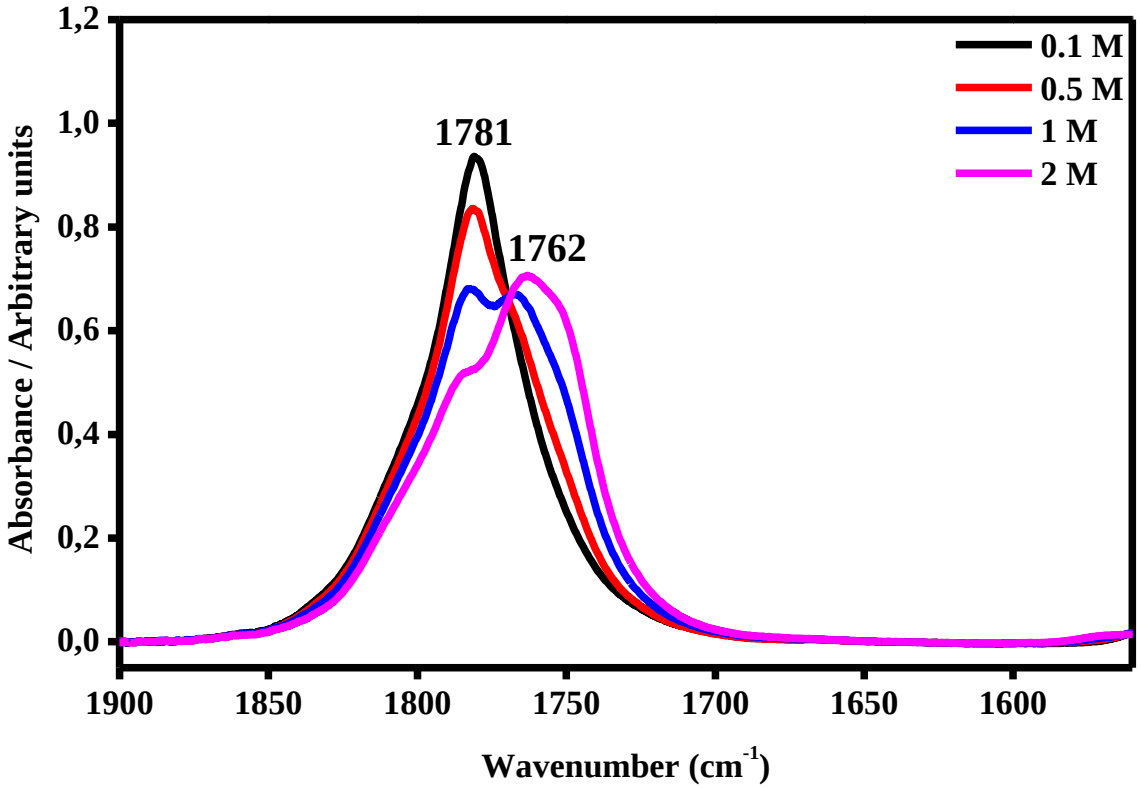

Figure 4.2.4.2.11. The IR band assigned to the C=O mode of free propylene carbonate denominated $\nu_{C=O}$ (~1781 cm^{-1}) and its satellite band at $\nu_{C=O}^{*}$ (~1762 cm^{-1}) in Li-PC liquid electrolyte at different salt concentrations: 0.1 M, 0.5 M, 1 M, and 2 M.

In Li-PC liquid electrolyte, the carbonyl stretching of the free propylene carbonate is indicated as the vibrational mode $\nu_{C=O}$ and it is found at 1781 cm^{-1} for all the investigated salt concentrations. At the higher concentrations, the interaction with lithium ions causes a downshift of the PC's band, with the consequent observation of the satellite band labeled as $\nu^{*}_{C=O}$ which is located at 1767 cm^{-1} for 1 M and at 1762 cm^{-1} for 2 M.

In Figure 4.2.4.2.12 are shown the trends of the relative intensities of the bands $\nu_{C=O}$ and $\nu^{*}_{C=O}$ calculated *versus* the salt concentration as the following Equations (4.2.4.2.9-4.2.4.2.10).

$$\frac{Iv_{C=O}}{Iv_{C=O} + Iv^{*}_{C=O}} \qquad (4.2.4.2.9)$$

$$\frac{Iv^{*}_{C=O}}{Iv_{C=O} + Iv^{*}_{C=O}} \qquad (4.2.4.2.10)$$

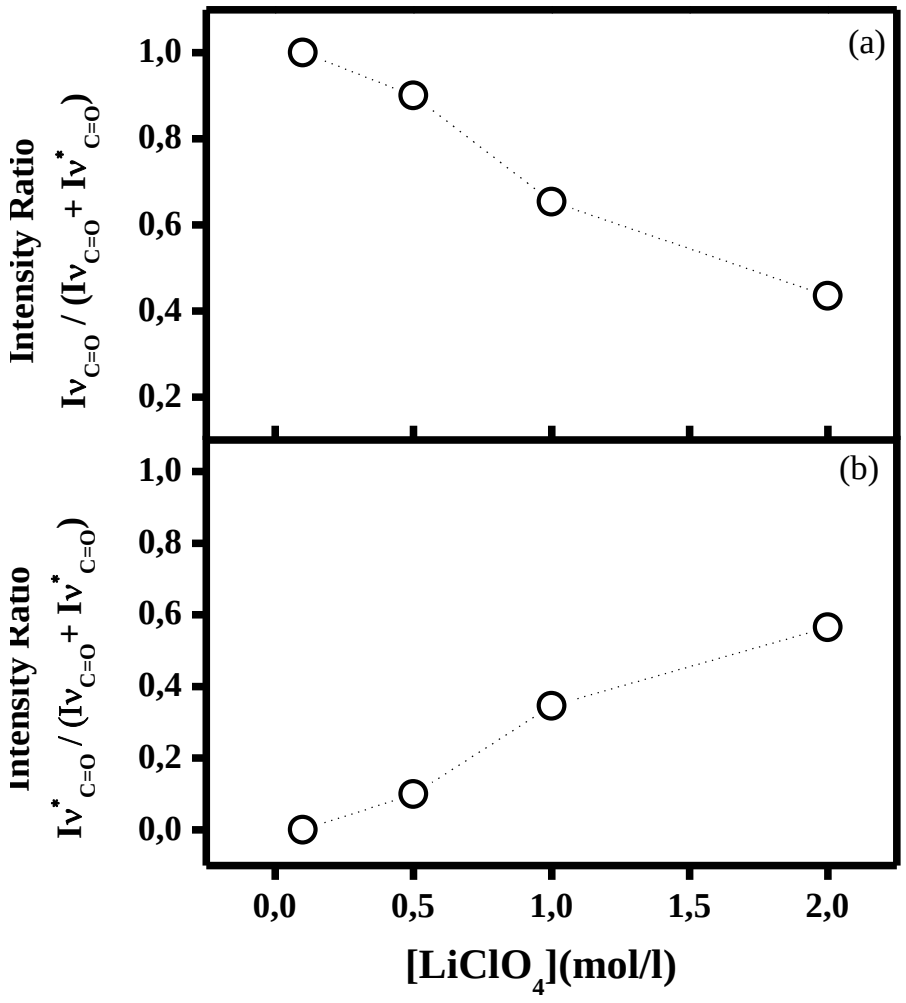

Figure 4.2.4.2.12. Trends of the ratio: (a) $Iv_{C=O} / (Iv_{C=O} + Iv^{*}_{C=O})$; (b) $Iv^{*}_{C=O} / (Iv_{C=O} + Iv^{*}_{C=O})$ *versus* the salt concentration in Li-PC liquid electrolyte.

The intensity of the band $\nu_{C=O}$ decreases when the $LiClO_4$ content in the liquid electrolyte increases. The intensity of the band $\nu^{*}_{C=O}$ which describes the ion association between the lithium cations and the C=O bond of the carbonate ester of the propylene carbonate, can increase as a function of the salt content in the liquid electrolyte.

The infrared spectra of Li-PC-EC are shown in Figure 4.2.4.2.13.

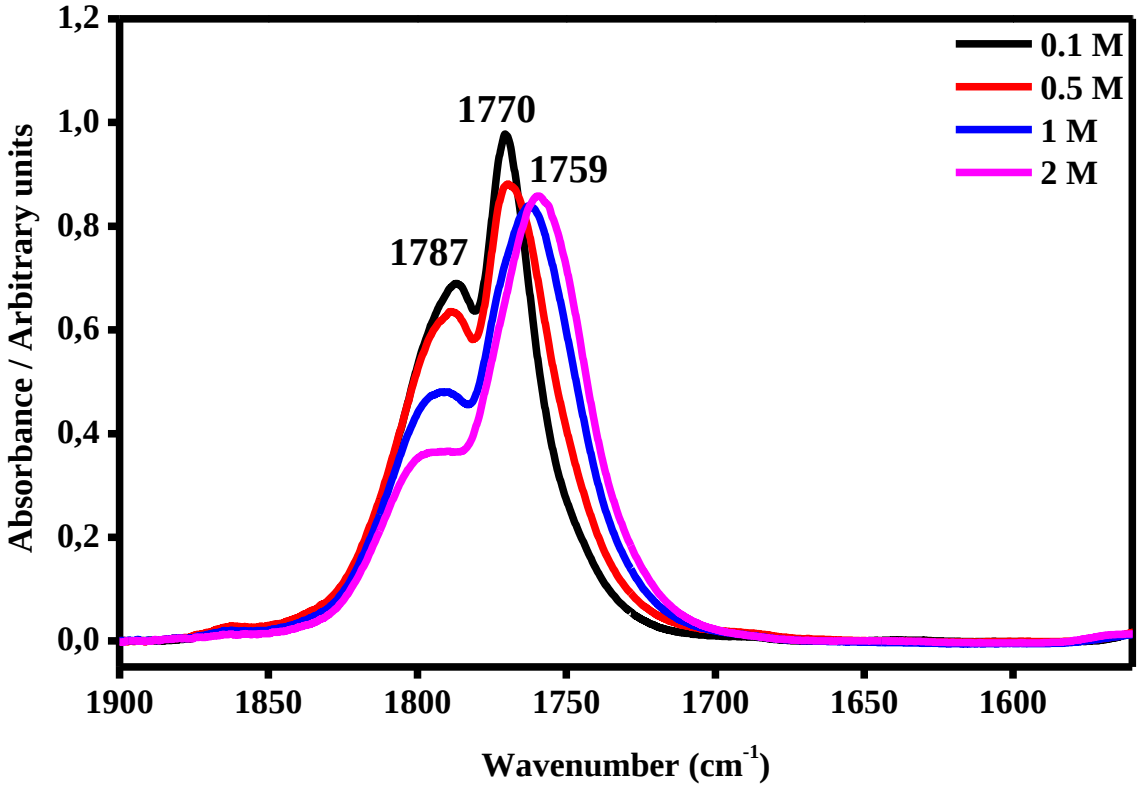

Figure 4.2.4.2.13. The IR band assigned to the C=O mode of free EC and PC carbonate denominated $\nu_{C=O}$ (~1787 cm^{-1}) and its satellite band at $\nu_{C=O}^{*}$ (~1770 cm^{-1} and ~1759 cm^{-1}) in Li-PC-EC liquid electrolyte at different salt concentrations: 0.1 M, 0.5 M, 1 M, and 2 M.

In this case, "free" C=O of both plasticizers is assigned to the vibrational mode labeled $\nu_{C=O}$ and it is found at 1787 cm^{-1} for 0.1M, at 1788 cm^{-1} for 0.5 M, at 1791 cm^{-1} for 1M and at 1792 cm^{-1} for 2 M. A result of the lithium associations to the PC and EC molecules, new satellite bands are found in the spectra. The satellite band is associated with the vibrational mode labeled $\nu^{*}_{C=O}$ and they are found at 1770 cm^{-1} for 0.1 M and at 1768 cm^{-1} for 0.5 M. Then at the higher concentrations, the satellite band is downshifted at 1761 cm^{-1} for 1 M and 1759 cm^{-1} at 2M.

In Figure 4.2.4.2.14 are shown the trends of the relative intensities of the bands $\nu_{C=O}$ and $\nu^{*}_{C=O}$ calculated *versus* the salt concentration as the following Equations (4.2.4.2.11-4.2.4.2.12).

$$\frac{Iv_{C=O}}{(Iv_{C=O} + Iv^{*}_{C=O})} \quad (4.2.4.2.11)$$

$$\frac{Iv^{*}_{C=O}}{(Iv_{C=O} + Iv^{*}_{C=O})} \quad (4.2.4.2.12)$$

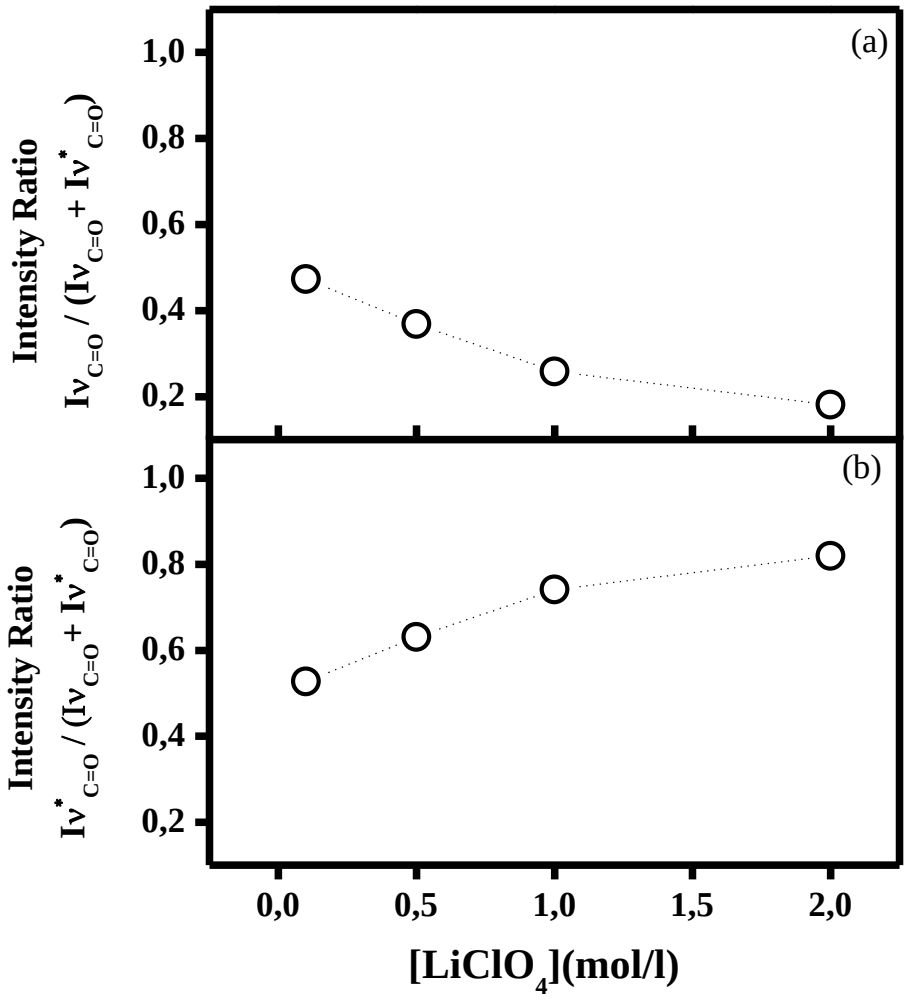

Figure 4.2.4.2.14. Trends of the ratio: (a) $Iv_{C=O}/\,(Iv_{C=O} + Iv^{*}_{C=O})$; (b) $Iv^{*}_{C=O}/\,(Iv_{C=O} + Iv^{*}_{C=O})$ *versus* the salt concentration Li-PC-EC liquid electrolyte.

The intensity of the band which is associated with the $\nu_{C=O}$ decreases when the $LiClO_4$ content in the liquid electrolyte increases, while the intensity of the band labelled as $\nu^{*}_{C=O}$ can be related to the phenomena of ion association between the lithium cations and the

C=O portion of the plasticizers. The intensity of $\nu^*_{C=O}$ band increases as a function of the salt content in the liquid electrolyte.

For the liquid electrolyte based on Li-PC-EC there is another band that is influenced by the salt concentration and the relative infrared spectra are shown in Figure 4.2.4.2.15.

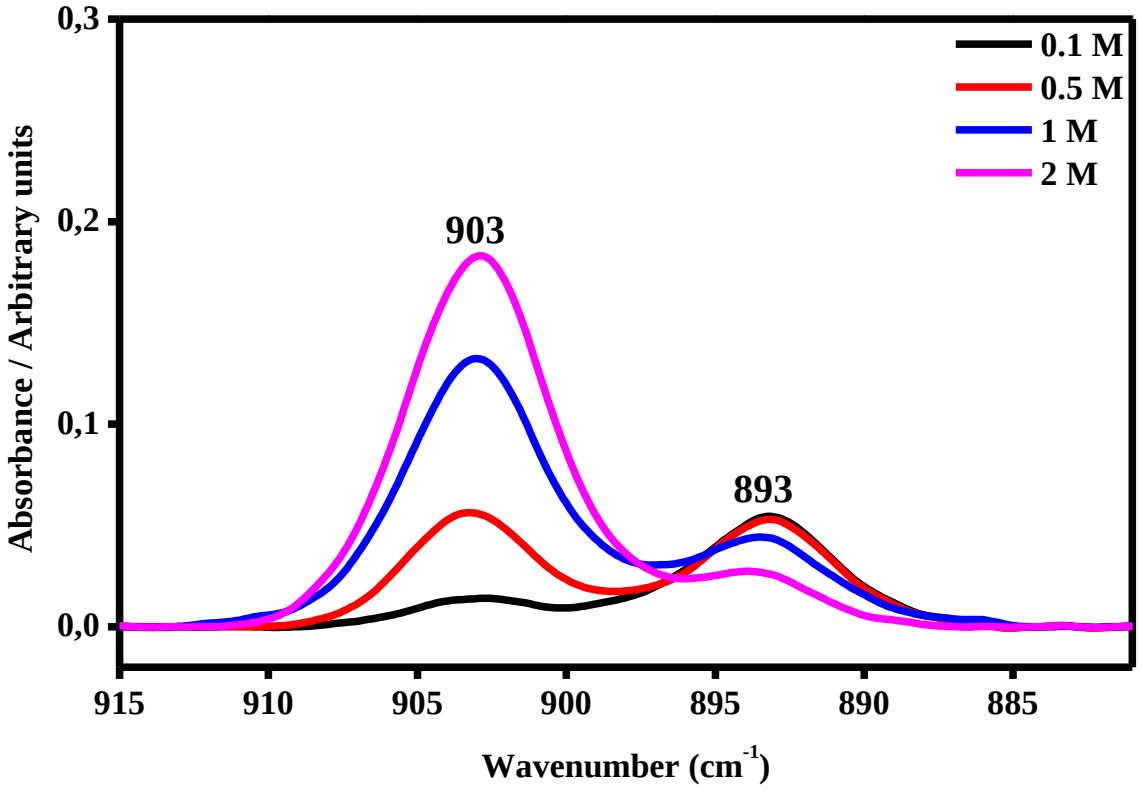

Figure 4.2.4.2.15. The IR band assigned to the skeletal ring breathing mode ν_7 (~893 cm^{-1}) of ethylene carbonate molecules and its satellite band at ν_7^* (~903 cm^{-1}) in Li-PC-EC liquid polymer electrolyte at different salt concentrations: 0.1 M, 0.5 M, 1 M and 2 M.

The band at 893 cm^{-1} is associated with ν_7 mode of the EC molecule and it describes the ring breathing vibration mode of the ethylene carbonate molecules [28, 31, 35, 36]. This band is not salt concentration-dependent. The Li^+ interaction with EC molecules by the ring-breathing mode is observed at the satellite band located at 903 cm^{-1} (ν_7^*) [31] and its intensity depends on the increase of the salt concentration.

In Figure 4.2.4.2.16 are shown the trends of the relative intensities of the bands ν_7 and ν_7^* calculated versus the salt concentration as the following Equations (4.2.4.2.13-4.2.4.2.14).

$$\frac{I\upsilon_7}{I\upsilon_7 + I\upsilon_7^*} \qquad (4.2.4.2.13)$$

$$\frac{I\upsilon_7^*}{I\upsilon_7 + I\upsilon_7^*} \qquad (4.2.4.2.14)$$

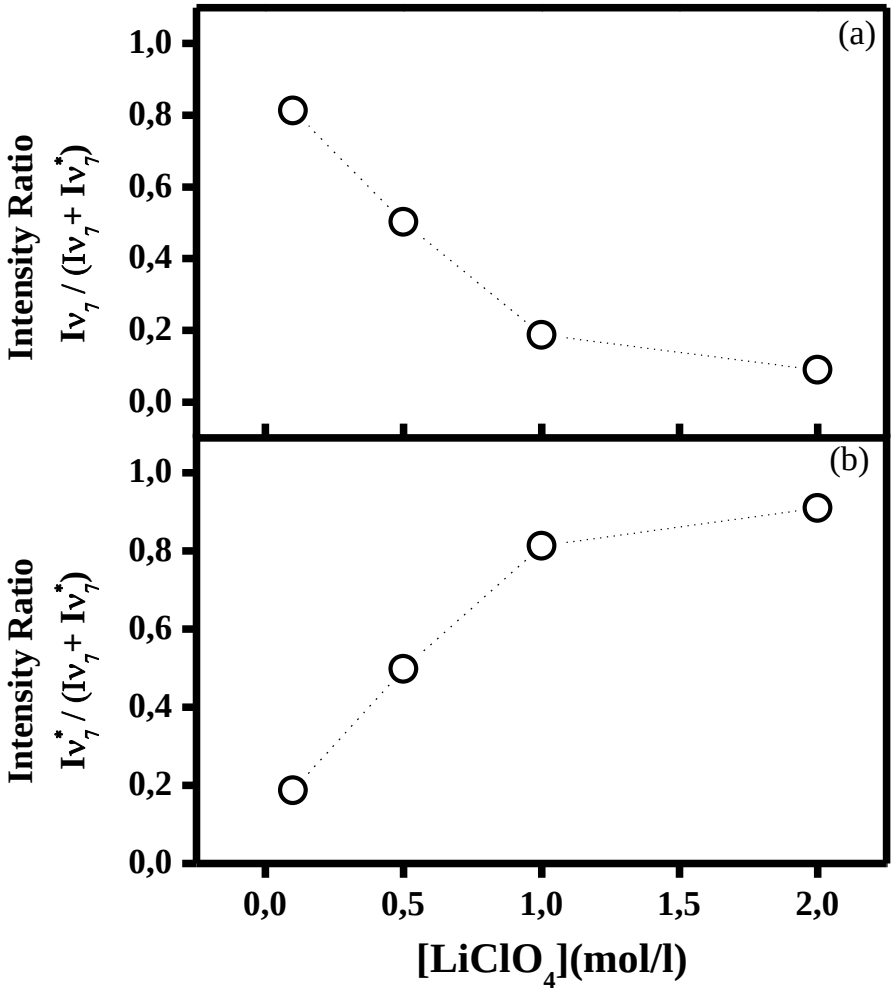

Figure 4.2.4.2.16. Trends of the ratio: (a) $I\upsilon_7/\ (I\upsilon_7 + I\upsilon_7^*)$; (b) $I\upsilon_7^*/\ (I\upsilon_7 + I\upsilon_7^*)$ *versus* the salt concentration Li-PC-EC liquid electrolyte.

Figure 4.2.4.2.16 shows that the intensity of the ν_7^* band increases with increasing $LiClO_4$ concentration because of the cation solvation between the lithium ions and the EC molecules, while the intensity of the ν_7 peak band is decreases.

4.2.4.3 ATR-FTIR investigations of interactions and ion associations in gel polymer electrolytes: PMMA-Li-PC and PMMA-Li-PC-EC

The Infrared spectra of gel polymer electrolytes of composition (20:80) % w/w PMMA-Li-PC and PMMA-Li-PC-EC containing various concentrations of $LiClO_4$ have been measured and analyzed to identify the ion associations in the gelled electrolytes.

The infrared spectra relative to the spectral region of the symmetric ring deformation of the PC in the PMMA-Li-PC are shown in Figure 4.2.4.3.1.

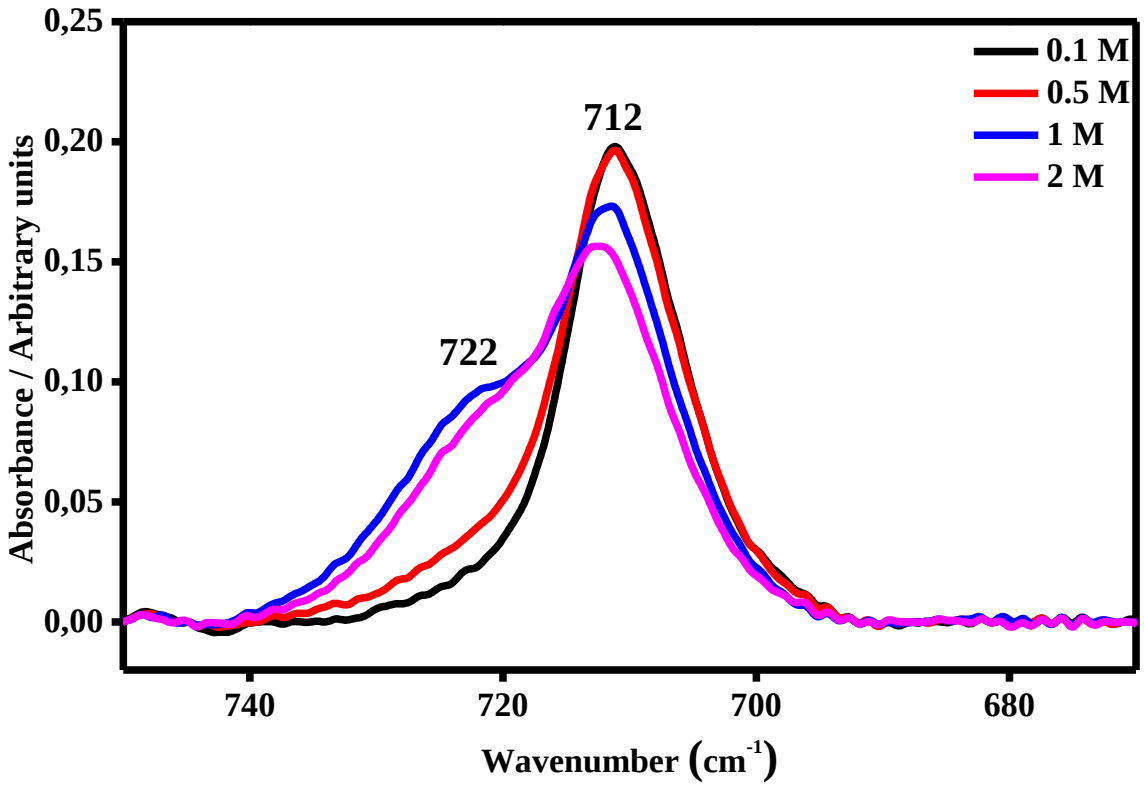

Figure 4.2.4.3.1. The IR mode denominated ν_{10} assigned to the symmetric ring deformation of propylene carbonate (712 cm^{-1}) and its satellite band (ν_{10}^{*}) due to the symmetric ring deformation interaction with lithium ions (722 cm^{-1}) in PMMA-Li-PC gel polymer electrolyte at different salt concentrations: 0.1 M, 0.5 M, 1 M and 2 M.

The symmetric ring deformation is labelled as the ν_{10} mode and it occurs at 711 cm^{-1} for the concentrations such as 0.1 M, 0.5 M and 1 M and at 712 cm^{-1} for 2 M. The strong interaction between the ring of the plasticizer and the lithium cation is found by the

appearance of a new shoulder indicated at a satellite band ν_{10}^*. The position of the satellite band is found at 722 cm^{-1} for both 1 M and 2 M.

In Figure 4.2.4.3.2 are shown the trends of the relative intensities of the bands ν_{10} and ν_{10}^*calculated *versus* the salt concentration as the previous Equations (4.2.4.2.1-4.2.4.2.2).

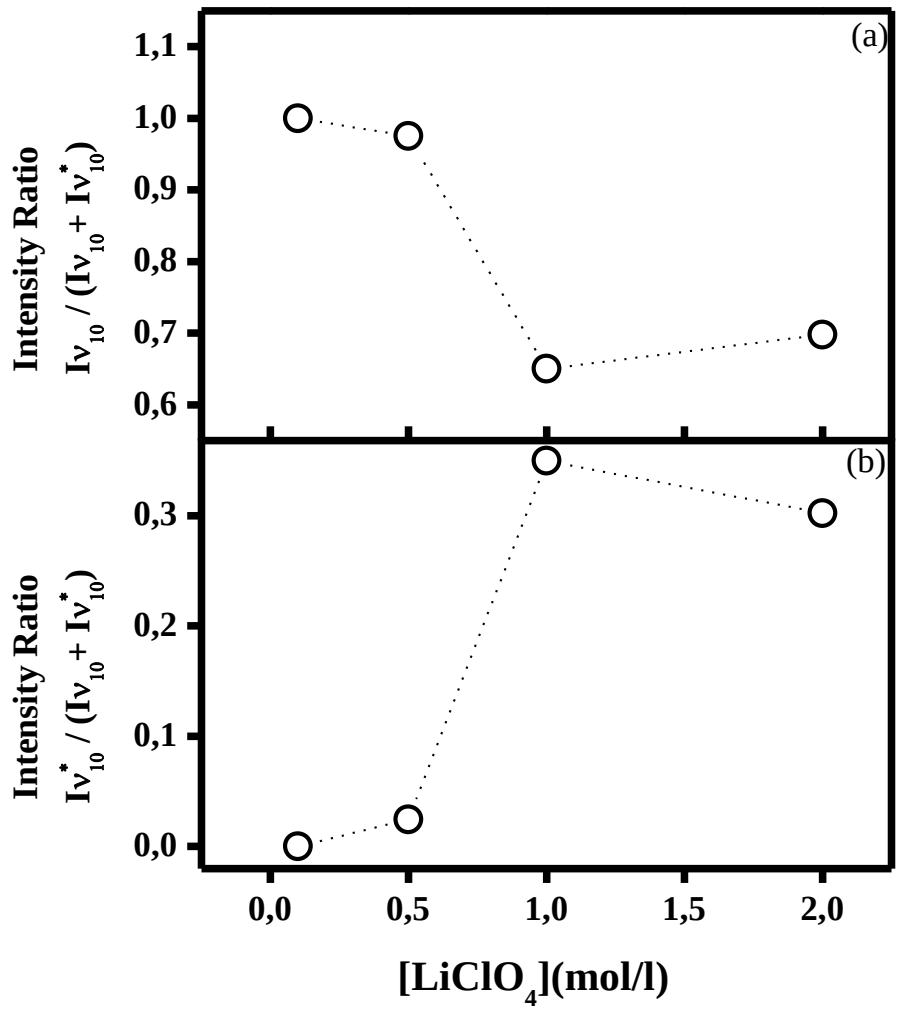

Figure 4.2.4.3.2. Trends of the ratio: (a) $Iv_{10}/\ (Iv_{10} + Iv_{10}^*)$; (b) $Iv_{10}^*/\ (Iv_{10} + Iv_{10}^*)$ *versus* the salt concentration (M) in PMMA-Li-PC gel polymer electrolyte.

The effect of a mix of PC and EC (molar ratio 1:1) was also investigated by FTIR spectroscopy in order to understand the role of a combination of two plasticizers on the ion associations in PMMA-Li-PC-EC gel polymer electrolyte.

The infrared spectra of the gel polymer electrolyte (20:80)% PMMA-Li-PC-EC at different salt concentrations are shown in Figure 4.2.4.3.3.

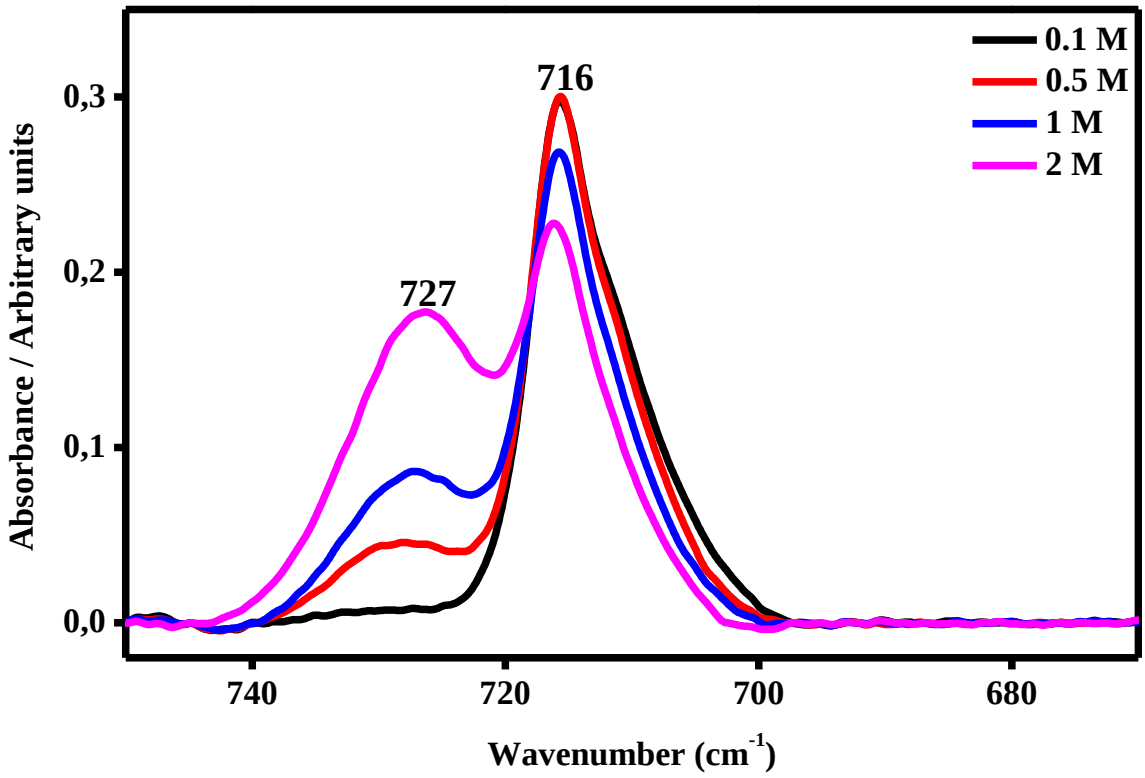

Figure 4.2.4.3.3. The IR band due to the sum of the PC mode denominated ν_{10} and the EC mode denominated ν_8 (716 cm^{-1}) and its satellite band ($\nu_8^* + \nu_{10}^*$) due to the interactions between the plasticizers and the lithium ions (727 cm^{-1}) in PMMA-Li-PC-EC gel polymer electrolyte at different salt concentrations: 0.1 M, 0.5 M, 1 M and 2 M.

The band located at 716 cm^{-1} describes the respective ring bending vibration in the PC and EC mix and it is indicated as the sum of the vibrational modes ($\nu_8 + \nu_{10}$). The relative satellite band indicated such as ($\nu^*_8 + \nu^*_{10}$) describes the strong interaction between the lithium ions and the mixture of PC-EC molecules. The satellite band is found in the high wavenumber side of the spectra and, it is located at 727cm^{-1} for 0.5 M, 1 M, and 2 M, respectively.

In Figure 4.2.4.3.4 are shown the trends of the relative ratios estimated against the salt concentration as the previous Equations 4.2.4.2.3-4.2.4.2.4.

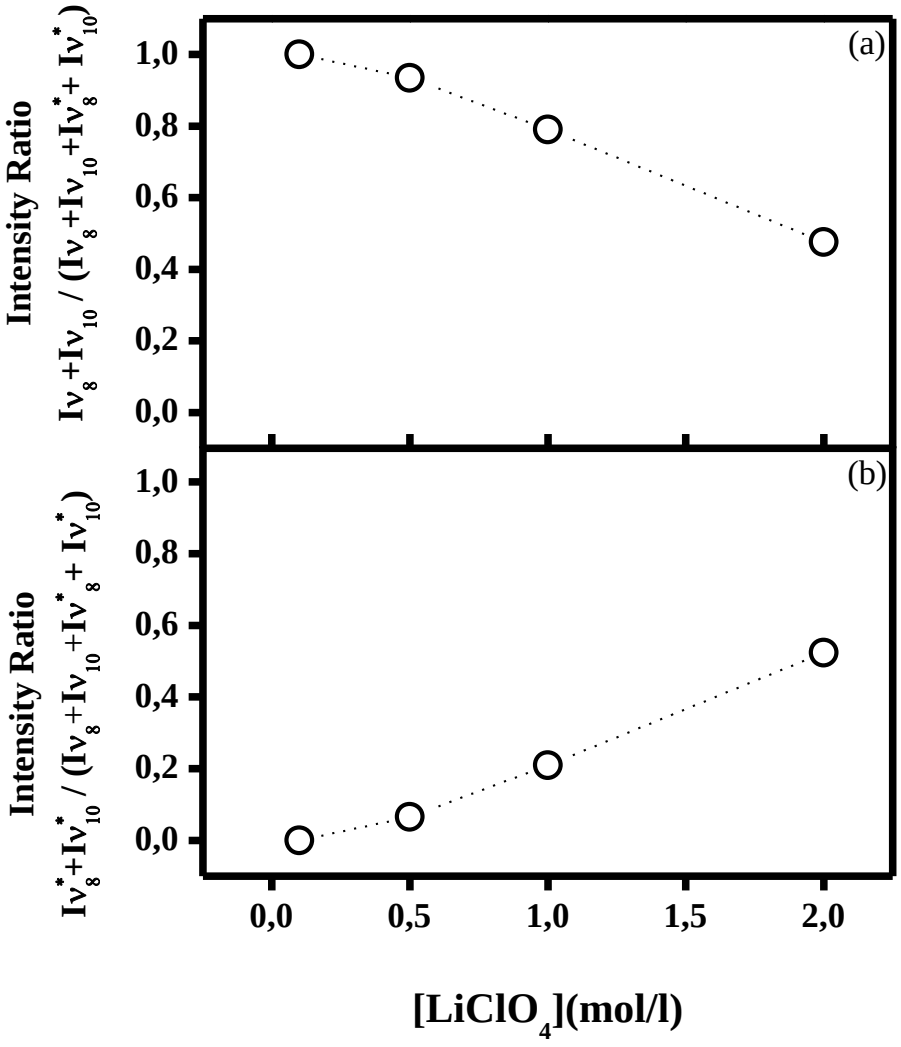

Figure 4.2.4.3.4. Trends of the ratio: (a) $Iv_8 + Iv_{10}/\ (Iv_8 + Iv_{10} + Iv_8^* + Iv_{10}^*)$; (b) $Iv_8^* + Iv_{10}^*/\ (Iv_8 + Iv_{10} + Iv_8^* + Iv_{10}^*)$*versus* the salt concentration in PMMA-Li-PC-EC gel polymer electrolyte.

The upper plot confirms, a decrease in the intensity of the (ν_8+ ν_{10}) mode in accordance with an increase of the salt concentration. The bottom plot confirms that the salt concentration increases, as well as the satellite band, increases too. The interactions between the lithium ions and the plasticizer molecules increase as a function of the amount of lithium ions in the gel.

In the Figure 4.2.4.3.5 are shown the IR spectra of PMMA-Li-PC collected between 930 cm^{-1} to 1300 cm^{-1}.

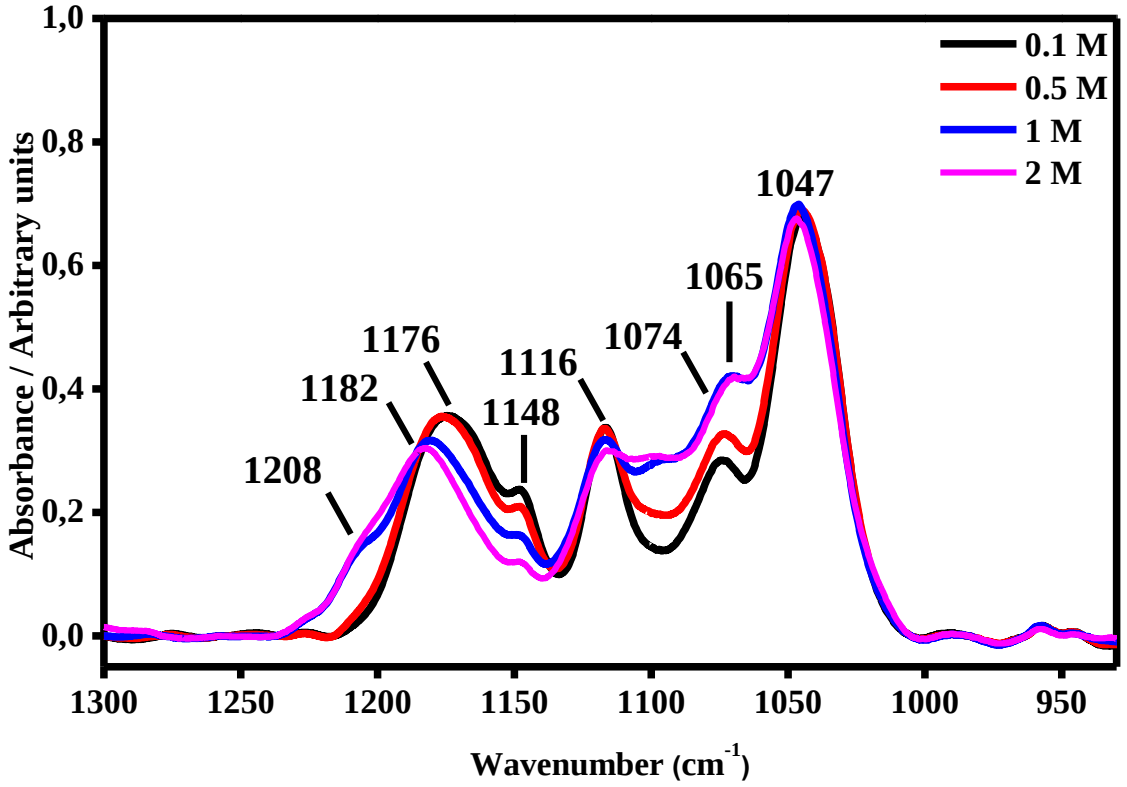

Figure 4.2.4.3.5. The IR spectra in the range between 930 cm^{-1} and 1300 cm^{-1} collected on PMMA-Li-PC at different salt concentrations: 0.1 M, 0.5 M, 1 M and 2 M.

The C-O-C skeletal stretching is located at 1175 cm^{-1} for 0.1 M, 1176 cm^{-1} and for 0.5 M, respectively. With the increase of the salt $LiClO_4$ content, this band is upshifted in the high wavenumber region. For 1 M the band is located at 1180 cm^{-1} and for the 2 M, it is found at 1182 cm^{-1}. The rising content of the $LiClO_4$ drives the appearance of a shoulder, which is measured at 1204 cm^{-1} for 1 M and 1208 cm^{-1} for 2 M and it is clear evidence of the association between the lithium cations and the PC-EC molecules. The ring oxygen stretching is located at 1074 cm^{-1} in the case of the lowest concentration while at the highest concentration (2 M) is downshifted at 10165 cm^{-1} because of the reduction polarity of the bond induced by the increasing amount of lithium ions.

The infrared spectra of PMMA-Li-PC-EC which describe the stretching of theC-O bond and wagging of the C-H bond have been analyzed and it is shown in Figure 4.2.4.3.6.

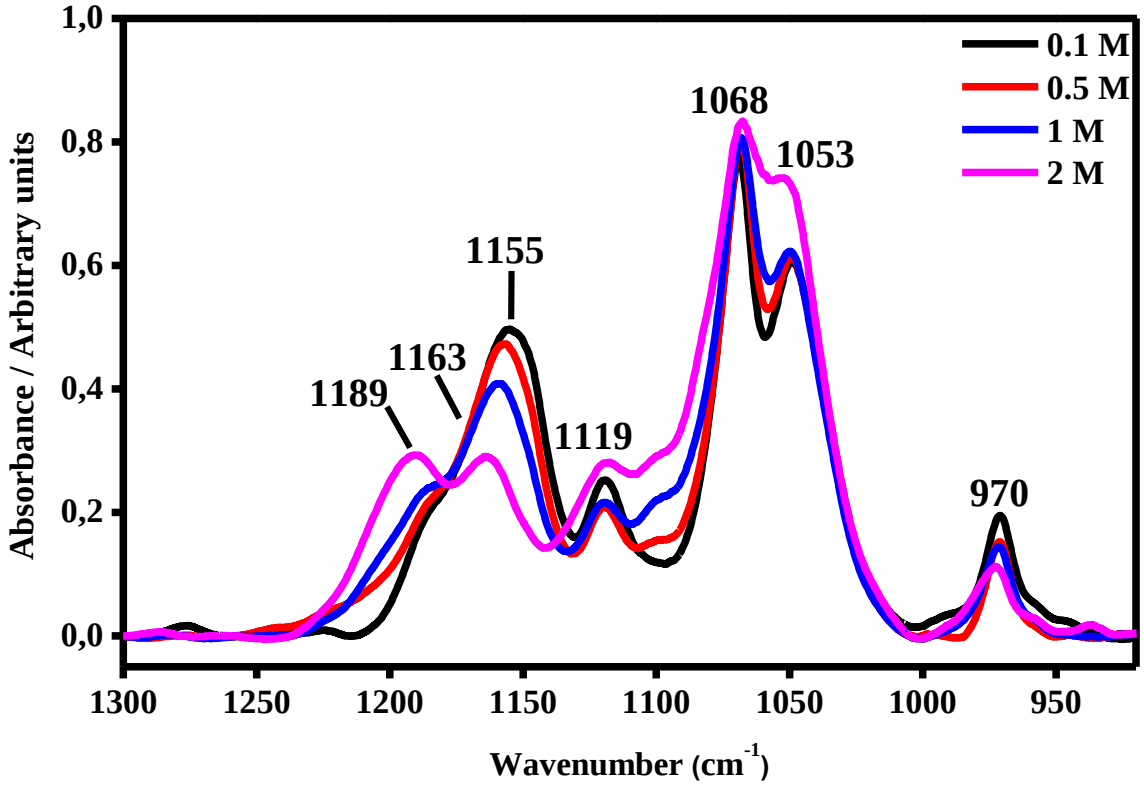

Figure 4.2.4.3.6. The IR spectra of O-C-O skeletal stretching of ethylene carbonate in PMMA-Li-PC-EC gel polymer electrolyte at (0.1 M, 0.5 M, 1 M, 2 M) salt concentrations.

The band at 1155 cm^{-1}(0.1 M) shifts at about 1163 cm^{-1} (2M), where a new band at 1189 cm^{-1} occurs. Also, the band located at 1068 cm^{-1} of the ring stretching of ethylene carbonate is affected by lithium solvation and it can change its profile.

The region of CH_2 wagging deformation for the gel polymer electrolyte (20:80) % w/w PMMA-Li-PC is shown in the infrared spectra of Figure 4.2.4.3.7.

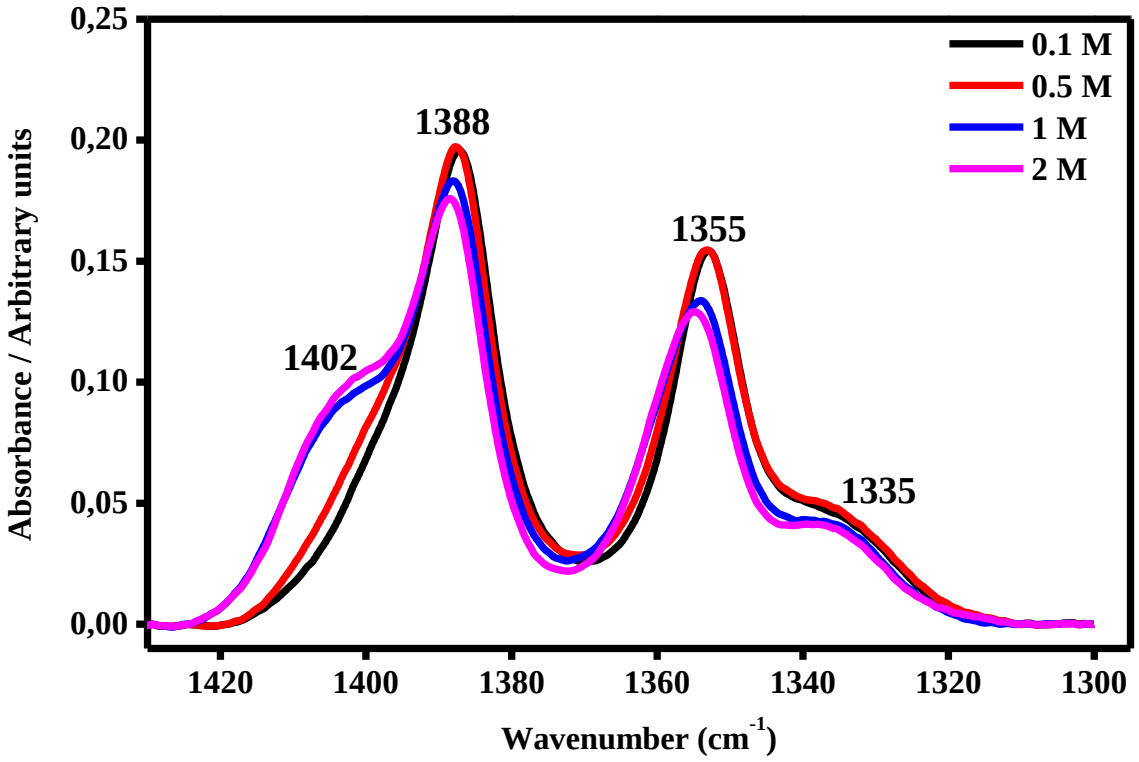

Figure 4.2.4.3.7. The IR band assigned to the CH_2 wagging mode denominated $\nu_{C\text{-}H}$ (~1388 cm^{-1}) and its satellite band at $\nu_{C\text{-}H}^{*}$ (~1402 cm^{-1}) in PMMA-Li-PC gel polymer electrolyte at different salt concentrations: 0.1 M, 0.5 M, 1 M and 2 M.

The CH_2 wagging vibrations are assigned to the vibrational mode labelled as $\nu_{C\text{-}H}$, as previously discussed. This band occurs at 1388 cm^{-1} for 0.1 M, at 1387 cm^{-1} for 0.5 M and at 1388 cm^{-1} for both 1M and 2 M. As the salt concentration increases, a new shoulder also known as the satellite band appears. The satellite band is associated with the vibrational mode $\nu^{*}_{C\text{-}H}$ and it describes the interaction between the lithium cations and the PC molecules. The satellite band is placed at 1403 cm^{-1} for 1 M and at 1402 cm^{-1} for 2 M.

In Figure 4.2.4.3.8 are shown the trends of the relative ratios estimated against the salt concentration as the previous Equations 4.2.4.2.5-4.2.4.2.6.

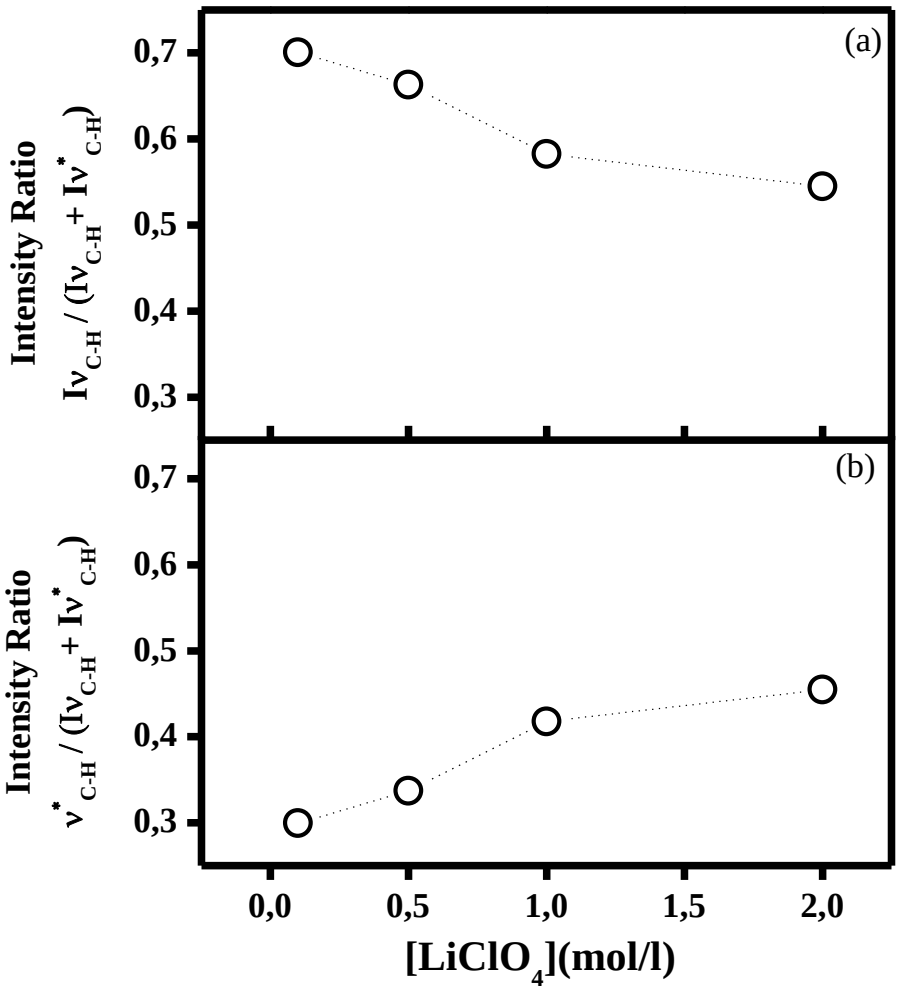

Figure 4.2.4.3.8. Trends of the ratio: (a) $Iv_{C-H}/\ (Iv_{C-H} + Iv^{*}_{C-H})$; (b) $Iv^{*}_{C-H}/\ (Iv_{C-H} + Iv^{*}_{C-H})$ *versus* the salt concentration PMMA-Li-PC gel polymer electrolyte.

From Figure 4.2.4.3.8, is possible to deduct that the contribution of the salt concentrations to the band profile is evident. From the upper plot is possible to observe a decreae of the relative intensity of the vibrational mode ν_{C-H} as an increase of the salt concentration in the gel polymer electrolyte. In the bottom plo,t the influence of the salt concentration on the vibration of the CH_2 wagging in PC molecules is described by an increase of the relative intensity of the ν^{*}_{C-H} mode.

In the case of the PMMA-Li-PC-EC gel polymer electrolyte, the infrared spectra related to the spectral region of the CH_2 wagging are shown in Figure 4.2.4.3.9. The vibrational band assigned to the CH_2 wagging in PC-EC molecules is associated with the vibrational mode ν_{C-H} and it is found at 1388 cm^{-1} for 0.1 M, 1389 cm^{-1} for 0.5 M, 1389 cm^{-1} for 1

M and 1390 cm^{-1} for 2 M, respectively. The influence of Li^+ cations on the deformation of CH_2 is indicated by the vibrational mode ν^*_{C-H}. This satellite band is placed at 1403 cm^{-1} for 0.5 M, at 1404 cm^{-1} for 1 M and at 1405 cm^{-1} for 2 M.

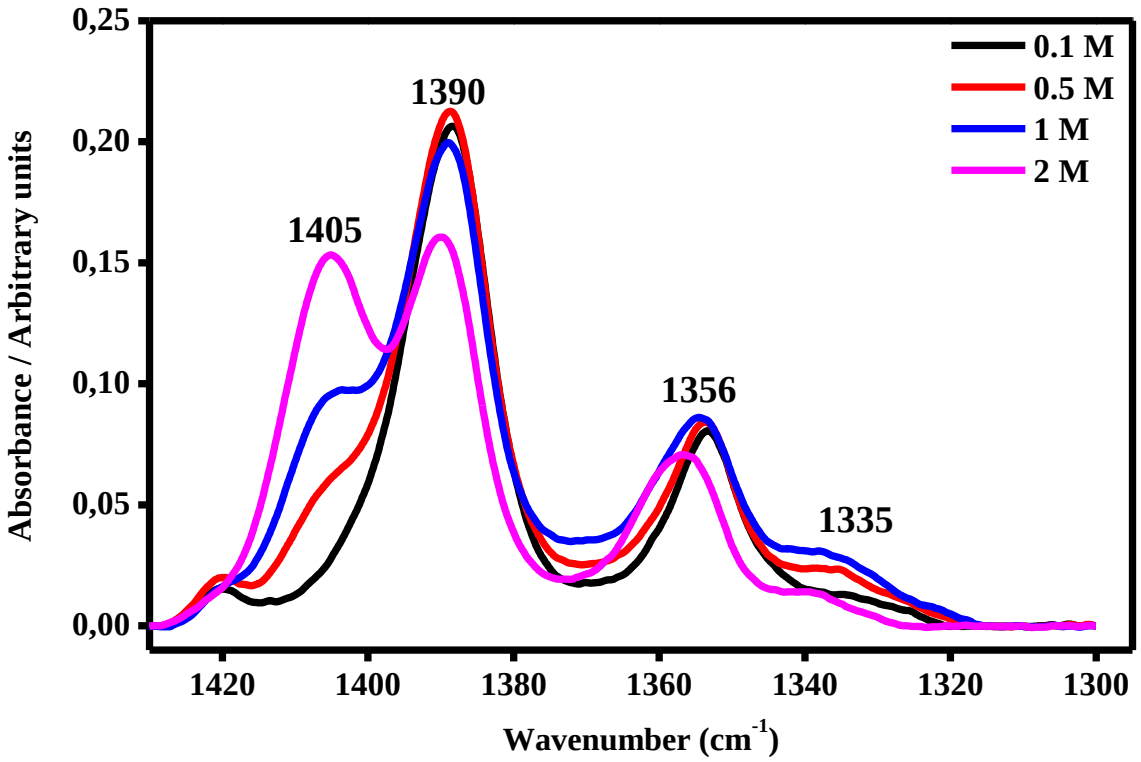

Figure 4.2.4.3.9. The IR band assigned to the CH_2 wagging mode denominated ν_{C-H} (~1390 cm^{-1}) and its satellite band at ν_{C-H}^* (~1405 cm^{-1}) in PMMA-Li-PC-EC gel polymer electrolyte at different salt concentrations: 0.1 M, 0.5 M, 1 M and 2 M.

The trends of the infrared intensity ratio *versus* the salt concentrations have been estimated in accordance with the previous Equations (4.2.4.2.7-4.2.4.2.8).

Figure 4.2.4.3.10 shows the infrared intensity ratio estimated against the $LiClO_4$ concentrations.

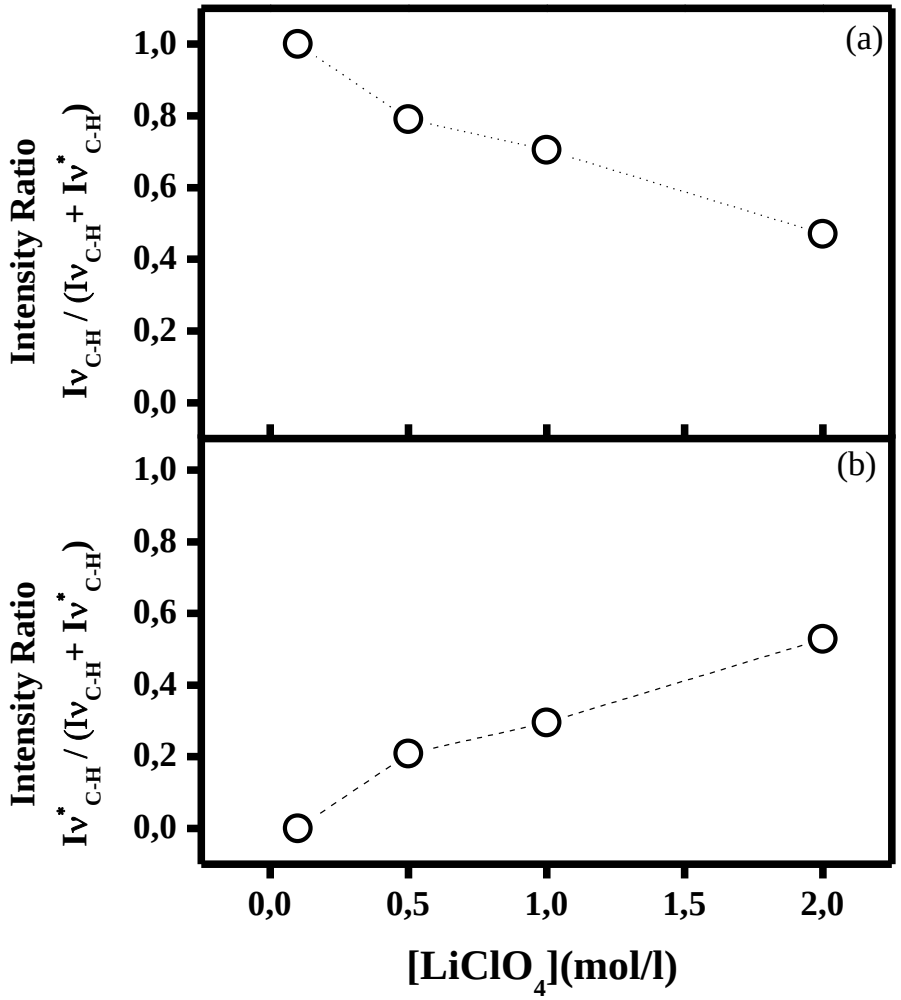

Figure 4.2.4.3.10. Trends of the ratio: (a) $Iv_{C-H}/\,(Iv_{C-H} + Iv^*_{C-H})$; (b) $Iv^*_{C-H}/\,(Iv_{C-H} + Iv^*_{C-H})$ *versus* the salt concentration in PMMA-Li-PC-EC gel polymer electrolyte.

From the upper plot, is possible to deduct that the EC molecules can experiment with the influence of the salt and its increases as confirmed by the trend depicted in the bottom plot.

Also, the bands ascribed to the C=O have been investigated in PMMA-Li-PC and PMMA-Li-PC-EC gel polymer electrolytes. The infrared spectra collected on the PMMA-Li-PC in the range between 1550 cm^{-1} and 1900 cm^{-1} are shown in Figure 4.2.4.3.11.

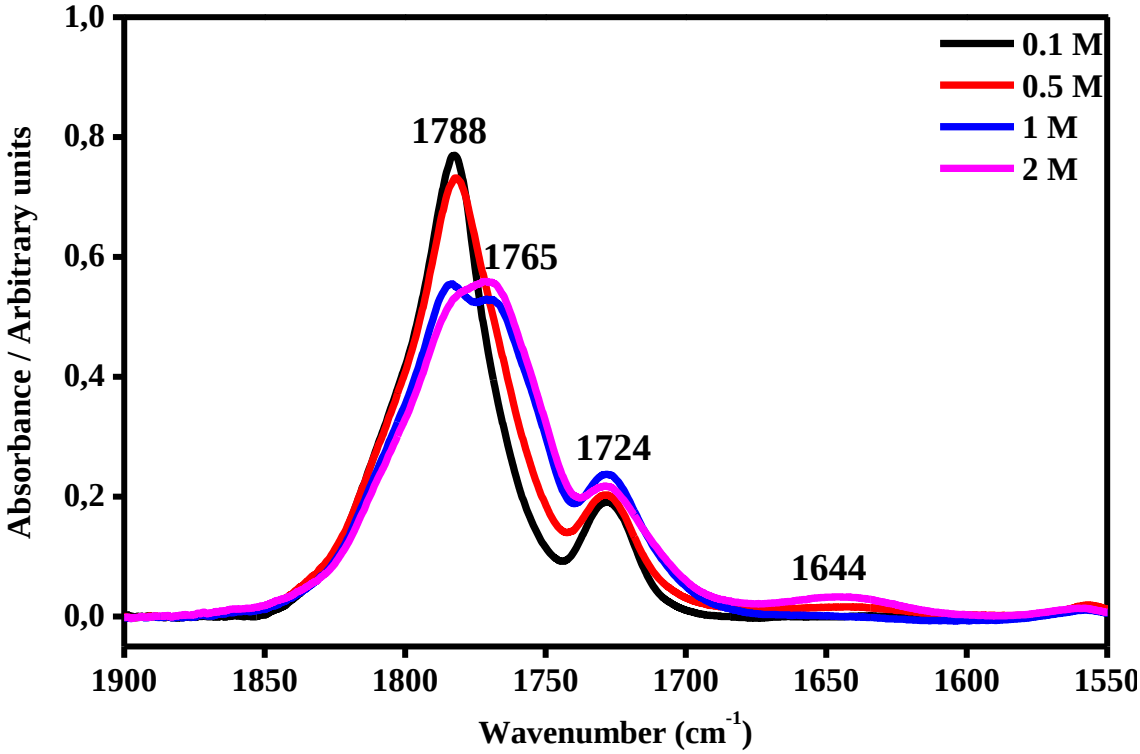

Figure 4.2.4.3.11. The IR band assigned to the C=O mode of free propylene carbonate denominated $\nu_{C=O}$ (~1788 cm^{-1}) and its satellite band at $\nu_{C=O}^{*}$ (~1765 cm^{-1}) in PMMA-Li-PC gel polymer electrolyte at different salt concentrations: 0.1 M, 0.5 M, 1 M and 2 M.

The carbonyl stretching of "free" PC falls at 1788 cm^{-1}($\nu_{C=O}$). The interaction between lithium cations causes a downshift of the band, and now the satellite band ($\nu^{*}_{C=O}$) appears at 1765 cm^{-1} at the higher concentrations.

The C=O stretching band of pure PMMA is located at 1724 cm^{-1} but after the interaction with lithium ions, the broad satellite band located at 1644 cm^{-1} appears.

In Figure 4.2.4.3.12 are shown the trends of the relative intensities of the bands: (a) $\nu_{C=O}$ and b) $\nu^{*}_{C=O}$ calculated *versus* the salt concentration as the previous Equations (4.2.4.2.9-4.2.4.2.10).

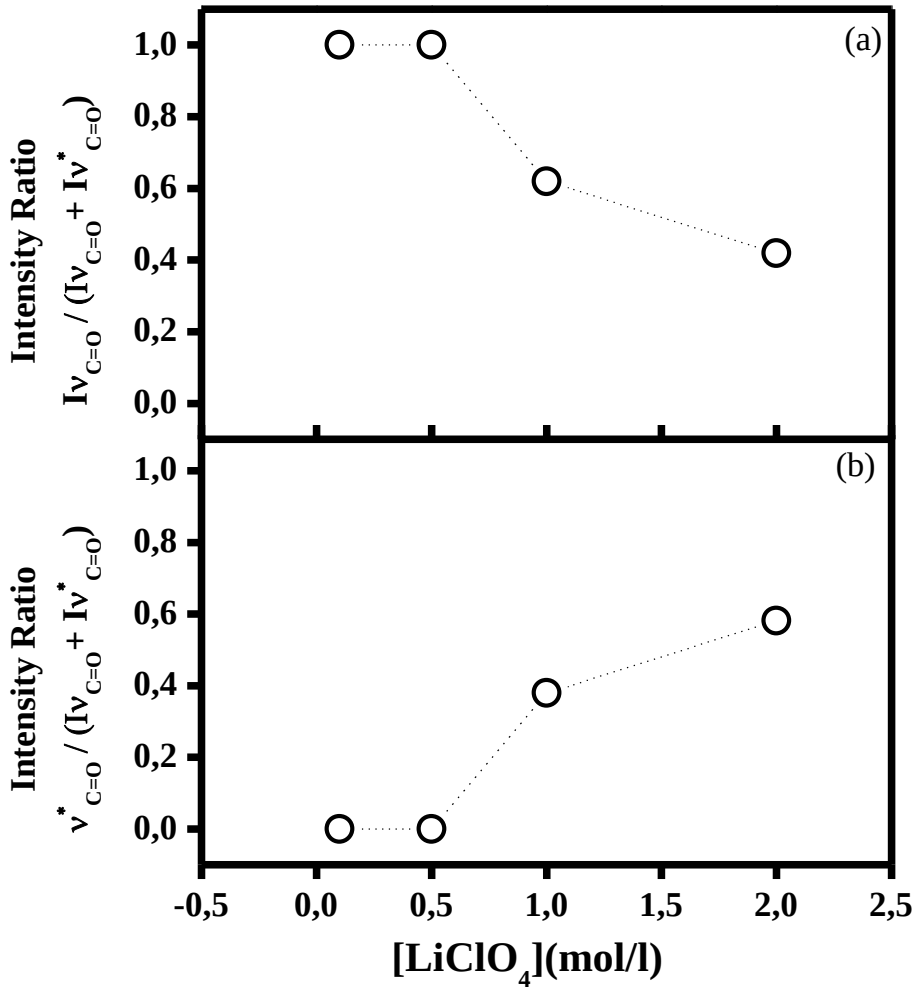

Figure 4.2.4.3.12. Trends of the ratio: (a) $Iv_{C=O}/\,(Iv_{C=O} + Iv^{*}_{C=O})$; (b) $Iv^{*}_{C=O}/\,(Iv_{C=O} + Iv^{*}_{C=O})$ *versus* the salt concentration in PMMA-Li-PC gel polymer electrolyte.

Considering the intensity ratios, from the upper plot is possible to deduct a decrease of the intensity of the band $\nu_{C=O}$ as a function of the increase of the salt content in the gel. While, from the bottom plot is evident that the concentration increases and the satellite bands due to the interaction between the PC molecules and the lithium ions increase.

The infrared spectra related to the spectral C=O vibration region in PMMA-Li-PC-EC are shown in Figure 4.2.4.3.13.

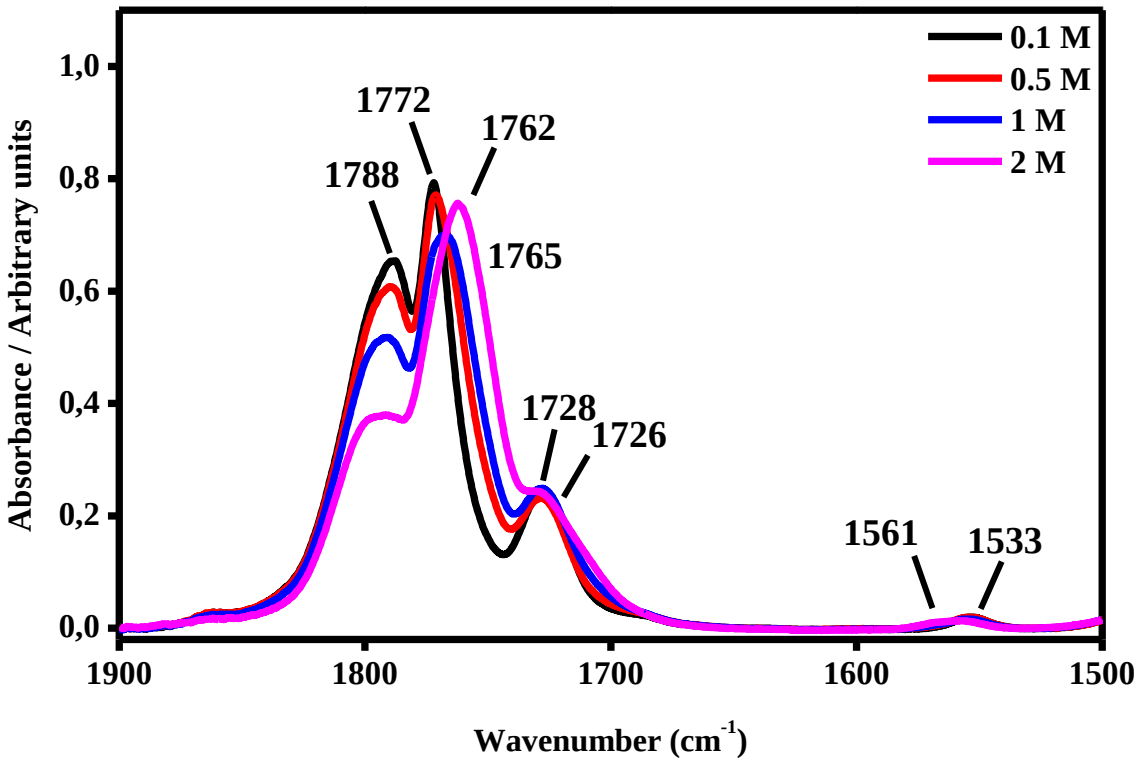

Figure 4.2.4.3.13. The IR band assigned to the C=O mode of free EC and PC carbonate denominated $\nu_{C=O}$ (~1788 cm^{-1}) and its satellite band at $\nu_{C=O}^{*}$ (~1772 cm^{-1} and ~1762 cm^{-1}) in PMMA-Li-PC-EC gel polymer electrolyte at different salt concentrations: 0.1 M, 0.5 M, 1 M and 2 M. In the inset, the trend of the intensity ratio $I_{\nu C=O*} / [I_{\nu C=O} + I_{\nu C=O*}]$ as a function of the salt concentrations.

The original bands of free C=O stretching in both PC and EC molecules [32] are located at 1788 cm^{-1}. When the lithium association occurs with PC and EC molecules, this band downshifted at 1772 cm^{-1} for the lower concentrations and at about 1762 cm^{-1} for the higher concentrations. The modes that fall at about 1728 cm^{-1} are assigned to the polymeric structure and when interactions with the lithium ions occur, a broad IR band at about 1553 cm^{-1}appears.

In Figure 4.2.4.3.14 are shown the trends of the relative intensities of the bands: (a) $\nu_{C=O}$ and, b) $\nu^{*}_{C=O}$ calculated *versus* the salt concentration as the previous Equations (4.2.4.2.11-4.2.4.2.12).

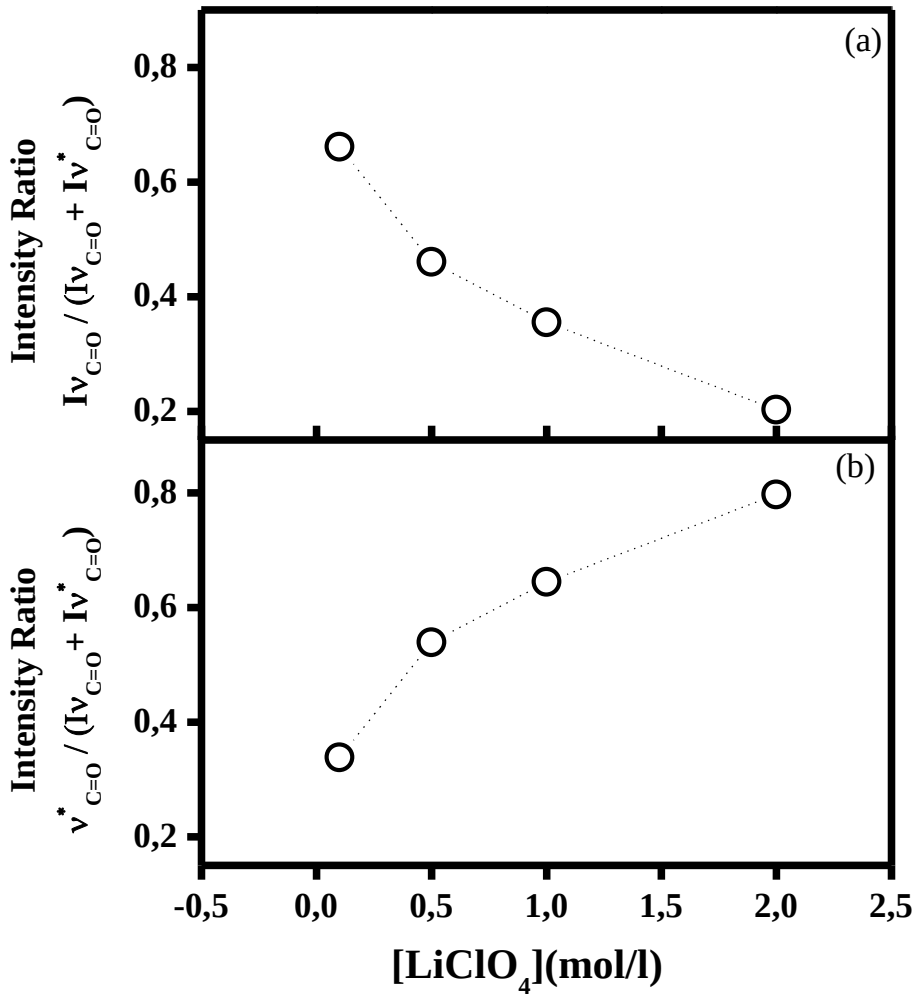

Figure 4.2.4.3.14. Trends of the ratio: (a) $Iv_{C=O}/\,(Iv_{C=O} + Iv^{*}_{C=O})$; (b) $Iv^{*}_{C=O}/\,(Iv_{C=O} + Iv^{*}_{C=O})$ *versus* the salt concentration in PMMA-Li-PC-EC gel polymer electrolyte.

In Figure 4.2.4.3.14, the upper plot confirms a decrease in intensity of the ($\nu_{C=O}$) mode in accordance with an increase of the salt concentration. The bottom plot confirms an increasing intensity for the upshifted band or satellite band ($\nu^{*}_{C=O}$) corresponding to the ion association between the Li^{+} cations and the solvent molecules in the gel polymer electrolyte.

Quite interesting is the band associated with the mode ν_7 of the EC molecules as shown in Figure 4.2.4.3.15. The band at 893 cm^{-1} identifies the ring breathing of EC (ν_7) and the new band at 904 cm^{-1} is ascribed to the coordination of the lithium ions to the ring of ethylene carbonate (satellite band, ν^{*}_7) which is $LiClO_4$ salt concentration-dependent.

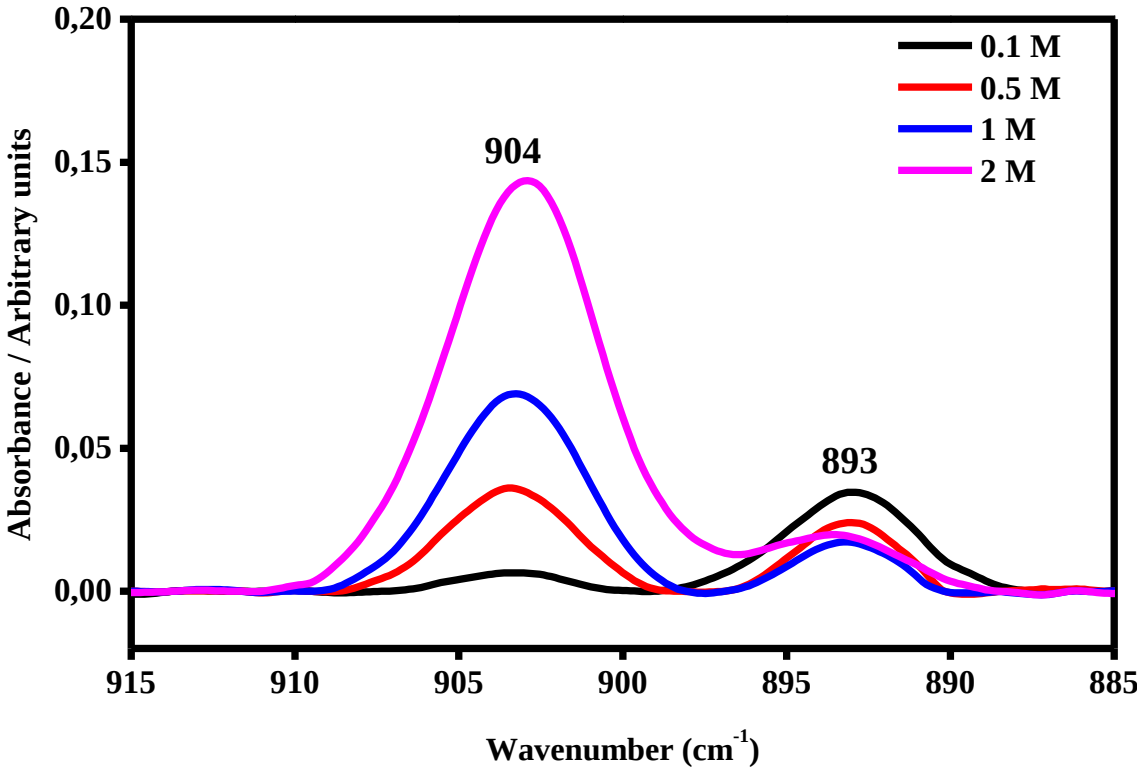

Figure 4.2.4.3.15. The IR spectra of ring breathing in ethylene carbonate (890cm^{-1}) and its ring coordination (900 cm^{-1}) in PMMA-Li-PC-EC gel polymer electrolyte at (0.1 M, 0.5 M, 1 M, 2 M) salt concentrations.

The quantitative estimation of the intensity ratios as a function of the salt concentrations have been calculated for both ν_7 and ν^*_7 modes according to the previous Equations 4.2.4.2.13 and 4.2.4.2.14 and they are depicted in Figure 4.2.4.3.16.

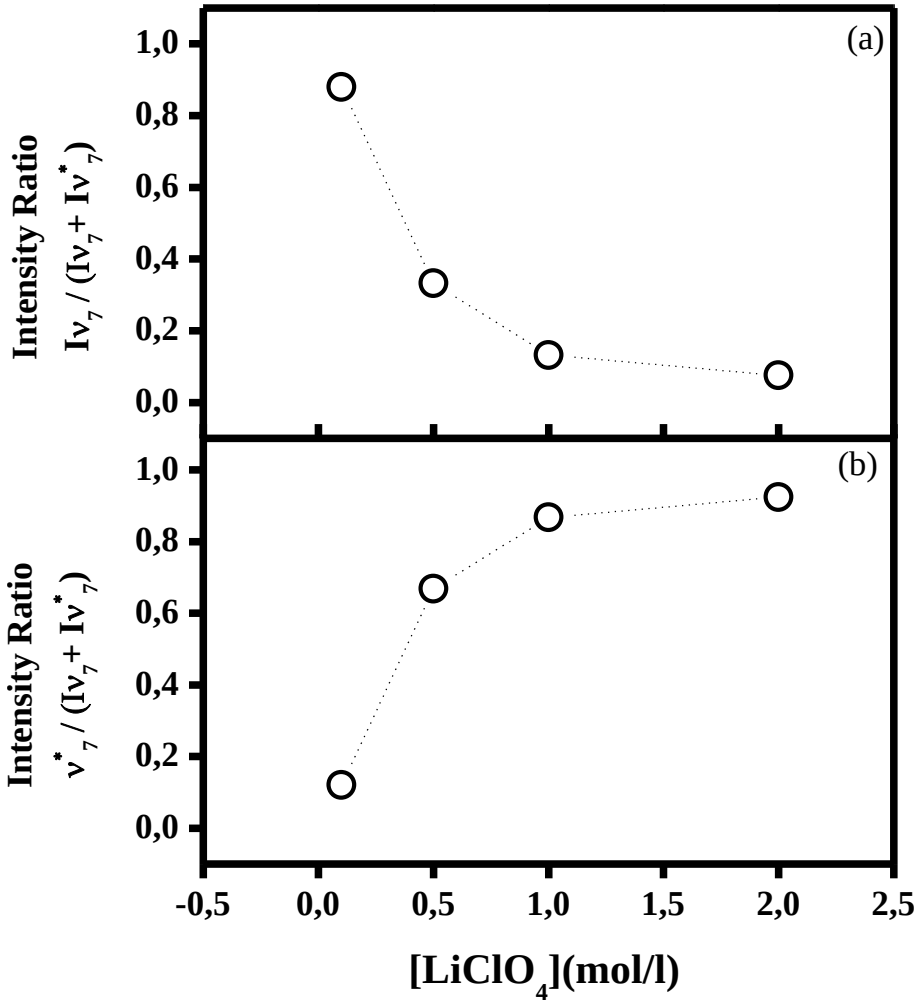

Figure 4.2.4.3.16. Trends of the ratio: (a) $Iv_7/\ (Iv_7 + Iv_7^*)$; (b) $Iv_7^*/\ (Iv_7 + Iv_7^*)$ *versus* the salt concentration in PMMA-Li-PC-EC gel polymer electrolyte.

The trend of the intensity ratio of the upper plot indicates that the increase of lithium salt content leads to a decrease in the intensity of the band ν_7, while the bottom plot shows that a low concentration the satellite band is very small and becomes more intense as the concentration increases.

4.2.4.4 Ion Pairing Phenomena in liquid electrolytes and gel polymer electrolytes

Because of the perturbation of lithium ions, the vibrational modes of ClO_4^- could be perturbed and could split in other bands corresponding to a particular interaction. As well known the tetrahedral free anion perchlorate ClO_4^- has nine vibrational modes and under

the tetrahedral symmetry (T_d) it shows four fundamental vibrational bands, where all of them are Raman active and only two are infrared active [28]. The changes in the band shape of these modes have been attributed to ion association [37]. The use of band fitting was useful to identify ion solvent interactions in the FTIR spectra of the polymer electrolytes and it led to the identification of four species: free ions $Li^+ClO_4^-$, solvent shared-separated ion pairs $Li^+ - solvent - ClO_4^-$, contact ion pairs and multiple ion aggregates $\{Li^+ClO_4^-\}_n$, as reported in Figure 4.2.4.4.1. The presence of each one is clearly strong evidence of [Li^+---*plasticizer*] interaction.

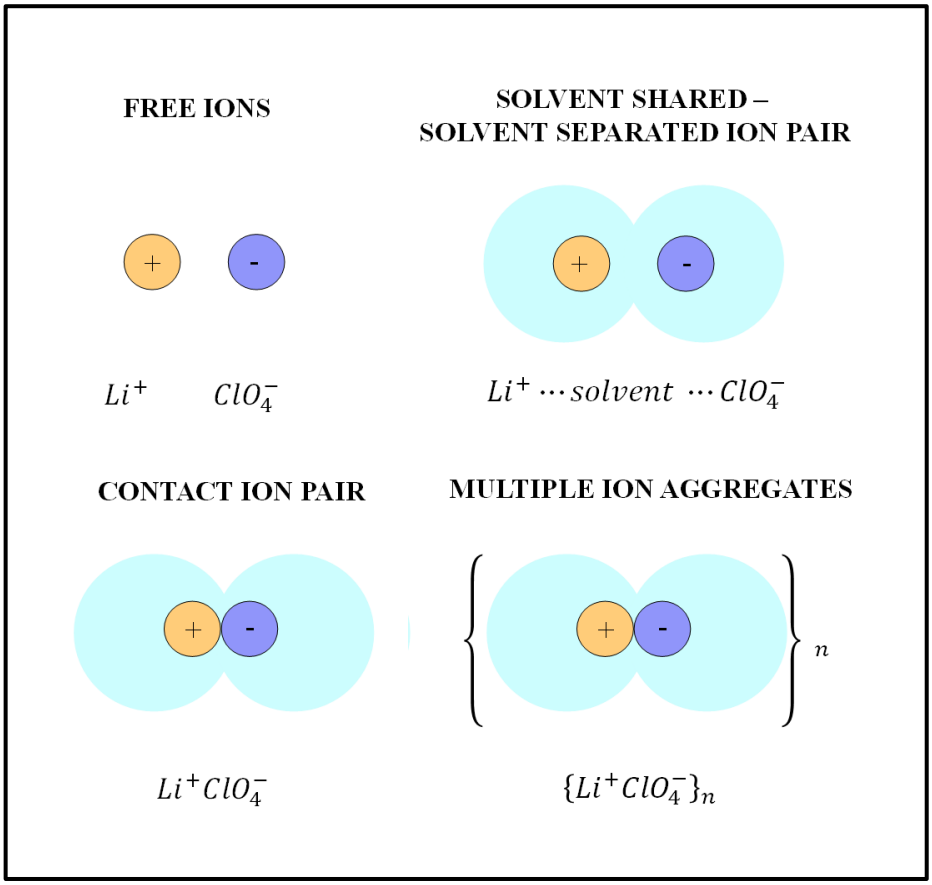

Figure 4.2.4.4.1. Type of ion associations of lithium perchlorate.

FTIR investigations have been conducted on liquid electrolytes (Li-PC and Li-PC-EC) and gel polymer electrolytes (PMMA-Li-PC and PMMA-Li-PC-EC) to confirm the ion-pairing formation in the samples.

The free ClO_4^- bands are located near 600 cm^{-1} and 1100 cm^{-1} and they are ascribed to the vibrational mode labelled as υ_{ClO4}^-, while the ion paring formation has been justified

by the appearance of a new shoulder which is assigned to the vibrational mode labelled as $\upsilon^{*}_{ClO4}^{-}$.

For Li-PC and Li-PC-EC liquid electrolyte systems, the relative infrared spectra collected in the region between 580 cm^{-1} to 650 cm^{-1} are shown in Figures 4.2.4.4.2 and 4.2.4.4.3.

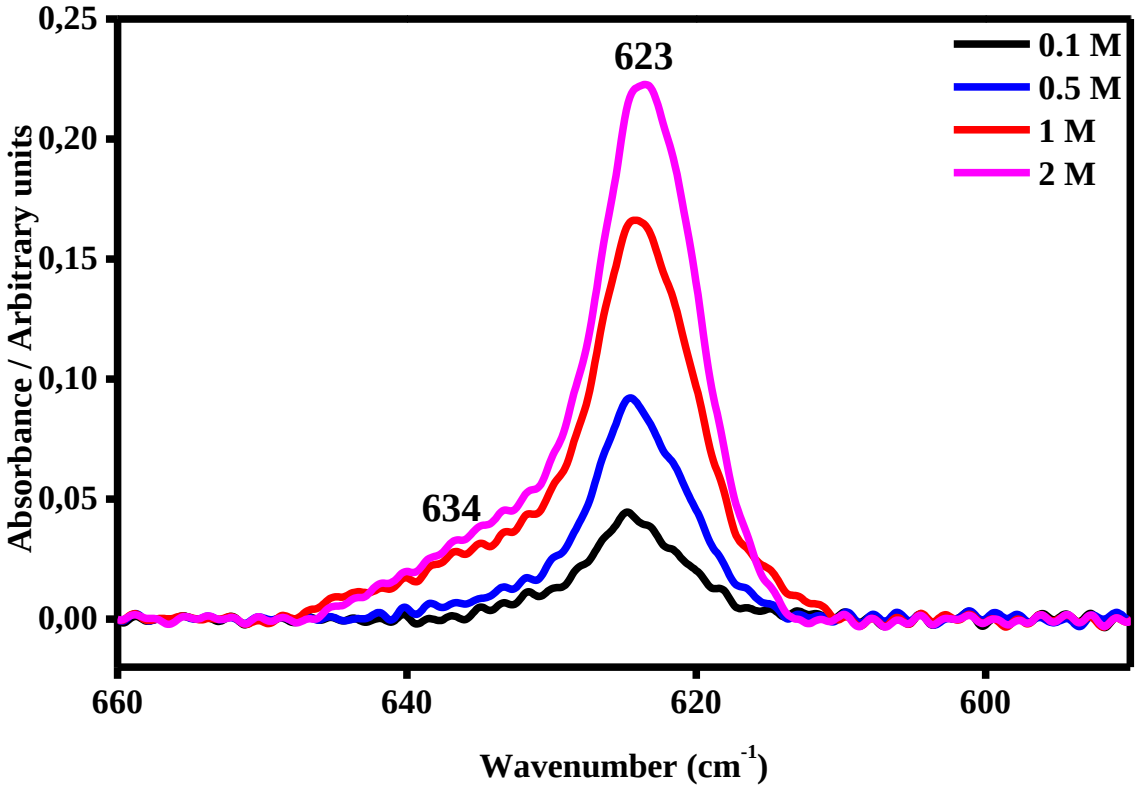

Figure 4.2.4.4.2. The IR band assigned to the ClO_4^- anion $I_{\nu ClO4}$ (~623 cm^{-1}) and its satellite band at $I_{\nu ClO4}^{*}$ (~633 cm^{-1}) in Li-PC gel polymer electrolyte at (0.1 M, 0.5 M, 1 M, 2 M) salt concentrations

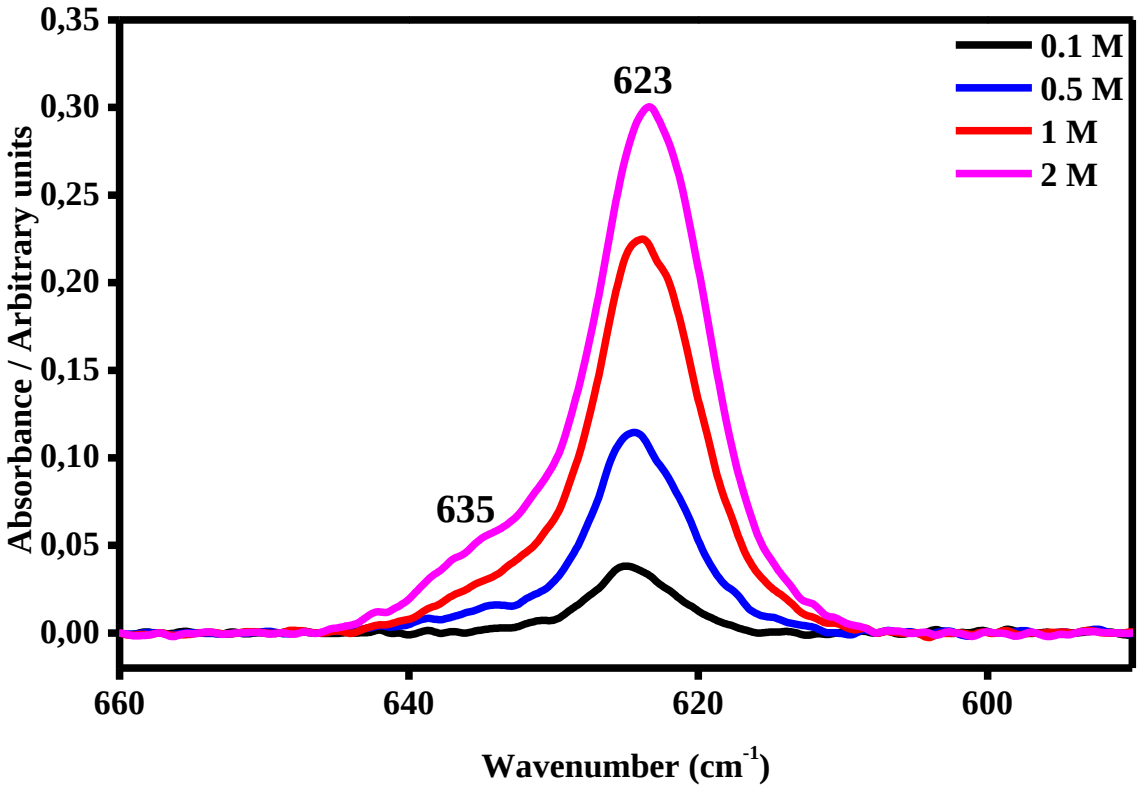

Figure 4.2.4.4.3. The IR spectra of ClO_4^- (623 cm^{-1}) and ion pair (634 cm^{-1}) in Li-PC-EC liquid electrolyte at (0.1 M, 0.5 M, 1 M, 2 M) salt concentrations.

For Li-PC liquid electrolyte the band which is assigned to the free ClO_4^- is found at 623 cm^{-1} for 0.1 M, then with the increasing of the salt content in the gelled system, a new shoulder *i.e.*, the satellite band is assigned at about 634 cm^{-1} and it is associated with ion pairs forming in the system [38, 39]. The same behavior is found for the Li-PC-EC, where the υ_{ClO4^-} mode occurs at 623 cm^{-1}, while the ion paring association which is described by the satellite band $\upsilon^*_{ClO4^-}$ is assigned at 635 cm^{-1}.

The trend of the intensity ratio has been calculated following the Equations (4.2.4.4.1-4.2.4.4.2) considering that as υ_{ClO4^-} and $\upsilon^*_{ClO4^-}$ modes have been normalized by intensity band at 1116 cm^{-1} that does not depend by the lithium perchlorate concentration.

$$\frac{Iv_{ClO_4^-}}{Iv_{1116}} \qquad (4.2.4.4.1)$$

$$\frac{Iv^*{}_{ClO_4^-}}{Iv_{1116}} \qquad (4.2.4.4.2)$$

Figures 4.2.4.4.4 and 4.2.4.4.5 show the intensity ratio of the modes υ_{ClO4}^- and $\upsilon^*_{ClO4}^-$ as a function of the salt concentration in the liquid electrolytes normalized with the band at 1116 cm^{-1}.

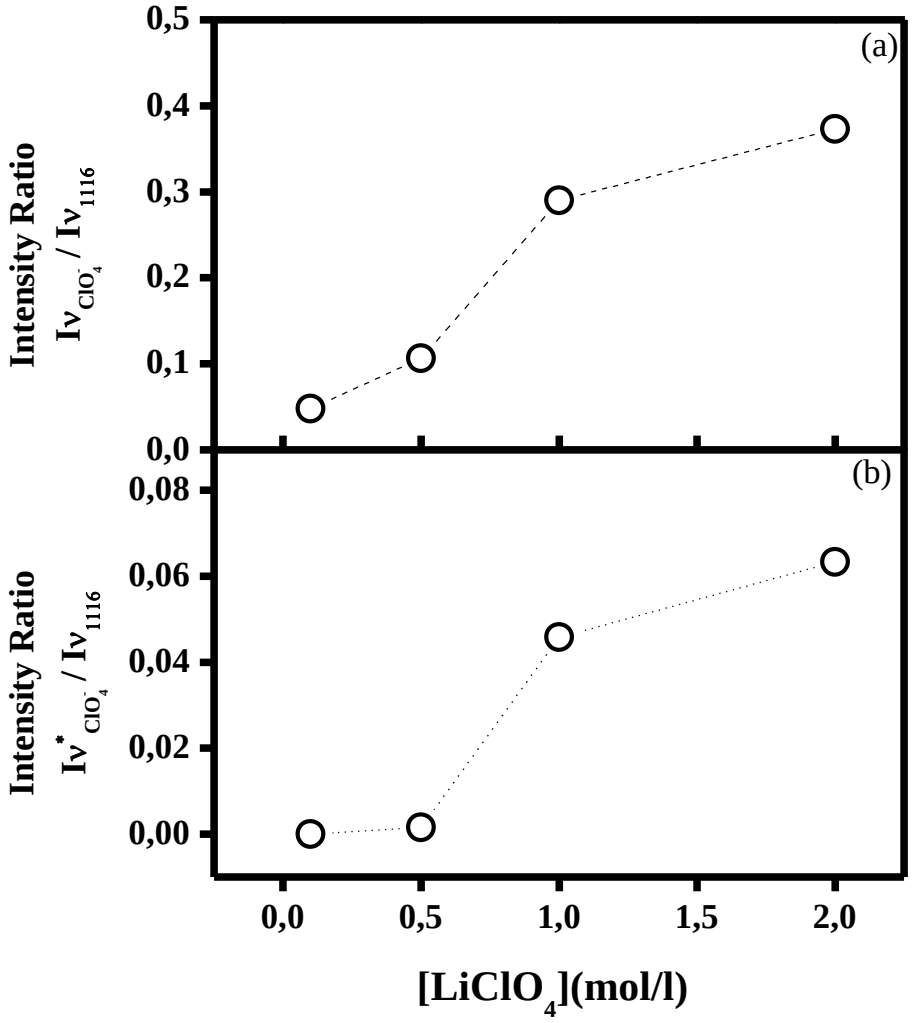

Figure 4.2.4.4.4. Trends of the ratio: a) $Iv_{ClO_4^-} / (Iv_{1116})$, b) ($Iv^*_{ClO_4^-} / (Iv_{1116})$*versus* the salt concentration in Li-PC liquid electrolyte.

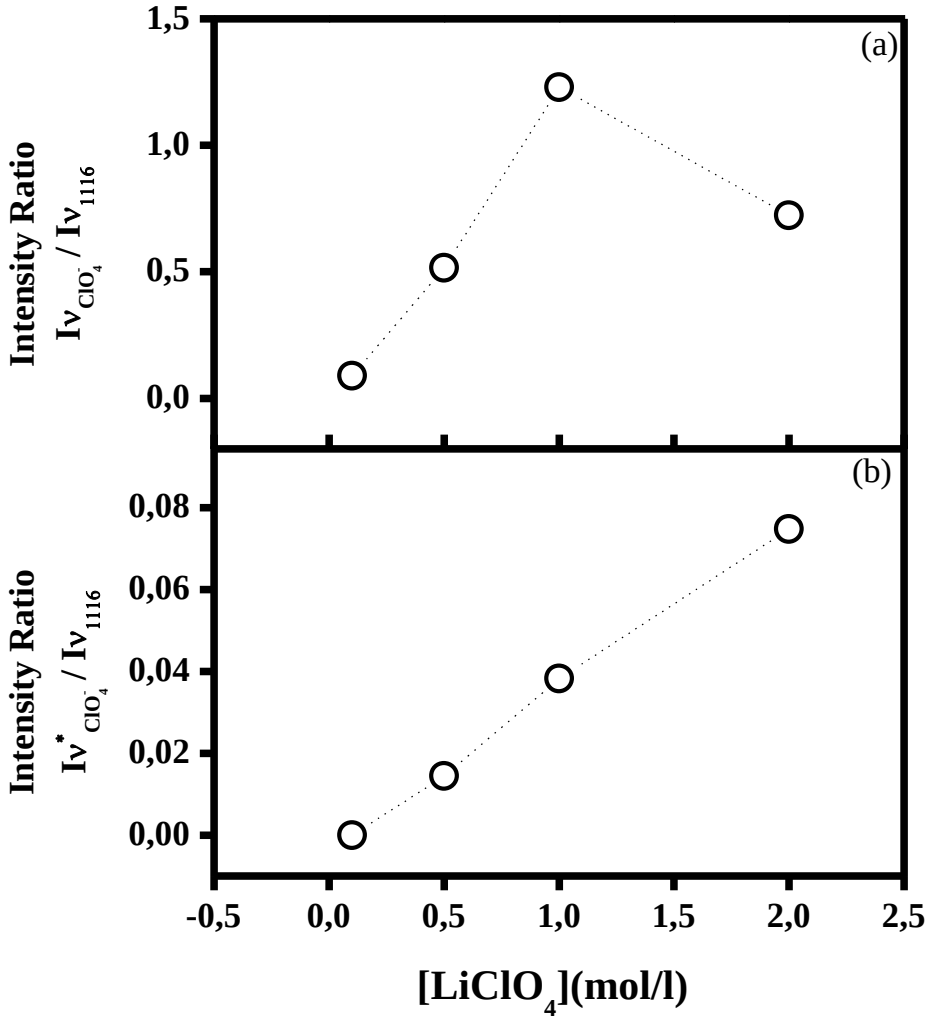

Figure 4.2.4.4.5. Trends of the ratio: a) $Iv_{ClO_4^-}/\ (Iv_{1116})$, b) ($Iv^*_{ClO_4^-}/\ (Iv_{1116})$*versus* the salt concentration in Li-PC-EC liquid electrolyte.

The data shown in the plots of both liquid electrolytes is thus proportional to the concentration of the free ion in each system. In both the liquid electrolytes the concentration of free ion is found to increase as the concentration of $LiClO_4$ is increased.

The infrared spectra of PMMA-Li-PC and PMMA-Li-PC-EC have been collected in the range between 580 cm^{-1} to 650 cm^{-1} and they are shown in Figures 4.2.4.4.6 and 4.2.4.4.7.

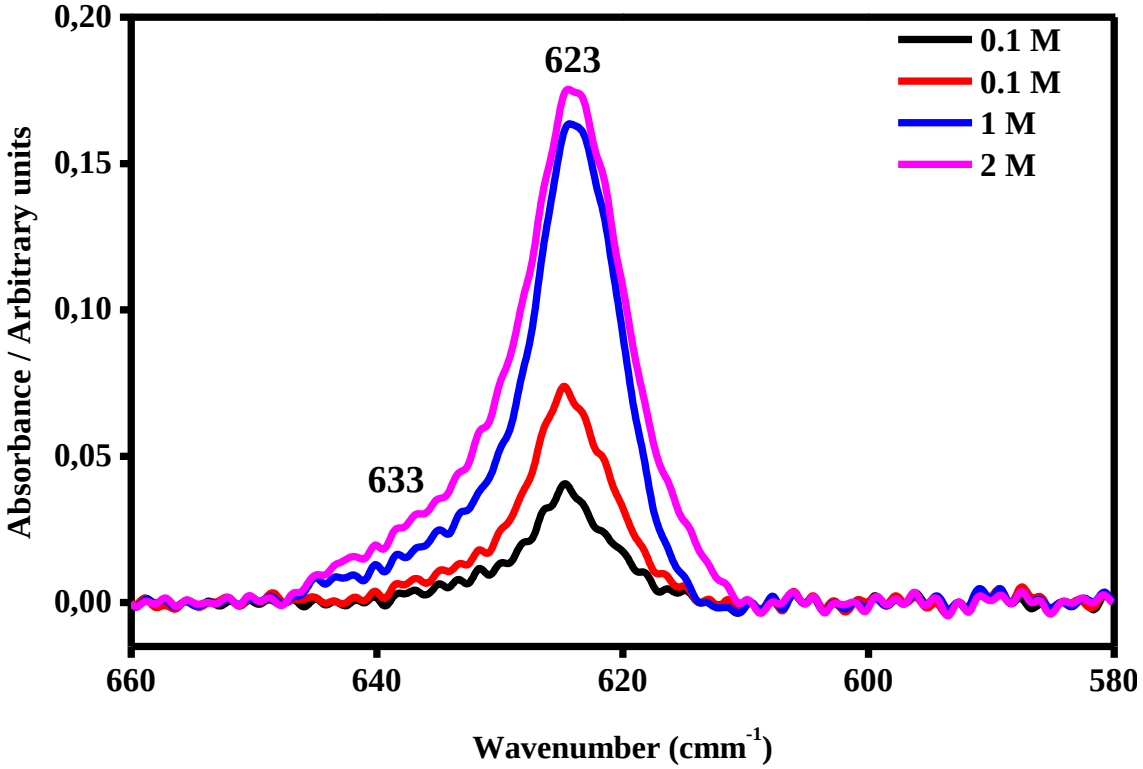

Figure 4.2.4.4.6. The IR spectra of free ClO_4^- (623 cm^{-1}) and ion pair (633 cm^{-1}) in PMMA-Li-PC gel polymer electrolyte at (0.1 M, 0.5 M, 1 M, 2 M) salt concentrations.

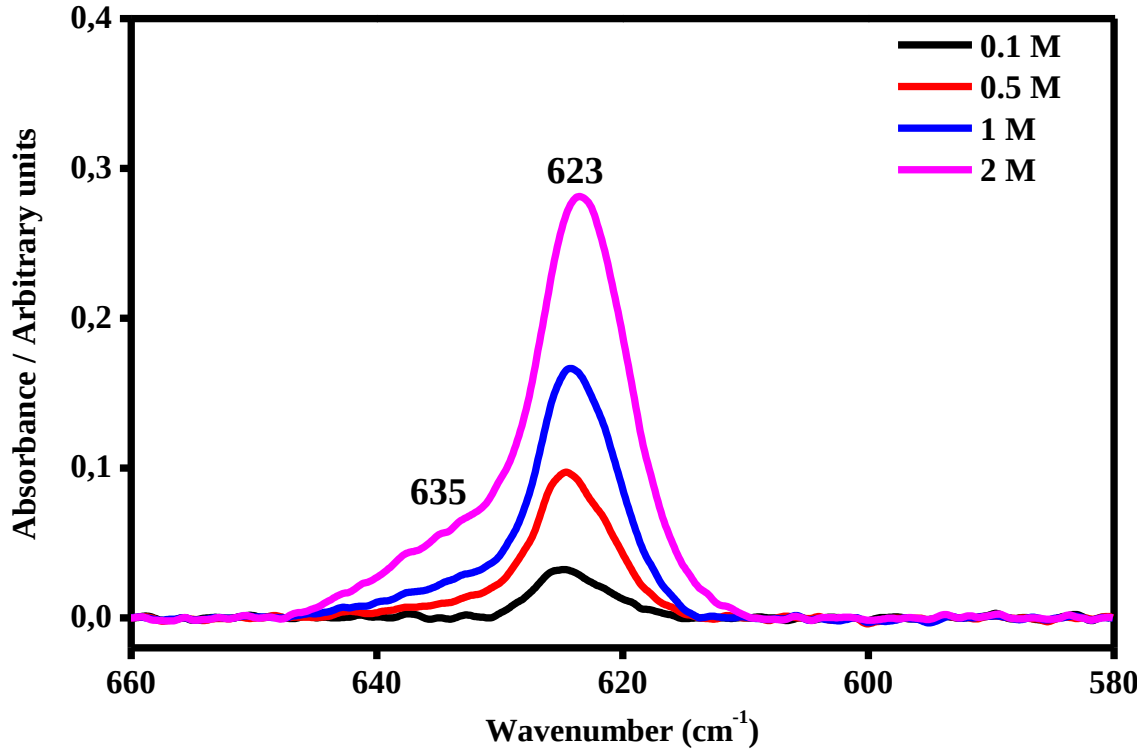

Figure 4.2.4.4.7. The IR spectra of free ClO_4^- (623 cm^{-1}) and ion pair (635 cm^{-1}) in

PMMA-Li-PC-EC gel polymer electrolyte at (0.1 M, 0.5 M, 1 M, 2 M) salt concentrations.

For the Li-PC-EC the free ClO_4^- is found at 623 cm^{-1} (υ_{ClO4^-}) and the ion-pairing band ($\upsilon^*_{ClO4^-}$) is assigned to 633 cm^{-1}, as shown in Figure 4.2.4.4.3. In PMMA-Li-PC-EC, the modes υ_{ClO4^-} and $\upsilon^*_{ClO4^-}$ are assigned at about 623 cm^{-1} and 635 cm^{-1}, respectively.

Also, in this case, the trends of the intensity ratios have been calculated according to the previous the Equations (4.2.4.4.1-4.2.4.4.2), considering that υ_{ClO4^-} and $\upsilon^*_{ClO4^-}$ modes have been normalized by intensity band at 1116 cm^{-1} which is no-dependent from lithium perchlorate concentration, as shown in Figures 4.2.4.4.8 and 4.2.4.4.9.

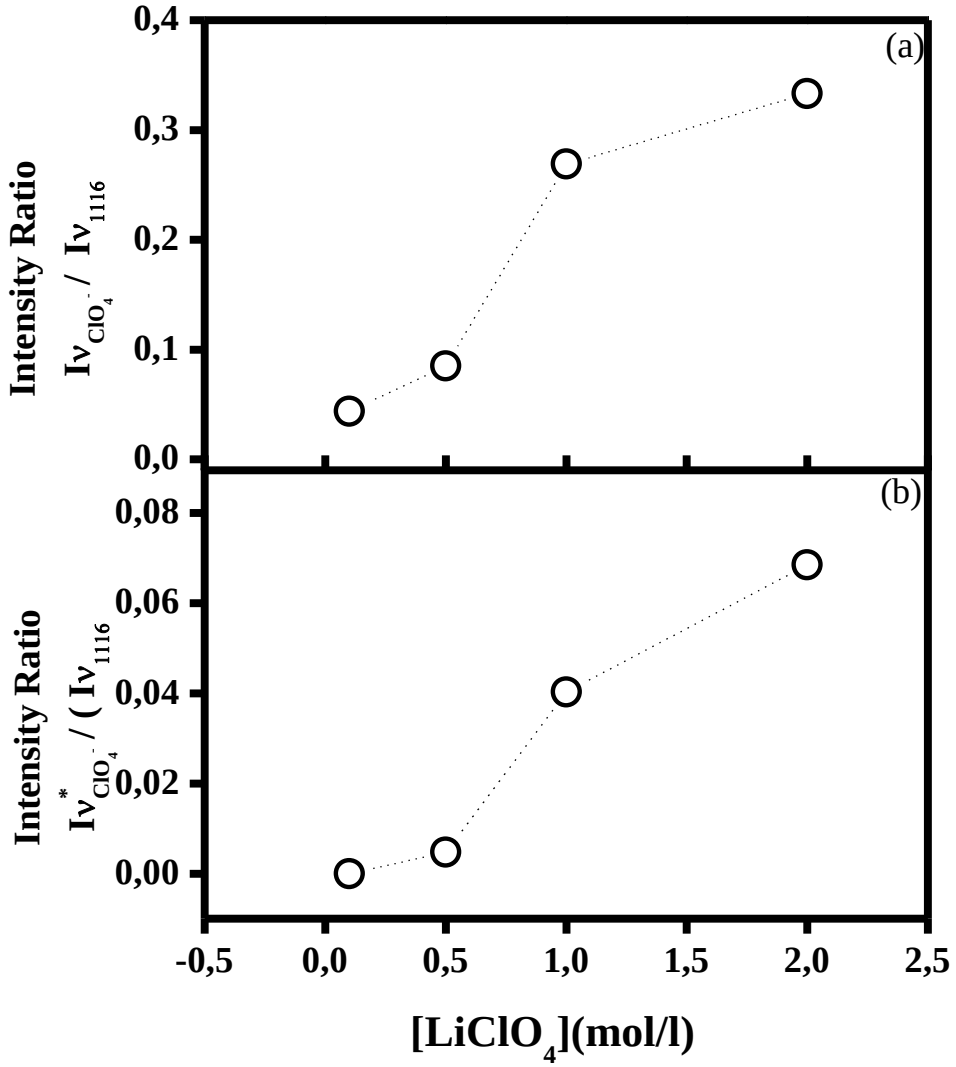

Figure 4.2.4.4.8. Trends of the ratio: (a) $Iv^*_{ClO_4^-} / (Iv_{ClO_4^-} + Iv_{1116})$*versus* the salt concentration in PMMA-Li-PC liquid electrolyte.

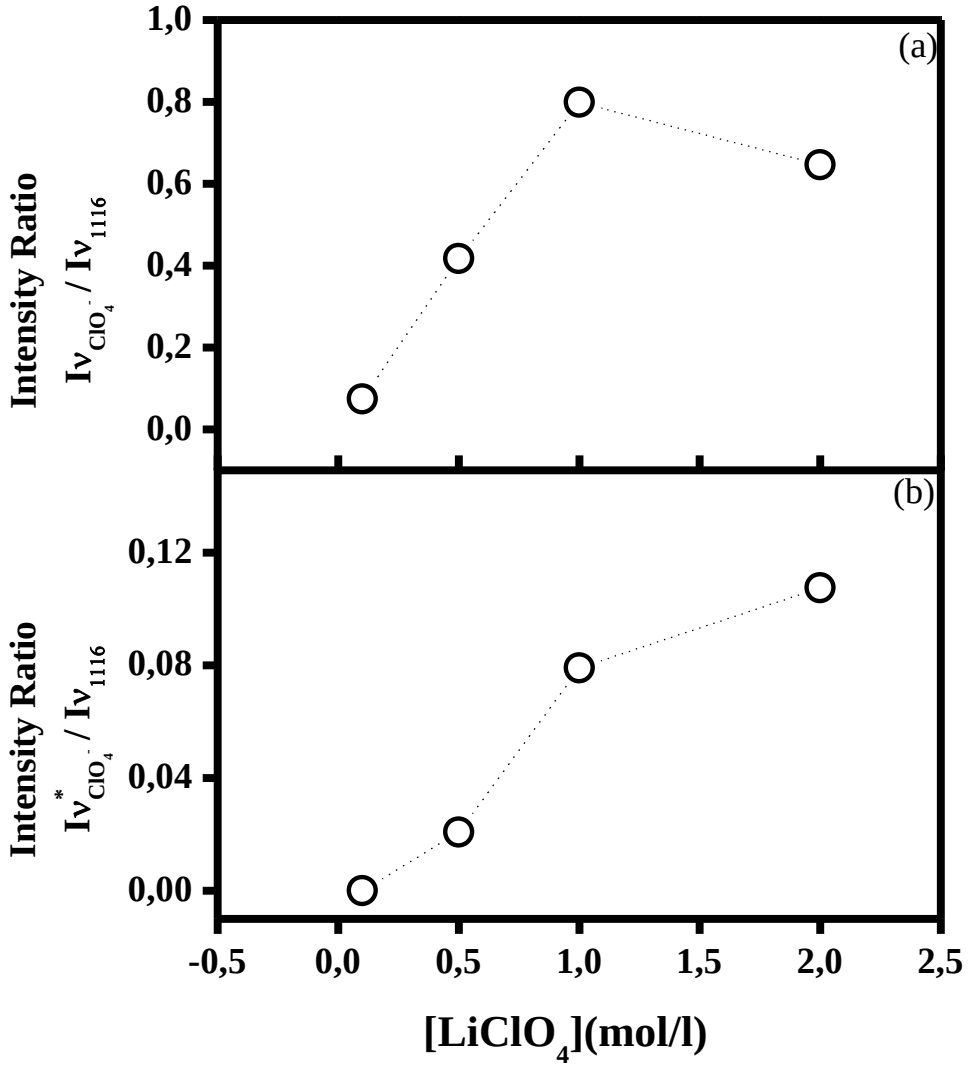

Figure 4.2.4.4.9. Trends of the ratio: (a) $Iv^*_{ClO_4^-} / (Iv_{ClO_4^-} + Iv_{1116})$*versus* the salt concentration in PMMA-Li-PC-EC liquid electrolyte.

In both the PMMA-Li-PC and PMMA-Li-PC-EC systems the concentration of free ion is found to increase as the concentration of $LiClO_4$ is increased. The change in free ion concentration can be compared to the ion conduction data shown in Figure 4.2.3.1.3. As might be expected, as the free ion concentration increases the ion conduction increase from 0.1M to 0.5M for all systems studied. However, for all systems except the PMMA-Li-PC-EC system, the ion conduction starts decreasing at concentrations higher than 0.5 M. The PMMA-Li-PC-EC also exhibits a decrease in ion conduction but exhibits this only at the highest concentration studied of 2M. An increase in conduction as the concentration of free ion is increased is predicated since the dielectric theory of ionic conduction predicts that the conduction is proportional to the number of charge carriers

and this is what is seen for lower ion concentrations as the concentration is increased. However, as the concentration is increased even more the number of vacant coordinating sites in the electrolyte can be reduced and this will start to reduce ionic conduction when a high enough concentration has been reached [40].

4.2.5 Linear Sweep Voltammetry

Linear Sweep Voltammetry (LSV) was used to define the anodic stability of liquid electrolytes and gel polymer electrolytes. The experimental set-up is composed of an electrochemical cell of two steel plates of dimensions (7.6 cm × 12.7 cm × 0.05 cm) as shown in Figure 4.2.5.1. The two electrodes of the cell are set a fixed distance (0.05 cm) and they are equipped with electronic junction connections.

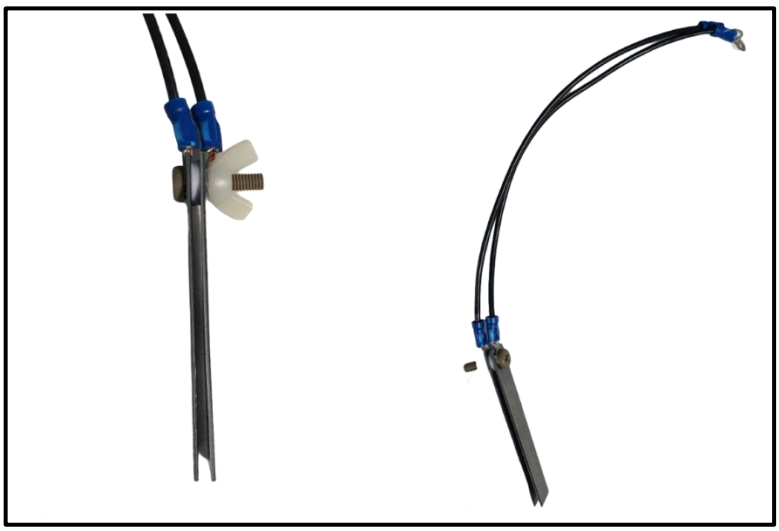

Figure 4.2.5.1. Electrochemical Cell used for Linear Sweep Voltammetry measurements to measure the anodic stability of liquid electrolytes and gel polymer electrolytes.

The anodic instabilities of liquid electrolytes and gel polymer electrolytes and the electrochemical resistance of the material under increasing potential have been evaluated by a sharp change in the current (slope) with respect to increased voltage scan in the anodic curves. The curves for Li-PC and Li-PC-EC liquid electrolytes at 1 M salt concentration used as references were determinated in the potential range between 0 V to 7 V and they are shown in Figure 4.2.5.2.

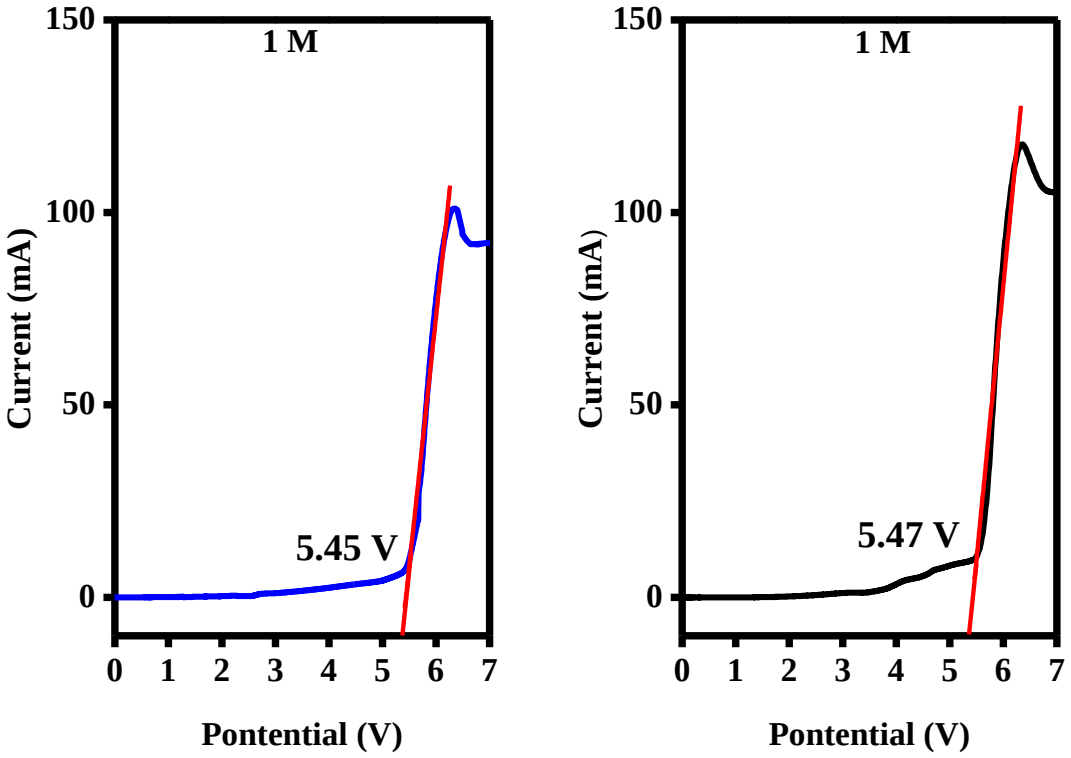

Figure 4.2.5.2. Linear Scan Voltammetry (black line) from 0 to 7 V and in the current range from 0 mA to 200 mA (scan rate of 10 mV s^{-1}) and the anodic stability (relative linear fit, red line) of Li-PC and Li-PC-EC liquid electrolytes at 1 M salt concentration.

Li-PC has good performance until 5.45V and the same situation is found for Li-PC-EC which is characterized by potential stability until 5.47 V.

The anodic stabilities of PMMA-Li-PC and PMMA-Li-PC-EC gel polymer electrolytes at 0.1 M, 0.5 M, 1 M and 2 M were estimated in the potential range from 0V to 7 V and they are shown in Figures 4.2.5.3 and 4.2.5.4, respectively.

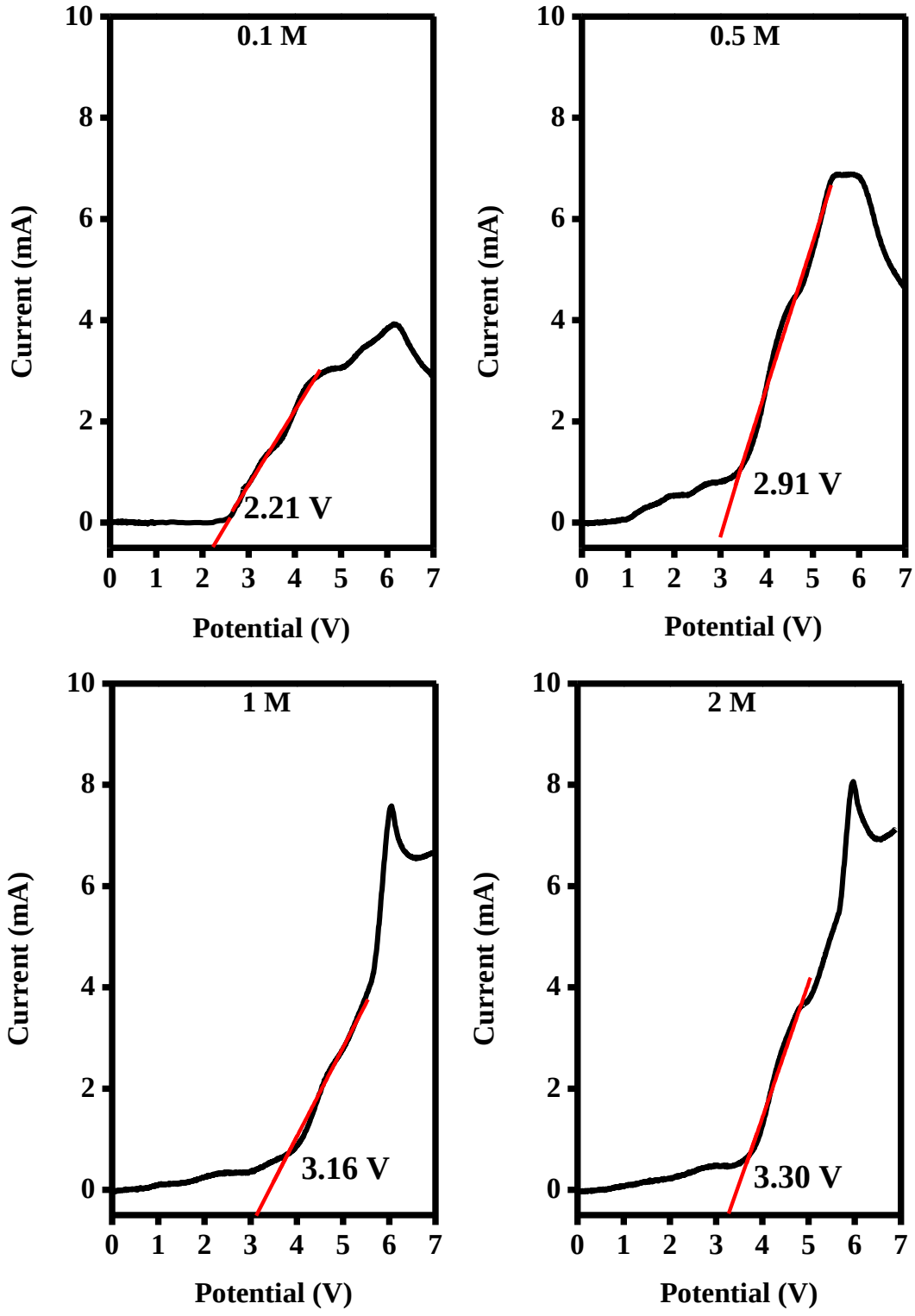

Figure 4.2.5.3. Linear Scan Voltammetry (black line) from 0 to 7 V and in the current range from 0 mA to 200 mA (scan rate of 10 mV s^{-1}) and the anodic stability (relative linear fit, red line) of PMMA-Li-PC gel polymer electrolyte at different salt concentrations (0.1 M, 0.5 M, 1 M, and 2 M).

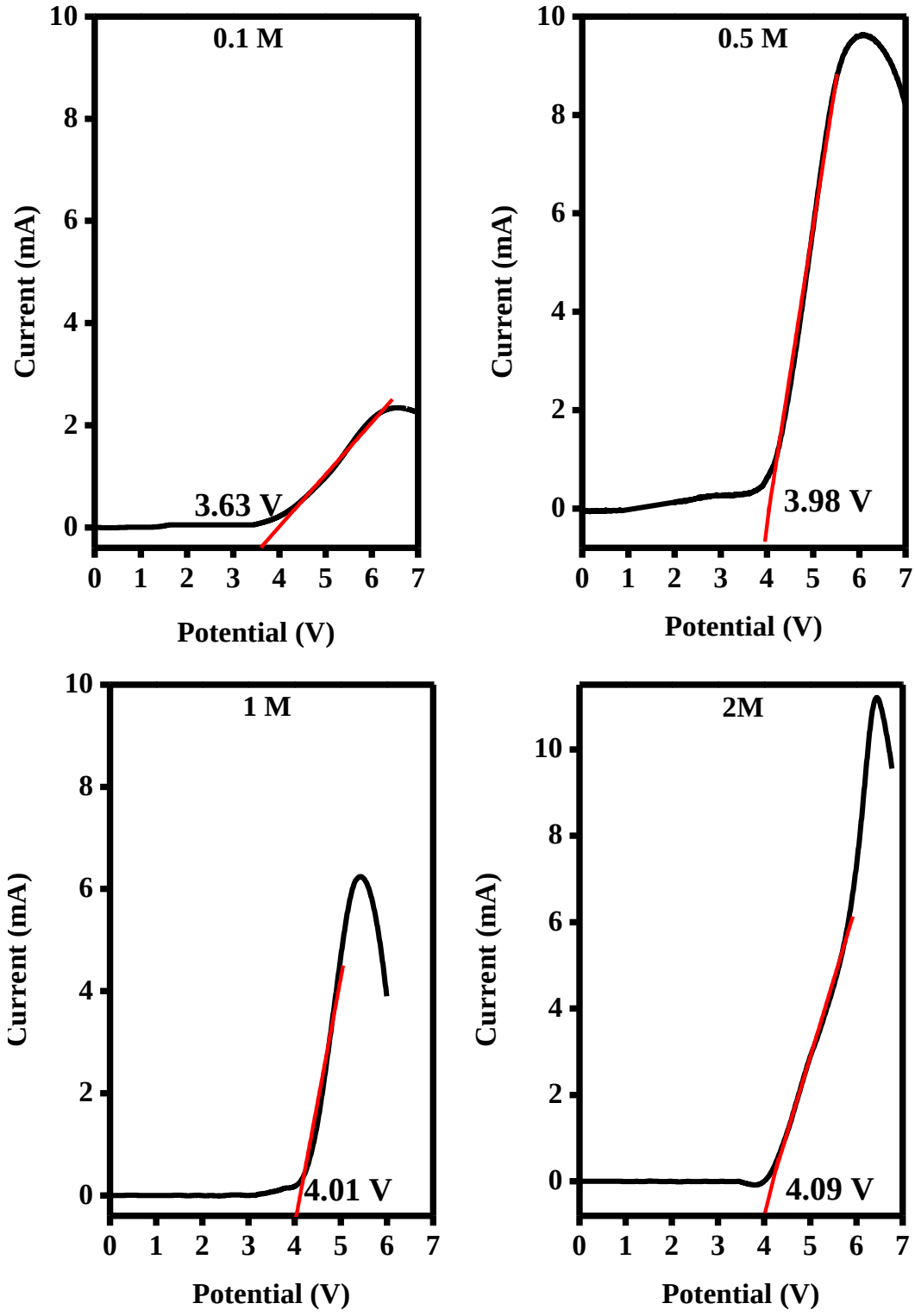

Figure 4.2.5.4. Linear Scan Voltammetry (black line) from 0 to 7 V and in the current range from 0 mA to 200 mA (scan rate of 10 mV s^{-1}) and the anodic stability (relative linear fit, red line) of PMMA-Li-PC-EC gel polymer electrolyte at different salt concentrations (0.1 M, 0.5 M, 1 M, and 2 M).

As depicted in Figures 4.2.5.3 and 4.2.5.4 all gel polymer electrolytes are stable up to about 4 V and this value is lower than the same registered for the liquid electrolytes. Considering these values, one can assume the electrolyte is compatible with most high voltage electrodic couples of lithium composition. Over 4 V a sudden rise of current which is due to the electrolyte decomposition at the inert electrode interface is registered. In the condition of high potential gel polymer electrolyte became sticky like rubber and the yellow-brown coloration is due to a partial residue of steel electrodes as shown in Figure 4.2.5.5.

Figure 4.2.5.5. Instability of gel polymer electrolytes registered under high applied potential (over 4 V).

The anodic stability can be related to the salt concentration. In fact, for gelled systems the stability of material increases with the increasing $LiClO_4$ content.
All the results are shown in Table 4.2.5.1.

	Anodic Stability Volt (V)	
[$LiClO_4$] mol/l	**Li-PC**	**Li-PC-EC**
1	5.45	5.47
[$LiClO_4$] mol/l	**PMMA-Li-PC**	**PMMA-Li-PC-EC**
0.1	2.21	3.36
0.5	2.91	3.98
1.0	3.16	4.01
2.0	3.30	4.09

Table 4.2.5.1. The anodic stability from 0 to 7 V and in the current range between 0 and 200 mA (scan rate 10 mV/s) of Li-PC and Li-PC-EC liquid electrolytes at 1 M and of

PMMA-Li-PC and PMMA-Li-PC-EC polymeric gel electrolytes at different salt concentrations: 0.1 M, 0.5 M, 1 M, and 2 M.

4.2.6 Thermal Analysis of Gel Polymer electrolytes

Differential Scanning Calorimetry (DSC) and Thermal Gravimetric Analysis were performed on the gelled electrolytes to investigate the effect of the salt content on the thermal properties of the gelled systems. DSC analyses were performed on PMMA-Li-PC-and PMMA-Li-PC-EC gel polymer electrolytes prepared at different salt concentrations (0.1 M, 0.5 M, 1 M, 2 M).

The estimation of the glass transition temperatures of each sample is determined from the DSC curves by the calculation of the second derivative Gibb's energy following the Equation 4.2.6.1 [41], following the T_g on the heating curve as a step change or discontinuity in the heat capacity baseline in each DSC curve:

$$c_p \equiv \left(\frac{\delta H}{\delta T}\right)_P \equiv T \left(\frac{\delta S}{\delta T}\right)_P \equiv -T \frac{\delta^2 G}{\delta^2 T^2} \qquad (4.2.6.1)$$

Where G is the Gibbs energy (J mol^{-1}), S is the entropy (J K^{-1}), c_p is the specific heat capacity at constant pressure (J kg^{-1} K^{-1}), H is the enthalpy (J) and T is the temperature (K), respectively.

Figure 4.2.6.1 shows the DSC thermogram collected on the pure PMMA powder and the second derivative (assists in determining T_g). It is possible to see the glass transition temperature of pure PMMA powder falls at 101.5 °C, which is at least 10 degrees lower than other values reported in the literature [41].

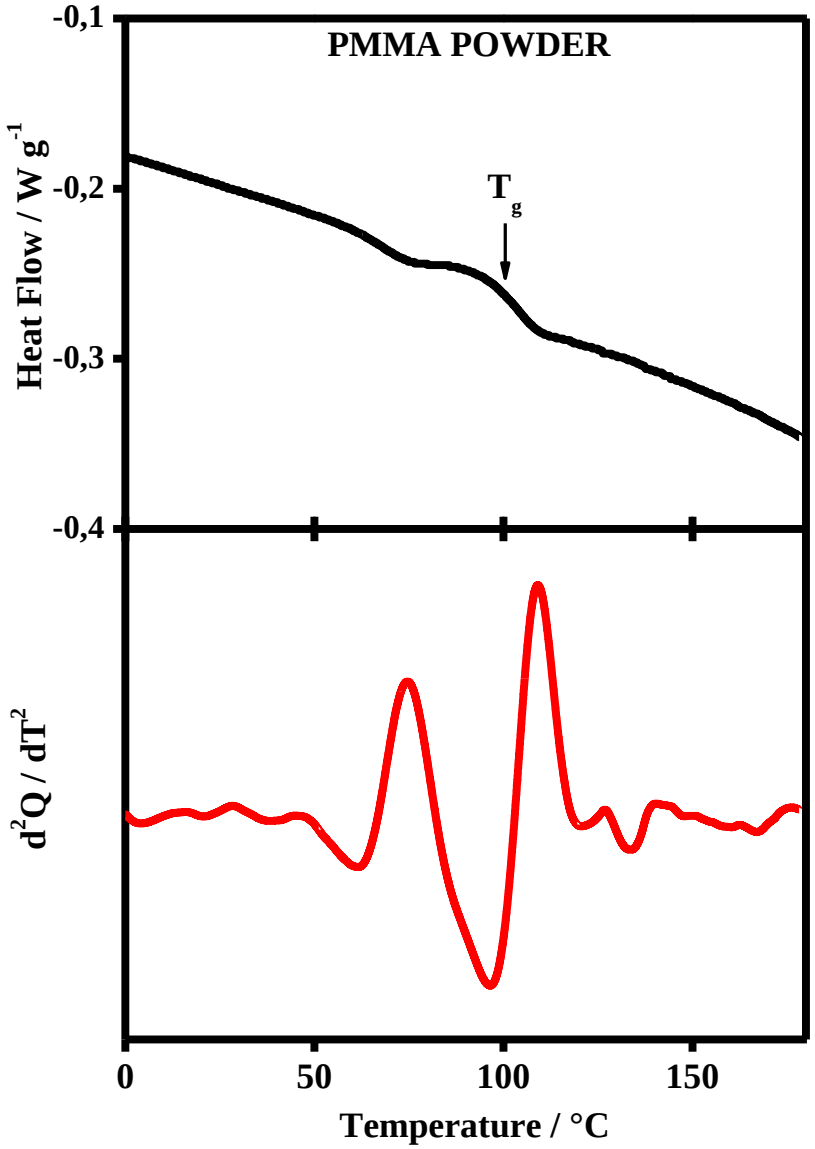

Figure 4.2.6.1. The Differential Scanning Calorimetry (DSC) curve (black solid curve) and the second derivative of the respective DSC signal (red solid curve) collected during a heating process with a rate of 10 °C/min on PMMA pure powder.

Figures 4.2.6.2 and 4.2.6.3 show the DSC thermograms of the PMMA-Li-PC and PMMA-Li-PC-EC gel polymer electrolytes at the different salt concentrations (0.1 M, 0.5 M, 1 M, 2M) and second derivative (assists in determining T_g).

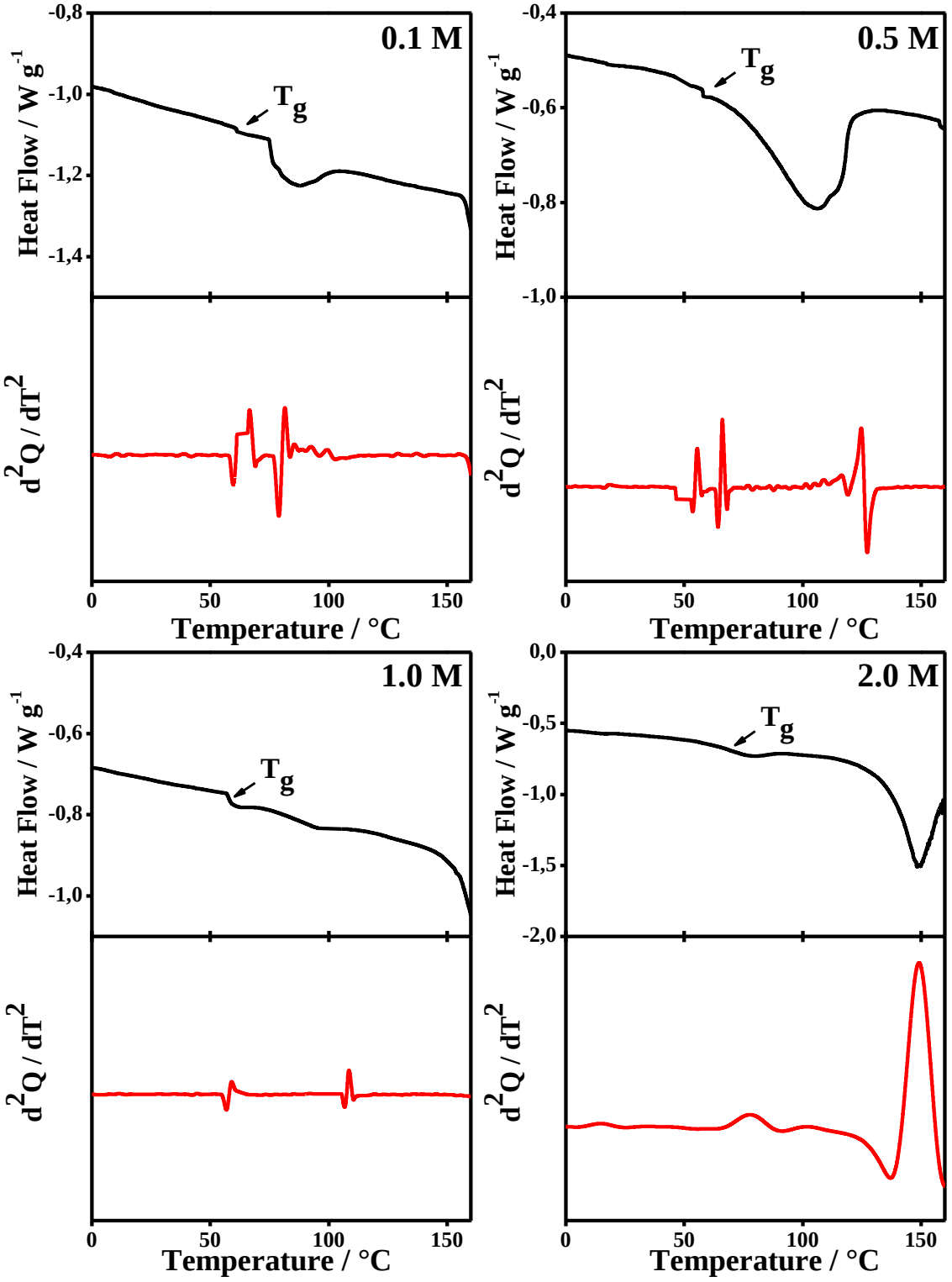

Figure 4.2.6.2. The Differential Scanning Calorimetry (DSC) curve (black solid curve) and the second derivative of the respective DSC signal (red solid curve) collected during a heating process with a rate of 10 °C/min on PMMA-Li-PC gel polymer electrolyte at different salt concentrations: 0.1 M, 0.5 M, 1 M, and 2 M.

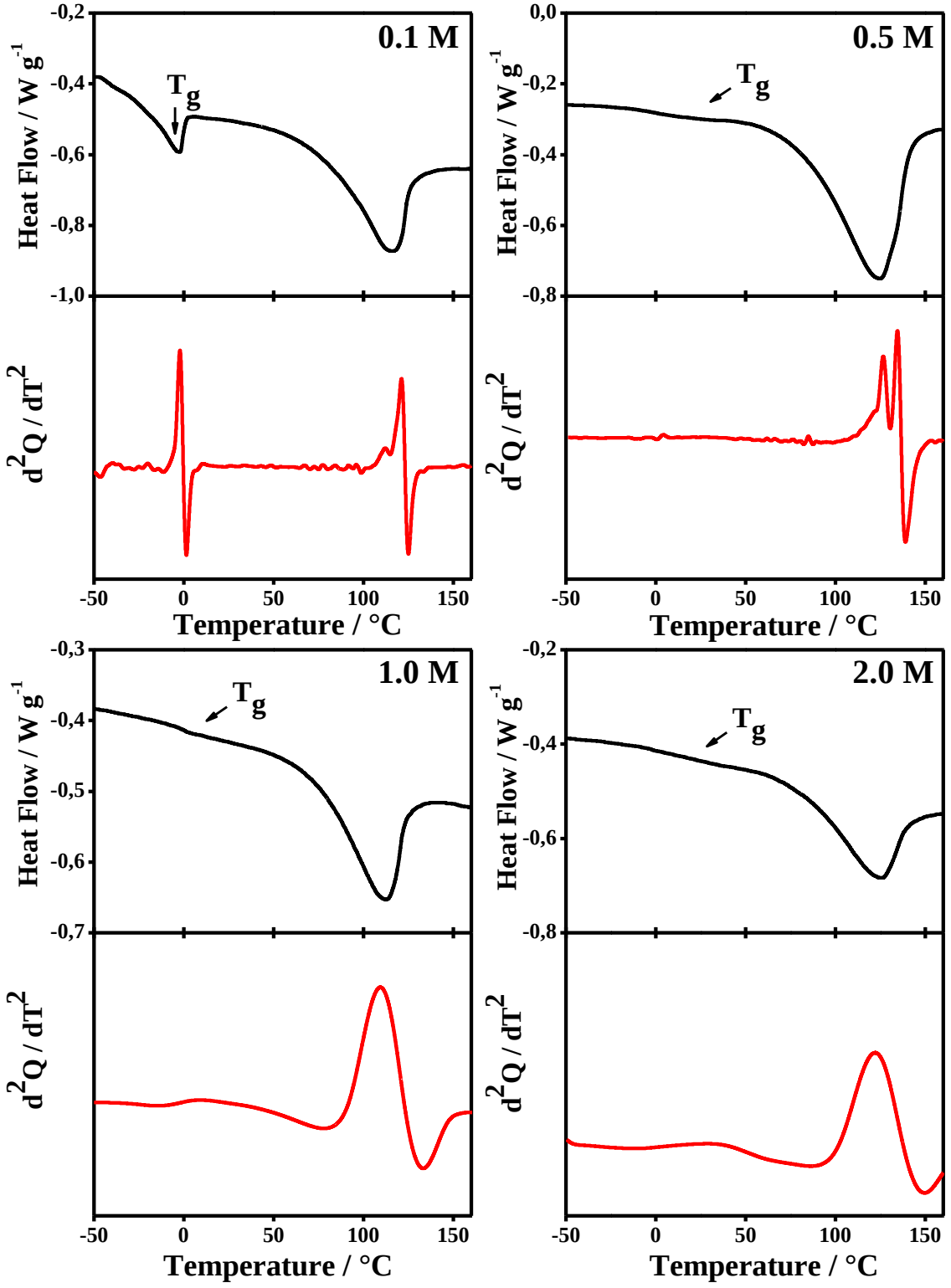

Figure 4.2.6.3. The Differential Scanning Calorimetry (DSC) curve (black solid curve) and the second derivative of the respective DSC signal (red solid curve) collected during a heating process with a rate of 10 °C/min on PMMA-Li-PC-EC gel polymer electrolyte at different salt concentrations: 0.1 M, 0.5 M, 1 M, and 2 M.

In Figures 4.2.6.2 and 4.2.6.3 endotherms around 100°C can be seen in the thermograms and these endothermic peaks close to 100°C are due to the vaporization of small amounts of water in the PMMA-Li-PC electrolyte systems [17]. However, for the systems studied here, IR spectra, which are very sensitive to the presence of water, indicated that there was no water present in any of the systems. TGA data collected provides information as to what these endotherms are.

Figure 4.2.6.4 shows TGA data for pure PMMA (upper image) and a representative TGA weight loss curve for the gel systems (lower image).

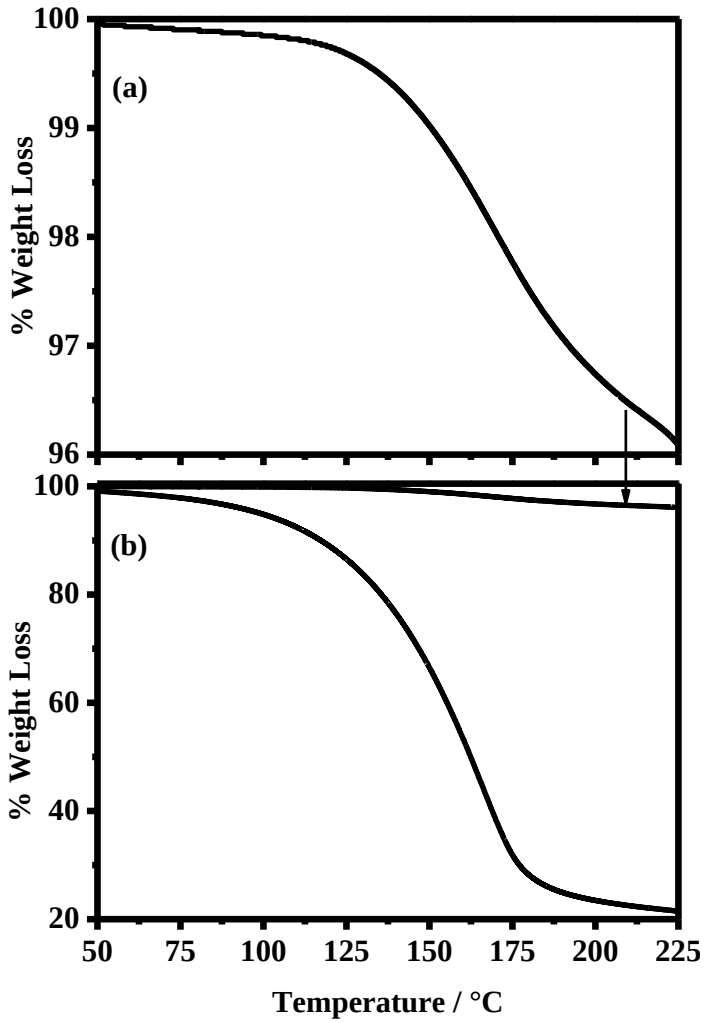

Figure 4.2.6.4. TGA data for PMMA polymer (top) and PMMA-Li (0.5M)-PC-EC gel (bottom). The PMMA data have been plotted in the bottom image for comparison as indicated by arrow.

Studies of pure PMMA polymer have found that it often contains unreacted methyl methacrylate (MMA) monomer, which has a boiling temperature of 101°Cas reported in the literature [42] the volatilization of unreacted residual monomer can be responsible for weight loss in PMMA at temperatures below 210°C. The amounts of MMA range from a fraction of 2 % to over 5% depending on the polymerization process forming the PMMA [43-46]. The observed weight loss seen in the upper image in Figure 4.2.6.4 appears to be due to the loss of unreacted monomer. The lower image in Figure 4.2.6.4 is the TGA for a typical gel system studied in this work. A weight loss of approximately 70% is observed in the temperature range from 100°C to 250°C before further weight loss for other degradation processes occurs at higher temperatures (not shown). Thermal analysis studies [45, 47] for PMMA polymer in this temperature range show weight loss can also be due to polymer chain degradation that results in monomer being formed. It is known that PMMA thermally degrades by three processes: a lower temperature process initiated by scissions of head-to-head linkages in the backbone forming monomer, a middle-temperature degradation of unsaturated end groups, and the highest temperature degradation due to breaking of other backbone bonds. The head-to-head bond breakage occurs at the lowest temperature of the three degradations (above 100° but below 250°C) because the bond dissociation energy of these linkages is estimated to be less than that of other C–C bonds in the backbone chain due to a large steric hindrance [35].

Comparing the TGA data for the PMMA and the gel, shown in Figure 4.2.6.4, one can see that while there is a large difference in the loss of weight between PMMA polymer and the gel, the temperature range for weight loss and shape of the curves are very similar indicating the weight loss process is associated with the same process, in this case monomer volatilization. In the pure PMMA, the size of the weight loss (~ 4%) indicates the loss is due to unreacted monomer being volatized [42]. In the gel the large weight loss (70%), is due to head-to-head chain scission and volatilization of the MMA monomer formed by degradation. The PC plasticizers in these gels, PC and EC, appear to facilitate head-to-head linkage degradation and the resulting large weight loss.

Some work on gel electrolytes has attributed the weight loss in this range to the plasticizer PC being volatized [48]. This does not seem likely for the systems studied here since the boiling temperatures for the two plasticizers used, PC (248°C) and EC (243°C) are much higher than where the loss starts at just above 100 °C. This loss would appear to be due

again to loss of any unreacted MMA monomer present for PMMA and to scissions of head-to-head linkages in the PMMA backbone and then volatilization of the resulting monomer from the gels. All the endotherms in the DSC thermograms for the gels are located in this temperature range (see Figures 4.2.6.2 and 4.2.6.3) and hence must be attributed to monomer volatilization. Importantly, the gels are stable up to temperatures around 100°C, which means that they have a good use range for electrolyte applications. Understanding the TGA data now allows focusing on information gained from glass transition data. The Tg have been labeled in Figures 4.2.6.2 and 4.2.6.3. The T_g for the 0.1 M PMMA-Li-PC-EC has a slightly different form than other T_gs seen in the thermograms, but was confirmed by the cooling thermogram (not shown) to be the glass transition temperature. The addition of solvents such as propylene carbonate and ethylene carbonate have a plasticization effect on the polymeric chains and decreases the glass transition temperatures of the PMMA polymer by facilitating chain movement [19]. This is seen in this study since the glass transition temperatures for the PC and PC-EC systems is lowered from the 101.5°C for pure PMMA.

For the PMMA-Li-PC system, the T_g drops around 40°C with the addition of a PC plasticizer and the lithium salt. The T_g then remains relatively constant for the 0.1-1.0 M concentrations of $LiClO_4$. While the PC lowers the glass transition temperatures in this concentration range, the fact that the T_g remains relatively constant, indicates that there are little interactions between the polymer and lithium ions.

The experimental values of T_g from DSC curves for all systems are summarized in Table 4.2.6.1.

[$LiClO_4$] (mol/l)	**PMMA T_g (°C)**	**PMMA-Li-PC T_g (°C)**	**PMMA-Li-PC-EC T_g (°C)**
0.0	101.5	/	/
0.1	/	61.9	-1.94
0.5	/	58.3	4.41
1.0	/	59.0	7.80
2.0	/	78.1	36.3

Table 4.2.6.1. Glass transition temperatures obtained from the DSC studies performed on PMMA and PMMA-Li-PC and PMMA-Li-PC-EC polymeric gel electrolytes at different salt concentrations: 0.1 M, 0.5 M, 1 M and 2 M.

At the lowest concentrations, the lithium ions interact predominantly with the solvent PC molecules and therefore the T_g reflects only interactions between the PMMA and the solvents molecules, the lithium ions are not significantly interacting with the polymeric chains [40]. However, when the concentration is increased to 2.0 M, the T_g increases showing interactions now occurring between the lithium ions and polymer chains. For the polymeric gel at the highest salt concentration, the amount of lithium ions becomes so high that ions can interact with solvent molecules, counterions, and polymeric chains [16]. The fact that the increasing salt concentration increases the interactions between the lithium ions, the solvent molecules, the counterions, and the polymeric chains was also shown in the IR investigations discussed above. Interactions with the polymeric chains induce an increase in the rigidity of the PMMA that is reflected in the increasing glass transition temperatures, T_g, as shown in Table 4.2.6.1. This increase indicates a decrease in polymer chain segmental motion. Since the Vogel-Tammann-Fulcher (VTF) model for ion transport in polymer electrolytes states that ion transport is assisted by polymer segmental motion, a higher T_g associated with less segmental motion [49], could be partially responsible for the small reduction in conductivity for the 2 M PMMA-Li-PC system seen in Figure 4.2.6.4. This factor and the small decrease in free ion concentration shown by IR data (see Figure 4.2.4.4.6 insert plot), probably both contribute to this small reduction in ionic conductivity.

The combined solvent PMMA-Li-PC-EC has the most reduction in glass transition temperatures, which in general by the VTF model, would favor higher ionic conduction. While the reduction in the glass temperature is much greater than the PMMA-Li-PC system, the T_gs also remain relatively constant for 0.1-1.0 M concentrations of $LiClO_4$ ranging from -1.94 to 7.80°C. This again indicates that there are little interactions between the polymer chains and lithium ions for these concentrations. When comparing these data to the ionic conduction data shown in Figure 4.2.3.1.6, the increase in ionic conductivity compared to the PMMA-Li-PC could be facilitated by the much lower T_g values for the PMMA-Li-PC-EC gel. However, since T_g is relatively constant up to the 1.0 M concentration, the change in ionic conduction appears to be due to the increase in free ion concentration with the increase in $LiClO_4$ concentration as shown in the insert plot in Figure 4.2.4.4.7 and not a change in segmental motion. When the concentration is increased to 2.0 M, the free ion concentration continues to increase (Figure 4.2.4.4.7 insert

plot); however, the concentration of salt is great enough that it can now interact with the polymer chains, raising the T_g by almost 30°C to approximately 36°C thus hindering segmental motion. The IR data discussed above and shown in Figure 4.2.4.3.11 also confirms that the lithium ions have strong interactions with the PC chains at this higher concentration. It is this reduction in segmental motion and not the concentration of free ions that greatly lowers the ionic conduction for the 2 M system as seen in Figure 4.2.3.1.6.

Results from the thermal analysis can help to explain the relatively higher value of ion conduction for the PMMA-Li-PC-EC system compared to other studies done in the literature. As discussed above, the PMMA used in this study could have as much as 4% unreacted monomer in the PMMA polymer. The very nonpolar monomer PMMA remaining in the PMMA polymer could have two effects. First, it is known that the MMA monomer in PMMA acts as a plasticizer [43, 50, 51]. In addition to the PC-EC plasticizers, the presence of the monomer plasticizer would further lower the Tg of the PMMA increasing ion conduction. The presence of the unreacted monomer acting as an additional plasticizer could be the reason that the Tg for the pure PMMA used in our work was found to be lower than other Tg values for PMMA found in the literature (see above). Interestingly, studies of PMMA-$LiClO_4$-PC and PMMA- $LiClO_4$-PC-EC systems described in the literature [15-21] have all heated the PMMA polymer used to prepare gels to temperatures of 55°C to 100°C under vacuum for up to 48 hours. This heating under vacuum was done to remove any water in the PMMA used. Since our IR data indicated that the PMMA used here did not contain water, the PMMA used in this study was not heated. It is well known in the literature [45, 47, 53-55], and our TGA data presented in this work has shown, that heating PMMA polymer will remove unreacted monomer. This is why DSC endotherms associated with the vaporization of MMA (see above) and TGA weight loss data, Figure 4.2.6.4, show the presence of monomer in our systems. This is compared to other studies in the literature on these systems using thermal analysis techniques [3-5] that do not show DSC endotherms at this temperature, *i.e.*, there was no monomer in their samples because of heating under vacuum. Again, the presence of the monomer in the samples could further lower the Tg increasing ion conduction. Second, the MMA molecule is very nonpolar. This nonpolar molecule acting as a plasticizer and being in close proximity to the PMMA backbone would further hinder

interactions between the polymer chains and lithium ions freeing ions to move in the plasticizer molecules in the gel. As described above, only when the concentration is at 2.0M is the concentration of lithium ions high enough so that interactions with the polymer chains are forced, raising the T_g and thus hindering segmental motion, lowing ion conduction. The concept of polymer monomer acting as a plasticizer is interesting and warrants further investigation.

4.2.7 Conclusions

In this work, two types of electrolytes have been studied: liquid electrolytes and gel polymer electrolytes. The liquid electrolyte systems are composed of $LiClO_4$ which is dissolved in a single plasticizer such as PC and in a mix of PC and EC at the different concentrations of 0.1M, 0.5 M, 1 M 2 M. The gel polymer electrolytes are based on the concentration (20:80) % w/w between the PMMA and the electrolyte solution of $LiClO_4$ in PC and in a mixture of PC and EC at the different salt concentrations (0.1 M, 0.5 M, 1 M, 2 M). Structural, electrochemical, and thermal studies were conducted to characterize both liquid electrolytes and gel polymer electrolytes.

Linear Sweep Voltammetry showing the anodic stability confirms the stability of the polymeric gel electrolyte studied for a voltage of about 4 V.

The highest value of conductivity has been found for the system (20:80) % w/w PMMA-Li-PC-EC and it is equal to $\sigma = 0.031$ S cm^{-1} at 1 M.

A detailed IR analysis of liquid electrolytes and gel polymer electrolytes has been done. These studies facilitated the understanding of the physical-chemical mechanisms of the ionic conductivity inside the polymeric gel electrolytes. It has been shown that increasing the salt concentration increases the interactions between the lithium ions, the solvent molecules, the counterions, and the polymeric chains.

DSC measurements, supported by IR data, revealed that the systems made with ethylene carbonate, PMMA-Li-PC-EC compared to the PMMA-Li-PC, have a lower Tg promoting segmental motion and have good concentrations of free ion. Both segmental motion and free ion concentrations were found to be significant in promoting high ionic conduction.

Thermal analysis indicated residual MMA monomer could be present in the PMMA used to make the gels. Since the monomer is known to plasticize PMMA the resulting increase

in polymer chain segmental motion could be responsible for the high ion conduction for the PMMA-Li-PC-EC system seen here when compared to other works done in literature [15, 20-21]. As a result of the present study, future research will be focused on PMMA-Li-PC-EC polymeric gel electrolyte in the manufacturing of electrochromic devices for energy-saving applications.

4.2.8 References

[1] V. K. Thakur, G. Ding, J. Ma, P. S. Lee, X. Lu, *Adv. Mater*., (2012) **24** 4071-4096.

[2] K. J. Siczek, in *"Next-Generation Batteries with Sulfur Cathodes"*, Academic Press, (2019) 7 79-115.

[3] K. Xu, *Chem. Rev.* (2004) **104** 4303-4417.

[4] M. Kucharski, T. Łukaszewicz, P. Mrozek, *Opto-electronics Rev.*, (2004) **12** 175-180.

[5] S. Sekhon, S. Deepa, S. A. Agnihotry, *Solid State Ionics*, (2000) **136-137** 1189-1192.

[6] Y. Alesanco, A. Vinuales, J. Rodriguez, R. Tena-Zaera, *Materials*, (2018) **11** 1-27.

[7] M. Kotobuki, in "*Polymer Electrolytes: Characterization Techniques and Energy Applications- First Editon",* Wiley (2020) 1-21.

[8] L. Long, S. Wang, M. Xiao, Y. Meng, *J. Mater. Chem. A*, (2016) **4** 10038-10069.

[9] M. U. Rani, R. Babu, S. Rajendran, *International Journal of ChemTech. Research*, (2013) **5** 1724-1732.

[10] M.Zhu, J. Wu, Y. Wang, M. Song, L. Long, S. H. Siyal, X. Yang, G. Sui, *Journal of Energy Chemistry*, (2019) **37** 126-142.

[11] I. Nicotera, C. Oliviero, G. Ranieri, A. Spadafora, M. Castriota, E. Cazzanelli, *J. Chem. Phys.*, (2002) **117** 7373-7380.

[12] I. Nicotera, L. Coppola, C. Oliviero, M. Castriota, E. Cazzanelli, *Solid State Ionics* (2006) **177** 581-588.

[13] M. Castriota, T. Caruso, R. G. Agostino, E. Cazzanelli, W.A. Henderson, S. Passerini, *J. Phys. Chem. A*, (2005) **109** 92-96.

[14] M. Castriota, D. Teeters, *Ionics*, (2005) **11** 220-225.

[15] G. B. Appetecchi, F. Croce, B. Scrosati, *Electrochimica Acta*, (1995) **40** 991-997.

[16] O. Bohnke, G. Frand, M. Rezrazi, C. Rousselot, C. Truche, *Solid State Ionics* (1993) **66** 105-112. C.

[17] O. Bohnke, C. Rousselot, P. A. Gillet, P. A., C. Truche, *Journal of the*

Electrochemical Society (1992) **139** 1862-1865.

[18] G. Frand, C. Rousselot, O. Bohnke, *The International Society for Optical Engineering*, (1992) **1728** 157-164.

[19] P. Pal, A. Ghosh, *J. Appl. Phys.* (2017) **122** 1-9.

[20] P. E. Stallworth, S. G. Greenbaum, F. Croce, S. Slane, M. Salomon, *Electrochimica Acta* (1995) **40** 2137-2141.

[21] K. M. Mahbor, *Solid State Ionics*, (2002) 321-328.

[22] M. Tretera, J. Reiter, J. Vondrák, M. Sedlaříková, *The Sixth International Conference ABA*, Brno, University of Technology, (2005) **14686** 60.

[23] B. Mei, O. Munteshari, L. Lau, B. Dunn, L. Pilon, *J. Phys. Chem. C*, (2018) **122** 194-206.

[24] C. Wohlfahrt, in *"Volume 6 Permativity Table - Static Dielectric Constants of Pure Liquids and Binary Liquid Mixtures",* Springer-verlag Berlin And Heidelberg Gmbh & Co. Kg, (2008) 5-69.

[25] H. A. Willis, V. J. Zichy, P. J. Hendra, P. J., *Polymer (Guildf).*, (1969) **10**, 737-746.

[26] A. H. Kusptov, G. N. Zhizhin, G. N., in *"Handbook of Fourier transform Raman and infrared spectra of polymer"*, Elsevier, Amsterdam (1998).

[27] S. Licoccia, M. Trombetta, D. Capitani, N. Proietti, P. Romagnoli, M. Di Vona,. *Polymer (Guildf)*, (2005). **46**, 4670-4675.

[28] Z. Wang, Z., B. Huang, H. Huang, L. Chen, R. Xue, F. Wang, F, *Solid State Ionics*, (1996) **85** 143–148.

[29] P. A. Brooksby, W. R. Fawcett, *Spectrochim. Acta - Part A Mol. Biomol. Spectrosc.* (2006) **64** 372–382.

[30] M. Deepa, S. A. Agnihotry, D. Gupta, R. Chandra, *Electrochim. Acta*, (2004) **49** 373-383.

[31] C. L. Angell, *Trans. Faraday Soc.*, (1956) **52** 1178-1183.

[32] D. Battisti, G. A. Nazri, B. Klassen, R. Aroca, *J. Phys. Chem.*, 1993, (1993) **97** 5826–5830.

[33] Y. Ikezawa, H. Nishi, H. *Electrochim. Acta*, (2008) **53** 3663-3669.

[34] L.H. Sim, S.N. Gan, C.H. Chan, R. Yahy, *Spectrochimica Acta Part A*, (2010) **76** 287-292.

[35] Z. Wang, Z., B. Huang, B., H. Huang, R. Xue, L. Chen, F. Wang, *J. Electrochem. Soc.*, (1996). **143** 5.

[36] B. Fortunato, B., P. Mirone, G. Fini, G., *Spectrochimica Acta*, (1971) **27** 1917-1927.

[37] Y. Chen, Y. Zhang, L. Zhao, *Phys. Chem. Chem. Phys. Phys*., (2004) **6** 537–542.

[38] M. Salmon, M. Xu, E. M. Eyring, S. Petrucci, *J. Chem. Phys*., (1994) **98** 8234.

[39] W. Wieczorek, G. Lipka, G. Zukowska, H. Wycislik, *J. Phys. Chem. B*, (1998) **102** 6968.

[40] A.V. Colin, *Prog. Solid St. Chem.*, (1987) **17** 145-261.

[41] U. Ali, K. J. B. A. Karim, N. A. Buang, *Polymer Reviews*, (2015) **55** 678-705.

[42] T. Hirata, T. Kashiwagi, J. E. Brown, *Macromolecules*, (1985) **18** 1410-1418.

[43] E. A. Ayaz, R. Durkan, A. Koroglu, B. Bagis, *Journal of Applied Biomaterials and Functional Materials*, (2014) **12** 228-233.

[44] C. Y. K. Lung, B. W. Darvell, *Dental Materials* (2005) **21** 1119-1128.

[45] P. Nising, T. Zeilmann, T. Meyer, *Chemical Engineering and Technology*, (2003) **26** 599-604.

[46] P. K. Vallittu, V. Miettinen, P. Alakuijala, *Dental Materials*, (1995) **11** 338-342.

[47] T. Kashiwagi, J. E. Brown, A. Inaba, K. Hatada, T. Kitayama, E. Masuda, *Macromolecules*, (1986) **19** 2160-2168.

[48] S. Ramesh, K. N. Bing, *Journal of Materials Engineering and Performance*, (2012) **21** 89-94.

[49] S. B. Aziz, T. J. Woo, M. F. Z. Kadir, H. M. A. Ahmed, *Journal of Science: Advanced Materials and Devices*, (2018) **3** 1-17.

[50] A. P. Farina, D. Cecchin, R. G. Soares, A. L. Botelho, J. M. F. Takahashi, M. O. Mazzetto, M. F. Mesquita, *Gerodontology*, (2012) **29** 155-160.

[51] W. J. Hayden, *General dentistry*, (1986) **34** 367-371.

[52] C. Y. K. Lung, B. W. Darvell, *Dental Materials* (2005) **21** 1119-1128.

[53] U. Kedjarune, N. Charoenworaluk, S. Koontongkaew, *Australian Dental Journal* (1999) **44** 25-30.

[54] D. J. Lamb, B. Ellis, D. Priestley, *Journal of Dentistry*, (1983) **11** 80-88.

[55] S. Y. Lee, Y. L. Lai, T. S. Hsu, *European Journal of Oral Sciences*, (2002) **110** 179-183.

4.3 Fabrication of *all-in-one* liquid -based electrochromic device made by Ethyl Viologen diperchlorate, 1,1'-Diethyl Ferrocene, Bisphenol-A glycerolate diacrylate and Irgacure 651 for Energy Efficient Windows

Abstract

In this work, the realization of an electrochromic device of size (10 cm × 10 cm) based on the (60:40) % w/w concentrations between Ethyl viologen diperchlorate ($EV(ClO_4)_2$), 1,1'-diethyl ferrocene (DEFc) in Propylene Carbonate (PC) as the electrochromic solution and Bisphenol-A glycerolate (1 glycerol/phenol) diacrylate (BPA) and 2,2-Dimethoxy-2-phenylacetophenone (Irgacure 651) mixture has been conducted. The use of the lithography technique for the realization of a spacer pattern with a thickness of about 15-20 µm has been shown. Electrochemical and optical properties of the electrochromic device have been studied. The device shows reversible electrochromic behavior as confirmed by cyclic color variation due to the reduction and oxidation process of the $EV^{2+}/EV^{\bullet+}$ couple. The electrochromic device shows a variation of the % transmittance in the visible region at 400 nm of 59.6 % in the OFF state and in the ON state at 1 V a value of 5.14 % and at 3 V of 0.48 %. At 606 nm the transmittance in the bleached state is 84.58% in the OFF state and then its decreases to 10.71% at 1V and 1.01% when it is fully colored in its ON state. In the NIR region at 890 nm the device shows transmittance of 74.3 % in the OFF state and a value of 52.5 % and 23.7 % at 1 V and 3 V in the ON state, respectively.

4.3.1. Introduction

The phenomenon of electrochromism is attracting much attention because of its diverse application in smart windows to lower power display systems [1-3] using different kinds of available electrochromic materials: organic [4] and inorganic [5, 6]. One interesting class of materials is the bipyridinium species based on N, N-diquaternization of 4,4'-bipyridine, also known as viologens [4,7]. Viologen specie is a reducing material that exhibits reversible redox reaction because of the one or two-electron reductions and they

have been studied for their visible color change associated with their reductions, high color contrast, switchable electrochromic properties and for the construction of flexible electrochromic devices [4,7-9]. These materials have been used in many applications *e.g.*, as electron mediators, electrochromic display components, relay compounds in energy storage systems and herbicides [10]. The color of the viologens depends on the type of the substituents (alkyl, benzyl, and aryl) in the nitrogen position [11]. The well-known 1,1'-ethyl viologen diperchlorate presents three redox states which are ascribable to the formation of the di-cation (EV^{2+}, colorless), radical cation ($EV^{\bullet+}$, blue) and neutral viologen specie (EV, brown) with their low reduction potentials. Electrochromic devices have been made-up in different configurations using viologen as cathodic and ferrocene as anodic specie obtaining shorter time responses in the switching process of the electrochromic device [12] also in addition with liquid ions for improving the electrochemical stability of the electrolyte in the ECD [13], polythiophene[14], CNTs n-type doped [15] in sandwich structures composed of a thiol-terminated viologen as layer immobilized on an electrode of nanoparticles of Au acting as plasmonic antenna [16], metal oxide-metal complexes such as Prussian blue [17] and metal-supramolecular polymers [18, 19] conductive organic polymers [20].

In the present work, we proposed the fabrication of an electrochromic device in viologen/ferrocene-based system of dimensions (10 cm × 10 cm) for future energy-efficient smart windows. Device fabrication has been characterized by the application of the photolithography technique which has been detailed in the experimental section according with detailed processing guidelines [21]. The Cyclic Voltammetry technique provides details of the redox process that occurred in the system. Spectroscopy characterization such as Raman spectroscopy and UV-Vis-Nir spectroscopy have been carried out for the investigation of the electrochromism and the color switching of the device as a function of the externally applied potential by identifying the active species.

4.3.2. Experimental Section

4.3.2.1. Materials

Ethyl viologen diperchlorate ($EV(ClO_4)_2$), 98% purity), 1,1'-diethyl ferrocene (DEFc, 98% purity), Bisphenol-A glycerolate (1 glycerol/phenol) diacrylate (BPA, 98% purity),

2,2-Dimethoxy-2-phenylacetophenone (Irgacure 651, 99 % purity) and Propylene carbonate (PC) was purchased from Sigma Aldrich Company and they have been kept stored in the refrigerator. SU-8 2010 photoresist and SU-8 Developer (1-methoxy 2-propanol acetate) were obtained from MicroChem, MA, USA. A commercial masking film was provided by Fineline Imaging, Thin Metal Parts, USA. Isopropanol (99.5 % purity) was purchased from Sigma-Aldrich Company. Sodium hydroxide (NaOH ≥ 97 %, purity) was also provided by Sigma-Aldrich Company. All the compounds were preserved inside the Clean Room to prevent from absorbing moisture prior to preparation and to further characterizations.

4.3.2.2 Preparation of *all-in-one* electrochromic solution (60:40) % w/w ($EV(ClO_4)_2$:DEFc:PC)-(BPA:Irgacure651)

The electrochromic solution was made by following the addition of ethyl viologen diperchlorate ($EV(ClO_4)_2$), 1,1'-diethyl ferrocene (DEFc) and propylene carbonate (PC) at the following concentration ratios (6.4:3.75:89.85) % w/w. The molar ratio between ethyl viologen diperchlorate and 1,1'-diethyl ferrocene is (1:1). A second mixture was prepared using Bisphenol-A glycerolate diacrylate (BPA) and the photo-initiator 2,2-Dimethoxy-2-phenylacetophenone (Irgacure 651) following the concentration ratio (98:2) % w/w. The mixture was heated at 100 °C because of the high viscosity of BPA and stirred to obtain a homogenous sample. The final electrochromic solution was prepared in the following concentration ratio (60:40) % w/w between the electrochromic solution ($EV(ClO_4)_2$:DEFc:PC) and (BPA:Irgacure 651) mixture. The liquid-electrochromic mixture was heated at 100°C for a few minutes and it was stored in a dark place. In Figure 4.3.2.2.1 are depicted: a) the electrochromic solution and b) the mixture of BPA and Irgacure 651 used for the electrochromic device. Figure 4.3.2.2.2 shows the electrochromic mixture (60:40) % w/w ($EV(ClO_4)_2$:DEFc:PC) and (BPA:Irgacure651).

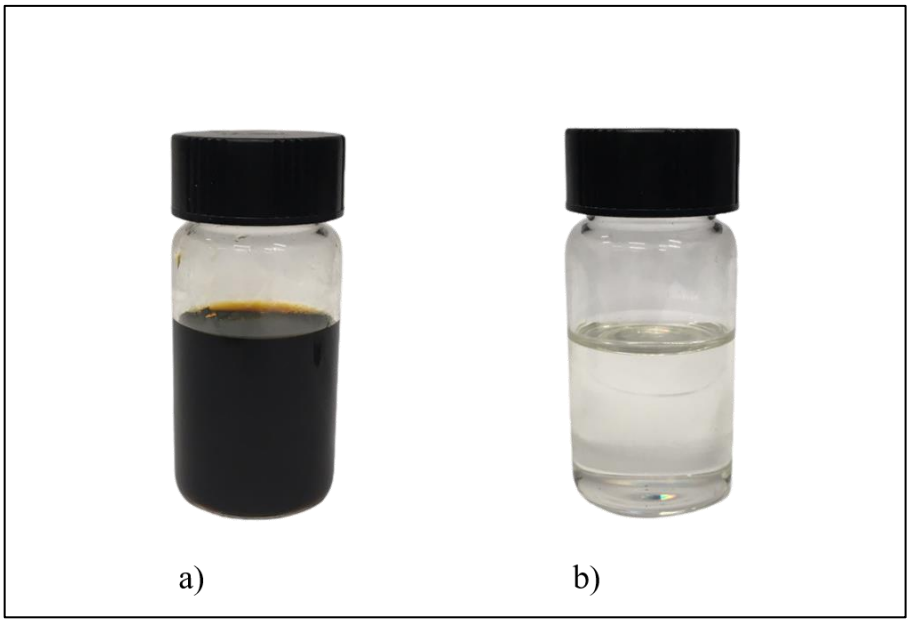

Figure 4.3.2.2.1. a) Electrochromic solution of ethyl viologen diperchlorate 1,1'-diethyl ferrocene (DEFc) and propylene carbonate in concentration of (6.4:3.75:89.85) % w/w and b) the mixture of Bisphenol-A glycerolate diacrylate and 2,2-Dimethoxy-2-phenylacetophenone.

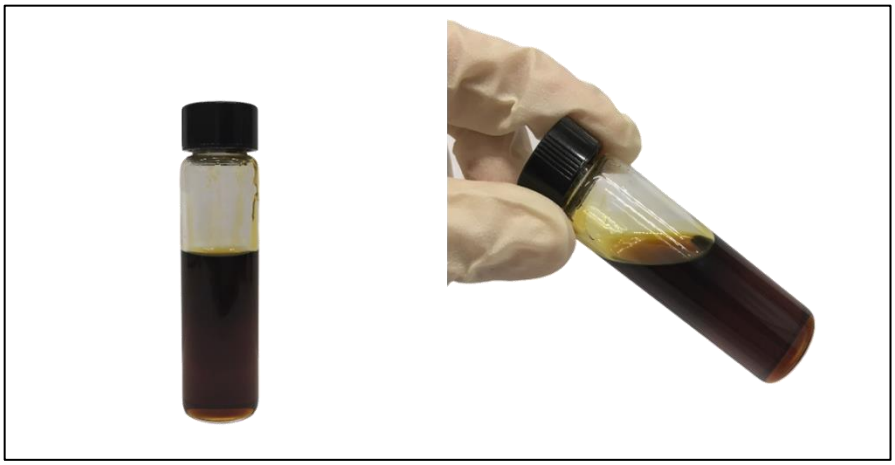

Figure 4.3.2.2.2 Electrochromic Mixture of ($EV(ClO_4)_2$:DEFc:PC) and (BPA:Irgacure 651) in concentration of (60:40) % w/w.

4.3.2.3 Fabrication of *all-in-one* (60:40) % (EV(ClO_4)$_2$:DEFc:PC)-(BPA:Irgacure651) electrochromic device having dimensions (10 cm ×10 cm)

The type of *all-in-one* electrochromic device was assembled following the schematic configuration:

ITO-coated glass/liquid-electrochromic mixture /ITO-coated glass

Where the ITO (indium tin oxide)–coated glasses are the two transparent electrodes where the electric field is applied and the liquid-electrochromic mixture is the electrochromic mixture in a concentration of (60:40) % w/w based on the mixture of ethyl viologen diperchlorate 1,1'-diethyl ferrocene (DEFc) and propylene carbonate in concentration of (6.4:3.75:89.85) % w/w and the mixture of Bisphenol-A glycerolate diacrylate and 2,2-Dimethoxy-2-phenylacetophenone in a concentration of (98:2) % w/w, respectively. A photoresist was used for the realization of a tidy pattern of spacers with a thickness (15-20 µm) by the application of the photolithography technique in accordance with the process guidelines provided by Microchem [21]. A schematic representation of the electrochromic device is given in Figure 4.3.2.3.1.

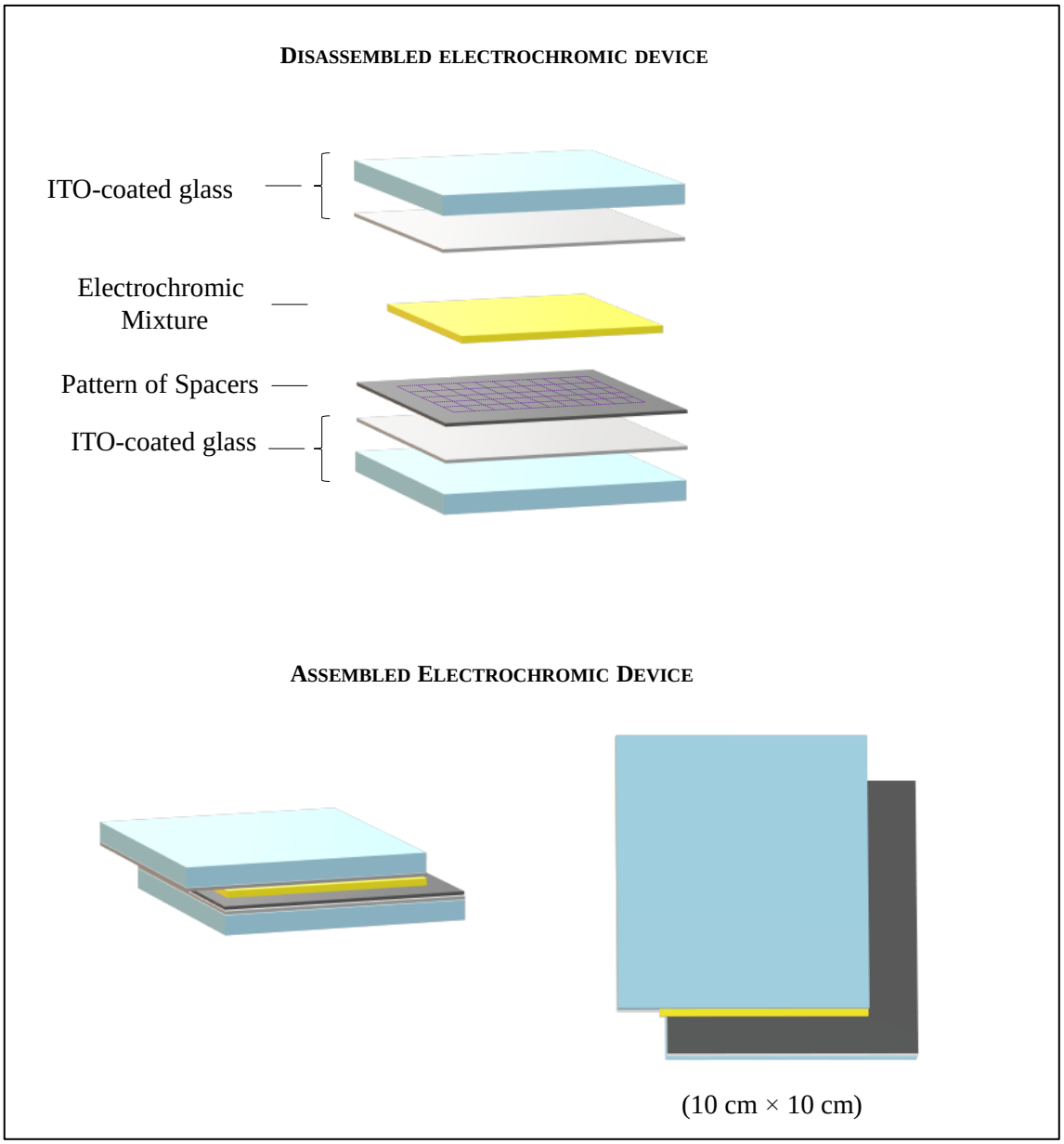

Figure 4.3.2.3.1. Schematic representation of the realized electrochromic device having dimensions (10 cm × 10 cm).

4.3.2.4 Photolithography process and production of a spacer-pattern (15-20) µm.

For the fabrication of the electrochromic devices, an accurate procedure was carried out in the clean room, where the yellow filter light (yellow illumination) was set in the room.

The yellow light is essential, specifically for UV-photo-sensitive applications because it blocks UV radiation reliably.

Previously all the ITO-coated glasses were cleaned with an aqueous solution of sodium hydroxide at 5 % w/w concentrations followed then by a de-ionized water rinse for the elimination of all traces of the cleaning solution. To dry off the glass, a jet of compressed air was used. The ITO-coated glasses were stored inside a Laminar Flow Cabinet- Helios to prevent further contaminations. The cleaning step is fundamental to obtaining maximum process reliability prior to applying the SU-8-2010 resist.

A flow chart depicted in Figure 4.3.2.4.1 shows all the separate steps of the process needed for the photoresist process to realize a thickness of the electrochromic device is included between (15-20 µm).

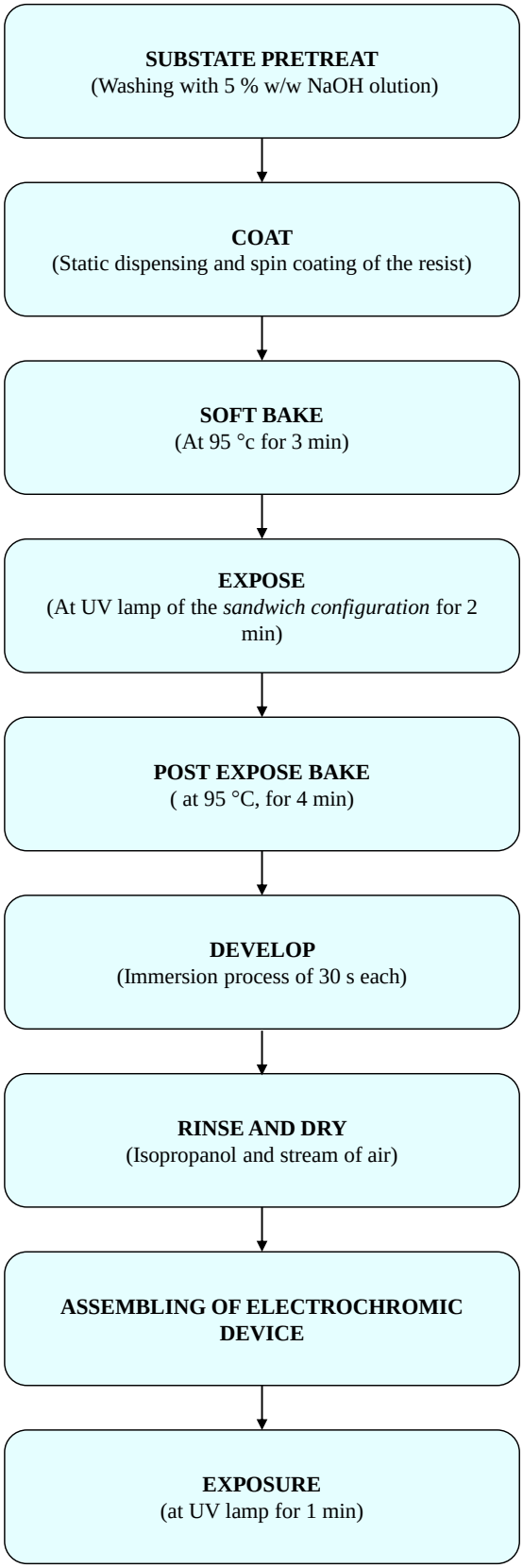

Figure 4.3.2.4.1. Flow Diagram for the Photoresist Process SU-8-2010 to produce a homogenous pattern of spacers of a thickness (15-20 μm).

A negative photoresist material such as SU-8-2010 was used to produce a uniform and tidy pattern of spacers in the electrochromic devices. After the *COAT STEP* which consists of the static dispensing of the resist on the surface of the substrate, spin coating conditions were set up to achieve the desired film thickness. In Figure 4.3.2.4.2 the static dispense (a) and the spin coater set up (b-c) are shown.

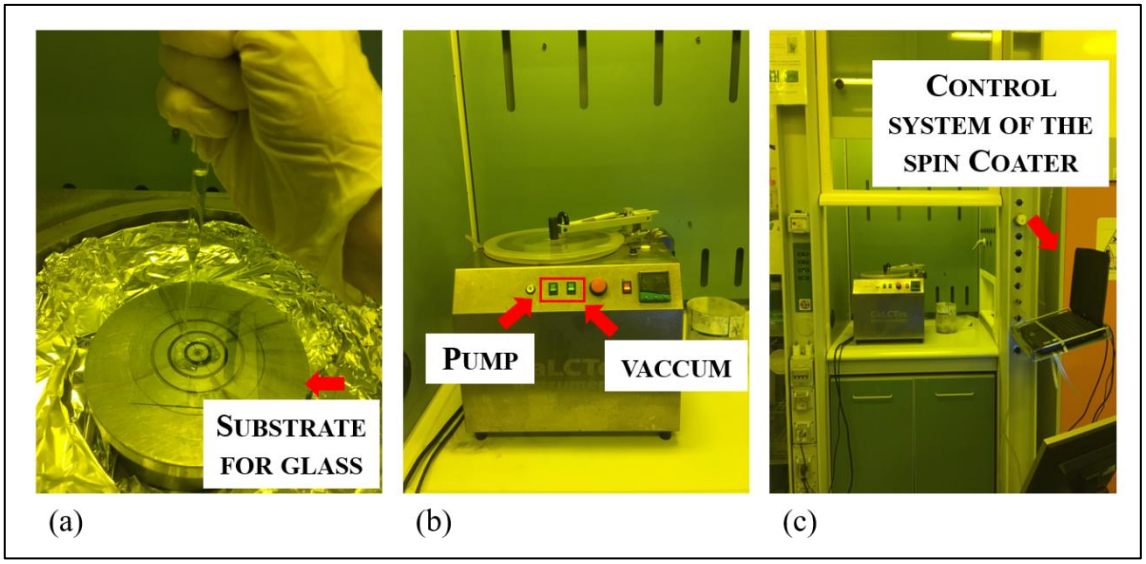

Figure 4.3.2.4.2. Static dispense of resist SU-8-2010 on the specific support (a) and spin coater set up used under the control of the operating system (b-c).

As datasheets recommended [21], film thicknesses of 15-20 microns can be achieved with a single coat process at 1500 rpm. The following SPIN COATING set-up was used: (1) ramp up from 0 rpm to 500 rpm with the acceleration of 100 rpm s^{-1} for a time of 5 seconds, (2) hold the rate of 500 rpm for a time of 5s, (3) ramp up to a final spin rate from 500 rpm to 1500 rpm at an acceleration of 250 rpm s^{-1} for a time of 4 s, (4) hold a rate of 1500 rpm for a total of 30 seconds, and (5) ramp down from 1500 rpm to 0 rpm with a deceleration of 300 rpm s^{-1} for 5 seconds. A next SOFT BAKE treatment is needed to evaporate the solvent and densify the film. So, the resist-spin coated on ITO-glass support is baked on a level hot plate at the temperature of 95 °C for a time of 3 min (Figure 4.3.2.4.3).

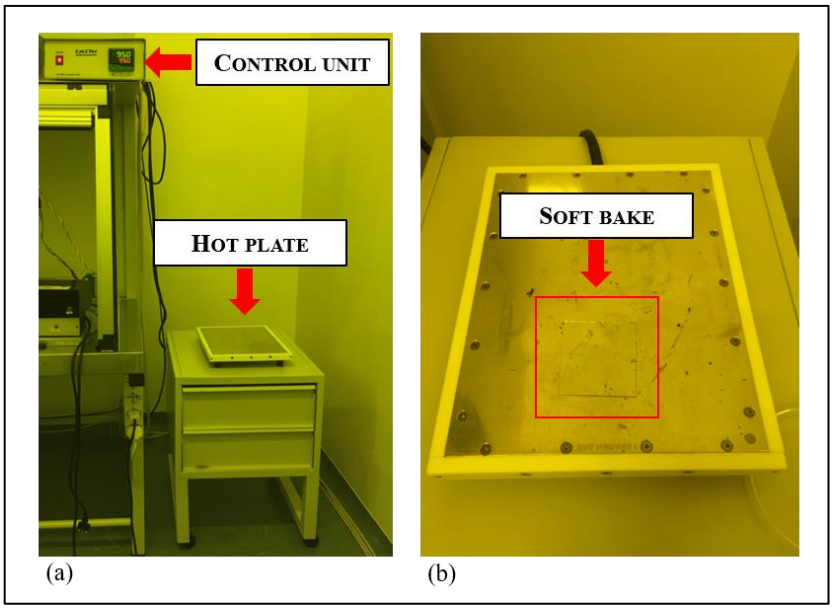

Figure 4.3.2.4.3. Bake set up composed of control unit and hot plate (a). Magnification of the soft bake step of the resist on the ITO-coated glass support at 95 °C for 3 min.

For the EXPOSE, a mask for lithography, as the type shown in the Figure 4.3.2.4.4 was used. A *sandwich configuration* containing the sample was realized as shown in Figure 4.3.2.4.5. The sandwich configuration is a multilayer system composed of four layers. There are two ITO-coated glasses that acts as supports, where insight of them, there is the resist-spin coated previously. The photolithography mask is put on the resist coating. The system is closed by two clips.

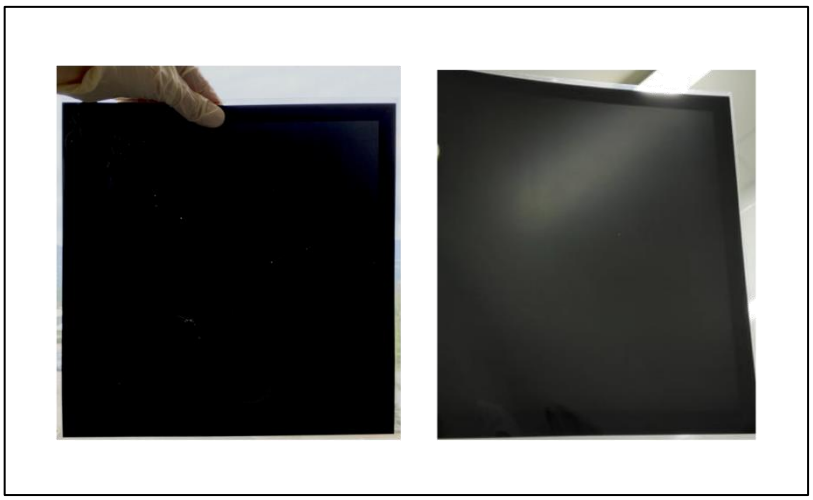

Figure 4.3.2.4.4. Top view of the photolithography mask (28 cm ×28 cm).

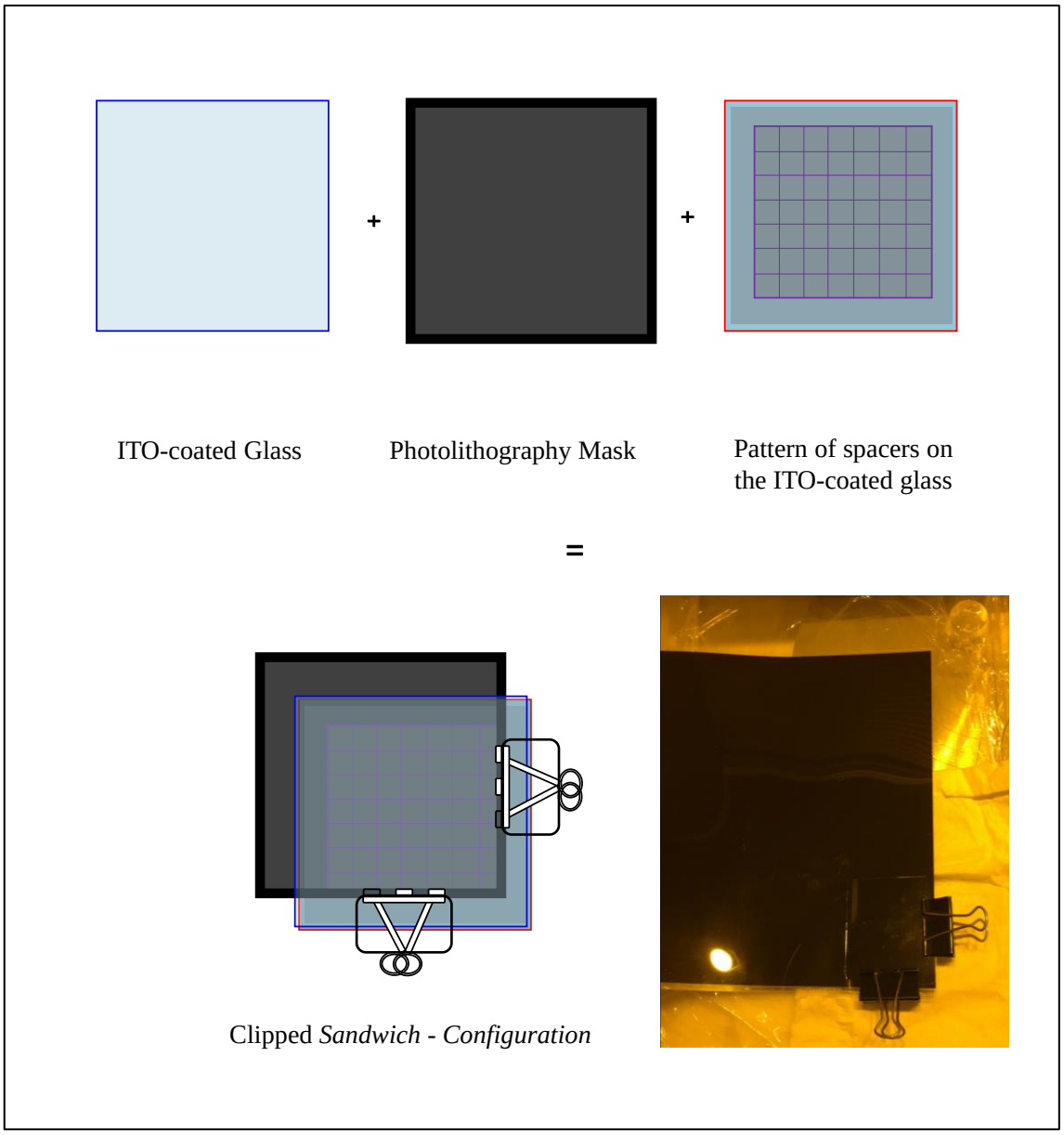

Figure 4.3.2.4.5. Schematic representation of the clipped *Sandwich – Configuration.*

The EXPOSE step was carried out at the UV lamp (350 - 400 nm) for a time of 2 min in a yellow-light condition. Following exposure, a POST EXPOSE BAKE (PEB) step of the sample was performed at the temperature of 95 °C for 4 min. to selectively cross-link the exposed portions of the film. A controlled bake treatment is recommended to further cross-link the imaged resist structures. For the DEVELOP of the resist, the SU-8-2010 developer was used under the operating chemical fume hood. The develop of the film was

performed with a multi-step of bathing or immersion process of the film in a developer solvent for 30 s (Figure 4.3.2.4.6).

Figure 4.3.2.4.6. Development of the resist SU-8-2010 in a bath of developing solvent.

Following the development step, the substrate was rinsed briefly with isopropanol and then dried with a gentle stream of air. Assembling of an electrochromic device was made, respectively of the surface area (10 cm × 10 cm). The electrochromic mixture of concentration (60:40) % w/w was put into the electrochromic device by squeezing technique. A small pressure was conducted on the device to eliminate all excess of the electrochromic mixture. The electrochromic device was sealed by epoxy glue and exposed at UV lamp for a time of 1 min to facilitate the polymerization of the BPA. For both electrochromic devices a tin wire of ITO was welded at the edges of the device both electrical cables for a better conduction process. The assembled electrochromic device is shown in Figures 4.3.2.4.7 (10 cm × 10 cm), respectively. The electrochromic device is

characterized by a light-yellow coloration that is due to the presence of the electrochromic mixture.

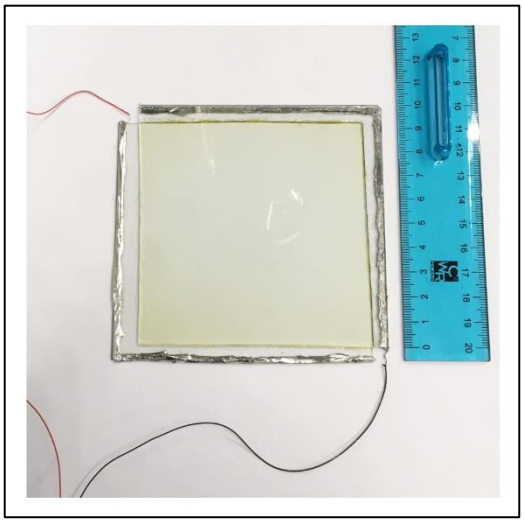

Figure 4.3.2.4.7. Electrochromic device (10 cm × 10 cm) based on electrochromic mixture in concentration (60:40) % w/w of Ethyl viologen diperchlorate 1,1'-diethyl ferrocene (DEFc) and propylene carbonate and bisphenol-A glycerolate diacrylate and 2,2-Dimethoxy-2-phenylacetophenone, respectively.

4.3.2.5 Characterization of *all-in-one* (60:40) % w/w ($EV(ClO_4)_2$:DEFc:PC)-(BPA:Irgacure651) electrochromic device

Cyclic Voltammetry measurements were carried out on the electrochromic devices in the cyclic potentials range from -2V to 2V at the scan rate of 50 mV s^{-1} using a Potentiostat/Galvonastat, model 2059 low instrument interfaced with Amel instruments – model 7800 interface (Amel Intruments). Junior Assist 2059 software was used for the acquisition of cyclic voltammetry measurement.

Raman spectra were acquired on Jobin Yvon micro-Raman LABRAM equipped with a CCD detector and an external Nd:YAG laser (λ = 532 nm emission, 50 mW power) as the excitation source. Neutral filter of optical density (OD 0.3) was employed to change the laser power. A 50x MPlan Olympus with a numerical aperture of 0.75 was used and the apparent diameter of the focused laser spot was about 2-3μm. The spectral resolution

was 2 cm^{-1}. All spectra were imported into OriginPro8 software for fitting manipulation. The baseline-correction procedure was required to adequately fit the band shapes.

UV-Vis-NIR measurements were performed by UV-Vis-NIR Spectrophotometer AvaSpec-2048-Avantes. The equipment included also, a Deuterium-Halogen light source (DH-2000 UV-Vis-Nir Lightsource Avantes) and Agilent E3632A DC Power Supply (0-15V, 7A). Analyses were conducted at room temperature. Each UV-Vis-NIR measurement was conducted in the wavelength range (200-1200 nm). Avaspec75 software was used for the acquisition of UV-Vis-NIR measurements. Origin Pro8 software was used for elaboration data.

4.3.3 Results and Discussion

4.3.3.1 Cyclic Voltammetry of *all-in-one* (60:40) % w/w (EV(ClO_4)$_2$:DEFc:PC)-(BPA:Irgacure651) electrochromic device

Basically, the device is based on the electrochromic mixture of propylene carbonate which contains the cathodic (ethyl viologen diperchlorate) and the anodic species such as the 1,1'-diethyl ferrocene. In the presence of 1,1'-diethyl ferrocene as the reducing agent, the ethyl viologen diperchlorate can be reduced under the application of an electric field following (Scheme 4.3.3.1.1) and it becomes a radical cation.

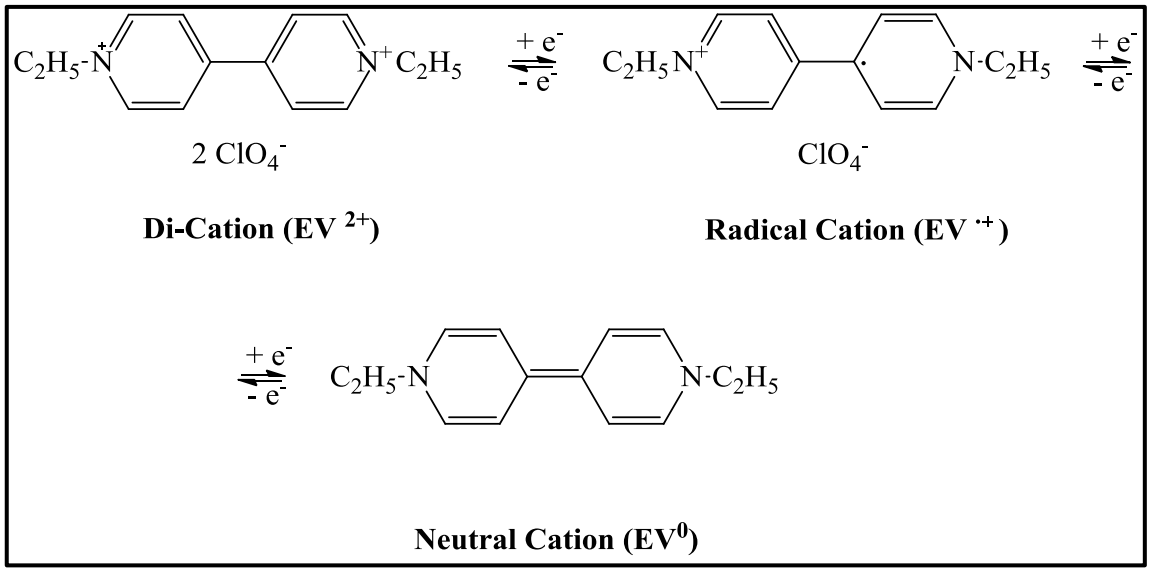

Scheme 4.3.3.1.1. Schematization of the redox process that occurred in the Ethyl Viologen diperchlorate under the application of a potential impressed on the electrode.

Scheme 4.3.3.1.2 shows the schematizing of the redox process of the 1,1'diethyl ferrocene when an external potential is applied to the electrochromic device.

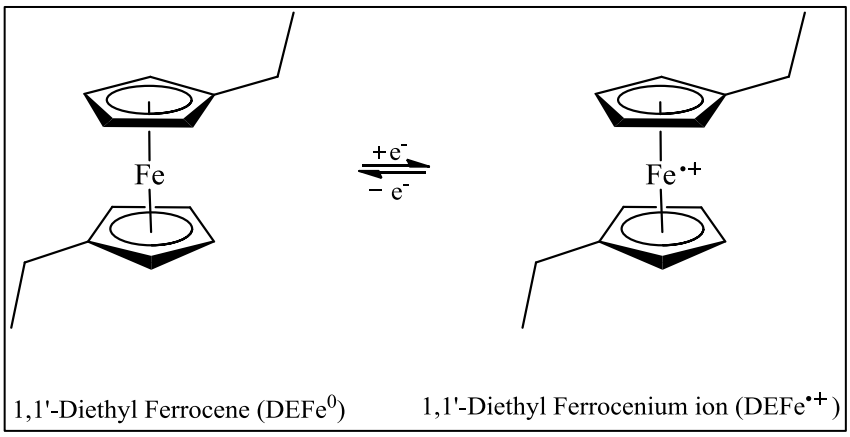

Scheme 4.3.3.1.2. Schematization of the redox process that occurred in the 1,1'-Diethyl Ferrocene under the application of a potential impressed on the electrode.

The electrochemical properties of the electrochromic devices in the concentration of (60:40) % w/w composed of the electrochromic mixture ($EV(ClO_4)_2$:DEFc:PC) and the mixture of BPA-Irgacure 651 have been carried out by Cyclic Voltammetry. Cyclic voltammetry measurements were conducted on the electrochromic device (10 cm × 10

cm) in the potential range from 2 V to -2 V at the scan rate of 50 mV s^{-1}. The reversible redox behavior of viologen can be confirmed *via* cyclic voltammetry. The cyclic voltammetry curve (I-V) registered for the electrochromic devices is shown in Figure 4.3.3.1.1. Ethyl viologen diperchlorate ($EV(ClO_4)_2$) can be a good candidate because it contains EV^{2+} which is a good electron acceptor and contains perchlorate ion which can act as the electrolyte.

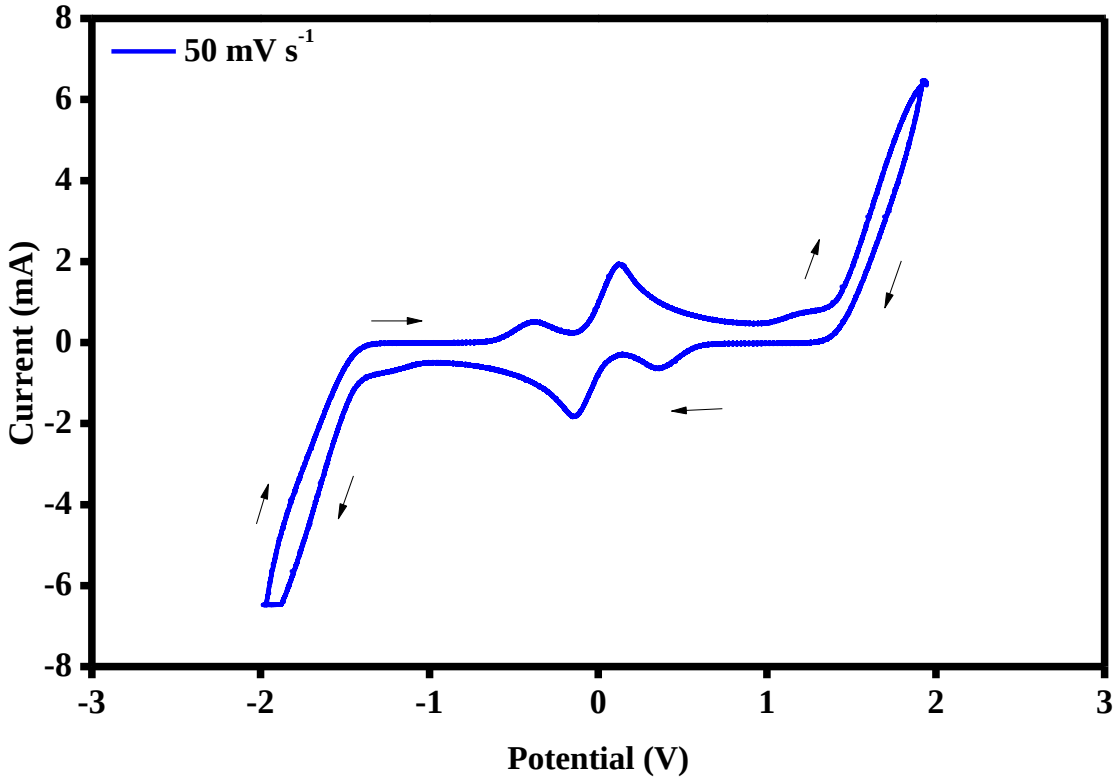

Figure 4.3.3.1.1. Cyclic voltammetry curves registered for electrochromic devices based on the concentration (60:40) % w/w composed of the Electrochromic mixture ($EV(ClO_4)_2$:DEFc:PC) and the mixture of (BPA-Irgacure 651), cycled at the scan rate of 50 mV s^{-1}.

In the obtained I-V curve, the cathodic current is imputable, at the same time to two processes for the $DEFc^0/DEFc^{\bullet+}$ and $EV^{2+}/EV^{\bullet+}$ couples. The first cathodic peak at about 0.35 V is ascribed to the oxidation of the $DEFc^0$ to $DEFc^{\bullet+}$ specie, while the second cathodic peak at about -0.14 V is referred to as the reduction of EV^{2+} (di-radical cation) to $EV^{\bullet+}$ (cation radical). The two cathodic steps of the involved species can be individuated by the color changes of the electrochromic device. The oxidation of the

$DEFc^0$ to $DEFc^{\bullet+}$ specie does not involve a color change, so the device preserves its light-yellow coloration. For what concern, the reduction of the EV^{2+} to $EV^{\bullet+}$, the device shows a color change from the light yellow to an intense dark blue color starting from about -1 V. The dark blue color of the electrochromic device is due to the presence of the radical cation $EV^{\bullet+}$.

The I-V curve is symmetric, so this means that in the reversed scan, the anodic current is composed of two peaks, which can describe both the reduction of the $DEFc^{\bullet+}$ to $DEFc^0$ at about -0.37 V and the oxidation of the $EV^{\bullet+}$ to EV^{2+} at about 0.13 V.

The color changes registered during the cyclic voltammetry are shown in Figures 4.3.3.1.2 a-b-c-d-e-f-g. When the external potential is 0 V, the electrochromic device is in the transparent state (light yellow coloration), while the dark blue color can be originated by the presence of reduced viologen's specie starting at about 1 V to 3 V.

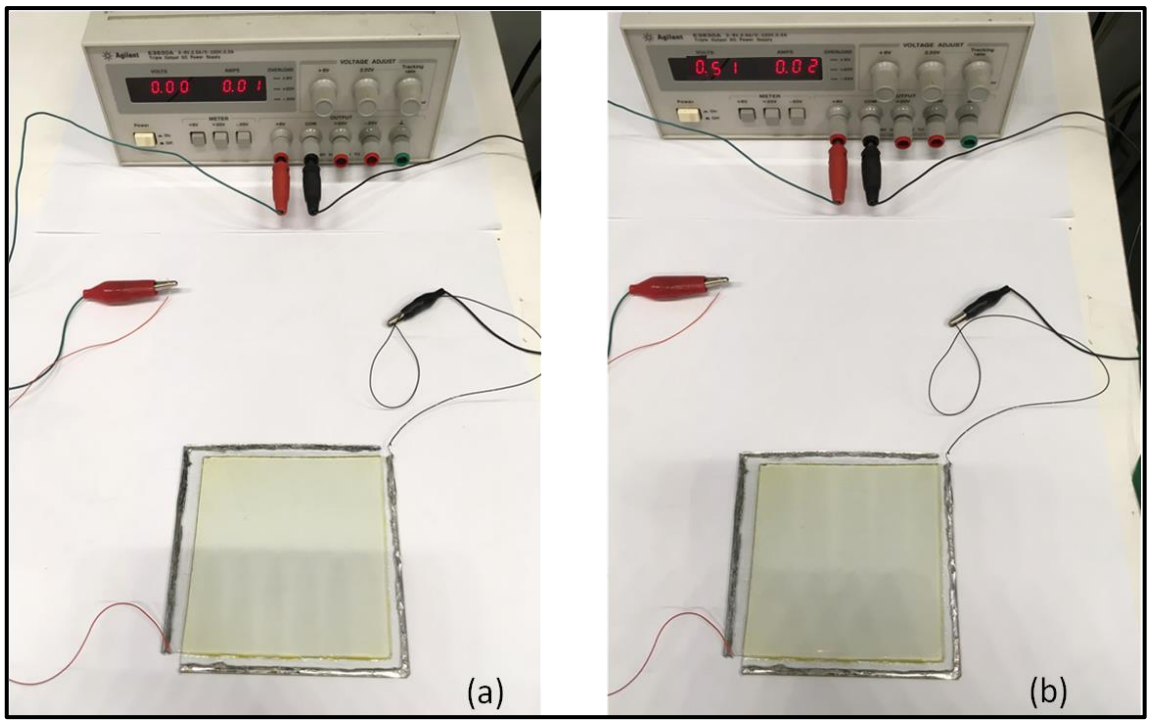

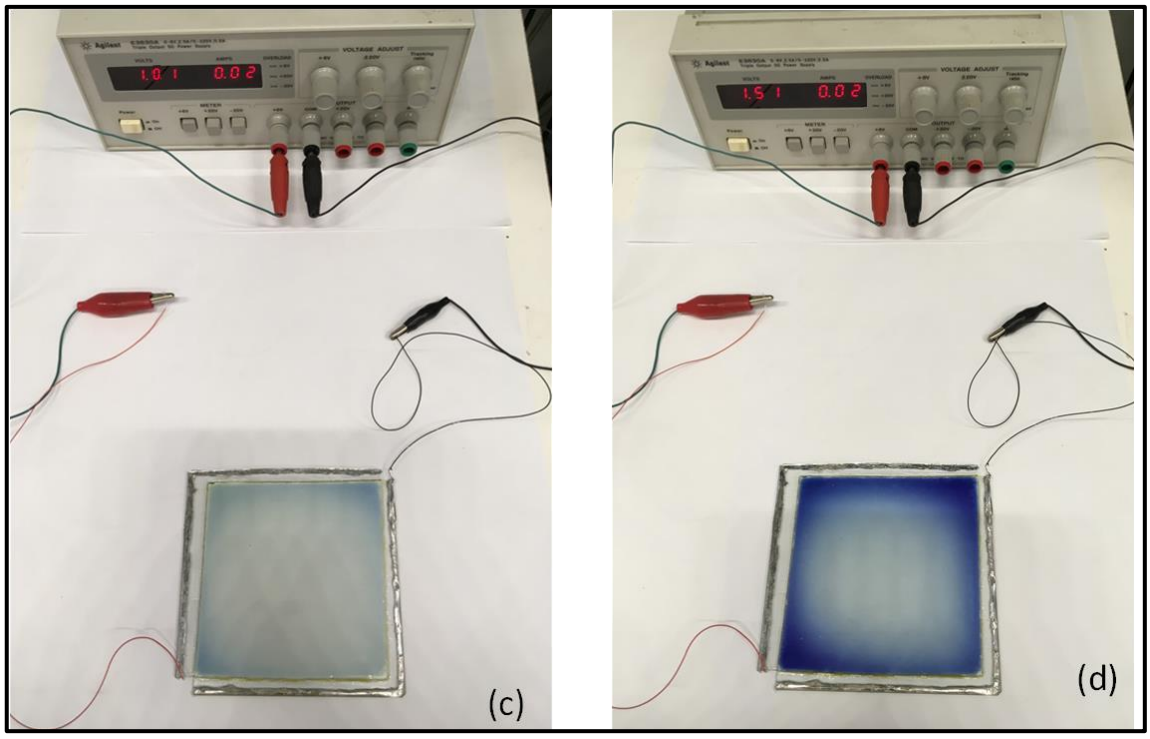
(c)
(d)

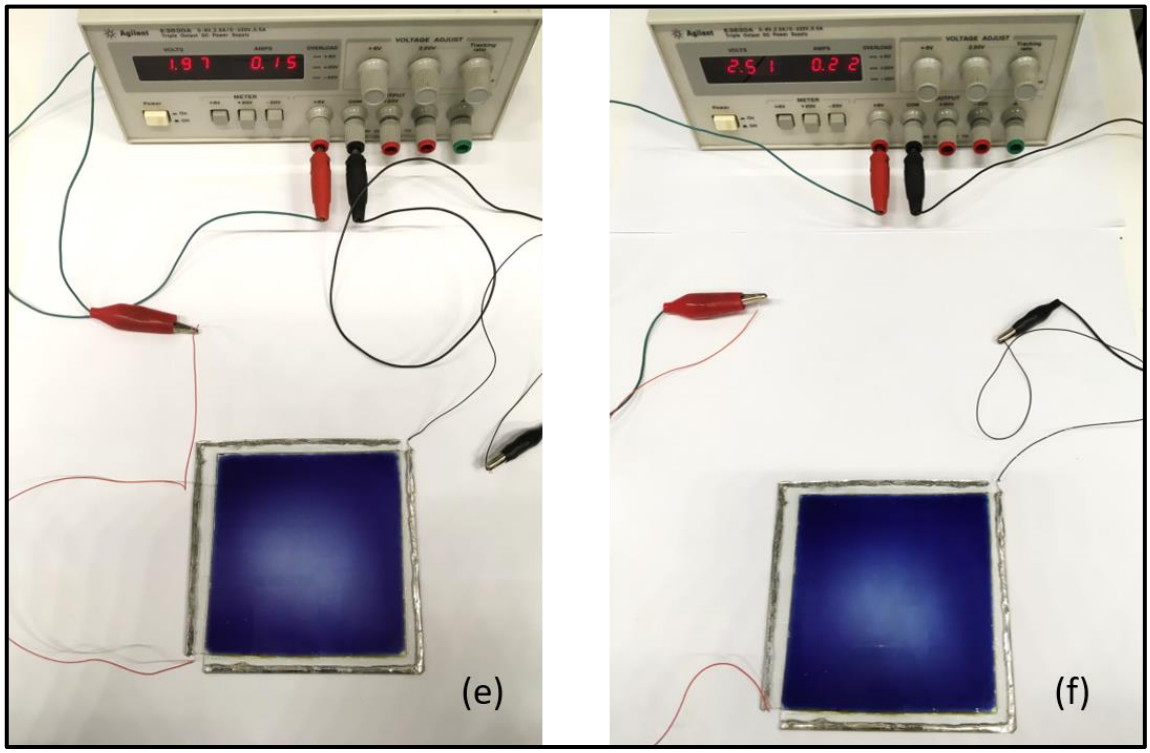
(e)
(f)

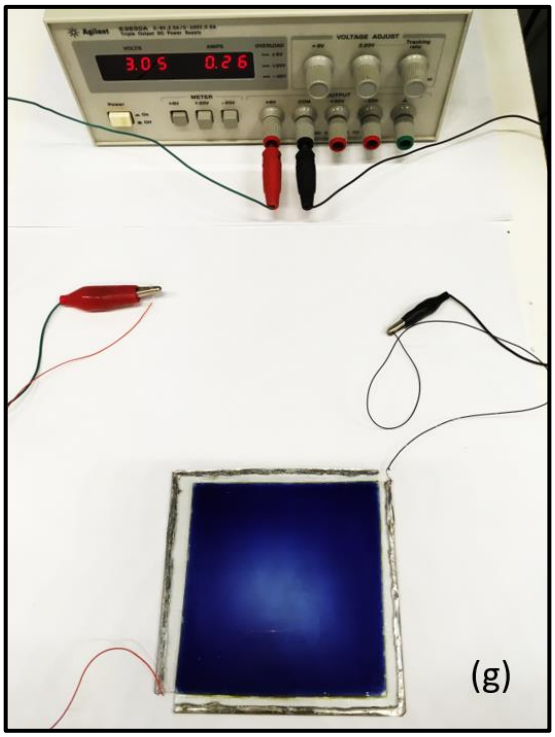

Figure 4.3.3.1.2. Electrochromic device having dimensions (10 cm × 10 cm) based on the electrochromic mixture in concentration (60:40) % w/w between ($EV(ClO_4)_2$):(DEFc):(PC) and (BPA-Irgacure 651) in the OFF state at a) 0V (light yellow coloration) and in the ON states b) 0.5V, c) 1V, d) 1.5 V, e) 2V, f) 2.5 V and g) 3 V (intense dark blue coloration)

4.3.3.2 Micro-Raman Characterization of *all-in-one* (60:40) % w/w ($EV(ClO_4)_2$:DEFc:PC)-(BPA-Irgacure 651) electrochromic device

Raman measurements have been conducted for the evaluation of the redox process that occurred to the $EV^{2+}/EV^{\bullet+}$ couple in the electrochromic device, which is responsible of the color variation in the device.

The ethyl viologen diperchlorate powder, $EV(ClO_4)_2$ has been used as starting reference and a tentative of attribution of its vibrational modes has been done in according with the literature [16, 22-24, 27]. Figures 4.3.3.2.1 and 4.3.3.2.2 show the reference spectra from $EV(ClO_4)_2$. The stretching of the N-CH_2CH_3 bond is found at 657 cm^{-1}. At 801 cm^{-1} and at 828 cm^{-1} the stretching of the C-N bond and the stretching of the C-C and N-H bond

of the pyridine group in the viologen occurred. At 936 cm^{-1} the vibration of the Cl-O bond in the perchlorate anion is found. The bands at 1064 cm^{-1} and 1180 cm^{-1} reflect the ring breathing vibration in the pyridine. The in-plane ring bending mode of the bond H-C-C is at 1237 cm^{-1}. The in-plane ring bending of the ring is found at 1248 cm^{-1}. The band at 1299 cm^{-1} describes the inter-ring vibration of the C-C bond and the bending inter-ring vibration of the H-C-C bonds. At 1355 cm^{-1} occurs the C-C inter-ring vibration, while the band at 1445 cm^{-1} describes the asymmetric C-H bending vibration. The bending vibration of the H-C-C bond and the stretching of the C-N bond occured at 1545 cm^{-1}. The C-C inner-ring vibrations of the ring are found at 1655 cm^{-1}. In the region between 2800 cm^{-1} and 3100 cm^{-1} are located the symmetric and the asymmetric stretching vibrations of the C-H bonds. The symmetric and asymmetric vibrational stretching of the C-H bond occured at 2882 cm^{-1} and at 2952 cm^{-1}. The bands at 2894 cm^{-1} and 2930 cm^{-1} describe the asymmetric and the symmetric stretching of the methylene group. The stretching of the C-H bond in the methyl group is found at 3002 cm^{-1}. The band at 3010 cm^{-1} is due to a combination of the bands at 1655 cm^{-1} and 1355 cm^{-1}. Bands located at 3080 cm^{-1} and 3112 cm^{-1} are referred to the stretching of the aromatic C-H bond.

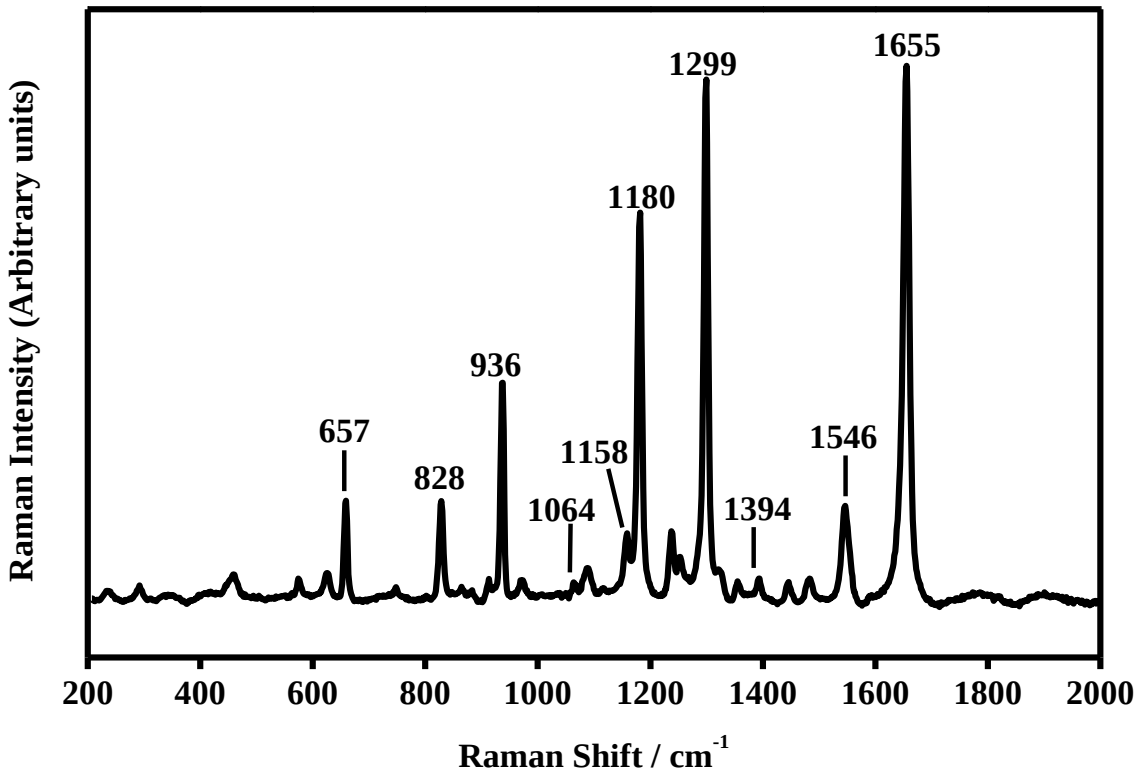

Figure 4.3.3.2.1. Raman spectrum of Ethyl viologen diperchlorate $EV(ClO_4)_2$ collected in the range between 200-2000cm^{-1}.

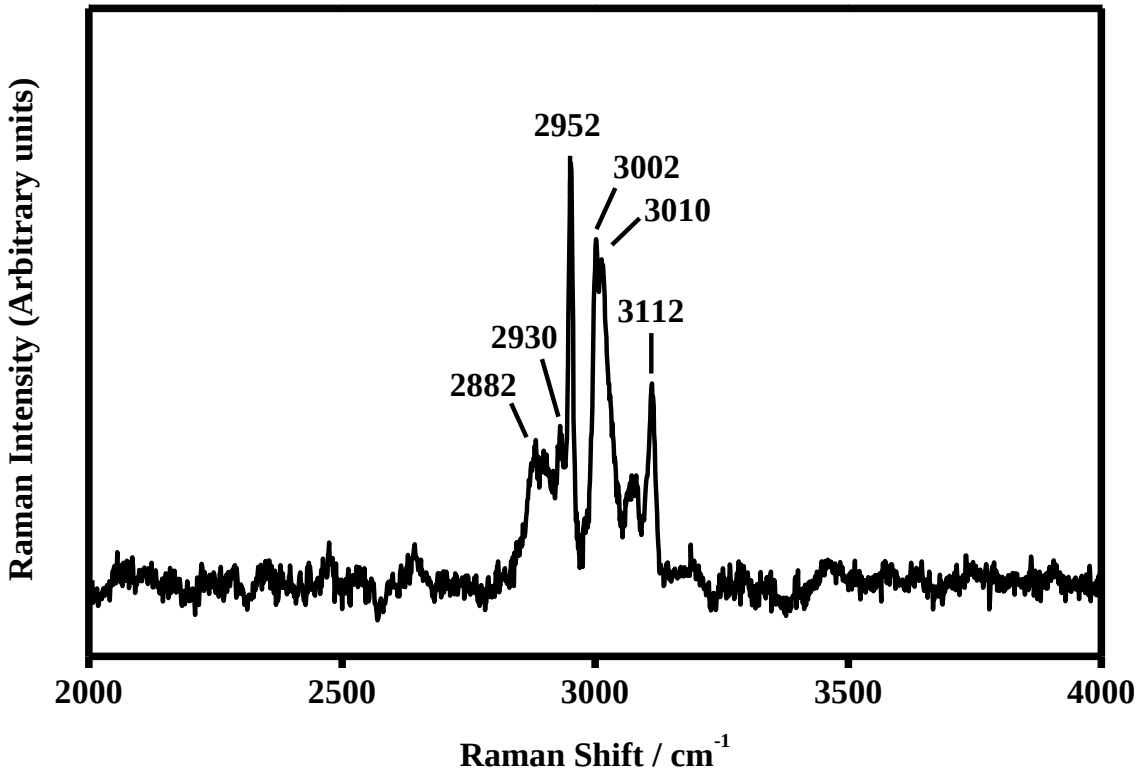

Figure 4.3.3.2.2. Raman spectrum of Ethyl viologen diperchlorate $EV(ClO_4)_2$ collected in the range between 2000-4000cm^{-1}.

Table 4.3.3.2.1 summarizes the main vibrational assignments collected on the ethyl viologen diperchlorate powder as EV^{2+} specie.

$EV(ClO_4)_2$ powder	
Peak Position (cm^{-1})	**Vibrational Assignments**
657	N-CH_2CH_3 stretching
801	C-N ring stretching
828	C-C and -N-H stretching of the pyridine group
936	Cl-O stretching in ClO_4^-
1064	C-N and C-C stretching (ring breathing vibration)
1180	N-CH_2CH_3 stretching
1237	H-C-C in-plane bending
1248	H-C-C in-plane bending of the ring
1299	C-C inter-ring vibration + H-C-C inter-ring bending

$EV(ClO_4)_2$ powder	
Peak Position (cm^{-1})	**Vibrational Assignments**
1355	C-C inter-ring vibration
1445	Asymmetric C-H bending
1545	H-C-C bending + C-N stretching
1655	C-C inner ring vibration
2882	C-H asymmetric stretching
2894	Asymmetric methylene stretching
2930	Methylene C-H symmetric stretching
2952	C-H symmetric stretching
3002	Methyl C-H stretching
3010	Combination of 1655 cm^{-1} + 1355 cm^{-1}
3080	Aromatic C-H stretching
3112	Aromatic C-H stretching

Table 4.3.3.2.1. Main Vibrational assignments of the diethyl viologen diperchlorate powder.

Following the structural evolution associated to the redox process of the ethyl viologen diperchlorate, as a function of the applied external potential (0 V- 3 V), the Raman spectra of the electrochromic device have been collected in the range 200-2000 cm^{-1} and they are shown in Figure 4.3.3.2.3 in according with literature [16, 25- 27].

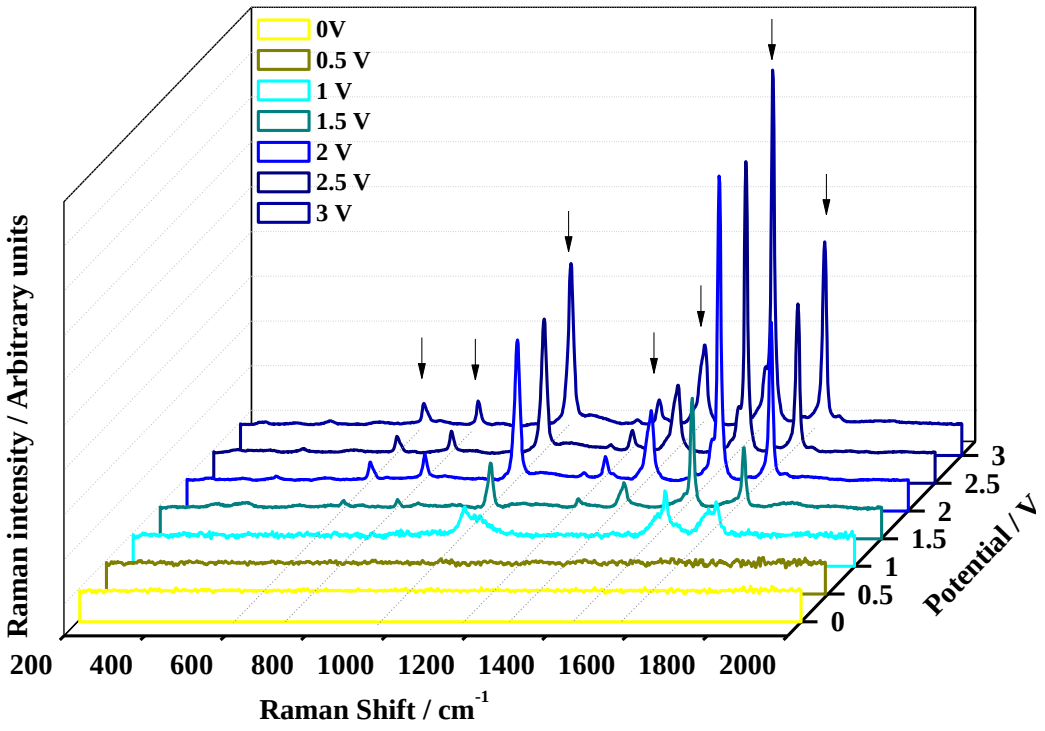

Figure 4.3.3.2.3. Raman spectra of the electrochromic device based on the concentration (60:40) % w/w based on ($EV(ClO_4)_2$:DEFc:PC) - (BPA-Irgacure 651) collected in the range 200 - 2000 cm^{-1} as function of the external applied potential: 0 V (OFF state, yellow line), 0.5 V (dark yellow line), 1 V(ON state, cyan line), 1.5 V (dark cyan line), 2 V (blue line), 2.5 V (navy blue line) and 3 V (royal blue line).

The Raman spectra collected on the electrochromic device under 0 V and 0.5 V relative to the EV^{2+} specie are not observable because they are masked by strong fluorescence and the laser wavelength excitation is not sufficient to induce an appreciable chemical bond resonance *i.e.*, no resonance Raman scattering of the di-cation specie in the ethyl viologen diperchlorate can be detected.

The Raman spectra recorded in the potential range between 1 V to 3 V, are characterized by the appearance of new bands of the stable radical cation of the ethyl viologen diperchlorate ($EV^{\bullet+}$). At 1 V, the electrochromic device assumes an observable initial color variation assumable to light blue. The light color change corresponds to the starting of the reduction of the EV^{2+} specie to the $EV^{\bullet+}$ specie. Characteristic bands associated to the reduced $EV^{\bullet+}$ specie are recorded in the Raman spectrum. The first band is located at

1030 cm^{-1} and it is ascribable to the ring breathing vibration of the bond C-C. The second band is found at 1528 cm^{-1} and it is due to the bending vibration of the C-H bond and to the ring vibration of the C-H bond. The bands at 1640 cm^{-1} characteristic of the EV^{2+} and the appearance of the band at 1655 cm^{-1} associated with $EV^{\bullet+}$ represent clear evidence of the reduction process of the ethyl viologen diperchlorate. Both are assigned to the ring vibration of the C-C bond. All these bands confirm the accomplished reduction of the ethyl viologen diperchlorate as di-cation specie EV^{2+} in the radical cation $EV^{\bullet+}$as also, justified by the starting color variation of the electrochromic device. The increasing potential leads to obtaining a more detailed Raman spectrum of the reduced specie. At 1.5 V the Raman spectra is characterized by the existence of bands that we found at 661 cm^{-1}, 797 cm^{-1}, 1027 cm^{-1}, 1246 cm^{-1}, 1360 cm^{-1}, 1529 cm^{-1} and 1658 cm^{-1}. The bending modes associated with the C-N-C and C-C-N bonds are located at 661 cm^{-1}. The band at 797 cm^{-1} is due to the ring stretching vibration of the C-N bond. Also, in this case, the Raman spectrum confirms the band which describes the ring breathing vibration of the C-C bond, which is now shifted at 1027 cm^{-1}. At 1246 cm^{-1} is located the in-plane bending vibration of the H-C-C bond and at 1360 cm^{-1} the inter-ring vibration of the C-C bond. Also, the band at 1529 cm^{-1} is imputable to the bending vibration of the C-H bond and to the ring vibration of the C-H bond. The C-C ring vibration is now shifted at 1658 cm^{-1}. At 2 V, the Raman spectrum confirms the bands at 661 cm^{-1}, 797 cm^{-1}, 1246 cm^{-1}, 1529 cm^{-1} and 1658 cm^{-1}. In addition, the band associated with the ring breathing vibration is shifted at 1028 cm^{-1}, while the band that describes the inter-ring vibration of the C-C bond is now found at 1361 cm^{-1}. A new band at 1194 cm^{-1} concerning the vibration of the N-(CH_2) bond is revealed.

At 2.5 V, the Raman spectrum is composed of all the bands at 661 cm^{-1}, 797 cm^{-1}, 1028 cm^{-1}, 1194 cm^{-1}, 1246 cm^{-1}, 1361 cm^{-1}, 1529 cm^{-1} and 1658 cm^{-1} as confirmed previously. When the external potential is set to 3 V, the color variation from light blue to the intense dark blue color is more evident. The formation of the radical cation $EV^{\bullet+}$ is justified by the intense blue coloration of the electrochromic device and the relative Raman spectrum is well-defined and confirms the bands at 661 cm^{-1}, 797 cm^{-1}. The vibration of the N-CH_2 bond and of the bending vibration of the H-C-C bond are now shifted at 1192 cm^{-1}, 1247 cm^{-1}, respectively. The Raman spectrum confirms also, the four strong Raman bands at

1028 cm^{-1}, 1362 cm-1, 1529 cm^{-1} and 1658 cm^{-1} of the fully reduced ethyl viologen diperchlorate.

Table 4.3.3.2.2 summarizes the main vibrational assignments of the reduced $EV^{\bullet+}$ specie, recorded in the potential range between 0V to 3 V in the range between 200-2000 cm^{-1}.

Peak Position / cm^{-1}							**Vibrational Assignments (200-2000 cm^{-1})**
OFF State	**ON State**						
0V	**0.5V**	**1V**	**1.5V**	**2V**	**2.5V**	**3V**	
/	/	/	661	661	661	661	C-N-C bending + C-C-N bending
/	/	/	797	797	797	797	C-N ring stretching
/	/	1030	1027	1028	1028	1028	C-C Ring breathing
/	/	/	/	1194	1194	1192	N-(CH_2) vibration
/	/	/	1246	1246	1246	1247	H-C-C in-plane bending vibration
/	/	/	1360	1361	1361	1362	C-C inter ring vibration
/	/	1528	1529	1529	1529	1529	C-H bending + C-H ring vibration
/	/	1640/ 1655	1658	1658	1658	1658	C-C ring vibration

Table 4.3.3.2.2. Main Vibrational assignments of the diethyl viologen diperchlorate present as $EV^{\bullet+}$ - radical form in the electrochromic device in the range potential between 1 V to 3 V in the range between 200-2000 cm^{-1}.

Figure 4.3.3.2.4 shows the Raman spectra collected on the electrochromic device under the potential ranging from 0 V to 3 V in the range between 2000-4000 cm^{-1}.

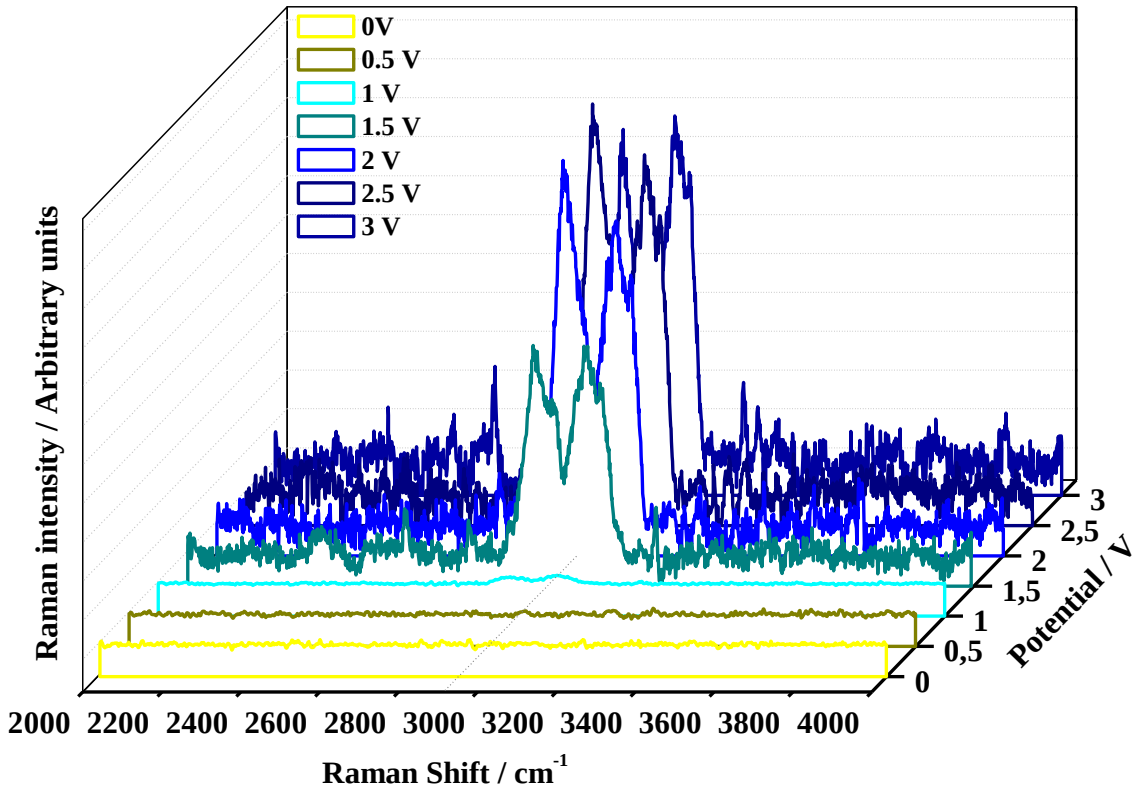

Figure 4.3.3.2.4. Raman spectra of the electrochromic device based on the concentration (60:40) % w/w based on ($EV(ClO_4)_2$:DEFc:PC) - (BPA-Irgacure 651) collected in the range 2000-4000 cm^{-1} as function of the external applied potential: 0 V (OFF state, yellow line), 0.5 V (dark yellow line), 1 V(ON state, cyan line), 1.5 V (dark cyan line), 2 V (blue line), 2.5 V (navy blue line) and 3 V (royal blue line).

At 0 V and 0.5 V the weak Raman bands are not detected because they are not in resonance with the used laser-excitation. From 1 V to 3 V, the bands located between 2880 cm^{-1} to 3050 cm^{-1} have been detected. The stretching vibration of the C-H bond is found at 2882 cm^{-1} (1V, 2V and 3 V) and at 2880 cm^{-1} (2.5 V). The band at 3015 cm^{-1} (for 1V, 2V and 2.5) and at about 3016 cm^{-1} is due to the combination of the bands at about 1655 cm^{-1} and 1355 cm^{-1}. The weak band at 3050 cm^{-1} (1.5 V), 3054 cm^{-1} (2 V) 3050cm^{-1} (2.5 V) and 3051 cm^{-1} (3V) is the overtone of the band at about 1528-1529 cm^{-1}. In Table 4.3.3.2.3 are summarized the main vibrational assignments of the reduced $EV^{\bullet+}$ specie, recorded in the potential range between 0V to 3 V in the range between 2000-4000 cm^{-1}.

Peak Position / cm^{-1}							Vibrational Assignments ($2000-4000\ cm^{-1}$)
OFF State	ON State						
0V	0.5V	1V	1.5V	2V	2.5V	3V	
/	/	2882	2882	2882	2880	2882	C-H asymmetric stretching
/	/	3010	3011	3010	3011	3011	Combination of 1655 cm^{-1} + 1355 cm^{-1}
/	/	/	3050	3054	3050	3051	Overtone of 2× 1528 cm^{-1} (1529 cm^{-1})

Table 4.3.3.2.3. Main Vibrational assignments of the diethyl viologen diperchlorate present as $EV^{\bullet+}$ radical form in the electrochromic device in the range potential between 1 V to 3 V in the range between 2000 cm^{-1} to 4000 cm^{-1}.

4.3.3.3 UV-Vis-NIR Investigations of *all-in-one* (60:40) %w/w ($EV(ClO_4)_2$:DEFc:PC)-(BPA:Irgacure651) electrochromic device

UV-Visible-NIR spectrophotometer has been used for the optical characterization of the electrochromic device of dimension (10 cm × 10 cm) based on the (60:40) % w/w ($EV(ClO_4)_2$):(DEFc):(PC) and (BPA-Irgacure 651) mixture. The transmittance of the electrochromic device has been measured in the range between 200 nm and 1200 nm, during the gradually increasing of the potential in the range from 0 V to 3 V. The transmission spectra are shown in Figure 4.3.3.3.1.

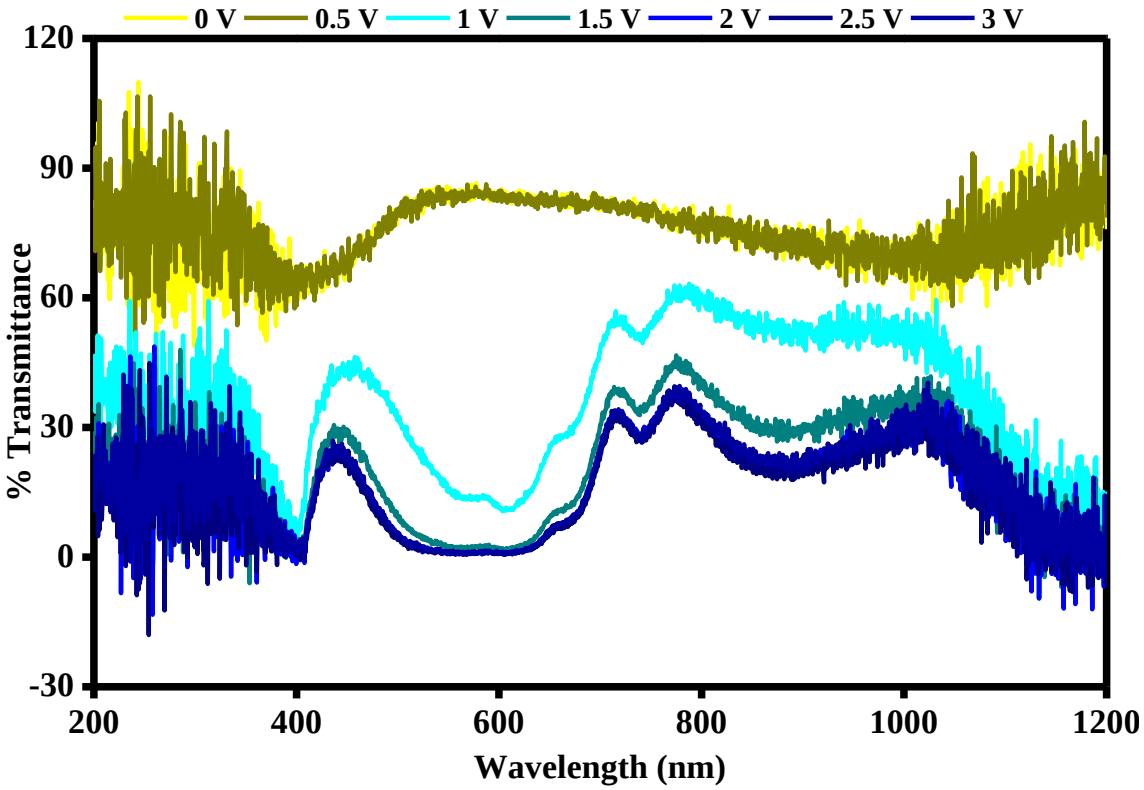

Figure 4.3.3.3.1. The optical transmittance spectra of the fabricated device at different potentials ranging from 0 V to 3 V registered between 200-1200 nm wavelengths.

The electrochromic device shows different transmittance properties as a consequence of the presence of the $EV^{2+}/EV^{\bullet+}$ couple. At 0 V the electrochromic device appears in its OFF state. It transmits all wavelengths of the UV-Vis-NIR region of the electromagnetic spectrum except at about 560 nm where there is a peak correspondent to EV^{2+} specie and thus appears transparent in its starting light-yellow color. Then, as the potential is increased from 0.5 V to 3 V (in steps of 0.5 V), the electrochromic device is going in its ON state which is associated with the color variation of the electrochromic device in the range of 510 nm to 650 nm of the visible region. The peak at 560 nm gets suppressed starting from the applied potential of 1 V and a clear change in transmission are visible both in the visible region at about 400 nm 606 nm wavelengths and in the NIR region at about 890 nm wavelength. The blue color of the device is directly observable to the visible eyes and it is ascribed to the reduced specie $EV^{\bullet+}$.

We investigated the transmittance modulation (%) of the electrochromic device when it is put in two operative conditions corresponding to the bleached state at 0V and to the colored states at 1 V and 3 V. The trends of the variation of the transmittance modulation have been evaluated at maximum contrast wavelength (400 nm, 606 nm, 890 nm) *i.e.*, where the device exhibited minimums transmittance in the UV-VIS-NIR region and they are plotted in Figure 4.3.3.3.2. In the top inset of Figure 4.3.3.3.2 are the optical transmittance curves of the electrochromic device in the OFF state (bleached, 0V) and in the ON state (colored, 1V, 3V) respectively in the range from 200 nm to 1200 nm.

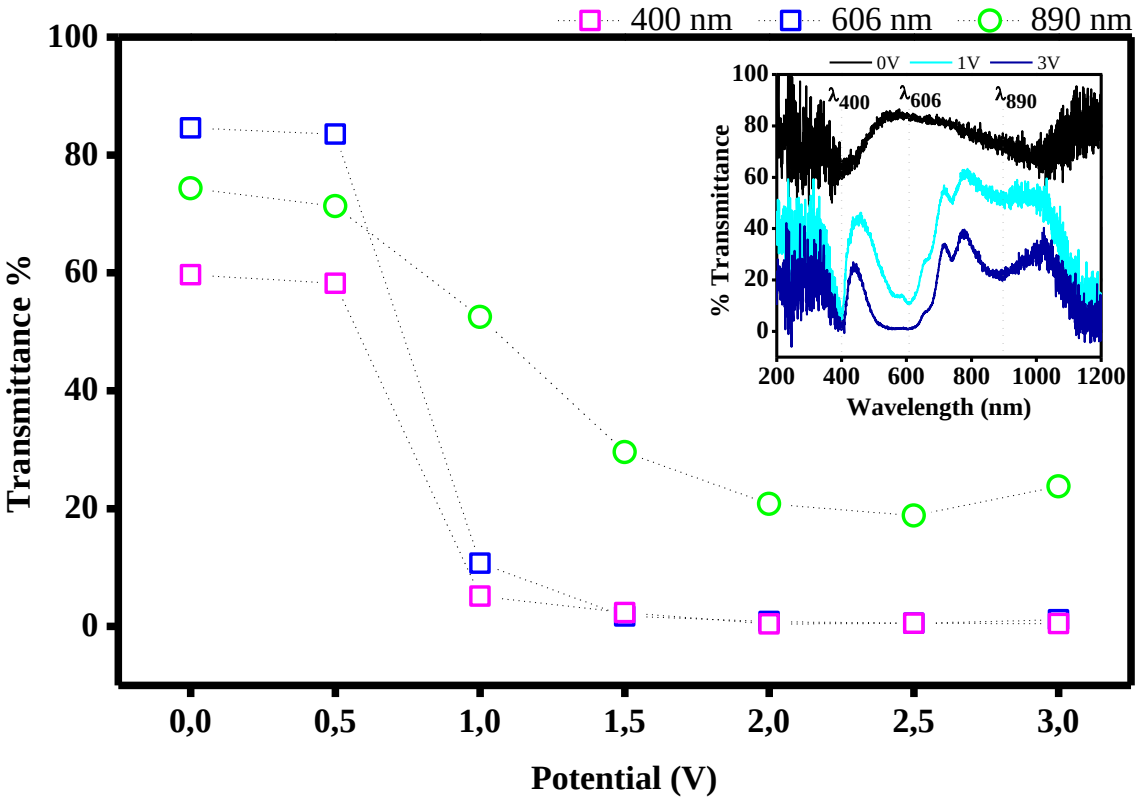

Figure 4.3.3.3.2. The transmittance modulation of the fabricated device at 400 nm, 606 nm, 890 nm wavelengths registered at different potentials ranging from 0 V to 3V. In the top inset, the optical transmittance curves when the electrochromic device is in the OFF state at 0 V (black curve) and in the ON states at 1 V (cyan curve) and 3V (royal blue curve) registered in the range from 200 nm to 1200 nm.

In the visible range, at 400 nm, the device shows transmittance of 59.6 % at 0V (OFF state, bleached state). At 1V, when the device undergoes the redox process, the value of

the transmittance decreases to 5.14 % and at the maximum color variation of 3 V, its transmittance is equal to 0.48 %. At 606 nm, the electrochromic device exhibits a transmittance of 84.6 % under 0 V and it is fully bleached (OFF state). Then, the transmittance is drastically reduced to 10.71 % at 1 V which corresponds to the first color variation when the system is put in the ON state and then, to 1.10 % at 3 V where the system is full blue colored.

In the near-infrared region wavelength region (NIR), the device shows transmittance of 74.3 % in the bleached state (0 V). In the ON states, at 1V the transmittance is reduced to 52.5 % and at 3 V it is equal to 23.7%.

Additionally, some optical properties such as the Color Contrast Ratio, CCR (%) and the Coloration Efficiency, CE have been calculated between the OFF state (0 V) and ON state (3 V) when the device is fully colored The Color Contrast Ratio, CCR (%) is defined as the contrast between bleached and colored state following the Equation 4.3.3.3.1 [28]:

$$CCR\ (\%) = \frac{T_{bleached} - T_{colored}}{T_{bleached}} \times 100 \qquad (4.3.3.3.1)$$

Where $T_{bleached}$ and $T_{colored}$ are the bleached/initial and the colored/final transmittance values at the wavelength of 400 nm, 606 nm, and 890 nm. The performances of the electrochromic device are interesting in both the complete visible range and in the near-infrared region. It exhibits higher contrast color ratios at 400 nm and 606 nm with values of 99.1 % and 98.7 %, while in the near-infrared region, the CCR % is 68%.

Coloration Efficiency is another crucial parameter which is defined as the change in optical density *(ΔOD)* at a particular wavelength *(λ)* per unit area of charge *(Q)* intercalated or extracted from the electrochromic film. It can be calculated according to the following (Equation 4.3.3.3.2) [28]:

$$CE(\lambda) = \frac{\Delta OD(\lambda)}{Q} = \frac{log\left(\frac{T_b}{T_c}\right)}{Q} \qquad (4.3.3.3.2)$$

Where T_b and T_c represent the transmittance in bleached and colored states at 400 nm, 606 nm, and 890 nm wavelengths.

The (60:40) % w/w concentration based on ($EV(ClO_4)_2$):(DEFc):(PC) and (BPA-Irgacure 651) electrochromic device promotes higher values of coloration efficiency in the investigated wavelength range. In the visible range, at 400 nm the value of CE is equal to 510.6 $cm^2\ C^{-1}$ and at 606 nm is 460.3 $cm^2\ C^{-1}$. In the NIR region, the electrochromic device presents also a CE equal to 120.9 $cm^2\ C^{-1}$.

Table 4.3.3.3.1 summarizes all optical data recorded for the electrochromic device.

λ (nm)	**Transmittance modulation (%)**			**Color Contrast Ratio, CCR (%)**	**Coloration Efficiency, CE ($cm^2\ C^{-1}$)**
	OFF State (bleached)	*ON State (colored)*			
	0 V	1V *Light Blue*	3V *Intense Blue*		
400	59.6	5.14	0.48	99.18	510.6
606	84.6	10.7	1.10	98.69	460.3
890	74.3	52.5	23.7	68.02	120.9

Table 4.3.3.3.1. Optical properties estimated for the electrochromic device at maximum wavelengths 400 nm, 606 nm, 890 nm.

4.3.4 Conclusions

An organic all-in-one electrochromic device consisting of Ethyl viologen diperchlorate, 1,1'-Diethyl Ferrocene, Bisphenol-A glycerolate diacrylate and Irgacure 651 in concentration (60:40) % w/w has been made. The electrochromic device shows a color change from transparent (OFF State) to intense dark blue color (ON State) starting from 1 V to 3 V, which is associated with the redox process of the $EV^{2+}/EV^{\bullet+}$ couple. Cyclic voltammetry measurements confirm the reversible behavior of the device under the application of an external potential. Micro-Raman spectroscopy has been conducted in the potential range between 0 V and 3 V it confirmed the presence of the $EV^{\bullet+}$ as justified by the blue color of the electrochromic device in the ON state. UV-Vis-NIR spectroscopy confirms the transmittance modulation of the device in the visible region at 400 nm where

the transmittance is varying from 59.6 % (OFF state, at 0 V) to 0.48 % (ON state, 3 V) and at 606 nm from 84.58% (OFF state, 0 V) to 1.01% (ON state, 3 V). In the NIR region, at 890 nm the device shows transmittance of 74.3 % (OFF state, 0 V) and a decrease up to 23.7 % (ON state, 3 V). The electrochromic device shows high values of CCR% in both visible and near-infrared region when it switched between OFF/ON states. At 400 nm it is characterized by a CCR % of 99.18 %, at 606 nm it shows a CCR % of 98.69 and a CCR % of 68.02 % at 890 nm. Also, it exhibits excellent values of CE in both visible and NIR regions. At 400 nm we obtained a CE of 510.6 cm^2 C^{-1}, while at 606 nm the device shows a CE of 460.3 cm^2 C^{-1} and it is suitable for the realization of smart windows with high coloration efficiencies. In the NIR region at 890 nm, it can be used for the energy-saving of buildings with a promising CE of 120.9 cm^2 C^{-1}.

4.3.5 References

[1] M. L. Moser, L.C. Chen M, E. Bekyarova, M.E. Itkis, R.C. Haddon, *Nano Lett.*, (2016) **16** 5386-5393.

[2] C. Faure, A. Guerfu, M. Dontigny, D. Clement, P. Hovington, U. Posset, K. Zaghib, *Electrochimica Acta*, (2016) **214** 313-318.

[3] C. G. Granqvist, *Solid State Ionics*, (1992) **53-56** 479-489.

[4] R. J. Mortimer, *Electrochimica Acta*, (1999) **44** 2971-2981.

[5] R. J. Mortimer *Annu. REv. Mater. Res*., (2011) **41** 241-268.

[6] K. W. Shah, S. X. Wang, D. X. Yun Soo, J. Xu, *Polymers*, (2019) **11** 1-25.

[7] K. Madasamy, D. Velayutham, V. Surynarayanan, M. Kathiresan, K. C. Ho, *J. Mater. Chem. C.*, (2019) **16** 4622-4637.

[8] P. Y. Chen, C. S. Chen, T. H. Yeh, *J. Appl. Polym, Sci*., (2014) **131** 1-6.

[9] J. Palenzuela, A. Vinuales, I. Odriozola, G. Cabanero, H. J. Grande, V. Ruiz, *ACS Appl. Mater. Interfaces*, (2014) **6** 14562-14567.

[10] L. Striepe, T. Baumgartner, *Chem. A Eur J.*, (2017) **23** 14924-16940.

[11] N. Jordao, L. Cabrita, F. Pina, L. C, Branco, *Chem. A Eur. J*., (2014) **20** 3982-3988.

[12] H. C. Lu, S. Y. Chang, C. W. Tung, K. C. Ho, *Sol Energy Mater. Sol. Cells*, (2016) **147** 75-84.

[13] B. Gelinas, D. Das, D. Rochefort, *ACS Appl. Mater. Interfaces*, (2017) **9** 28726-28736.

[14] A. Chaudhary, D. K. Pathak, S. Mishra, P. Yogi, P. R. Sagdeo, R. Kumar, *Sol Energy Mater. Sol. Cells*, (2018) **188** 249-254.

[15] S. M. Kim J. H. Jang, K. K. Kim, H. K: Park, J. J. Bae, W. J. Yu, I. H. Lee, G. Kim, D. D. Loc, U. J. Kim, E.H. Lee, H. J. Shin, J. Y. Choi, Y. H. Lee, *J. Am. Chem. Soc.*, (2009) **131** 327-331.

[16] B. Liu, A. Blaszczyk, M. Mayor, T. Wanslowski, *ACS Nano*, (2011) **5** 5662-5672.

[17] M. Deepa, A. Awadhia, S. Bhandari, *Phys. Chem. Chem. Phys*., (2009) **11** 5674-5685.

[18] S. Mishra, H. Pandey, P. Yogi, S. K. Saxena, S. Roy, P. R. Sagdeo, R. Kumar, *Solid State Communications* (2017) **261** 17-20.

[19] F. S. Han, M. Higuchi, D. G. Kurth, *Adv. Mater*., (2007) **19** 3928-3931.

[20] P. M. Beaujuge, J. R. Reynolds, *Chemical Reviews*, (2010) **110** 268-320.

[21] https//kayakuam.com/wpcontent/uploads/2019/09/SU8200DataSheet2100and 2150Ver5.pdf.

[22] T. Ma, L. Liu, J. Wang, J. Chen, *Angew. Chemie*., (2020) **132** 11630-11636.

[23] T. Lu, T. M. Cotton, J. K. Hurst, D. H. P. Thompson, *J. Phys. Chem*., (1988) **92** 6978-6985.

[24] X. Tang, T. Schneider, D. A: Buttry, *Langmuir*, (1994) **10** 2235-2240.

[25] S. Mishra, P. Yogi, A. Chaudhary, D. K. Pathak, S. K. Saxena, A. S. Krylov, P. R. Sagdeo, R. Kumar, *Indian J. Phys*., (2019) **93** 927-933.

[26] S. Mishra, H. Pandey, P. Yogi, S. K. Saxena, S. Roy, P. R. Sagdeo, R. Kumar, *Opt. Mater., (Amst)*, (2017) **66** 65-71.

[27] T. Lu, T. M. Cotton, *J. Phys. Chem.*, (1987) **91** 5978-5985.

[28] R. J. Mortimer, P. M. S- Monk, D. R. Rosseinsky, Electrochromic Materials and Devices, Wiley-VCH Verlag GmbH & Co. KGaA, (2015).

4.4 *Industrial-level* production of electrochromic devices: Design and Implementation of an automated assembly system of electrochromic devices

Abstract

In this work, the implementation of the automated assembly systems of large-area electrochromic devices of dimensions (36 cm × 27 cm) has been proposed. Three automated systems have been realized: a Knife Coating system, a Filling system and a Glue Dispensing-Assembling System. The first system is based on the knife coating technique of an electrochromic mixture. The second system has been used for the assembling of the electrochromic devices under vacuum conditions and exposition of the devices at the UV lamp system for a required time which is realized by the third system. Their use would like to contribute to the scientific knowledge in the field of electrochromic devices and the fabrication of smart windows.

4.4.1. Introduction

The aim of this study is to emphasize the importance of *scale-up* methodology for the unit operations in the fabrication of electrochromic devices and for the implementation of Smart Windows for energy saving and efficiency of buildings.

As well-known, starting from the last 50 years, the electrochromic technology has established itself as a leader in the sector of energy efficiency, which can offer on the market efficient products capable which are capable to modulate in a reversible and gradual way the light transmission over visible or infrared wavelength range controlled by an applied electrical signal. The possibility of achieving energy savings through variable transmission windows is a good opportunity to take advantage of because it has been estimated that heating, ventilation, and air conditioning (HVAC) savings can reach up to 30% [1-5].

In this study, the implementation of three systems useful for the fabrication of large-electrochromic devices has been proposed. The first system is a Knife -Coating system. The knife coating is a versatile technology, also known in the past and widely used to

apply coatings to substrates based on the use of a rigid knife which has the scope to produce a controlled and high coating of the material [6]. In principle, its aim is to realize a uniform thickness of material on support using the knife-coating technique for deposition of homogeneous layers on large areas, with a processing speed that can be performed at >10 m/min [7]. Currently, manufacture of functional thin films e.g., for organic solar cells has been reported at speeds lower than 5 m/ min [6]. Then a Glue Dispensing-Assembling System and a Filling system have been proposed.

4.4.2. Experimental Section

4.4.2.1. Proposal strategy for the implementation of the electrochromic devices at an industrial level: Basic principles

The implementation of an automated process for the scale-up at the industrializing level of future electrochromic devices (36 cm × 27 cm) is discussed. The idea regarding the industrial production of large-area electrochromic devices to be used as potential smart windows have been focused on the fabrication of three automated basic systems. Each one has been projected to perform a specific function. A simplified block diagram that mainly, describes the six steps on whicht the automated process of implementation of devices is shown in the Scheme 4.4.2.1.1.

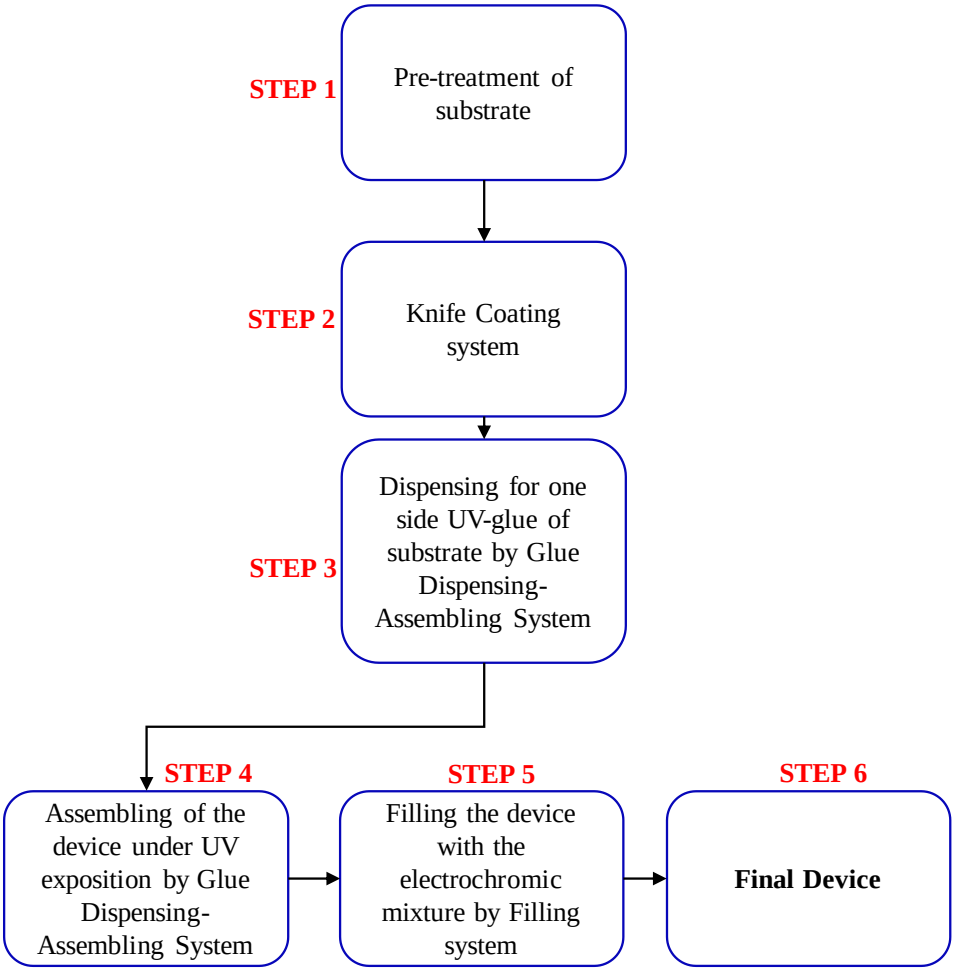

Scheme 4.4.2.1.1. Schematic diagram of the automated process of Electrochromic devices fabrication.

STEP 1 involves the pre-treatment of the substrate to remove of all substances not belonging to the substrate. *STEP 2* involves the application of the knife coating method on one glass substrate to obtain coatings of specific thickness. *STEP 3* is the dispensing of the UV-glue by the Glue Dispensing-Assembling System. *STEP 4* involves the sealing of the device followed by the UV-glue curing for a specific time of exposition in a vacuum chamber. *STEP 5* includes the filling of the device with the electrochromic mixture in immersion using the Filling system. In the end, *STEP 6* consists of the final device which is produced at the industrial level.

4.4.3 Results and Discussion

4.4.3.1 Design and Fabrication of the automated systems

An automated system for the deposition of a thin layer of the electrochromic mixture was fabricated. The operating principle of the system is based on the knife coating also known as Doctor Blading and its schematic representation is depicted in Figure 4.4.3.1.1. The Knife Coating technique is a technique used to make uniform and thin films, starting from a solution that is distributed on a flat surface using a movable knife. The Knife Coating is suitable to coat the substrate with a very wide range of wet film thicknesses ranging from 20 to several hundred microns [6-8].

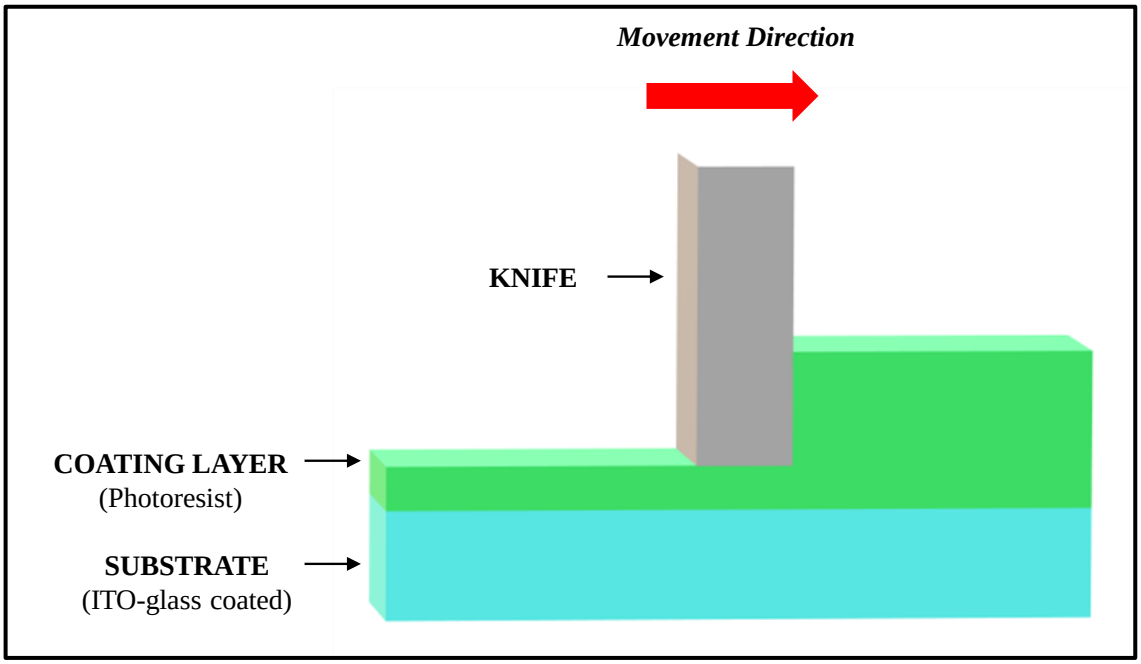

Figure 4.4.3.1.1. A schematic representation of the Knife Coating technique used for the implementation of the automated system for the deposition of a thin layer of electrochromic mixture.

The Knife Coating system is composed of several components such as 1) a Knife with the function of spreading on the substrate (glass) of the plane a generic compound (like photoresist in our case; 2) a Mobile Carriage which is equipped with two digital micrometers. The thickness of the layer is metered by adjusting the gap between the doctor blade and the substrate. The knife is connected to this carriage and it can move

along backward and forwards on the plane of the system along the y-axis; 3) a Vacuum Controller connected to a vacuum pump, it is equipped with a three-way valve and by vacuum outlet in the plane of the system. The design of the Knife Coating system is depicted in Figure 4.4.3.1.2.

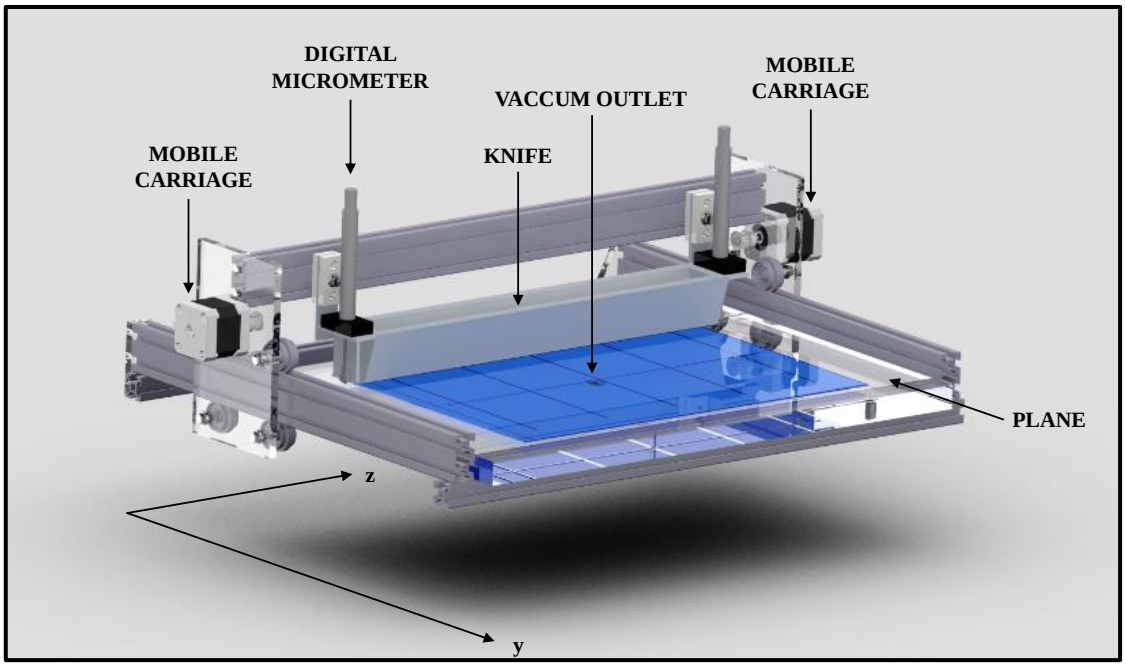

Figure 4.4.3.1.2. The Knife Coating system for achieving a covered layer on glass substrates.

The different perspective views of the Knife Coating system are shown in the design table of Figure 4.4.3.1.3, where: a) lower section, b) right lateral section, c) frontal section, d) left lateral section and e) upper section.

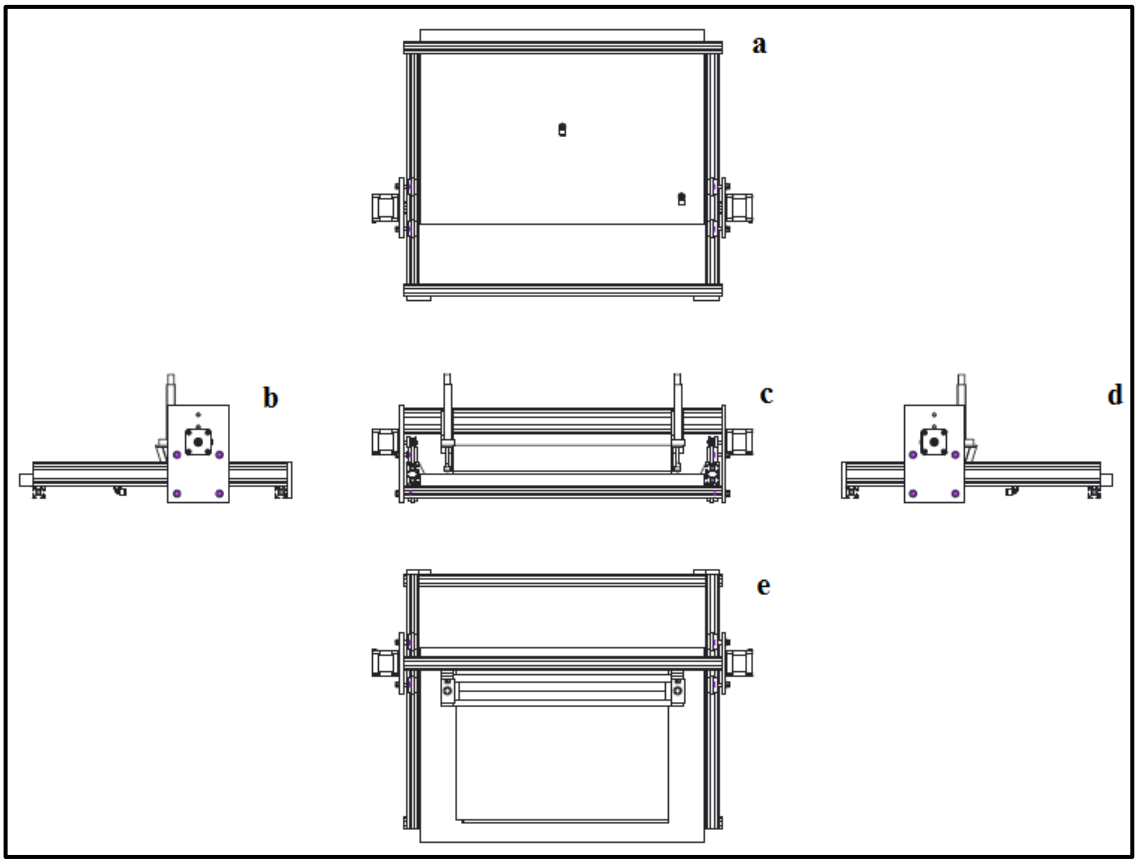

Figure 4.4.3.1.3. Different perspective views of the Knife Coating system: a) lower section, b) right lateral section, c) frontal section, d) left lateral section and e) upper section.

The design tables of the frontal, lateral and upper sections of the Knife Coating system are shown in Figures 4.4.3.1.4 a-b, 4.4.3.1.5 a-b and 4.4.3.1.6 a-b.

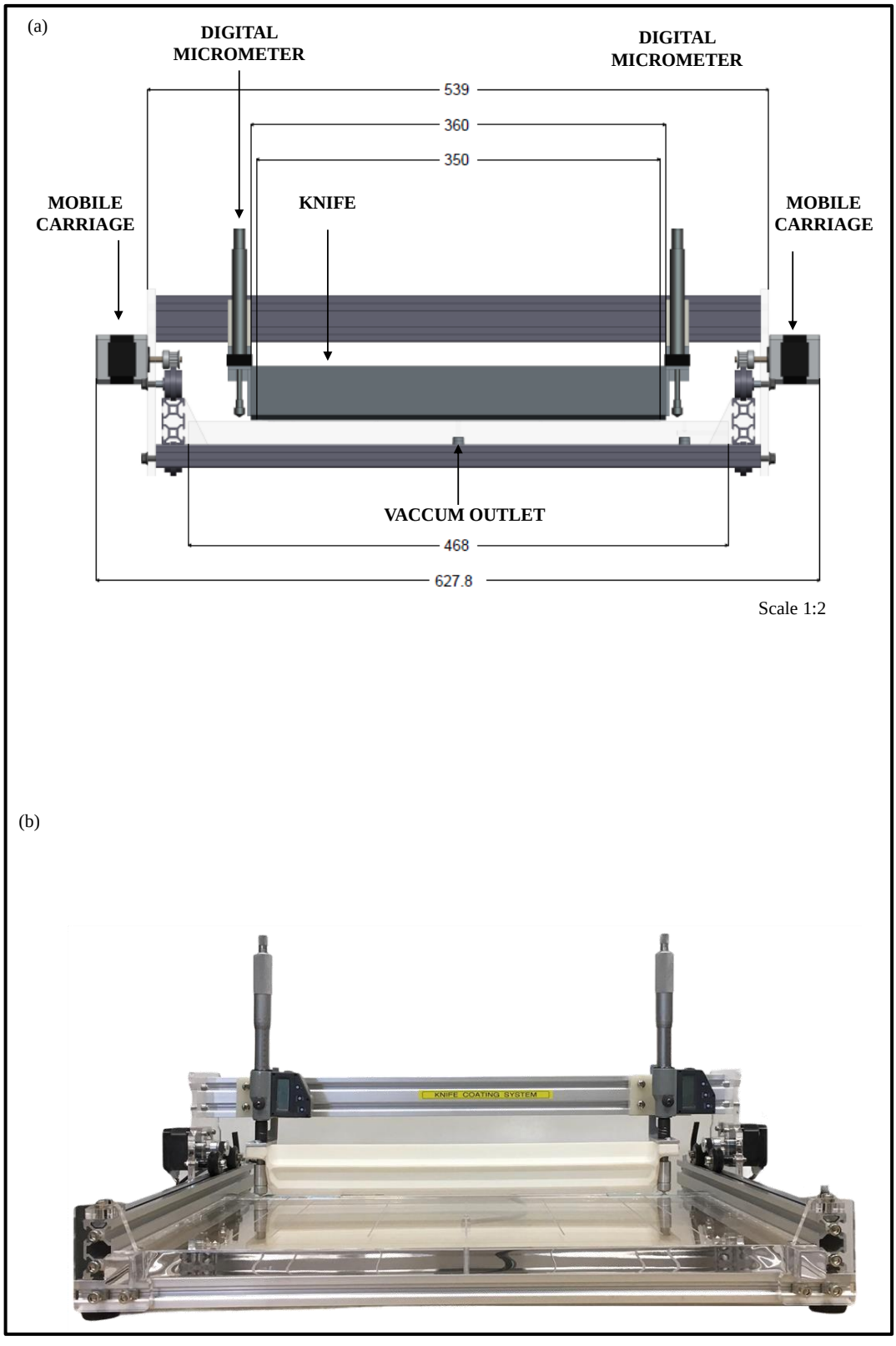

Figure 4.4.3.1.4. a) The frontal view of the rendering and b) the real view of the Knife Coating system. The dimensions of the system in the design table are expressed in millimeters on the scale of 1:2.

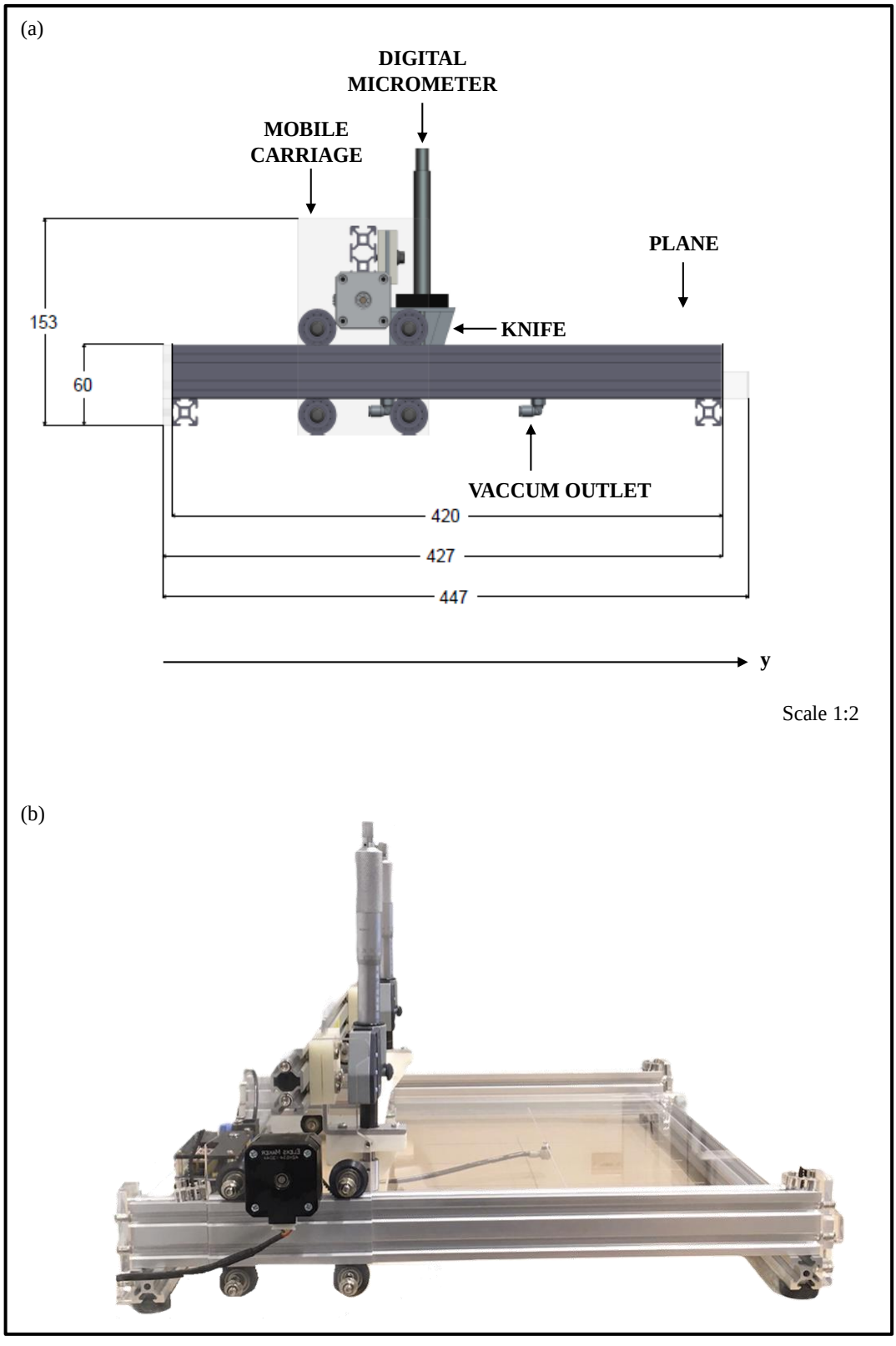

Figure 4.4.3.1.5. a) The lateral view of the rendering and b) the real view of the Knife Coating system. The dimensions of the system in the design table are expressed in millimeters on the scale of 1:2.

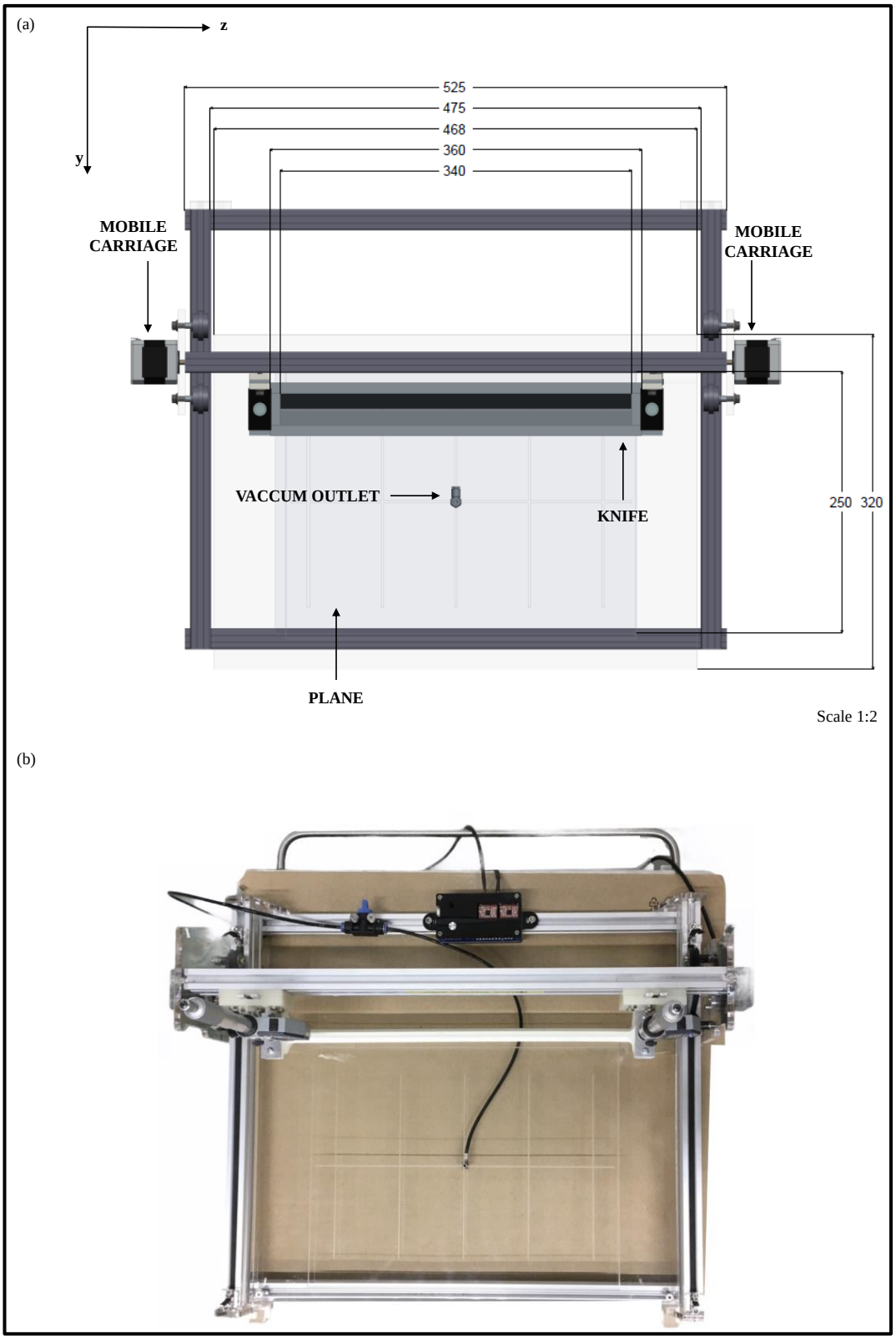

Figure 4.4.3.1.6. a) The upper view of the rendering and b) the real view of the Knife Coating system. The dimensions of the system in the design table are expressed in millimeters on the scale of 1:2.

A Filling system has been projected to fill the future device.

The projected filling system is equipped with several components such as: 1) a reserve tank that contains the electrochromic mixture; 2) a filling vacuum controller connected to a vacuum pump. The filling vacuum can be controlled by the filling power switch of the controller. 3) a system of membranes that are necessary for the realization of the vacuum condition. The device is immersed into the reverse tank and it can be blocked inside the membrane system using a regulating fixing system. The activation of the vacuum pump can extract the air inside the electrochromic device. A negative pressure is going to be generated in the cell allowing the filling of the cell. The Filling system in the a) frontal and b) lateral view is shown in Figure 4.4.3.1.7. The Knife Coating and the Filling system are depicted in the Figure 4.4.3.1.8

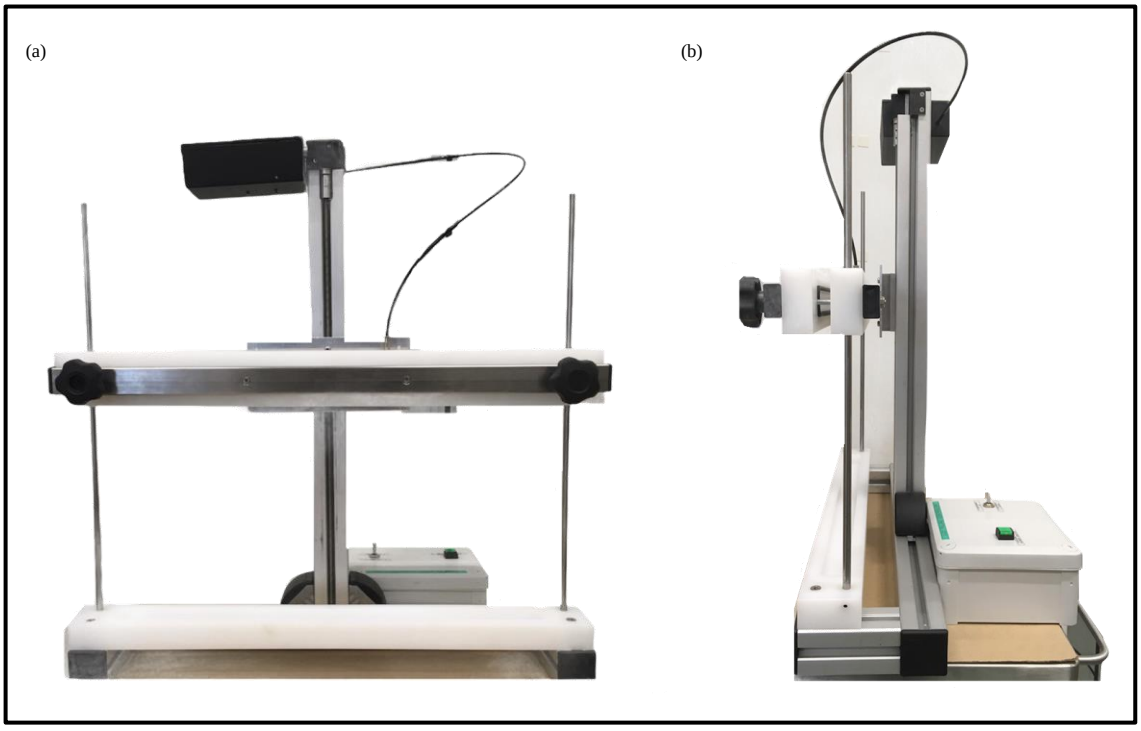

Figure 4.4.3.1.7. The Filling System in the a) frontal and in the b) lateral perspective.

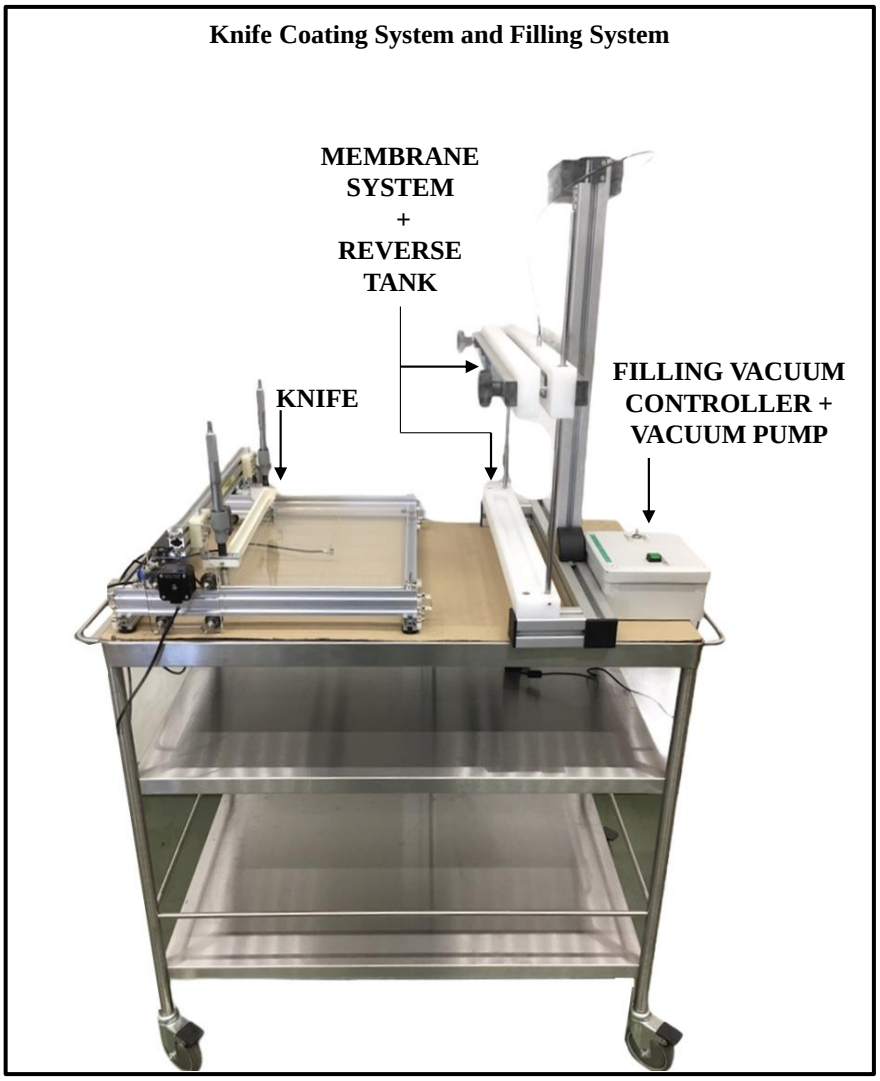

Figure 4.4.3.1.8. The Knife Coating system (left) and the Filling system (right).

An automated system for the assembling of electrochromic devices has been projected. The aim of this system is to achieve two goals: 1) the auto-dispensing of the glue on the surface of the substrate; 2) the assembling of the final device conducted by the UV exposition for a required time. The assembled system is composed of several components. 1) an automatic Glue Dispensing system (or Automatic Liquid Dispenser); 2) a Dispensing Controller (DIANSU bs-982 Taiwan Tech. A. Material (0-100 psi) which is equipped with time, pressure and vacuum control and a hand switch, respectively. The controller can be used both in AUTO/MANUAL mode; 3) a Compressor (ROHS model n. AF18A); 4) a Vacuum Controller to control the input/output lines of the vacuum and

of the air which is connected to a vacuum pump. The vacuum line and the line of the air can be controlled for the chamber and for the single panel of the chamber too; 4) an UV Control system is needed for the curing of the glue in the device. This system can be activated when the vacuum condition inside the chamber is achieved. It can be operating in both AUTO/MANUAL mode; 5) a Personal Computer interface which is equipped with the Laser GRBL software.

The design of the automated Glue Dispensing-Assembling System is depicted in Figures 4.4.3.1.9 (open chamber configuration) and 4.4.3.1.10 (closed chamber configuration).

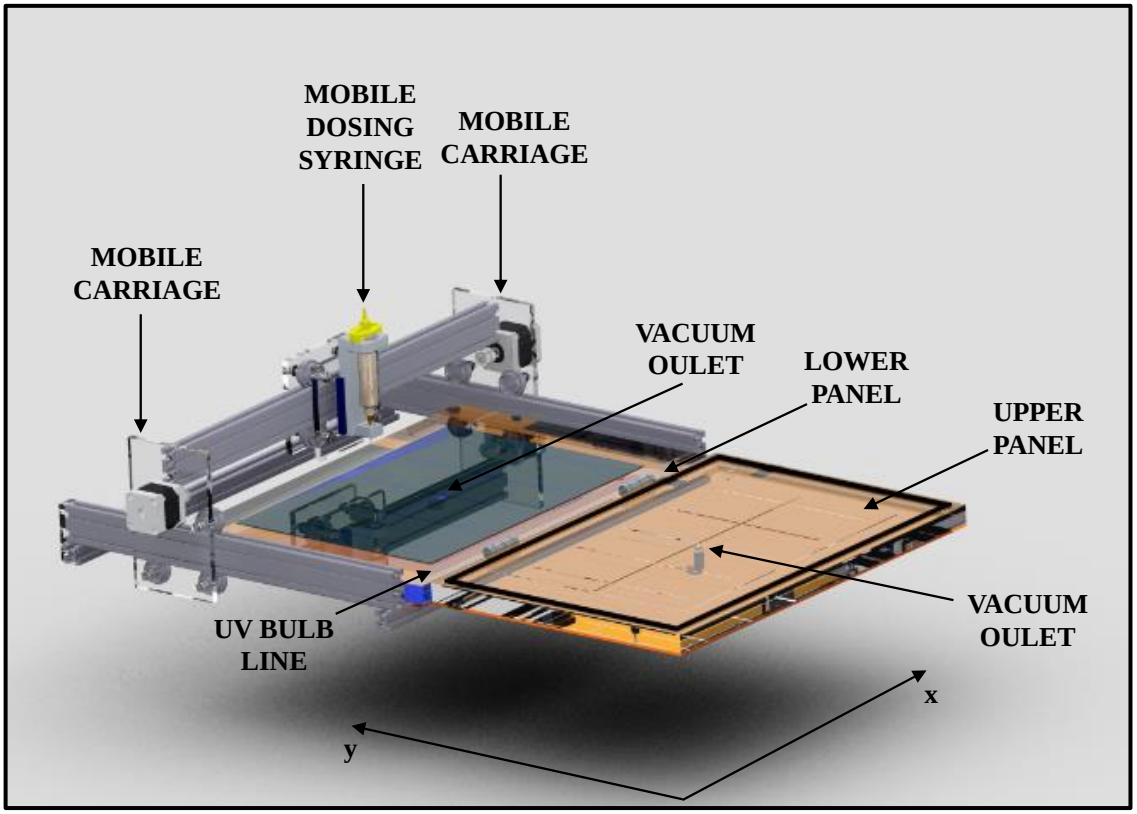

Figure 4.4.3.1.9. The Glue Dispensing-Assembling System in the open chamber configuration.

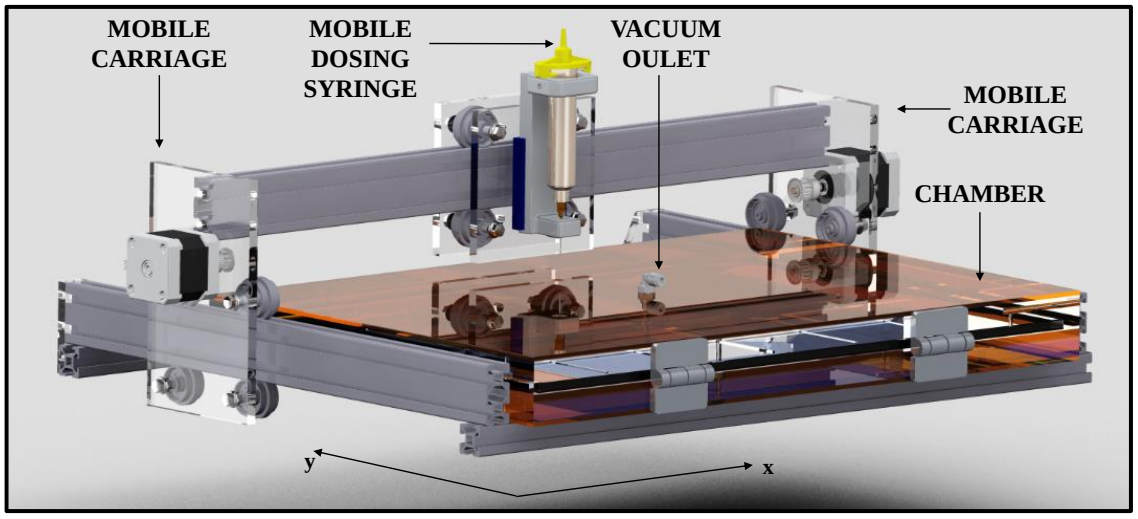

Figure 4.4.3.1.10. The Glue Dispensing-Assembling System in the closed chamber configuration.

The skeletal structure of the Glue Dispensing-Assembling system and the Closed Chamber are depicted in Figure 4.4.3.1.11 and 4.4.3.1.12.

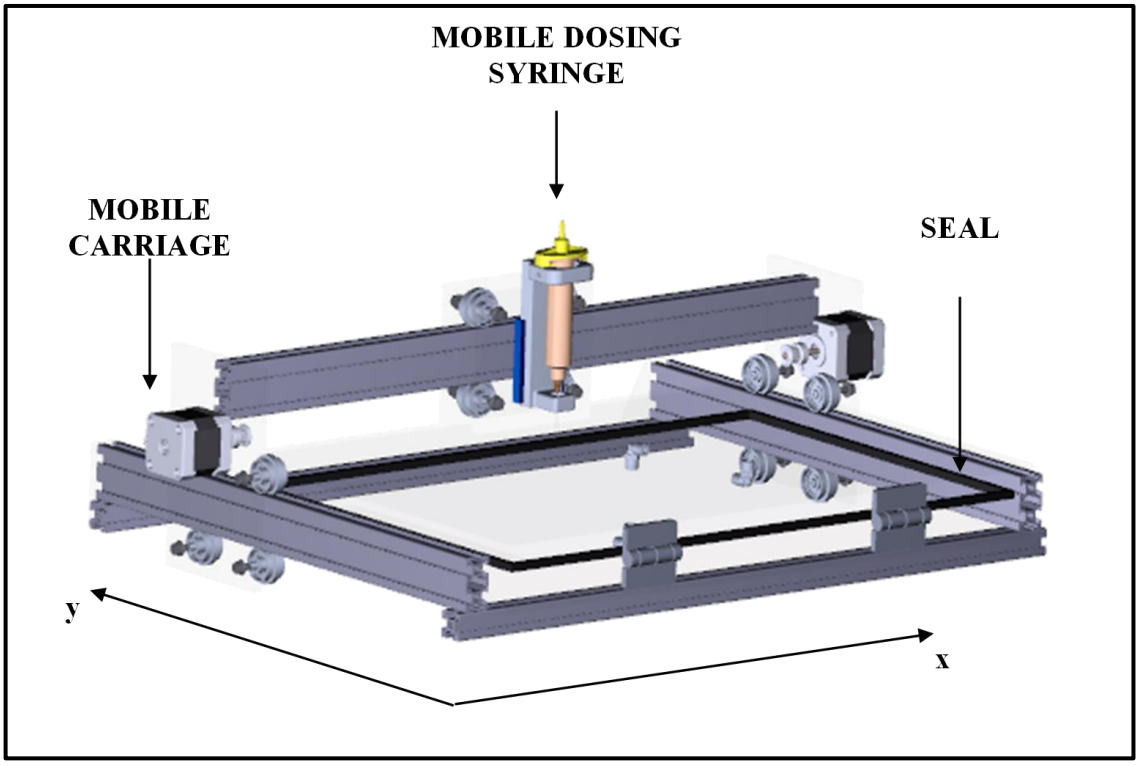

Figure 4.4.3.1.11. The skeletal structure of the Glue Dispensing-Assembling System.

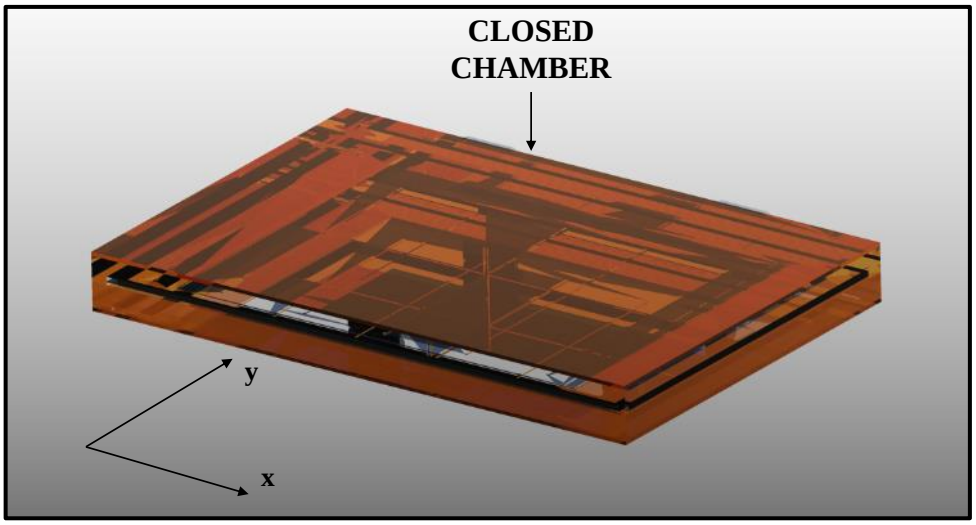

Figure 4.4.3.1.12. The closed chamber of the Assembling System.

The different perspective views of the Glue Dispensing-Assembling system are shown in the design table of the Figure 4.4.3.1.13 where: a) lower section, b) right lateral section, c) frontal section, d) left lateral section and e) upper section.

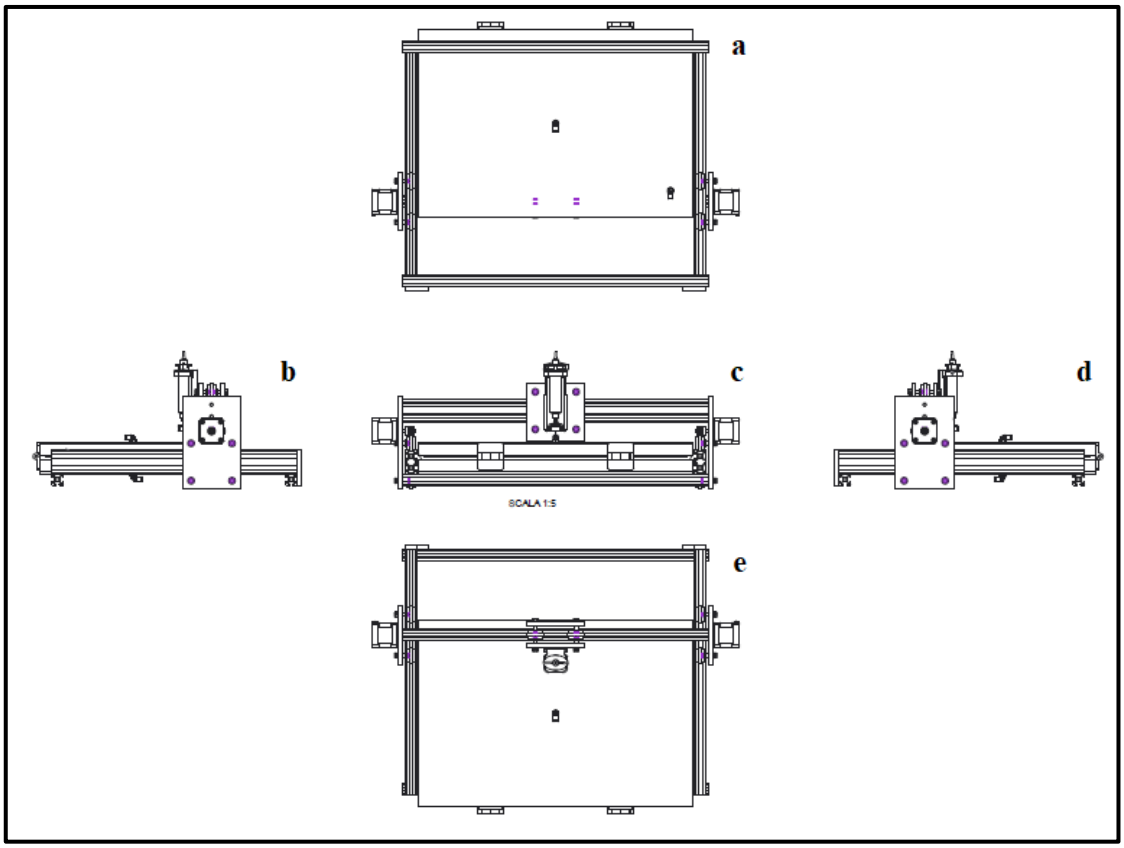

Figure 4.4.3.1.13. Different perspective views of the Glue Dispensing-Assembling

system: a) lower section, b) right lateral section, c) frontal section, d) left lateral section and e) upper section.

The design tables of the frontal, lateral and upper sections of the Glue Dispensing-Assembling system are shown in Figures 4.4.3.1.14, 4.4.3.1.15 and 4.4.3.1.16.

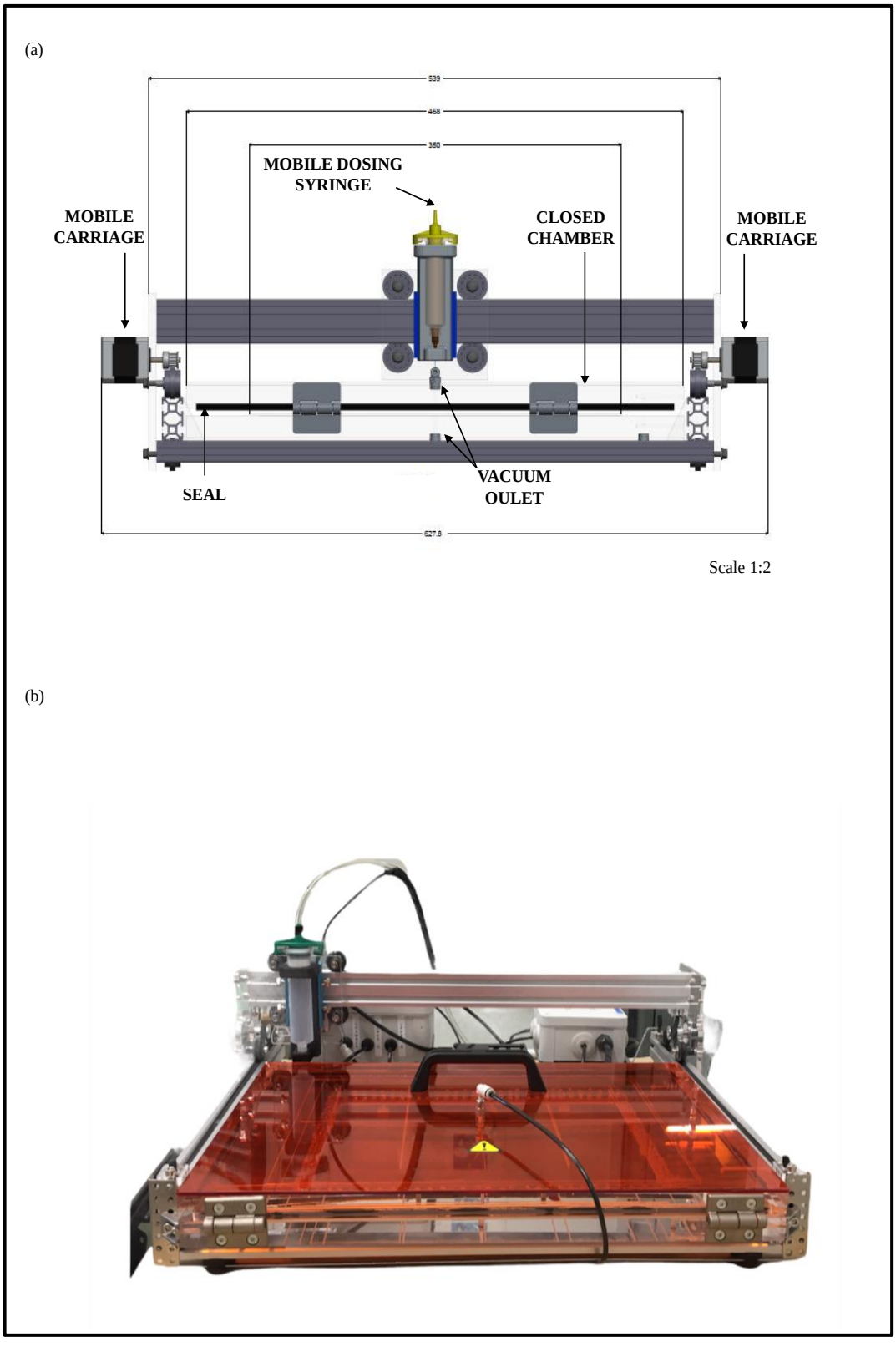

Figure 4.4.3.1.14. a) The frontal view of the rendering and b) the real view of the Glue Dispensing-Assembling system. The dimensions of the system in the design table are expressed in millimeters on a scale of 1:2.

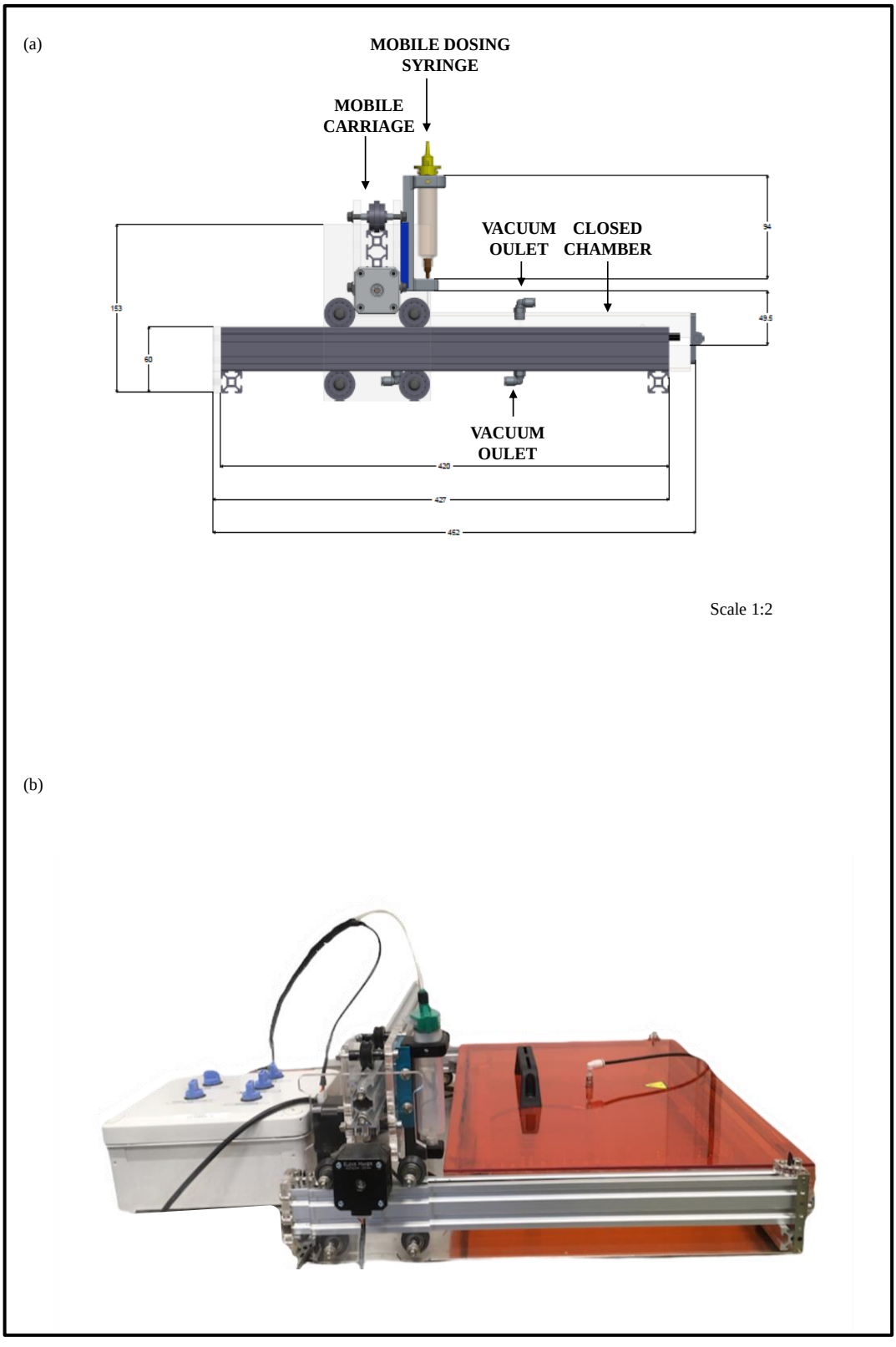

Figure 4.4.3.1.15. a) The **l**ateral view of the rendering and b) the real view of the Glue Dispensing-Assembling system. The dimensions of the system in the design table are expressed in millimeters on a scale of 1:2.

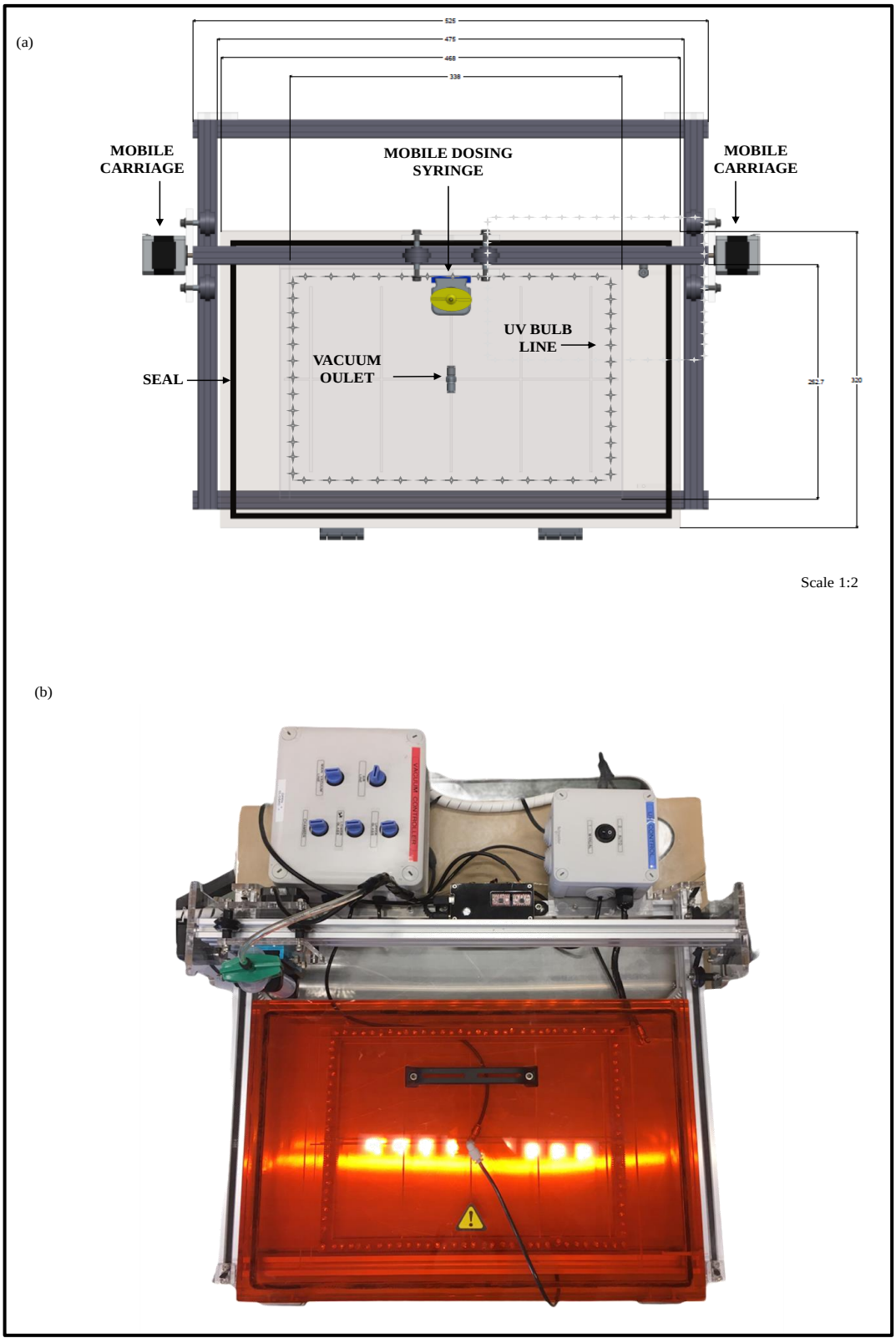

Figure 4.4.3.1.16. a) The upper view of the rendering and b) the real view of the Glue Dispensing-Assembling system. The dimensions of the system in the design table are expressed in millimeters on a scale of 1:2.

The Glue Dispensing-Assembling system in all components is depicted in Figure 4.4.3.1.17.

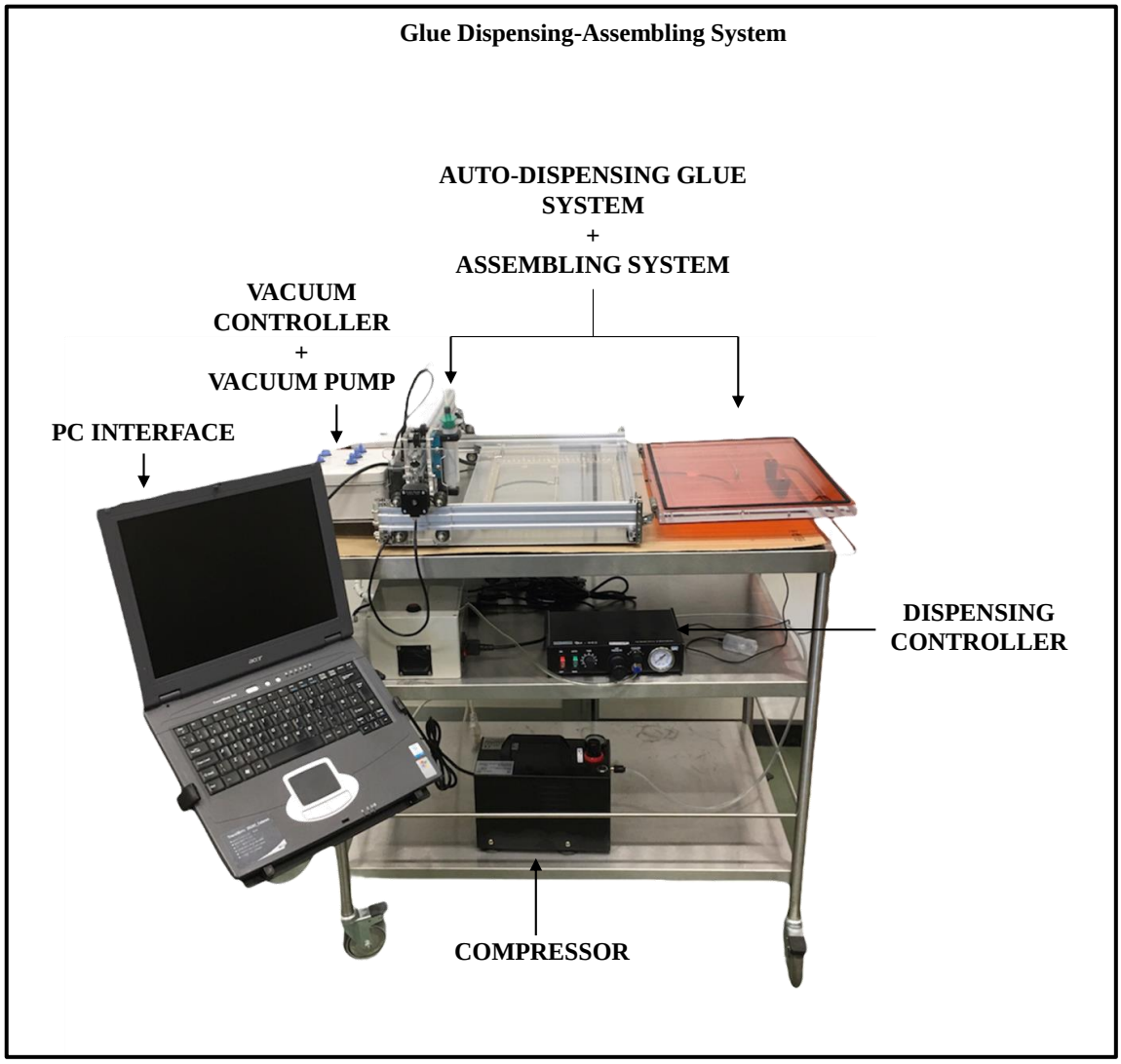

Figure 4.4.3.1.17. The Glue Dispensing-Assembling System for the electrochromic devices.

The Mobile Dosing Syringe is provided of a dispenser stand where the syringe can be alloyed and several Steel Needle/Tips to realize a continuing dispensing of the chosen glue as shown in Figure 4.4.3.1.18.

Figure 4.4.3.1.18. The Mobile Dosing Syringe, the UV-LOCA TP-2500F Glue and the available tips.

The time required for the glue's curing was experimental established in accordance with the technical datasheet of the UV-LOCA TP-2500F [9].

Regarding, the definition of the pattern of the glue dispensing on the substrate's surface, the Laser RGBL software [10] has been installed on the personal computer. The software allows the selection of the best path for the dispensing of the glue on substrates of different sizes. In Figure 4.4.3.1.19 is shown a snapshot of the control interface of the software, where there is an ideal path (continue red line) for the dispensing glue on a substrate.

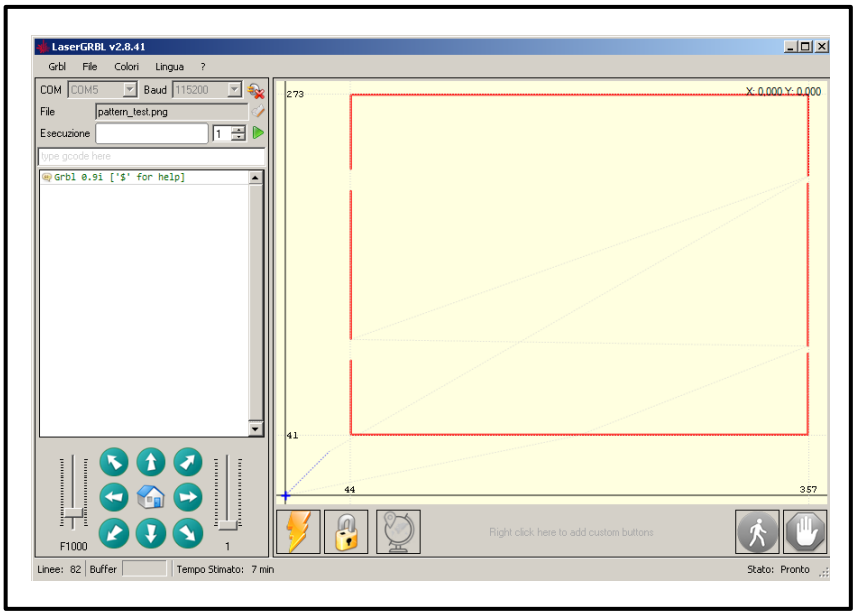

Figure 4.4.3.1.19. The user's interface of the Laser RGBL software installed on the PC of the Glue Dispensing-Assembling System.

An example of continued dispensing of glue and the Glue Dispensing-Assembling system in the ON state during the testing of the exposition of the UV-light performances is shown in Figure 4.4.3.1.20 a-b.

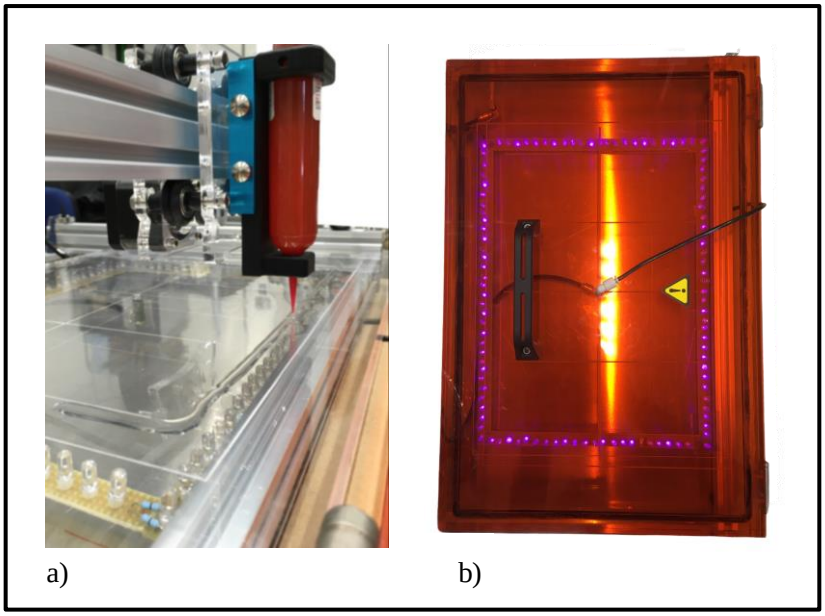

Figure 4.4.3.1.20. a) Example of a continued glue dispensing and b) the Glue Dispensing-Assembling system in the ON state during the exposition of the electrochromic cell to the UV light.

4.4.3.2 Etching Procedure of patterned ITO glasses

To produce large-electrochromic devices, the control of the electrical properties is fundamental to obtaining a homogenous coloration of the devices. To prevent the potential drop and to assure the electrical control of the device under the application of a voltage, specific treatments of the transparent conducting substrates (commercial glasses) are needed.

Basically, the working idea consists of the application of the etching procedure to realize on the indium-tin-oxide coated side an ordered pattern of tracks by removing the coating and creating a kind of transparent pattern.

The main operating steps of the etching treatment of the ITO sheets are given in the schematic block diagram depicted in Scheme 4.4.3.2.1.

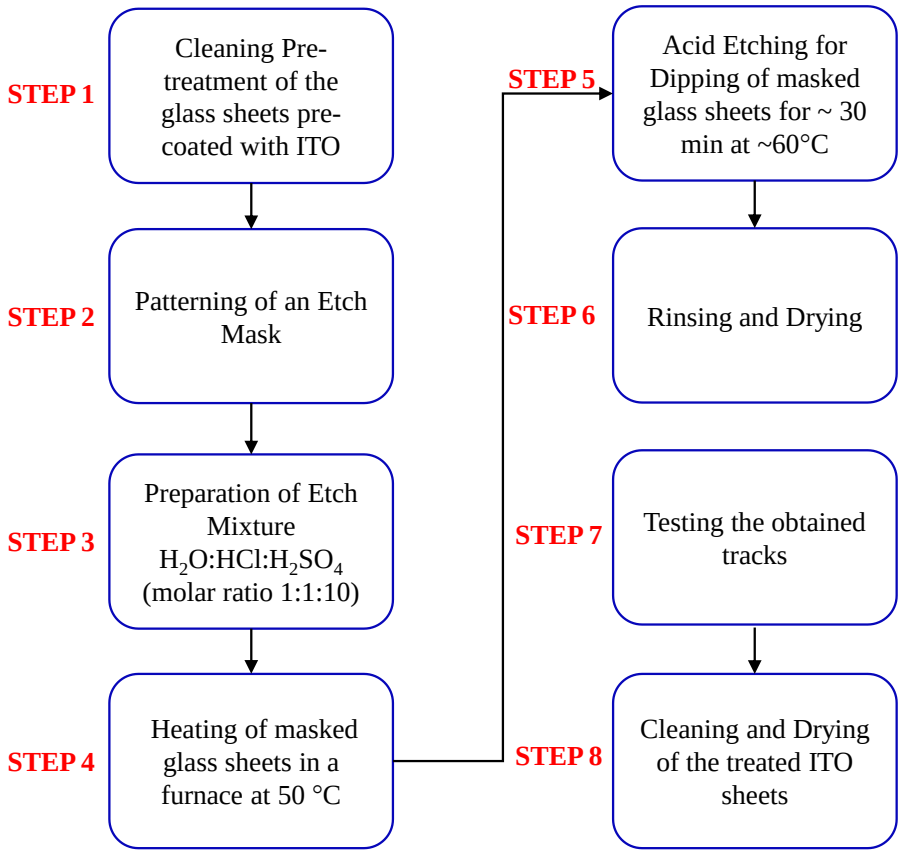

Scheme 4.4.3.2.1. Schematic diagram of the Etching procedure for the fabrication of the ITO tracks.

The accurate procedure was carried out in the clean room, where the yellow filter light (yellow illumination) was set in the room. *STEP 1* involves the cleaning pre-treatment of the ITO coated sheets to the removal of all substances not belonging to the substrate. *STEP 2* involves the creation of an etching mask by covering the ITO side of the glass sheets with patterning tape. *STEP 3* consists of the preparation of the etch mixture based on the acid solution of deionized water, hydrochloric acid (37 %) and sulfuric acid (98%) in the molar ratio (1:1:10). The acid etch solution is heated at the etching temperature of about 60 °C and the control of the temperature is performed by a temperature-controlled system comprising of a suitable sensor (control precision ±0.2 °C). *STEP 4* involves the heating of the masked ITO sheets in a furnace at about 50 °C for about 30 min. *STEP 5* includes the dipping of the ITO masked sheets in the etch solution for 30 min at ~60 °C. The process involves the removal of the ITO material following the tracks and no hurting to the glass substrates. *STEP 6* consists of the final rinsing with deionized water and drying with a gentle stream of air. The obtained ITO tracks are tested using a digital tester. STEP 8 involves a final cleaning and drying procedure of the treated ITO sheets.

In Figure 4.4.3.2.1 is shown the etching mask realized by taping the side of the glass sheet of size (16 cm × 16 cm) covered by ITO. The minimum size of the realized ITO track width is 0.5 mm.

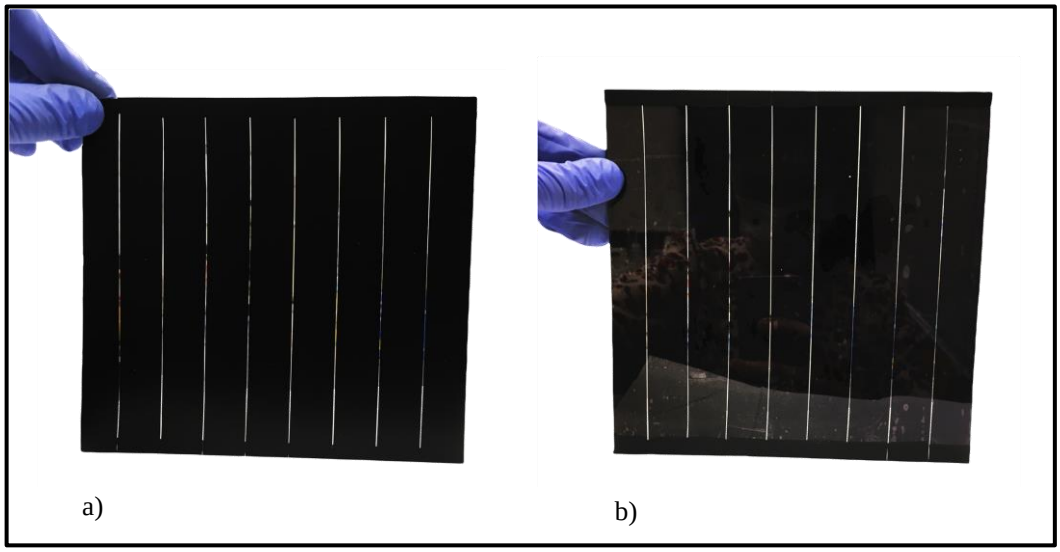

Figure 4.4.3.2.1. a) Frontal view of the etch mask created on the ITO-coated glass side and b) Frontal view of the non-conductive side of the commercial glass.

The setup used for the dipping of the masked ITO glass sheets is shown in Figure 4.4.3.2.2.

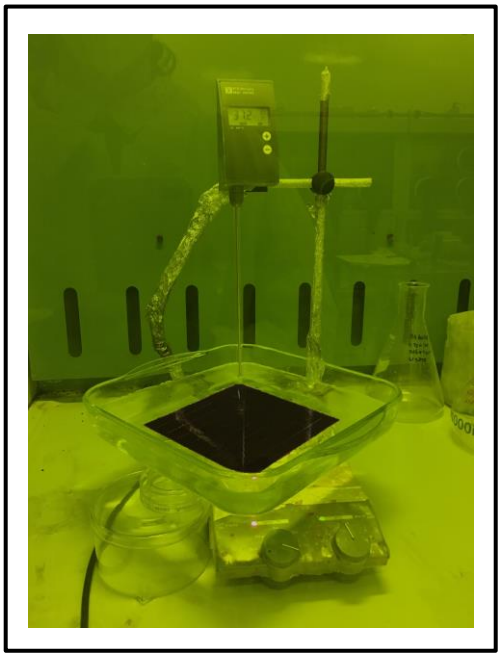

Figure 4.4.3.2.2. Setup for the dip of masked glass sheets in the acid etch solution.

In Figure 4.4.3.2.3 are shown the obtained ITO tracks and their magnification.

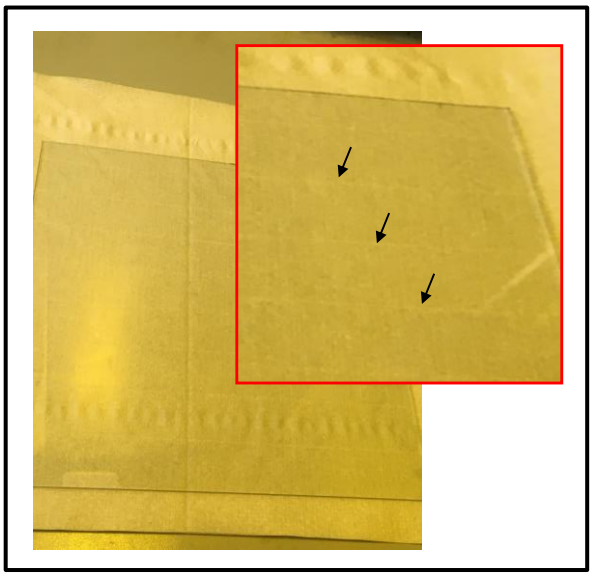

Figure 4.4.3.2.3. The obtained ITO tracks on the surface of a glass sheet. In the upset (red square) is shown the magnification of the glass sheet surface and the ITO tracks are indicated by the black arrows.

Two ITO glass sheets have been treated using the etching process and then they have been used to realize a prototype of an electrochromic device of sizes (16 cm × 16 cm). The two glass sheets have been assembled forming a matrix of pixels, where each pixel can be powered separately. In Figure 4.4.3.2.4 is shown the electrochromic device (16 cm × 16 cm) and the magnification of the grid of the pixels.

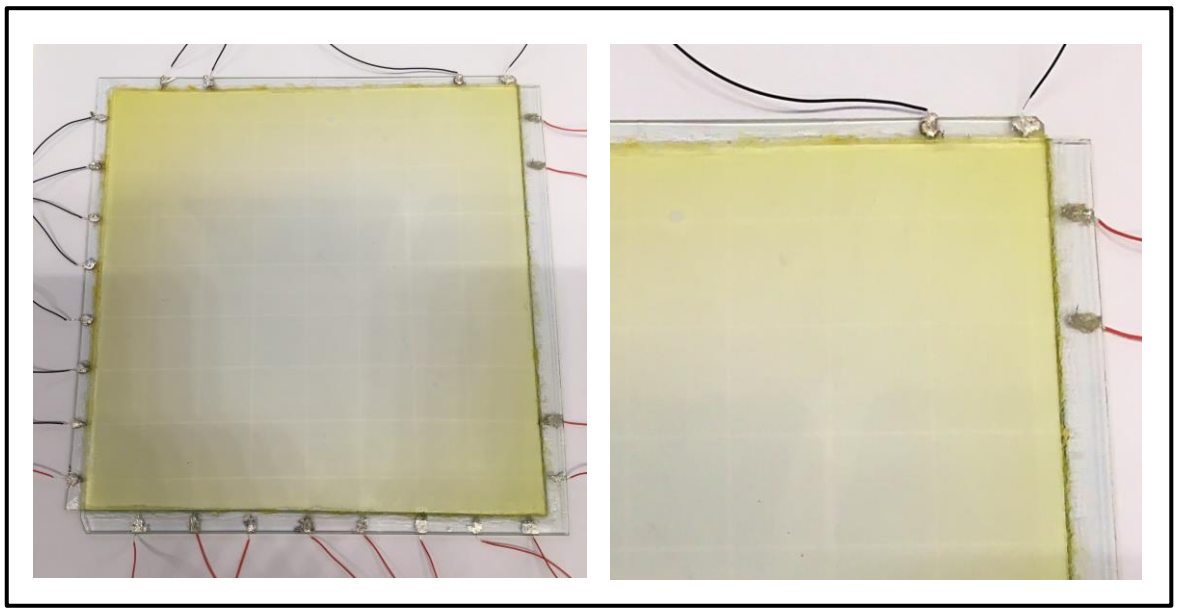

Figure 4.4.3.2.4. Prototype of an electrochromic device (16 cm × 16 cm) based on Ethyl viologen diperchlorate, 1,1'-Diethyl Ferrocene, Bisphenol-A glycerolate diacrylate and Irgacure 651.

In Figure 4.4.3.2.5 are shown the OFF/ON states of an individual pixel of the prototype of an electrochromic device based on the mixture of Ethyl viologen diperchlorate, 1,1'-Diethyl Ferrocene, Bisphenol-A glycerolate diacrylate and Irgacure 651 of size (16 cm × 16 cm).

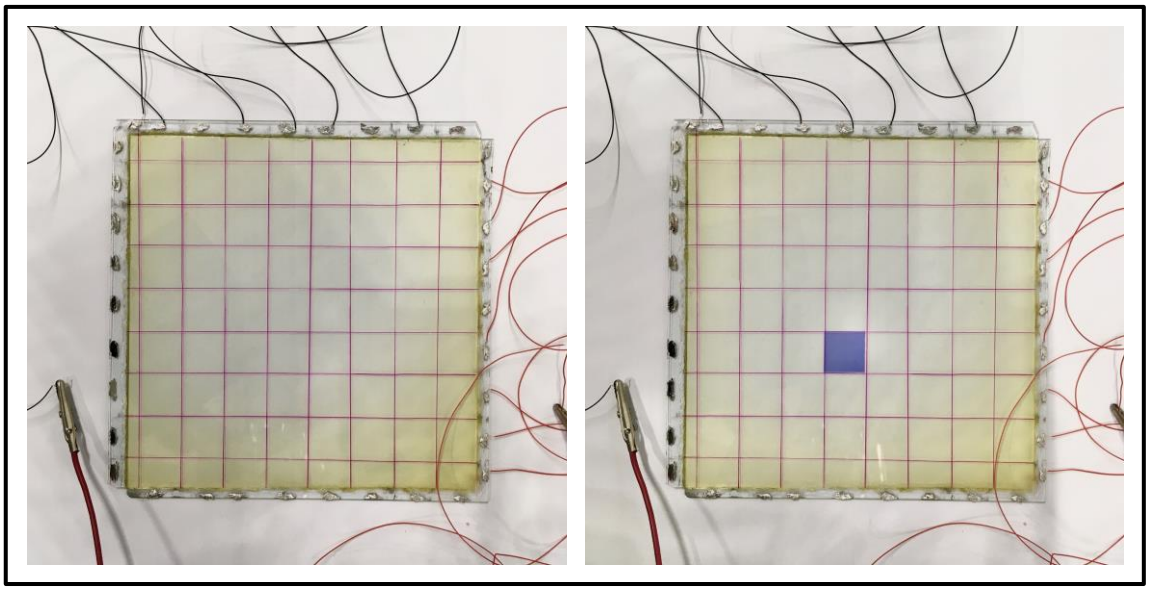

Figure 4.4.3.2.5. Prototype of an electrochromic device (16 cm × 16 cm) based on the individual switching OFF/ON of the pixels.

4.4.4 Conclusions

The implementation of three automated assembly systems for the future fabrication of an electrochromic device of large-area has been proposed. A Knife Coating system, a Filling system and a Glue Dispensing-Assembling System have been developed. The Knife Coating system is projected for the deposition of materials of a desired thickness. The Filling system can be adopted for the automated filling of a device and the last one, the Glue Dispensing -Assembling Systems has been projected to propose an automated and industrialization idea of sealing the device after the exposure to the UV lights. The Etching procedure has been applied to developing the fabrication of the ITO tracks on glass sheets suitable for electrochromic devices. A large-area prototype of an electrochromic device based on the mixture of Ethyl viologen diperchlorate, 1,1'-Diethyl Ferrocene, Bisphenol-A glycerolate diacrylate and Irgacure 651 of size (16 cm × 16 cm) has been developed.

4.4.5 References

[1] M. Casini, M. *Renew. Energy*, (2018) **119** 923-934.

[2] C. Granqvist, P. Lansaker, N. Mlyuka, G. Niklasson, E. Avendano, E. *Sol. Energy Mater. Sol. Cells*, (2009) **93** 2032-2039.

[3] A. Azens, C. G. Granqvist, *J. Solid State Electrochem*., (2003) **7** 64-68.

[4] F. Aleo, A. Pennisi, S. Scalia, F. Simone, *Electrochim. Acta*, (2001) **46** 2243-2249.

[5] R. Baetens, B. P. Jelle, A. Gustavsen, *Sol. Energy Mater. Sol. Cells*, (2010) **94** 87-105.

[6] A. Herrera, *Journal of Coated Fabrics*, (1991) **20** 289-301.

[7] B. Roth, R. R. Sondergaard, F. C. Krebs, in *"Chapter 7-Roll-to-roll printing and coating techniques for manufacturing large-area flexible organic electronics"* Woodhead Publishing, (2015).

[8] A. Berni, M. Mennig, H. Schmidt, in "*Chapter 2- Doctor Blade* in *Sol-Gel Technologies for Glass Producers and Users*". Springer, Boston, MA, (2004).

[9] https://multi-com.eu/detailsid_pr14301keyuv-loca-tp-2500f-liquid-opticalclear-adhesive-glue-50-gsmenuservice_tools.html.

[10] https://lasergrbl.com/.

General Conclusions and Future Perspectives

This thesis work focused on the study of promising electrochromic materials and some classes of electrolytes needed for the construction of the electrochromic devices to be used for energy-saving of buildings.

Electrochromic devices based on thin films of tungsten trioxide and titanium dioxide have been fabricated and interesting results have been obtained for what concerns their application of modulation of the incident radiation in the UV-Vis-NIR region.

Micro-Raman Spectroscopy confirms that the annealing treatments at 100°C and at 300°C let the WO_3 and TiO_2 thin films in the amorphous states while the highest thermal treatment at 500°C induces the formation of the crystalline phase of the two metal-oxides.

WO_3 and TiO_2 thin films have been characterized by Cyclic Voltammetry. The Randles-Sevcik method has been assessed experimentally for the estimation of the diffusion coefficient of the lithium ions in the liquid electrolyte and gel polymer electrolyte.

Diffusion coefficients have been established in both liquid electrolyte and gel polymer electrolyte media. The highest values of the diffusion coefficient in the liquid electrolyte have been found for the WO_3 and TiO_2 films treated at 300 °C which are at the same scan rate (300 mV s^{-1}) equal to D_{jpc}= 1.628 $\times 10^{-11}$ cm^2 s^{-1} and D_{jpc}= 0.731 $\times 10^{-11}$ cm^2 s^{-1}, respectively. The WO_3 and TiO_2 films treated at 300 °C show the highest values of diffusion coefficient also in the gel polymer medium: D_{jpc}= 0.673 $\times 10^{-11}$ cm^2 s^{-1} and D_{jpc}= 0.317 $\times 10^{-11}$ cm^2 s^{-1}. Single electrodes of WO_3 and TiO_2 annealed at 100 °C, 300 °C and 500 °C have been assembled in electrochromic devices and then characterized by Cyclic Voltammetry, which confirms their electrochromic properties.

UV-Vis-NIR spectroscopic analysis has shown that, among the different electrochromic devices built by using WO_3 and TiO_2 annealed at 100 °C, 300 °C and 500 °C, the best devices have been that made by the TiO_2 annealed at 500°C and WO_3 annealed at 100 °C and 30 0°C (W_1Ti_5 and W_3Ti_5). At 550 nm the W_1Ti_5 and W_3Ti_5 devices show higher values of coloration efficiency equal to 179.10 cm^2/C and 139.93 cm^2/C. Whereas, in the NIR region, the same devices show higher values of coloration efficiency equal to 234.81 cm^2/C and 209.03 cm^2/C. The switching times of W_1Ti_5 and W_3Ti_5 devices are equal to 10s and 100 s. These electrochromic devices could be used in order to control the light flux but also the heat flux and so, those devices could be used for energy-saving applications.

A detailed study of the electrolytes (liquid and gel polymer), which are the essential component of a typical electrochromic device regarding the ion conductions, have been conducted to select the best one for the future production of electrochromic devices. Liquid electrolytes based on the solution of $LiClO_4$ in propylene carbonate and in a mix of propylene carbonate and ethylene carbonate at the different concentrations (0.1M, 0.5 M, 1 M 2 M) have been studied. PMMA-based gel polymer electrolytes have been prepared in $LiClO_4$ solution in propylene carbonate and in a mix of propylene carbonate and ethylene carbonate at the salt concentrations (0.1M, 0.5 M, 1 M 2 M).

The increased interactions between the lithium ions, the solvent molecules, the counter ions and the polymeric chains, as a function of salt concentration, have been deeply studied. DSC technique revealed that the systems made by PMMA and the mix of propylene carbonate and ethylene carbonate, show lower T_g with respect to those systems that use only propylene carbonate. Thermal analysis indicated residual MMA monomer could be present in the PMMA used to make the gels. Since the monomer is known to plasticize PMMA the resulting increase in polymer chain segmental motion could be responsible for the high ion conduction for the PMMA-Li-PC-EC system. The stability of the polymeric gel electrolytes has been obtained for a voltage of about 4 V by Linear Sweep Voltammetry investigations. The highest value of conductivity (σ = 0.031 S cm^{-1} at 1 M) has been found for the system (20:80) % w/w PMMA-Li-PC-EC.

All-in-one electrochromic device viologen-based; 10 cm × 10 cm has been made by the photolithography technique. The electrochromic device shows a color change from the OFF to the ON state associated with the redox process of the $EV^{2+}/EV^{\bullet+}$ couple. The reversible behavior of the device has been studied by Cyclic Voltammetry. Micro-Raman spectroscopy has been conducted in the potential range between 0 V and 3 V and it confirmed the presence of the $EV^{\bullet+}$ responsible of the blue color of the electrochromic device in the ON state.

The optical properties of the electrochromic devices have been studied by UV-Vis-NIR spectroscopy. The transmittance at 400 nm results to be 59.6 % in the OFF state (at 0 V) while in the ON state the transmittance is equal to 0.48 % (3 V). At 606 nm the transmittance changes from 84.58% (OFF state, 0 V) to 1.01% (ON state, 3 V). Quite important for energy-saving applications, are the transmittance values obtained in the NIR region. In this region, at 890 nm, the transmittance decreases from 74.3 % in the OFF

state (0 V) to 23.7 % in the ON state (3 V). High values of CCR% (color contrast ratio) were obtained in both visible and NIR regions: at 400 nm, the CCR % is around 99.18 %, at 606 nm the CCR % is about 98.69 and at 890nm it is equal to 68.02 %. In addition, high values of CE (coloration efficiency) have been obtained. At 400 nm the CE is equal to 510.6 cm^2 C^{-1}, while at 606 nm the device shows a CE of 460.3 cm^2 C^{-1}. These values of CE in the visible region support their use as smart windows with high coloration efficiencies. In the NIR region, at 890 nm, the CE is 120.9 cm^2 C^{-1} which indicates that the device can be used to promote the energy saving of the building.

Prototype of electrochromic devices of magnitude 16 cm × 16 cm based on the mixture of Ethyl viologen diperchlorate, 1,1'-Diethyl Ferrocene, Bisphenol-A glycerolate diacrylate and Irgacure 651 have been fabricated. The Etching technique has been applied to realize ITO tracks on the ITO-glass substrates, obtaining then a matrix of pixels. The ON/OFF states of the prototype are shown in Figure 5.1. As shown, in the device each pixel of an electrochromic matrix can be switched ON and OFF separately.

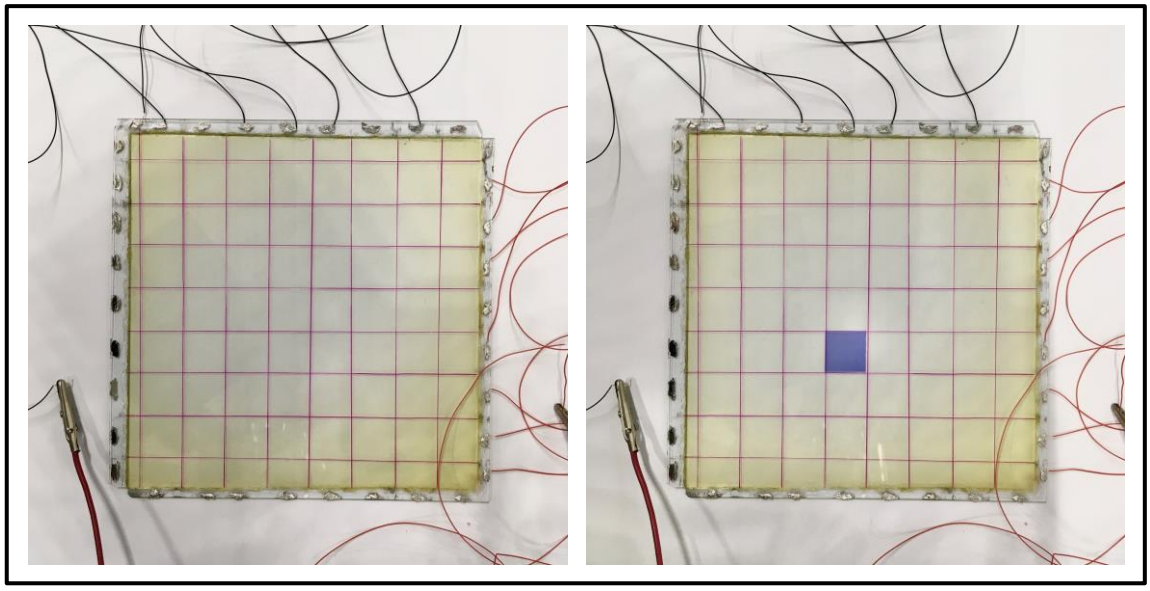

Figure 5.1. Prototype of an electrochromic device (16 cm × 16 cm) based on the matrix of pixels, where each pixel can be switched OFF/ON.

In order to make a scale-up of the device developed on a laboratory scale, during this thesis has been projected and developed some preliminary instruments which can allow

obtaining a semi-automatic plan pilot: a Knife Coating system, Filling system and a Glue Dispensing-Assembling System.

In conclusion, the field of electrochromic technology is wide and this thesis represents only a starting point for further studies about new electrochromic materials and large-area devices.

Acknowledgment

I would like to thank my Scientific Supervisor, Dr. M. Castriota, for giving me the opportunity to be part of his research team. He has been my scientific and moral guide on this journey. He introduced me to the scientific research world and he taught me how important it is to know how to organize one's scientific research.

A special thanks also go to Dr. D. Teeters for his precious human support and scientific advice during my stage at the "The University of Tulsa, OK, United States". He taught me how interesting, difficult, and charming the scientific world and he encouraged me anytime. I will always be deeply grateful for the time spent far from home and that I was fortunate enough to have him as my scientific guidance.

A special thanks also go to Prof. Enzo Cazzanelli for his precious advice and scientific support.
Finally, big thanks go also to all people that contributed to my academic growth.

La borsa di dottorato è stata cofinanziata con risorse del
Programma Operativo Nazionale Ricerca e Innovazione 2014-2020 (CCI 2014IT16M2OP005),
Fondo Sociale Europeo, Azione I.1 “Dottorati Innovativi con caratterizzazione Industriale”

UNIONE EUROPEA
Fondo Sociale Europeo